

UNIVERSITY OF OKLAHOMA

GRADUATE COLLEGE

FRACTURING OF LAYERED RESERVOIR ROCKS

A DISSERTATION

SUBMITTED TO THE GRADUATE FACULTY

In partial fulfillment of the requirements for the

Degree of

DOCTOR OF PHILOSOPHY

By

SETH BUSETTI
Norman, Oklahoma
2009

FRACTURING OF LAYERED RESERVOIR ROCKS

A DISSERTATION APPROVED FOR THE
SCHOOL OF GEOLOGY AND GEOPHYSICS

BY

Dr. Ze'ev Reches, Chair

Dr. Kyran Mish

Dr. Shankar Mitra

Dr. Kurt Marfurt

Dr. Jean-Claude Roegiers

Dr. Leonid Germanovich

© Copyright by SETH BUSETTI 2009
All Rights Reserved

ACKNOWLEDGEMENTS

I am grateful to my advisor Dr. Ze'ev Reches, who guided this research and challenged me to pursue the highest standard of excellence. Ze'ev readily offered his time and erudition, deftly tempered by sagely anecdotal wisdom. Many thanks go to Dr. Kyran Mish, who graciously offered his mentorship for several semesters and loaned the workstation for the FEM simulations. Thank you to the remaining members of the advising committee: Dr. Shankar Mitra, Dr. Kurt Marfurt, Dr. Jean-Claude Roegiers, and Dr. Leonid Germanovich. I appreciate your willingness and uncommon flexibility in helping me pursue this degree. I cannot overstate my gratitude to Devon Energy and ConocoPhillips for the internship experiences, participation in research, and for the extensive financial support. Devon Energy provided for all of the Barnett Shale material. ConocoPhillips funded the computational resources as well as a significant part of the field work. With great sincerity, I wish to recognize my wife Alexis for her encouragement, patience, and enduring sacrifice during these challenging years. Now I can go get a real job.

Finally, I dedicate this work to the One who has lavishly blessed me with so many undeserved gifts at every stage of the process. It has truly been four years of bread and fish, and not a single stone or serpent! I will endeavor to return the investment tenfold.

IT IS HE WHO MADE THE EARTH BY HIS POWER,

WHO ESTABLISHED THE WORLD BY HIS WISDOM,

AND BY HIS UNDERSTANDING STRETCHED OUT THE HEAVENS.

Jeremiah 10:12

TABLE OF CONTENTS

ACKNOWLEDGEMENTS.....	<i>iv</i>
LIST OF TABLES.....	<i>vii</i>
LIST OF FIGURES.....	<i>viii</i>
ABSTRACT.....	<i>xiv</i>
 CHAPTER 1: INTRODUCTION AND FRACTURING MODELS	
<i>Introduction</i>	<i>1</i>
<i>Objectives and Organization</i>	<i>2</i>
<i>Background: Fracturing Models</i>	<i>3</i>
<i>References</i>	<i>19</i>
 CHAPTER 2: NUMERICAL SIMULATION OF ROCKS WITH DAMAGE RHEOLOGY	
<i>Abstract</i>	<i>24</i>
<i>Introduction</i>	<i>25</i>
<i>Rock Rheology</i>	<i>28</i>
<i>Progressive Damage in Rocks</i>	<i>32</i>
<i>Explicit Dynamic Finite Element Solution</i>	<i>40</i>
<i>Finite Element Damage Model</i>	<i>41</i>
<i>Finite Element Simulations</i>	<i>44</i>
<i>Results of Simulations</i>	<i>61</i>
<i>Discussion</i>	<i>68</i>
<i>Summary</i>	<i>69</i>
<i>References</i>	<i>70</i>
<i>Appendix A: Fracture Energy Equivalence</i>	<i>75</i>
 CHAPTER 3: MORPHOLOGY AND DYNAMICAL ANALYSIS OF TRANSIENT HYDRAULIC FRACTURE PROPAGATION IN A ROCK LAYER WITH DAMAGE RHEOLOGY	
<i>Abstract</i>	<i>77</i>
<i>Introduction</i>	<i>78</i>
<i>Complex Hydrofractures</i>	<i>80</i>
<i>FEM Modeling</i>	<i>87</i>
<i>Results: Simulation of Propagation Dynamics</i>	<i>96</i>
<i>Synthesis and Interpretation</i>	<i>119</i>
<i>Summary</i>	<i>137</i>
<i>References</i>	<i>139</i>

<i>Appendix A: FEM Continuum Damage Model</i>	143
<i>Appendix B: Explicit Dynamic FEM Solution</i>	145
CHAPTER 4: MECHANICAL ANALYSIS OF HYDRAULIC FRACTURING IN THE BARNETT SHALE	
<i>Abstract</i>	148
<i>Introduction</i>	149
<i>Part I: Mechanical Models for Hydraulic Fracturing</i>	153
<i>Analytical Model for Reactivation of Natural Fractures</i>	153
<i>FEM Model for Fracture Propagation</i>	160
<i>Part II: Application of the Models to Barnett Shale Stress Data</i>	169
<i>Reservoir/Geologic Setting</i>	169
<i>Present Geomechanical Analysis</i>	180
<i>Summary</i>	195
<i>References</i>	198
CHAPTER 5: ZONES OF HIGH FRACTURE DENSITY IN LAYERED ROCKS	
<i>Background</i>	201
<i>Field Studies Near Cedar Mountain, Utah</i>	217
<i>Field Studies of the Jackfork Group, Oklahoma and Arkansas</i>	225
<i>Summary</i>	243
<i>References</i>	244
CHAPTER 6: CONCLUSIONS AND FUTURE WORK.....	
<i>Conclusions</i>	250
<i>Recommendations for Future Work</i>	253
<i>References</i>	256

LIST OF TABLES

Table	Page
2.1 Material Parameters for Berea Sandstone	48
2.2 Model Parameters for Berea Sandstone Rheology	48
3.1 Summary of Simulations (Hydrofracture)	93
4.1 Stress Data for Barnett Shale Wells	174
4.2 Results of Fracture Reactivation Model	175
5.1 Outcrop Gamma-Ray Log Measurements	232

LIST OF FIGURES

Figure		Page
1.1	Irwin (1958 near field solutions for the stress fields around a slit-like plane crack	7
1.2	Schematic of opening and closure of a crack increment	8
1.3	Schematic of a semi-infinite body with (a) straight edge crack and (b) surface half-penny crack	9
1.4	Schematic of cusped crack profile with cohesion zone	12
1.5	Load-displacement curve for rock with acoustic emissions log and schematic illustrations of microfracture process ahead of the crack tip	14
1.6	An example of damage schemes used in numerical simulations to simulate damage propagation during dike segment interaction	17
2.1	Flow-chart showing organization of Chapter 2	27
2.2	Stress-strain curves for limestone and sandstone	30
2.3	Typical stress-strain response for rock under confining pressure and corresponding microcrack maps	31
2.4	Bar charts from tensile propagation experiments on Berea Sandstone showing that the distribution of damage increases nonlinearly near the fracture	33
2.5	Plot for the experimental deformation modulus, D	35
2.6	Post-yield curves for plastic strain and damage evolution used in the FEM rheology	43

2.7	Schematic of four point beam experimental configuration and experimental stress-strain curves for Berea sandstone	49
2.8	Sample configuration for dogbone extension experiments and experimental stress-strain curves for Berea sandstone	50
2.9	Plots of experimental results for damage evolution in compression and tension	51
2.10	3D FEM model of the four point beam configuration and simulated stress-strain curve	52
2.11	3D FEM model of the dogbone configuration and simulated stress-strain curves	53
2.12	Schematic of (a) Mohr-Coulomb and (b) Barcelona yield surfaces in principal stress space	57
2.13	Plot of stress paths in p' - q space for the dogbone configuration	64
2.14	Contour plots of the tensile damage parameter for the four point beam configuration at four stages of deformation	65
2.15	Contour plots of tensile damage for the dogbone setup with 10 MPa confining pressure	66
2.16	Plot of curvature and damage versus distance from the center of the four point beam simulations	67
3.1	Photograph of induced hydrofractures in an excavated coal mine	82
3.2	Photograph of laboratory induced hydrofracture	84
3.3	Laboratory induced hydrofracture in PMMA	86
3.4	FEM model configuration for a single hydrofracture segment	89

	Propagating through the reservoir and into a sandstone layer	
3.5	Schematic of the constitutive model for the FEM damage rheology (a) and plots of post-yield stress-strain (b) and damage in tension and compression (c)	91
3.6	Plot of pressure loading conditions for uniform and distributed internal pressure loads in an initial crack	95
3.7	Damage contour maps from FEM simulations showing damage main morphological features of hydrofracture segments	99
3.8	An example of a simulated complex hydrofracture formed under a strongly heterogeneous tectonic stress regime	101
3.9	Plots showing evolution of the damage parameter versus normalized dissipated fracture energy	109
3.10	Plots showing sequence of damage build-up in the main fracture path	113
3.11	Contour map showing the effect the loading conditions on cumulative damage evolution from 11 FEM simulations	115
3.12	Contour plots of the ratio of damage in compression to damage in tension for all 22 hydrofracture simulations	118
3.13	Plot showing crack half-width displacement and kinetic energy for (a) extension test 1 and (b) extension test 3	123
3.14	Plot of damage vs. normalized dissipated damage energy showing changes in stability and damage transference	127
3.15	Stress paths for a region in-plane (a) and out-of-plane (b) to the main fracture path, plotted for four tectonic stress states	131
3.16	Morphological features preserved on joint surfaces	135

3.17	Photographs of branching and segmented fractures	136
4.1	Map showing location of the Barnett Shale play and major structural features	150
4.2	Stereographic projection showing the calculated limits for fracture orientations reactivated in dilation or shear-slip	155
4.3	Mohr-circle plots showing the reactivation conditions for fractures in dilation (a and b) and in shear (c)	156
4.4	Finite element model configuration and schematic of the geologic scenario for hydrofracture propagation simulations	162
4.5	Examples of simulated hydrofracture segments formed under a range of stress regimes	166
4.6	Contour map showing the effect of loading conditions on cumulative damage evolution	167
4.7	Seismic structural interpretations of collapse-related flexures and fracture corridors in the Barnett Shale study area	171
4.8	Pump-in test for well SW1-MDT2	177
4.9	Pump-in test for well SW1-MDT3	177
4.10	Hydrofracture stage 2 for well Sh3	178
4.11	Hydrofracture stage 3 for well Sh3	178
4.12	Hydrofracture stage 3 for well SW1	179
4.13	Top-view map of distribution of monitored microseismic events for four hydrofracture stages in a horizontal well, Barnett Shale	184
4.14	Plot showing cumulative damage vs. simulation time from	188

	FEM simulations	
4.15	Plot showing microseismic event count vs. Estimated Stimulation Volume for well Sh3	189
5.1	Relations between fracture spacing and layer thickness, (a) plot of fracture spacing data for three lithologies, (b) photograph of layers in the Jackfork Group, (c) a 2D schematic for the case of extension	203
5.2	Plot of the relationships between V_p and porosity for two rock types	205
5.3	(a) Compilation of fracture intensities in field and experiments and (b) a scheme for the four classes of intensity	208
5.4	1-D logs showing fracture spacing distribution along a single scan line	210
5.5	Photograph and statistical data for (a) quasi-uniform (b) clustered and (c) branching fractures in rock layers	211
5.6	Histograms for measured fracture distributions from Figure 5.5	214
5.7	Cumulative distribution logs showing fracture distribution relative to the normal distribution	215
5.8	Histogram for scanlines 7a-7e for fractures in Figure 5.5b	216
5.9	Location map of the study area close to Cedar Mountain, Utah	218
5.10	Photograph and profilometer view on a fracture surface with plumose marks from the Cedar Mountain field location	220
5.11	Stratigraphic sections for the Carmel Formation, Utah	221
5.12	View of a fractured bedding surface near Cedar Mountain	223

5.13	Interpreted photograph and scanlines for a fault zone near Cedar Mountain	224
5.14	Location of the Jackfork sandstone quarries in Sawyer, OK and Kirby, AR	226
5.15	Interpreted photograph and fracture orientation data for sandstone layers at the Sawyer Quarry.	227
5.16	Photograph of three faces of the ‘upper sand’ at the Kirby Quarry	229
5.17	Gamma ray logs and cross section showing facies in the upper sand at the Kirby Quarry	230
5.18	Photograph of fractured layer highlighting fluid flow	234
5.19	Plots showing spacing distributions for facies 1	237
5.20	Plots showing spacing distributions for facies 2	238
5.21	Plots showing spacing distributions for facies 3	239
5.22	Mean spacing vs. layer thickness for facies 1, 2, and 3	240

ABSTRACT

The development of fractures in rock layers reflects a history of complex, non-linear, time-dependent mechanical processes. The processes strongly depend on the rock rheology, particularly the behavior during progressive deformation, layering effects such as the mechanical stratigraphy, and the local stress conditions. In the past, the complex mechanics associated with fracture initiation and propagation contributed to the application of simplified models based on linear rheology and using quasi-static solutions. While this approach is effective in solving infinitesimal strain problems, it provides no explanation for strain localization, damage accumulation and rock failure, and it oversimplifies fracture propagation. The objective of the present work is to contribute to the understanding of these processes.

The approach of this study is as follows. (Chapter 1) Theoretical advancements on fracturing and the concept of continuum damage mechanics are compared with rock mechanics experiments to understand progressive deformation, failure, and fracture propagation for rock. It is demonstrated that non-local (away from the crack-tip) yielding behavior must be considered to understand complex fracturing. (Chapter 2) A numerical rheology based on the elastic-plastic-damage properties of Berea sandstone is developed and calibrated to experimental rock mechanics data. A method for translating the stress-strain curve and acoustic emissions data into a material model included in the commercial finite element code Abaqus is presented. Two rock mechanics experiments are simulated in 3-D to test the rheology model. (Chapter 3) The rheology is implemented into finite element models based on classical hydraulic fracturing configurations. The explicit dynamic finite element method is used to

simulate damage and transient propagation of a hydrofracture segment. It is shown that the complexity of fracturing depends on the local stress-strain response, which is controlled by the evolving damage pattern. The dynamical characteristics of arrest, rupture, branching, and segmentation of the fracture are described in terms of damage evolution. (Chapter 4) An analytical model for natural fracture reactivation is paired with the finite element simulations to understand the development of complex hydraulic fracture networks in the subsurface. The models' predictions are compared with data from hydraulically stimulated wells in the Barnett Shale. Recommendations are made for optimizing hydrofracture operations in wells for different states of stress (Chapter 5). The occurrence of zones of anomalously high fracture density is characterized in a carbonate sequence near Cedar Mountain Utah, and in Jackfork Group sandstone layers in Oklahoma and Arkansas. The results indicate that fracture density should be examined as a function of the evolving rock properties of the host layer in addition to the layer thickness.

The investigation contributes to understanding the process of damage and fracturing during the deformation of rock layers. The results describe the development of mechanical inhomogeneity in fractured rock layers and can be applied to explain the formation of complex hydraulic fractures in unconventional reservoirs.

CHAPTER 1

INTRODUCTION AND FRACTURING MODELS

Layered sedimentary rocks are mechanically heterogeneous due to the presence of innumerable fractures that control deformation and fluid flow. Understanding the mechanisms of fracture formation and their effect on the reservoir is particularly important in tight reservoirs where the fracture networks significantly contribute to the porosity and permeability. This is exemplified in unconventional reservoirs where artificial stimulation is required to produce from rock that would otherwise not be economic. A central task is to characterize the fracture sets (spatial distribution, orientation, intensity and timing) in the reservoir by direct measurement or by modeling and then to determine the effect of the fracture network on hydraulic injections. A common approach is to first identify the structural architecture and then interpret the deformation history via kinematic and/or mechanical modeling. To model the pattern of fractures, direct measurement of the fractures and stress conditions are taken in a few locations and various models are used to predict the stress-strain distribution and the expected fracture pattern everywhere else. Modeling the growth of hydraulic fractures requires mechanical analysis that involves solving for the geologic and operational conditions required to propagate internally pressurized fractures and comparing simulated geometries with actual patterns from the field – i.e., from microseismic events maps.

For practical reasons, this mechanical analysis is frequently based on the simplified assumption that rocks are homogeneous and deform elastically. Two outstanding observations challenge the usefulness of the above two simplifications and have motivated the present study. First, zones with intense fracturing that were identified in numerous field outcrops (Chapter 5) cannot be explained using linear elastic deformation. However, their development and behavior can be explained by nonlinear inelastic deformation with damage evolution (Chapter 2). The latter model accounts for strain localization, strength degradation, and complex failure during finite strain. Thus, even rock layers with very homogeneous lithology become mechanically heterogeneous over time. Second, while investigating hydraulic fracturing operations in Barnett Shale wells (Chapter 4) during a summer internship with Devon Energy, I found evidence for complicated relationships between the propagating hydrofractures, the fractured host rock, and the local state of stress (Chapter 3). The simple analysis tools, which do not consider the effect of natural fracture networks and oversimplify mechanical stratigraphy, are unable to explain the hydrofracture complexity displayed in the field. The main objective of the present dissertation is to improve the tools to explain fracture development by considering realistic mechanical models.

Objectives and Organization

The purpose is to investigate the mechanical processes of fracture development in rock layers, focusing on how the rock rheology affects fracturing. The principal application is the development of mechanical models to understand the formation of hydraulic fracture networks. These topics are presented as three stand-alone

manuscripts (Chapters 2, 3, and 4), and Chapters 1 and 5 comprise supplemental material.

Chapter 1 presents an overview of models for fracturing in rocks, with emphasis on theoretical models for hydraulic fracturing.

Chapter 2 introduces the mechanical basis for progressive deformation in rocks within the context of continuum damage mechanics. A finite element (FE) rheologic model is developed from experimental data for Berea sandstone and then is tested using 3D benchmark simulations in the FE software Abaqus/Explicit.

Chapter 3 implements the numerical rheology in an explicit-dynamic FE model based on a common hydrofracture configuration.

Chapter 4 uses the results of chapter 3 and an analytical model for natural fracture reactivation to investigate hydraulic fracture operations in the Barnett Shale.

Chapter 5 includes ongoing field work on zones of high density fractures in layered sedimentary sequences. Fracture characterization in the Carmel formation carbonates near Cedar Mountain, Utah, and for Jackfork Group rock layers in sandstone quarries in Oklahoma and Arkansas are summarized.

BACKGROUND: FRACTURING MODELS

Rock fractures are divided into faults (shear fractures) with displacement parallel to their surfaces, and joints (tensile fractures) that display dilation normal to their surfaces or no displacement. Some experimental works demonstrated a transition from tensile to shear fracturing (e.g., Ramsey and Chester, 2004). The general term fracture will be used throughout to describe both tensile and shear fractures.

Formation and growth of natural tensile fractures are attributed to several tectonic loading systems. First, bending extension stresses in convex curvature of flexed layers in folds (e.g., Stearns and Friedman, 1972; Cosgrove and Ameen, 2000; Cooper et al., 2001; Buseti, 2003; Maerten et al., 2001). Second, regional extension, via uplift (i.e. basin inversion and exhumation) or crustal relaxation of buried layers (Verbeek and Grout, 1997), in general, forming regionally continuous sets of fractures. Third, far-field compression, where tensile stresses are locally induced by flaws in the rock and failure is enhanced by pore pressure effects (Lorenz et al., 1991; Germanovich and Dyskin, 2000). Fourth, localized extension associated with faults of all types (e.g. Chester et al., 1993; Gross et al., 1997; Finkbeiner et al., 1997; Mayer and Sharp, 1998; Stewart, 2001; Fossen et al., 2005).

Additionally, dikes (Pollard, 1978) and manmade hydraulic fractures (Hubbert and Willis, 1957) are tensile fractures created by the injection of pressurized fluid into fresh or naturally fractured host rock. The classical approach to hydraulic fracture propagation assumes that increasing the internal fluid pressure in a borehole controls propagation according to a straightforward sequence. First, when the injection pressure reaches the minimum horizontal stress at the borehole, which includes overcoming hoop stresses, the rock achieves a local state of stress equilibrium. If the injection pressure then exceeds the tensile strength of the rock, the fracture is capable of mode I propagation. Additional pressure widens the crack depending on the elastic constants of the host rock, and in turn, proportionately lengthens the crack. It is convenient to consider the pressure distribution in terms of the net (or driving) pressure, $P_{\text{net}} = P_f - \sigma_{\text{hmin}}$, where P_f is the fluid pressure load and σ_{hmin} is the minimum

horizontal stress. The Hubbert and Willis (1957) criterion approximates the conditions for fracture propagation as being where the net pressure is equal to or greater than the tensile strength of the rock. The exact dimensions are determined with respect to a priori assumptions for the crack growth (i.e., radial propagation) and the expected pressure-drop along the hydrofracture – for example, approximated using a polynomial function (Haimson and Fairhurst, 1967). As will be demonstrated below and in Chapter 3, this approach may be appropriate for simple hydrofractures, but more advanced mechanical solutions are required for complex propagation.

Fracture mechanics theory indicates that large fractures develop by growth of small, initial flaws that locally amplify stresses, and a fracture propagates when local stresses exceed the strength of the host material (Lawn, 1993). The stresses at the proximity of a fracture are represented by the stress intensity factor, K , which is a function of the remote extension stress (e.g., tectonic), the fracture geometry, and the internal pressure in the crack. Thus, a hydraulic fracture can be idealized as an internally pressurized mode I fracture. Pure tensile fracturing is never the actual case as mode II and III components are always present and influential, even if they are small (e.g., Wu, 2006). As K approaches the fracture toughness K_C , a material property, a fracture begins to grow slowly under subcritical conditions ($K < K_C$) (Atkinson, 1987; Olson, 2004). The fracture propagates unstably and at high velocity when K reaches K_C (Lawn, 1993). Branching and complex fracture growth were attributed to high velocity (dynamic) fracture propagation (Sagy et al., 2001)

FRACTURING OF AN IDEALIZED ELASTIC SOLID

Advancements to Hubbert and Willis' early solution for hydrofracture propagation replaced simple propagation criteria with the crack-tip solutions of linear elastic fracture mechanics (LEFM) (Griffith, 1920; Irwin, 1958). The LEFM method for modeling mode I fracturing constitute developments of the 'near field' solutions for the stress and displacement fields around a slit-like plane crack, Fig. 1.1 (Irwin, 1958). Using this approach, a hydraulic fracture simply reflects a particular loading condition - an internally loaded, mode I crack, and if tectonic stresses are superposed, a mode I crack with mode II and III components. The LEFM approach assumes that the crack tip is infinitesimally sharp and that the material is an idealized Hookean solid with unbounded strength (Lawn, 1993). Irwin's solutions for the stress and displacement around the crack tip are a function of the Young's modulus E , Poisson's ratio ν , stress intensity factor K (a function of crack geometry and load distribution), and location on the crack, r and θ (defining mode I, II, or III opening):

$$\sigma_{ij} = K(2\pi r)^{-1/2} f_{ij}(\theta) \quad [1a]$$

$$u_i = (K/2E)(r/2\pi)^{1/2} f_i(\theta) \quad [1b]$$

for mode I cracks, $\theta = \pm\pi$, $r = X$, and $X = c-x$ (Fig. 1.2), yielding the generalized form:

$$u(X) = (K/E') (8X/\pi)^{1/2} \quad [1c]$$

The stress intensity factor K for a continuous internal pressure distribution on straight and penny shaped crack geometry is shown to be, Fig. 1.3:

$$K = 2(c/\pi)^{1/2} \int_0^c [\sigma_1(x)(c^2 - x^2)^{1/2}] dx \quad (\text{straight crack}) \quad [2a]$$

$$K = 2(c/\pi)^{1/2} \int_0^c [r\sigma_1(r)(c^2 - r^2)^{1/2}] dx \quad (\text{penny shaped crack}) \quad [2b]$$

Crack-tip field and stress-intensity factor, K

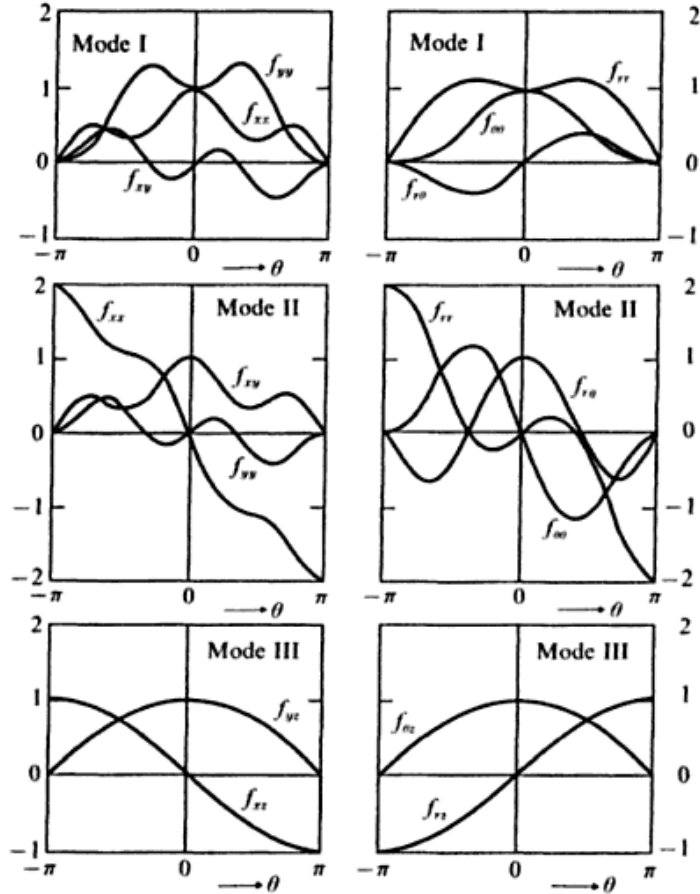


Figure 1.1. Irwin (1958) near field solutions for the stress fields around a slit-like plane crack. Angular distributions shown for the three modes of fracturing, for rectangular (left) and polar (right) components. From Lawn (1993).

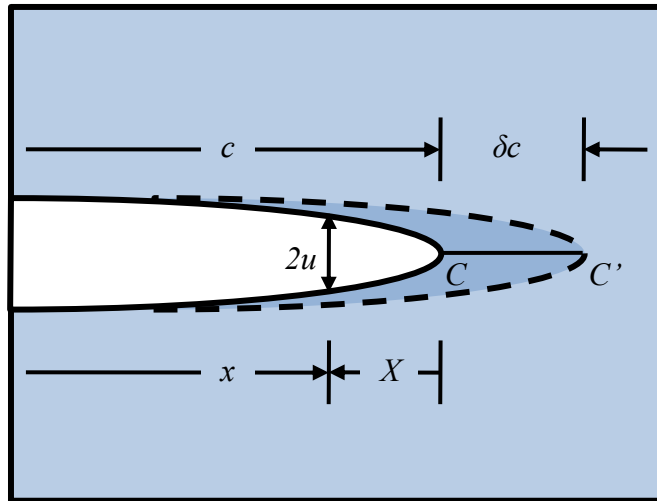


Figure 1.2. Opening (or closure) of crack increment CC' in specimen of unit thickness. Open crack has parabolic profile, in accordance with eq. 1c (after Lawn, 1993)

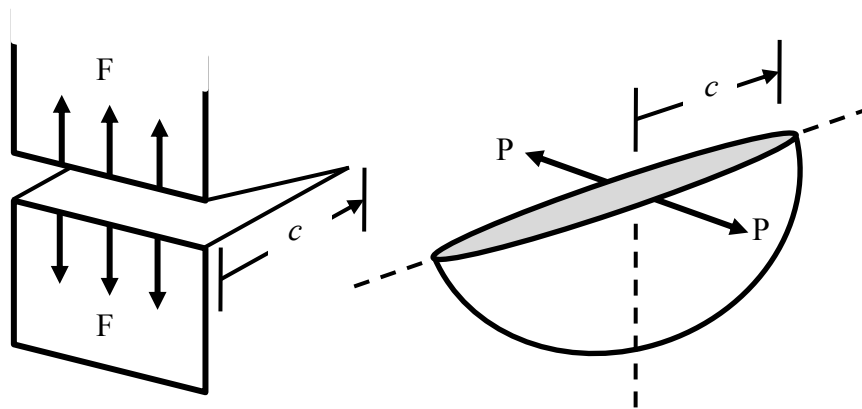


Figure 1.3. Semi-infinite body with concentrated loads on a fracture surface: (a) straight edge crack, line force F per unit length at mouth; (b) surface half-penny crack, point force P at center (after Lawn, 1993). A hydrofracture is a special loading condition, where P is a distributed internal pressure load.

According to LEFM, propagation occurs when the stress intensity factor K_I reaches the critical value of the fracture toughness, K_{IC} , a material property. The amount of energy involved in the process determines how far the crack propagates. When the fracture energy from loading, G , reaches the intrinsic limit of the material, G_C , the fracture extends by length, dc , where $G = -dU/dc = K_I^2 E / (1 - \nu^2) + K_{II}^2 E / (1 - \nu^2) + K_{III}^2 (1 + \nu^2) / E$, and for mode I, $G_{IC} = K_{IC}^2 E / (1 - \nu^2)$. The term U is the mechanical energy of the system and includes the elastic potential within the material and the potential energy from external loading.

Various hydrofracture models based on the form in equation [1b] were developed. For instance, two linear elastic hydraulic fracturing (LEHF) models that are widely used in industry are the PKN model (Perkins and Kern, 1961) and the KGD model (Kristianovic and Zheltov, 1955). The main differences between these models and others are the assumed crack geometry and the factors that go into formulating the internal pressure distribution. One practical feature of the original Hubbert and Willis approach is that the LEHF models generate simple, idealized fracture shapes for which length and height may be determined. The assumption of linear elasticity at the crack-tip introduces a singularity that dominates the local stress field at the crack-tip (e.g., Kanninen and Popelar, 1985). Further, the singularity affects the internal pressure condition, which, if based on lubrication theory, must be relaxed by introducing a fluid lag region (Kristianovich and Zheltov, 1955; Desroches, et al., 1994). While the LEHF crack may approximate the behavior relative to the remote stress field, it distorts stress values and limits the usefulness to explain real fracture behavior. Barentblatt and

others proposed that a solution to this problem was to relax the elastic conditions in the region of the crack-tip.

FRACTURING OF AN ELASTIC SOLID WITH CRACK-TIP AND FRONTAL ZONE YIELDING

In the modification, a small zone defined by a nonlinear cohesive stress function $p_\gamma(X)$ replaces the singularity at the tip of the crack (Barenblatt, 1962). The cohesive zone accounts for the fact that materials do have a stress limit, governed by interatomic stresses (Barenblatt, 1962) or plastic yield stresses (Dugdale, 1960). The cohesive zone at the crack tip (Fig. 1.4) introduces a new crack profile that is no longer parabolic but takes on a cusped form, where the fracture narrows at the crack tip. In this case, propagation occurs when the stress intensity factor K reaches the critical value of the fracture toughness of the cohesive zone, or the intrinsic toughness, given for a straight crack as (Lawn, 1993):

$$K_0 = (2/\pi)^{1/2} \int_0^\lambda p_\gamma(X) dX/X^{1/2} \quad [3]$$

where λ is the length of the nonlinear cohesive zone, defined by $p_\gamma(X)$. The contribution of the cohesive zone to the fracture resistance ($R_\mu = -K_\mu$) defines the cohesive zone yield criteria and is the area under the curve $p_\gamma(X)$, referred to as the load-displacement curve or equivalently the fracture energy. The J-integral technique (Rice, 1968) effectively solves the energy balance around the nonlinear cohesive zone so long as the stress-strain characteristics are reversible. If dissipative processes are considered, additional steps are required, for example, limiting plastic deformation by enforcing monotonic loading or by introducing a shielding zone (Lawn, 1993). In the latter case, line integrals are solved for each zone and the resulting global K or G

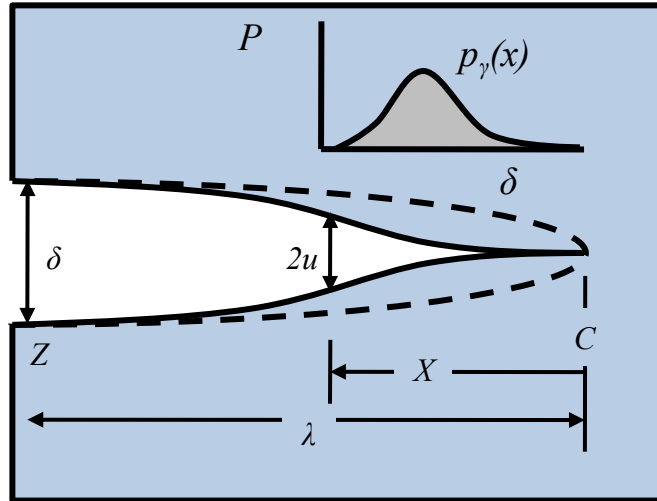


Figure 1.4. Crack profile at cohesion zone (solid curve) relative to the parabola (dashed curve) solution of an elastic material. Note how cohesive stresses close contour into a cusp at crack tip C. Overlain at top is the stress-separation function (after Lawn, 1993).

comprises a superposition of cohesive zones for the intrinsic crack-tip (K_0 or G_0) and extrinsic shielding regions (K_μ or G_μ).

$$K = K_0 + K_\mu \quad [4]$$

The shielding concept (Thompson, 1986) accounts for the fact that many materials exhibit toughening at the crack tip which is independent of external loading conditions and results in an effective ‘blunting’ of the crack tip. Shielding mechanisms include a zone of dislocations, microcracks, and phase transformations preceding the crack tip. The contribution of the shielding zone to the fracture resistance ($R_\mu = -K_\mu$) is the J-integral around the shielding zone (Lawn, 1993):

$$J_\mu = -R_\mu = -2 \int_w^0 U(y) dy \quad [5a]$$

$$= 2w \int_0^{\epsilon_\mu} \sigma_\mu(\epsilon_\mu) d\epsilon_\mu \quad [5b]$$

where w is the half-width of the shielding zone and $\sigma_\mu(x)\epsilon_\mu(x)$ defines the constitutive relationship for the zone, for example, the stress-strain relationship for microcracking. The application of a nonlinear crack-tip and a zone of shielding is of particular relevance to fracture propagation in rocks, which exhibit macroscopic propagation via coalescence and linkage of microcracks within a damage front (Lockner and Byerlee, 1977; Lockner et al., 1992). Experimental observations indicate that the physical location of the crack-tip in rocks is ambiguous due to propagation of a nonlinear crack-tip and frontal zone. Fig. 1.5 shows a load-displacement curve for rock and the corresponding microcracking process ahead of the crack tip: (i) initial state, (ii) crack initiation, (iii) small growth and linkage, and finally (iv) large growth and linkage (Takahashi and Abe, 1987).

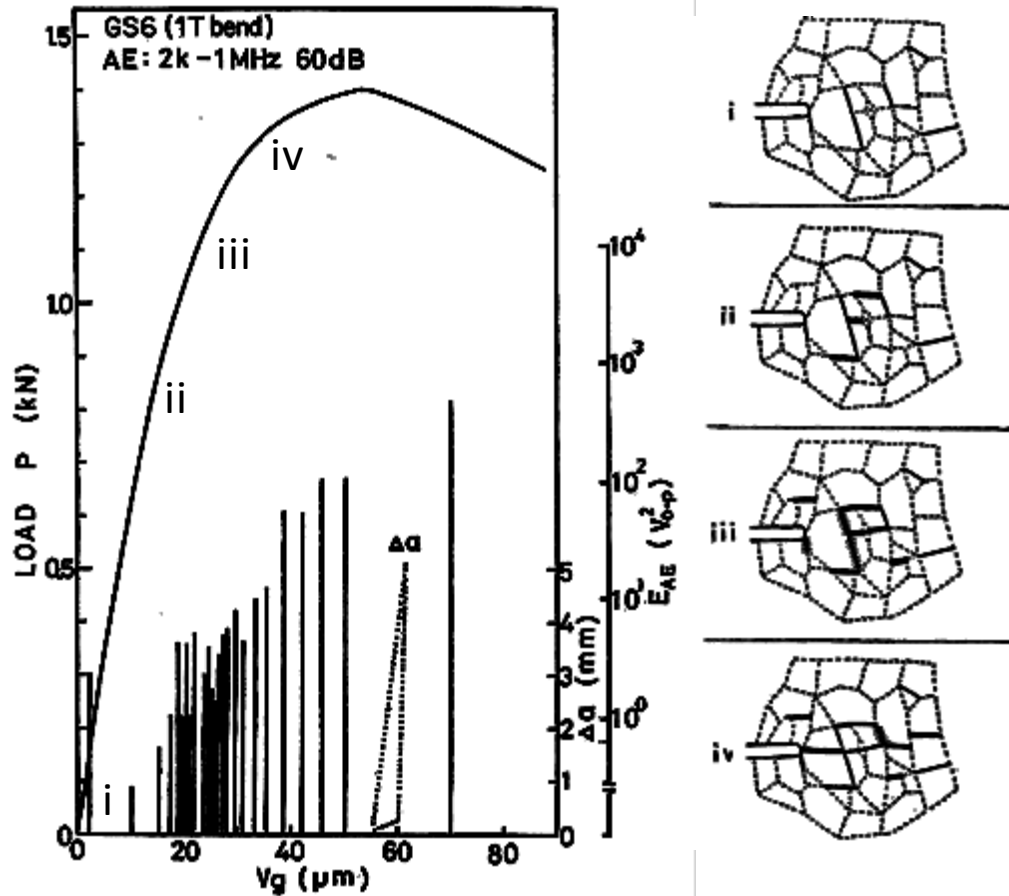


Figure 1.5. Load-displacement curve for rock with acoustic emissions log (left) and schematic illustrations (right) for the microfracture process ahead of a tensile crack tip for four stages (modified from Takahashi and Abe, 1987). (i) Initial state. Dotted lines indicate potential microcrack sites. Solid lines are pre-existing cracks. (ii) A few tensile microcracks initiate on the weakest plane near the notch tip, generates AE with small amplitude. Beginning of detectable nonlinearity in load-displacement record. (iii) Growth and linkage of microcracks cause an increase in AE activity and local slip along shear surfaces occurs. Increasing nonlinear deformation behavior. (iv) Large scale linkage of microcracks and fracture of the remaining strongest bonding. Onset of macroscopic crack extension.

The procedure of superposing cohesive and shielding zones to account for the requirements of inelasticity at the crack-tip and to constrain the effect of hysteresis is straightforward for steady-state propagation – that is, when the crack extension is time-invariant and proceeds in sequence as the established wake in the frontal zone ahead of the crack-tip sufficiently develops according to [5b]. This is not the case for transient propagation (Lawn, 1993). In the geologic setting where there are both extrinsic and intrinsic spatial and temporal heterogeneities the crack must encounter as it propagates in time, the state of the frontal zone defined by [5b] must be continually updated to reflect the new conditions at each space-time increment.

While this task “poses a considerable problem in theoretical fracture mechanics” (Lawn, 1993), it is demonstrated below that this is tenable within the context of continuum damage mechanics, and can be solved transiently using the finite element method. The approach is to propagate a hydrofracture within its own damaged frontal zone, as determined by the constitutive behavior of the rock layer. The damage zone and associated fracture propagation may occur within the crack-tip zone due to crack tip stresses, but it is not restricted as such – since in a rock layer the damage could just as well source from interaction with a preexisting discontinuity, a layer boundary, etc. In the subsequent FE models in Chapter 2, 3, and 4, we will utilize the continuum damage approach to ensure that the hydrofracture recognizes itself during propagation and adjusts to the associated, evolving local stress-field.

FRACTURING OF AN INELASTIC SOLID WITH DAMAGE

Fracture propagation occurs within zones of local weakening following strain hardening (Rice, 1975), and is determined by the constitutive behavior of the host

material. This is the justification for the insertion of cohesive and shielding zones in the frontal zone of a crack modeled by fracture mechanics theory, as was just discussed. These zones reflect the physical requirement of enhanced constitutive behavior in critically stressed regions of an otherwise simple, idealized material. Numerous rock mechanics experiments confirm that during progressive deformation, the critically stressed regions are not limited to the tips of distinct initial cracks, but may occur randomly within the host due to the presence of innumerable micro-flaws (Griffith, 1920), or within an idealized homogeneous medium that has non-uniform geometry or material contrasts (e.g., Eshelby, 1957). In brittle rocks, yielding is characterized by non-linear inelasticity associated with stress induced damage accumulation (e.g., Ashby and Hallam, 1986; Lockner et al., 1992; Reches and Lockner, 1994). Chapter 2 describes the general concepts of nonlinear damage evolution, degraded elastic stiffness, and microcrack interaction (e.g., Kachanov et al., 1990; Lyakhovskiy et al., 1993; Katz and Reches, 2004) and discusses a few approaches for modeling damage in a continuum. Various researchers have applied the concepts of continuum damage theory in numerical simulations of damage propagation and multi-segment crack interaction and linkage. One example is highlighted below.

Weinberger et al. (2000) used a continuum damage scheme to compare numerical simulations and field observations for stress, deformation, and damage distribution around propagating dike segments in sandstone (Fig. 1.6). The models were based on a rheology for damaged rock (Lyakhovskiy et al., 1997) that consisted of a linear elastic matrix populated with a set of penny-shaped cracks (Kachanov, 1992). In their

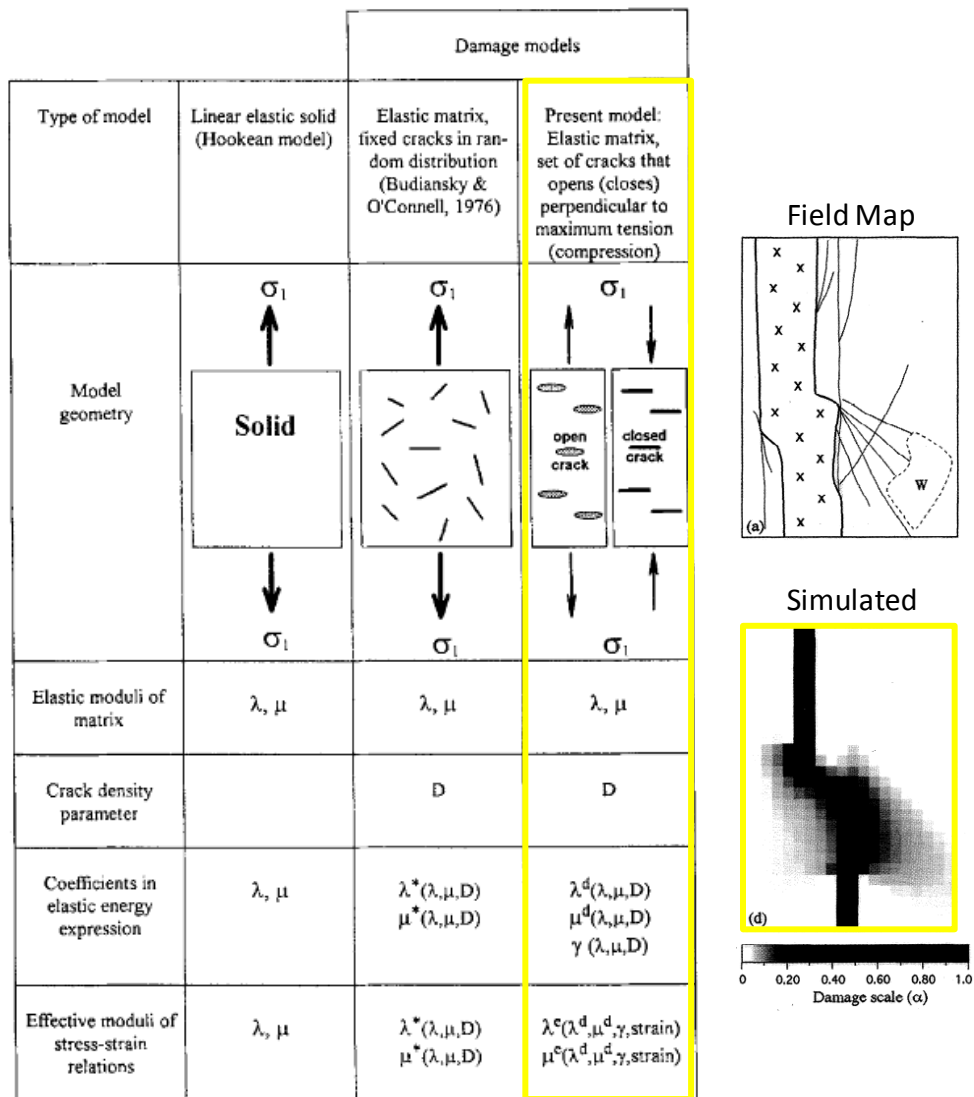


Figure 1.6. Damage schemes used in numerical simulations to simulate damage propagation during dike segment interaction (far right). The schemes are based on solving for the effect of embedded cracks in an elastic modulus. Undamaged model (left), Budiansky and O'Connell (1976) model (center), and Lyahhovskiy et al. (1997) model (right). Modified from Weinberger et al. (2000).

scheme, the energy expression considers the effective moduli, $\lambda^e(\lambda^d, \mu^d, \lambda, \text{strain})$ and $\mu^e(\lambda^d, \mu^d, \gamma, \text{strain})$ for a medium damaged by a mode I crack with energy release rate given by the J-integral:

$$J = K_1^2(1-\nu^2)/E \quad [6a]$$

$$U^d = 1/\rho(I_1^2\lambda/2 + I_2(\mu^d-\gamma\beta^2) - 2\gamma\beta I_1\sqrt{I_2} \quad [6b]$$

where β reflects the state of strain (Lyakhovskiy et al., 1997). A few of their results are relevant to complex fracture propagation (Chapter 3), and demonstrate the effects of damage propagation. (a) In-plane propagation is associated with symmetric widening and intensification of damage lobes ahead of the crack tip. (b) Out-of-plane propagation increases by reducing the distance between crack segments. In such cases, damage accumulation asymmetrically transfers to a region between the cracks and occurs by segment linkage. (c) High magnitudes of shear stress are more likely to produce discontinuous segments. Lastly, (d) increasing the effective lithostatic pressure significantly reduces the distribution and intensity of damage.

It is the aim of the present modeling to use a related approach to investigate the classical hydraulic fracturing problem. In the next chapter, a finite element model is presented to simulate progressive damage, yielding and failure for an elastic-plastic-damage rheology.

REFERENCES

- Ashby, M.F. and Hallam, S.D., 1986, The failure of brittle solids containing small cracks under compressive stress states. *Acta Metall.*, v. 34, p. 497-510.
- Atkinson, B.K., 1987, Introduction to fracture mechanics and its geophysical applications. In Atkinson, B.K., ed. *Fracture mechanics of rocks*, Academic Press, London, UK, p. 1-27.
- Barenblatt, G., 1962, The mathematical theory of equilibrium crack in the brittle fracture. *Adv. Appl. Mech.*, v. 7, p. 55-125.
- Buseti, S., 2003, Fracture characterization and analysis of the Pennsylvanian Jackfork Group, Ouachita Mountains, Southeastern Oklahoma. Master's thesis, University of Oklahoma, Norman, Oklahoma, 99p.
- Chester, F.M., Evans, J., and Biegel, R.L., 1993, Internal structure and weakening mechanisms of the San Andreas fault. *Journal of Geophysical Research*, v. 98, p. 771-786.
- Cooper, S., Lorenz, J., Goodwin, L., 2001. Lithologic and structural controls on natural fracture characteristics: Teapot Dome, Wyoming. Sandia National Laboratories, Sandia Report SAND2001-1786, 67p.
- Cosgrove, J. and Ameen, M.S., 2000, A comparison of the geometry, spatial organization and fracture patterns associated with forced folds and buckle folds. *Geological Society Special Publications*, v. 169, p. 7-21.
- Desroches, J., Detourney, E., Lenoach, B., Papanastasiou, P., Pearson, J.R.A., Thiercelin, M., and Cheng, A., 1994, The crack tip region in hydraulic fracturing. *Royal Society (London), Proceedings, Series A – Mathematical and Physical Sciences*, v. 447, no. 1929, p. 39-48.
- Dugdale, D., 1960, Yielding of steel sheets containing slits. *Journal of Mech. Phys. Sol.*, v. 8, p. 100-108.
- Eshelby, J.D., 1957, The determination of the elastic field of an ellipsoidal inclusion, and related problems. *Proc. Roy. Soc.*, v. 252, p. 376-395.
- Finkbeiner, T., Barton, C.A., and Zoback, M.D., 1997, Relationships among in-situ stress, fractures and faults, and fluid flow; Monterey Formation, Santa Maria Basin,

- California. American Association of Petroleum Geologists Bulletin, v. 81, no. 12, p. 1975-1999.
- Fossen, H., Johansen, T., Hesthammer, J., and Rotevatn, A., 2005, Fault interaction in porous sandstone and implications for reservoir management; examples from southern Utah. American Association of Petroleum Geologists Bulletin, v. 89, p. 1593-1606.
- Germanovich, L.N., and Dyskin, A.V., 1997, Fracture mechanisms and instability of openings in compression (in Neville Cook special issue). International Journal of Rock Mechanics and Mining Sciences, v. 31, no. 1-2, p. 263-284.
- Griffith, A.A., 1920, The phenomena of rupture and flow in solids. Philosophical Transactions of the Royal Society, London, v. A221, p. 163.
- Gross, M.R., Bahat, D., Becker, A., 1997, Relations between jointing and faulting based on fracture-spacing ratios and fault-slip profiles: A new method to estimate strain in layered rock. Geology, v. 25, p. 887-890.
- Haimson, B. and Fairhurst, C., 1967, Initiation and extension of hydraulic fractures in rocks. Society of Petroleum Engineers Journal, p. 310-318.
- Hubbert, M. K. and Willis, D.G., 1957, Mechanics of hydraulic fracturing. Transactions of the American Institute of Mining, Metallurgical, and Petroleum Engineers 210, p. 153-68.
- Irwin, G.R., 1958, Fracture. In Handbuch der Physik. Springer-Verlag, Berlin, v. 6, p. 551-590.
- Kachanov, M., Montagut, E.L.E., and Laures, J.P., 1990, Mechanics of crack-microcrack interactions. Mechanics of Materials, v. 10, p. 59-71.
- Kachanov, M., 1992, Effective elastic properties of cracked solids: critical review of some basic concepts. Appl. Mech. Rev., v. 45, p. 304-335.
- Kanninen, M.F. and Popelar, C.H., 1985, Advanced fracture mechanics. Oxford University Press, Oxford, 584 p.
- Katz, O. and Reches, Z., 2004, Microfracturing, damage, and failure of brittle granites. Journal of Geophysical Research, v. 109, B01206.

- Kristianovic, S.A., and Zheltov, Y.P., 1955, Formation of vertical fractures by means of highly viscous liquid. Proc. 4th World Petrol Cong., Rome, v. 2, p. 579-586.
- Lawn, B., 1993, Fracture of brittle solids – second edition. Cambridge University Press, 378 p.
- Lockner, D., Reches, Z., and Moore, D.E., 1992, Microcrack interaction leading to shear fracture. In Tillerson and Wawersik eds., Rock Mechanics Proceedings of the 33rd US Symposium, p. 807-816.
- Lockner, D. and Byerlee, J.D., 1977, Acoustic emission and creep in rock at high confining pressure and differential stress. Bulletin of the Seismological Society of America, v. 67, p. 247-258.
- Lorenz, J.C., Teufel, L.W., and Warpinski, N.R., 1991, Regional fractures; I, A mechanism for the formation of regional fractures at depth in flat-lying reservoirs. American Association of Petroleum Geologists Bulletin, v. 75, p. 1714-1737.
- Lyakhovskiy, V., Podladchikov, Y., and Poliakov, A., 1993, Rheological model of a fractured solid. Tectonophysics, v. 226, p. 187-198.
- Lyakhovskiy, V., Reches, Z., Weinberger, R., and Scott, T.E., 1997, Non-linear elastic behavior of damaged rocks. Geophysics Journal International, v. 130, p. 157-166.
- Maerton, L., Pollard, D., and Maerton, F., 2001, Digital mapping of three-dimensional structures of the Chimney Rock fault system, central Utah. Journal of Structural Geology, v. 23, p. 585-592.
- Mayer, J. and Sharp, J., 1998, Fracture control of regional ground-water flow in a carbonate aquifer in a semi-arid region. Geological Society of America Bulletin, v. 110, p. 269-283.
- Olson, J.E., 2004, Predicting fracture swarms – the influence of subcritical crack growth and the crack-tip process zone on joint spacing in rock. From: Cosgrove, J.W., and Engelder, T., eds. The initiation, propagation, and arrest of joints and other fractures. Geological Society, London, Special Publications, v. 231, p. 73-87.
- Perkins, T., and Kern, L., 1961, Widths of hydraulic fractures. Journal of Petroleum Tech., v. 222, p. 937-949.

- Pollard, D.D., 1978, Forms of hydraulic fractures as deduced from field studies of sheet intrusions. Proceedings of 19th U.S. Rock Mechanics Symposium, v.1, no. 19, p.1-9.
- Ramsey, J.M. and Chester, F.M., 2004, Hybrid fracture and the transition from extension fracture to shear fracture. *Nature*, v. 428, p. 63-66.
- Reches, Z. and Lockner, D., 1994, Nucleation and growth of faults in brittle rocks. *Journal of Geophysical Research*, v. 99, no. B9, p. 18,159-18,173.
- Rice, J.R., 1968, A path independent integral and the approximate analysis of strain concentration by notches and cracks. *Journal of Applied Mechanics*, v. 35, p. 379-386.
- Rice, J.R., 1975, On the stability of dilatants hardening for saturated rock masses. *Journal of Geophysical Research*, v. 80, p. 1,531-1,536
- Sagy, A., Reches, Z., and Roman, I., 2001, Dynamic fracturing of rock fragmentation and joint density: Field and experimental observations. *Journal of Structural Geology*, v. 23, p. 1223-1239.
- Stearns, D.W. and Friedman, M., 1972, Reservoirs in fractured rock. In: King, R.E., ed. *Stratigraphic Oil and Gas Fields*. American Association of Petroleum Geologists Memoir, v. 16, p. 82-106.
- Stewart, S.A., 2001, Displacement distributions on extensional faults: Implications for fault stretch, linkage, and seal. *American Association of Petroleum Geologists Bulletin*, v. 85, p. 587-599.
- Takahashi, H. and Abe, A., 1987, Fracture mechanics applied to hot, dry rock geothermal energy. In: Atkinson, B.K., ed. *Fracture Mechanics of Rock*, Academic Press, London, p. 241-276.
- Thompson, R.M., 1986, Physics of fracture. In: Ehrenreich, H. and Turnbull, D., eds. *Solid State Physics*, v. 39, p. 1-129.
- Verbeek, E., and Grout, M., 1997, The Post-Laramide joint network of the Colorado Plateau. In: Close, J. and Casey, T., eds. *Natural fracture systems in the southern Rockies*, Four Corners Geological Society, p. 7-22.

Weinberger, R., Lyakhovsky, V., Baer, G., and Agnon, A., 2000. Damage zones around en echelon dike segments in porous sandstone. *Journal of Geophysical Research*, v. 105, no. B2, p. 3,115-3,133.

Wu, R., 2006, Some fundamental mechanisms of hydraulic fracturing. Doctoral Dissertation, Georgia Institute of Technology, Atlanta, Georgia, 280 p.

CHAPTER II

NUMERICAL SIMULATION OF ROCKS WITH DAMAGE RHEOLOGY

ABSTRACT

A finite element (FE) rock rheology is developed for simulating the development of reservoir structures using the code Abaqus/Explicit. During finite deformation, rocks exhibit non-linear behavior, inelasticity, and progressive weakening due to stress-induced damage and failure. To model this behavior, stress-strain values and damage characteristics from rock mechanics experiments for Berea sandstone are converted into an elastic-plastic-damage FE material model. The constitutive behavior is a modification of Mohr-Coulomb plasticity. A continuum damage scheme models strain-based stiffness degradation and fracture propagation. Two experimental configurations are simulated to calibrate the rheology: four-point beam bending (Weinberger et al., 1994) and dog-bone shaped samples under triaxial extension (Ramsey and Chester, 2004; Bobich, 2005). The simulations agree with experiments for confining pressure P_c of 10-150 MPa and reflect the stages of deformation. For $P_c < 60$ MPa, the onset of damage occurs in localized zones with 0.05-0.1% extensional strain and increases exponentially until failure at 0.1-0.3%. Prior to first fracture, stiffness degrades ~10%. Multiple fractures occur in regions of 15-20% stiffness reduction. The simulations suggest that the rheology can be implemented in complex problems.

INTRODUCTION

The structural architecture and stress-strain character of a reservoir reflect a diverse history shaped by intrinsically complex, non-linear, time-dependent mechanical processes. These processes damage the rocks leading to non-uniform properties, locally evolving stress fields, and heterogeneous patterns of strain. The rheology of the layers determines the stress-strain response, which strongly affects the style of deformation; thus, it is essential to consider realistic material behavior. Mechanical analysis typically requires solving partial differential equations that are essentially insoluble by analytical methods unless very simple configurations are assumed. Alternatively, numerical methods have proven to be better suited for non-linear problems with arbitrary shapes. The finite element (FE) method has emerged as the prominent tool for analyzing complex geometries and large-deformation problems in many industries (e.g., Fish and Belytschko, 2007). In recent years, various technological developments including a focus on improved accessibility have established FE as an attractive tool in reservoir geomechanics.

Our goal here is to develop methodology and advance the tools needed to analyze complex geologic structures by numerical simulations. The problems require evolving constitutive behavior and heavily depend on strain-history. We use the explicit dynamic solver of the FE software Abaqus/Explicit to simulate non-linear deformation of rocks. Abaqus has a large library of material models suitable for modeling rock, and is very flexible to implement relevant geologic boundary conditions. We develop a rheology for rock using a constitutive model included in the software. Our models focus on brittle rock behavior under upper crustal conditions and include elastic-

plastic behavior, progressive damage and failure. We use data from rock mechanics experiments conducted under confining pressure to calibrate the FE material models. It is thus likely that the developed rheology reflects representative structural deformation for many rocks under reservoir in-situ conditions.

We first (Fig. 2.1) describe the fundamental mechanical behavior of many reservoir rocks for upper crustal conditions during strain hardening and failure. The patterns of damage observed during rock mechanics experiments are described along with common phenomenological schemes for approximating damage. Next, we discuss the finite element damage model used in the simulations, which is based on continuum damage theory. We then describe calibration and implementation of a damage rheology for rock into finite element models. A product is a constitutive model and failure criteria for Berea sandstone based on elastic-plastic damage rheology. Finally, we discuss the results of our simulations in comparison to experimental results.

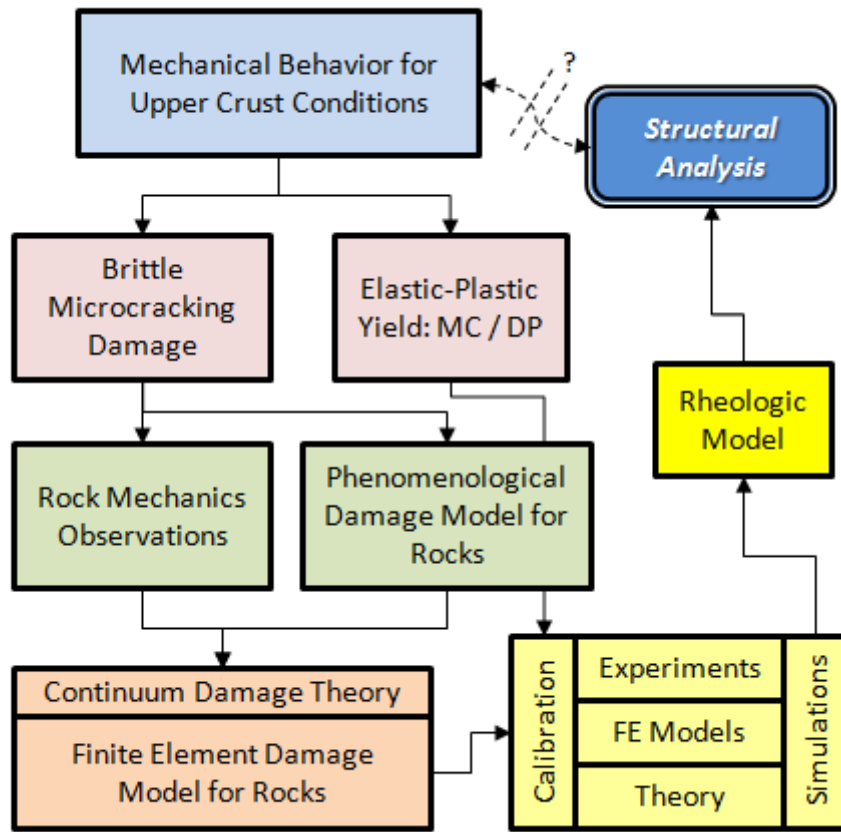


Figure 2.1. Organization of the paper.

ROCK RHEOLOGY

The rheology of a rock describes its response to applied forces. Processes such as disaggregation, microfracturing and fracturing, cataclasis, brecciation, and faulting indicate non-recoverable behavior in the brittle regime. Reorganization microstructures such as twinning and dislocations, strain localization features like compaction and shear bands, and highly deformed structures including shear zones and tight folds reflect behavior in the ductile regime. Frequently, local strain or stress exceeds the failure limits of the rocks creating permanent, heterogeneous strain patterns. In some structurally complex areas such as thrust belts, the deformation-history reveals strain in excess of 100%. Consequently, to analyze the development of many geologic structures it is essential to understand how rocks behave beyond infinitesimal strain, as predicted in elastic theory, and into finite strain, implying non-linear inelasticity.

The complex mechanics governing this realistic behavior are difficult to solve, and various rheologic proxies were used such as non-linear elastic (Johnson and Rasolofosaon, 1996), visco-elastic (Reches et al., 1994), viscoelastic with damage (Lyakhovskiy et al., 1997) and poroelastic with damage (Hamiel et al., 2004). Here, we consider elastic-plastic with damage rheology. In this scheme, pressure dependent yield strength controls the onset of brittle microcracking (damage) and internal dissipation processes (plasticity), which are physically coupled to control finite deformation. We focus first on the expression of brittle damage. This section will not elaborate on plastic mechanisms; however, a later section addresses pressure dependent plastic yielding following Mohr-Coulomb and Drucker-Prager failure

models and a modified version (Lublimer et al., 1989) that we use to model rock rheology.

TYPICAL STRESS-STRAIN BEHAVIOR

The stress-strain response of rocks depends on lithology and conditions and sense of loading (tension or compression) (Fig. 2.2). Figure 2.3 displays curves for axial, volumetric, and inelastic strain, and also mapped microcracks for a few stages of deformation (Katz and Reches, 2004). The stress-strain curves display five main stages interpreted as: 1) initial non-linear stress change associated with crack and pore dilation and closure, 2) elastic stage (linear or non-linear), 3) non-linear strain hardening, associated with the onset of brittle microcracking and plasticity, 4) continued hardening characterized by progressive crack coalescence in a fracture process zone, and finally, 5) ultimate failure, strain softening and macroscopic crack propagation.

NON-LINEAR INELASTICITY

It is generally accepted that the linear-elastic deformation stage for brittle rocks corresponds to small amounts of extensional or compressional strain ($<1\%$) (Segall and Pollard, 1983; Weinberger et al., 1994). Elastic behavior reflects recoverable deformation and by definition involves no internal energy dissipation. Rock mechanics experiments show that following initial elasticity, early stage deformation is dominated by the rapid accumulation of damage and microcracks (e.g., Ashby and Hallam, 1986; Lockner et al., 1992; Reches and Lockner, 1994).

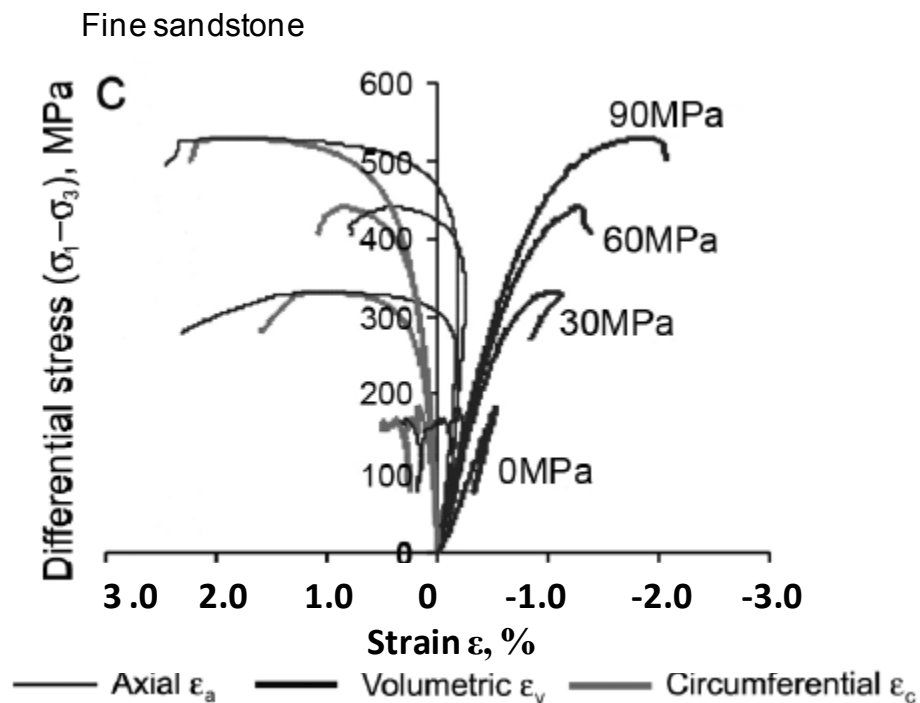
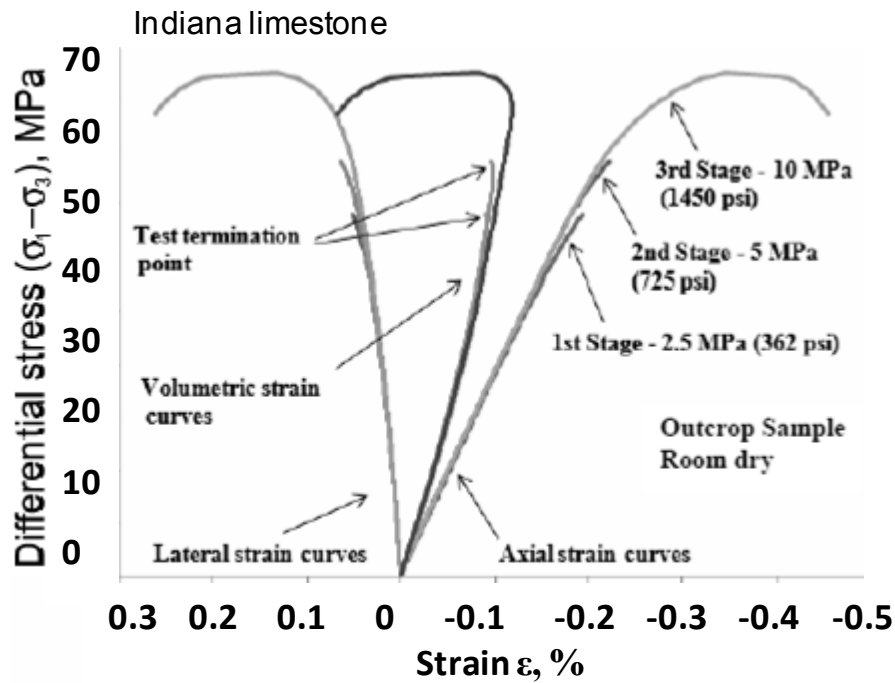


Figure 2.2. Stress-strain curves for limestone (top) and sandstone (bottom). The axial, volumetric and lateral or circumferential strains are plotted for a range of confining pressures. The five stages of deformation (see Figure 2.5) can be identified on these plots as well. While the general behavior is similar for all brittle rocks, each lithology has a unique response. Top, modified from Jambunathan, 2008; bottom from Lukaszewski, 2008. Note that the scales are different.

Mt. Scott Granite

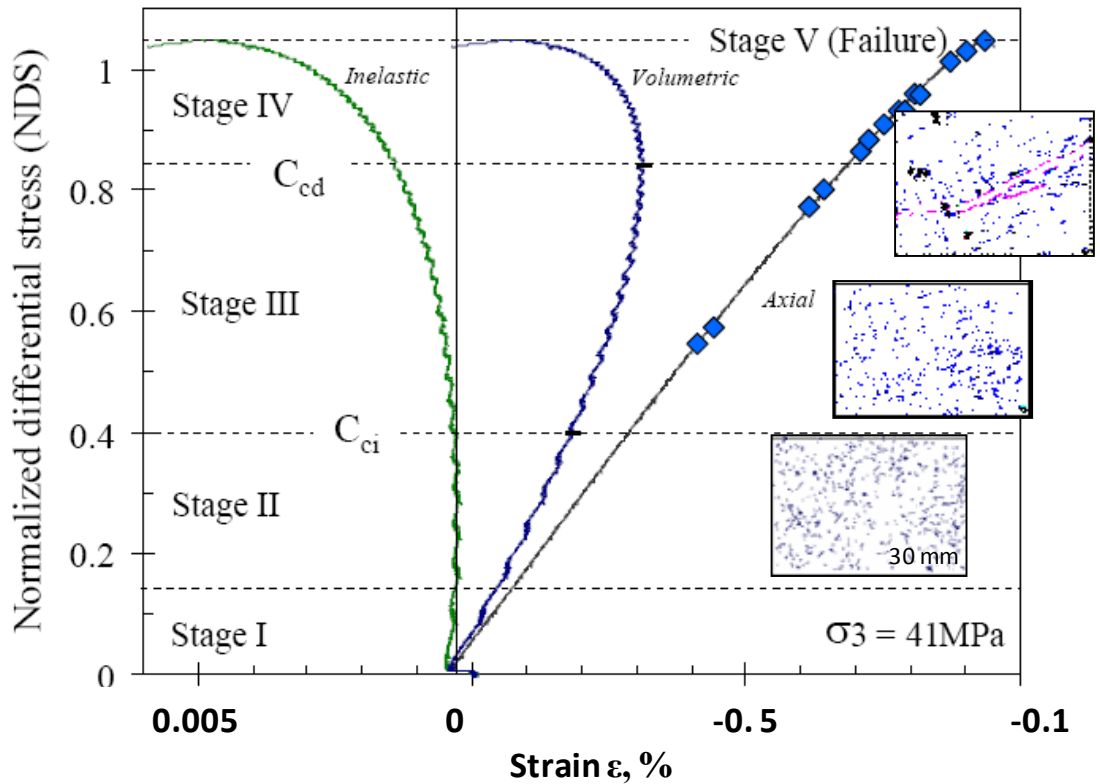


Figure 2.3. Stress-strain curves for rock under confining pressure. The curves are axial (black), volumetric (blue), and inelastic (green) strain. The four main stages of deformation are (also see text) (I) crack/pore closure, (II) linear elasticity, (III) strain hardening and microcracking, (IV) crack coalescence and formation of a process zone, and (V) macroscopic propagation. Note that the inelastic and volumetric strain increase nonlinearly during strain hardening. Insets show mapped microcracks for stages I, III, and V, ranging from preexisting background damage at bottom to a coalesced macroscopic fracture at top (modified from Katz and Reches, 2004).

The rock progressively weakens depending on the evolving internal distribution of cracks and microcracks (Walsh, 1965; Walsh and Brace, 1964), the extent of plastic deformation and microfracturing (Handin and Hager, 1957; Mogi, 1973), and localized effects such as stress shielding (Thompson, 1986) and dilatancy (Brace et al., 1966; Nur, 1975). Strain hardening on the stress-strain curve indicates loss of stiffness relative to the previous state. Experiments linked this stage to the evolution of stress-induced damage and degraded elastic stiffness (Katz and Reches, 2004), eventually leading to local instability and fracturing (e.g., Rice, 1975). A rapid stress drop typically follows failure, the steepness of the drop corresponding to the brittleness of the rock. Post-failure loading results in finite, constant-stress deformation localized along zones of weakness (as in the topmost microcrack map of Fig. 2.3).

PROGRESSIVE DAMAGE IN ROCKS

DAMAGE OBSERVATIONS

The location, timing, and amount of microcracking damage can be quantified using maps of thin sections, SEM, and acoustic emissions (AE) logs. Many experiments have shown that the total amount of damage increases non-linearly beginning at the onset of inelasticity (e.g., Eberhardt, 1998; Bobich, 2005; Stanchits and Dresen, 2003; Backers et al., 2005; Chen et al., 2006). Backers et al. (2005) mapped damage accumulation in sandstone during three-point bending of a beam with an initial notch. Maps of AE and SEM images identified a region of microcracks that rapidly increased in density approaching the main fracture (see Fig. 2.4). They observed that tensile

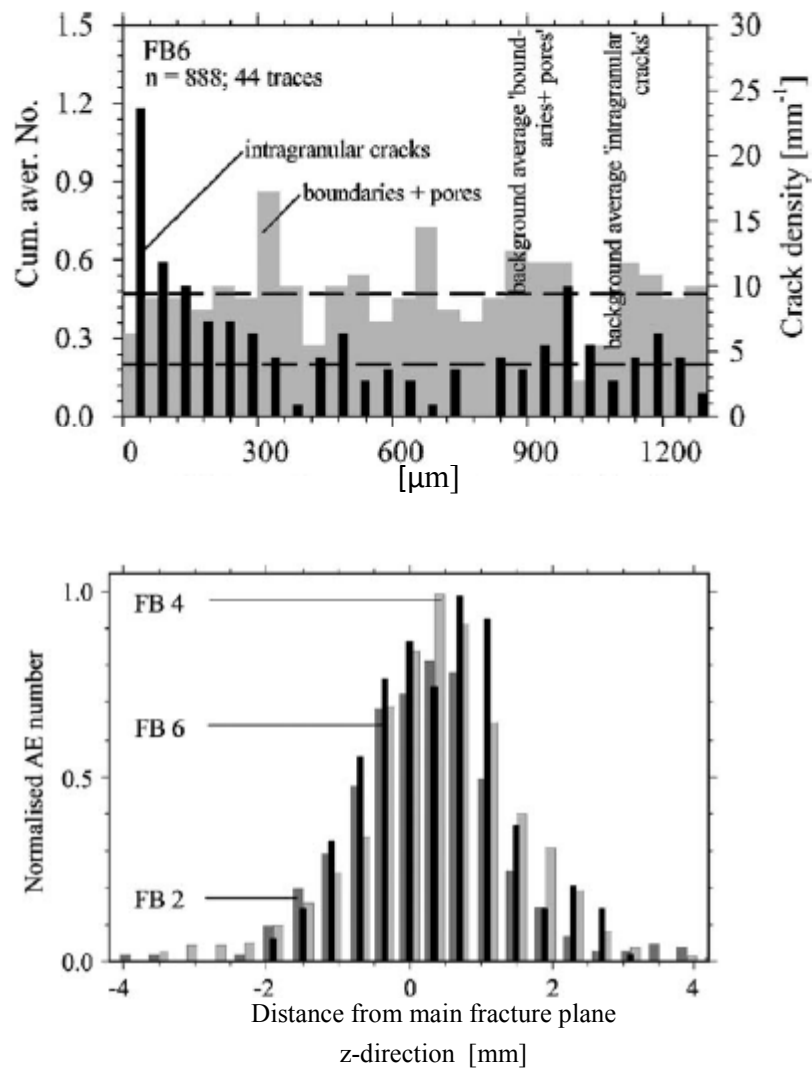


Figure 2.4. Tensile fracture propagation experiments on Berea sandstone by Backers et al. (2005) showing that the distribution of damage increases nonlinearly near the fracture. The x axis is distance from the main crack in mm, the y axis is the acoustic emissions count and also the crack density in mm^{-1} in the top chart. Top, the intergranular microcrack density (black) increases toward the main fracture while the pore and grain boundaries remain randomly distributed – the average distribution is marked by the horizontal dashed lines. Below, microcrack density for various strain rates, FB4 is fast, FB2 intermediate, and FB6 is slow. The total width of the process zone is about 4-8 mm.

fracture propagation sourced from a dense cluster of microcracks ahead of the crack tip. Reches and Lockner (1994) mapped AE during compression loading of granite. They found that during early loading, microcracking occurred randomly throughout the sample, but as the load approached the ultimate strength of the rock, microcracks localized in a shear zone. At failure, a dominant shear fracture propagated from within a region of dense microcracks, interpreted as a process zone weakened by intensified crack dilation and interaction.

DEFORMATION MODULUS

The accumulation of microcrack damage and the associated change in shape of the stress-strain curve (Fig. 2.3) led to the concept of the *deformation modulus* (Fig. 2.5) (Katz and Reches, 2004). The deformation modulus measures the local slope of an experimental stress-strain curve and provides a phenomenological approximation of the material properties at different stages of deformation. Stiffness, deformation, and load carrying capacity relate by the familiar equation:

$$\sigma = E:\varepsilon \quad [1a]$$

where σ is the Cauchy stress tensor, E is the stiffness matrix, and ε is the elastic strain tensor. Non-linear strain hardening indicates that there is a change in stress $d\sigma$ over a given strain increment $d\varepsilon$, such that:

$$d\sigma = E:d\varepsilon \quad [1b]$$

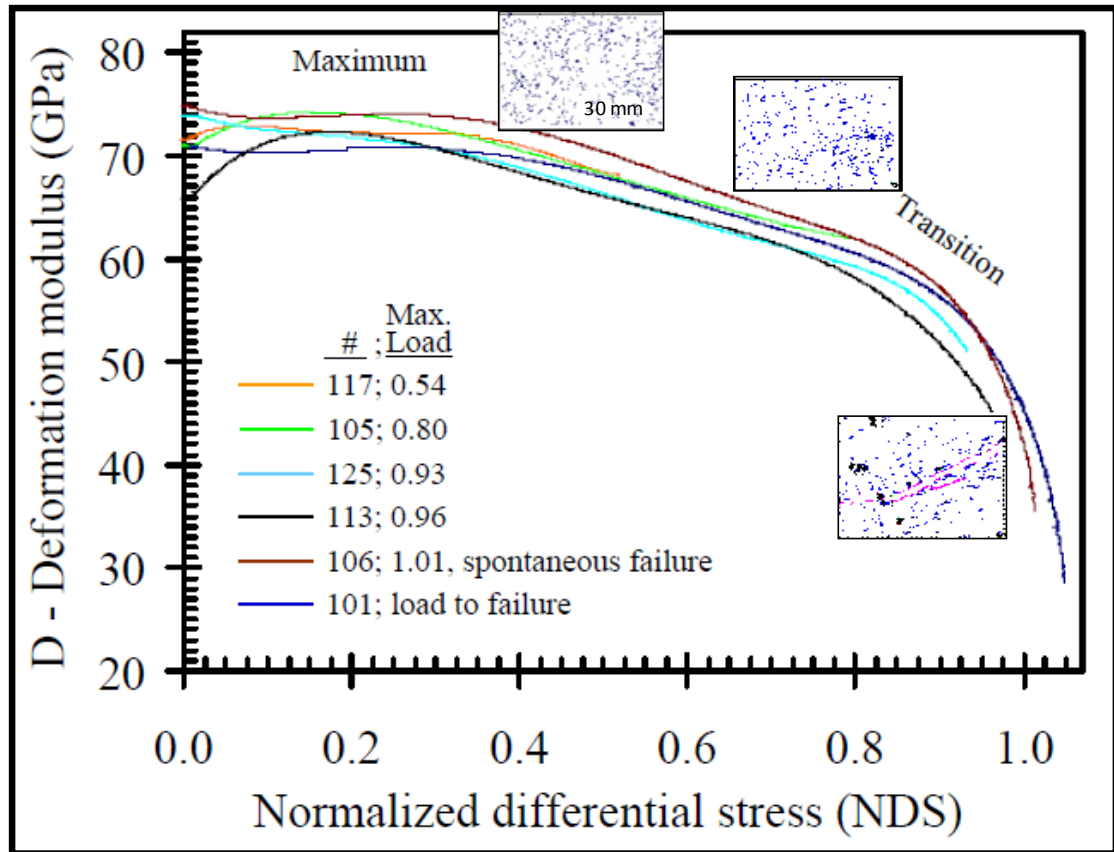


Figure 2.5. The experimental deformation modulus measures the local change in slope of the stress-strain curve: $D=d(\sigma_1 - \sigma_3)/d\varepsilon$ and approximates the degree of stiffness degradation. At left, D is equivalent to the original stiffness of the rock. With increasing deformation, D nonlinearly decreases until the rock locally loses all strength. The inset maps are for microcrack density at the appropriate stage of deformation and are the same as in Figure 2.3. Figure modified from Katz and Reches, 2004.

Since the material stiffness changes during deformation (Fig. 2.5), the initial elastic stiffness, reflected by the Young's modulus E , loses relevance. A more general material tensor D is substituted to include the effects of permanent, inelastic deformation attributed to pervasive stress-induced damage (Katz and Reches, 2004). D represents the weakening behavior but does not explain individual mechanisms. Rearranging [1b] and using differential stress $(\sigma_1 - \sigma_3)$ in place of σ , gives the definition for the deformation modulus, D :

$$D = d(\sigma_1 - \sigma_3) / d\varepsilon \quad [2]$$

At the initial state, when $D = D_{\max}$, D is equivalent to the Young's modulus. At various incremental states, $D = D' < D_{\max}$ (Fig. 2.5). The ratio of the deformed to undeformed states provides a *dimensionless approximation for stiffness degradation*:

$$D' / D_{\max} \approx E' / E_0 \quad [3]$$

where E_0 is the initial Young's modulus and E' is for the deformed state. Katz and Reches (2004) recorded the change in deformation modulus during rock mechanics experiments on Mount Scott granite and found that D degrades along a quasi-sinusoidal curve (Fig. 2.5). The change in D coincided with 1) increased ratio of plastic to elastic strain, and 2) increased crack volumetric strain (CVS), measured as the difference between the measured volumetric strain and elastic strain (calculated from Hooke's formula: $CVS = (\varepsilon V)_{exp} - (\sigma_1 - \sigma_3)(1-2\nu)/E$; see Katz and Reches, 2004).

While the evolving deformation modulus captures the key stages of progressive deformation (Fig. 2.3, 2.5), the mechanisms of damage require further discussion. All theoretical damage models result in the non-linear stress-strain curve reflected

experimentally by D , however the assumptions for the underlying mechanisms vary significantly. It can be postulated that the change in material stiffness observed as $D_0 \rightarrow D'$ physically relates to the production of crack volume. Increased microcracking serves to reduce the net load carrying area in a volume of rock, captured by a damage parameter d :

$$d = (A_{\text{total}} - A_{\text{net}})/A_{\text{total}} \quad [4a]$$

where the term $(A_{\text{total}} - A_{\text{net}})$ is the damaged area. The effect of degraded material stiffness is solved by scaling the true stress by the area lost due to microcracking.

Thus, we arrive at the “effective-stress” concept within continuum damage mechanics (Kachanov, 1958):

$$\sigma_{\text{eff}} = \sigma/(1-d) \quad [4b]$$

Therefore, the stiffness matrix D is scaled by the damage parameter d , yielding the current stiffness D' and the *dimensionless approximation for stiffness degradation*:

$$D' = (1-d)D \quad [4c]$$

$$D'/D = (1 - d) \quad [4d]$$

To avoid confusion with the more common geological usage of the term effective-stress (i.e., the effect of pore pressure), we refer to various models based on direct scaling of stiffness by the effective load bearing area as “stiffness reduction” models. However, we cannot completely avoid overlap and must continue to use the term effective-stress; however, henceforth this paper refers to the concept as it is used in continuum damage theory.

MICROFRACTURE DENSITY FUNCTION

The “stiffness reduction” models approximate the effect of the damage parameter d from a discrete fracture population. Rather than attempting to directly calculate the area change due to microcracking, a microfracture density function, ρ (Kachanov, 1992) is constructed: $\rho = (1/A)\Sigma L^2$ or $\rho = (1/V)\Sigma L^3$. L is half the crack length and Σ indicates the summation of all cracks in the representative area or volume, A or V . The crack lengths can be measured directly in thin section or SEM as was done by Katz and Reches (2004) or generated numerically (see the body of publications by Kachanov, e.g. 1992). The density function ρ forms the basis for a dimensionless stiffness multiplier:

$$E'/E_0 = f(\rho) \quad [5a]$$

If the damage parameter $d \approx f(\rho)$, then it is the compliance that relates linearly to crack density (as in [4d]). Two popular schemes (see Katz and Reches, 2004; Kachanov, 2007) are the “non-interaction approximation” *NIA* (Kachanov, 1992) and the “self consistent scheme” *SCS* (Budiansky and O’Connell, 1976). Both models assume an isotropic medium embedded with randomly oriented, circular “penny-shaped” cracks. The *NIA* assumes that compliance relates linearly to crack density, assumes that cracks do not interact (or interaction effects cancel each other out), and that total stiffness degradation scales by the summation of all crack-generated strains, reflected as:

$$E'/E_0 = 1/(1+\pi\rho) \quad [5b]$$

where E'/E_0 is the ratio of the damaged to original stiffness, π reflects the circular shape of the crack, and ρ is the fracture density function. Alternatively, the *SCS*

assumes that stiffness relates linearly to crack density and anticipates a certain degree of local crack shielding. SCS places cracks in a matrix with an effective (reduced) modulus in order to achieve strong softening behavior due to interactions, and predicts degradation as:

$$E'/E_0 = (1 - \pi\rho) \quad [5c]$$

The results of numerical simulations (Kachanov, 1992; Davis and Knoppoff, 1995) have shown that the SCS tends to lose accuracy at high crack densities by over-approximating the effect of crack interactions (Kachanov, 2007), an observation that was supported experimentally (Katz and Reches, 2004).

EXPERIMENTAL DENSITY

In order to compare predictions of the NIA and SCS with experimental data, Katz and Reches (2004) created microfracture density functions from mapped microfracture populations in thin sections during compression tests on Mount Scott granite. The microfracture maps are related to the evolving deformation modulus D . Two key findings stand out. First, they observed that intragranular tensile cracks dominated the low stress stage whereas intergranular shear cracks dominated during higher stress. This suggests that while both shear and tension fracturing mechanisms are always operable, a single mode of fracturing cannot explain all stages of deformation. This is important because in most rocks the yield stress is different for mode I and II cracks. Second, Katz and Reches observed that the shear cracks elongated and coalesced, forming shear zones, whereas the early tensile cracks remained intergranular throughout deformation. Presumably, during an extension experiment the tensile crack

development would dominate. Coalescence and shear zone development indicate a strong dependence on the strain history; there is a damage “memory” that affects future events. An excessively static damage scheme will inevitably result in spurious predictions. Principally, the mechanisms for damage and the magnitude of damage interaction (i.e., inelastic energy dissipation) are transient phenomena. The solution is to introduce an evolving stress function that is dependent on the state of stress as well as the strain history, and is a task for an advanced numerical method - i.e., FE.

EXPLICIT DYNAMIC FINITE ELEMENT SOLUTION

To solve the problem, we use the explicit dynamic FE procedure. The explicit technique is often used to solve non-linear dynamics problems with finite strain and complicated evolving contact definitions. The dynamical approach is particularly useful in our subsequent modeling, and in Chapter 3 we discuss it in more detail when we apply the rheology to study the dynamical processes of segmentation and branching during hydraulic fracturing. A brief review of the explicit FE technique is also included in Appendix B of Chapter 3. Contact in our models is straightforward; however, we do run into convergence difficulties during the coupling of plastic softening with damage weakening using an implicit solver – these issues are alleviated using the explicit technique. In the following section, we focus on summarizing the finite element damage model.

FINITE ELEMENT DAMAGE MODEL

The finite element damage model (Lubliner et al., 1989; Lee and Fenves, 1998; Abaqus) advances the general concepts of the deformation modulus and stiffness reduction models. A damage parameter (d) is used to scale the true stress and constitutes a dimensionless approximation for stiffness degradation. In the stress-strain relationship above [1a], the damage parameter d scales the material matrix D . For the initial stage $D = D_0$, $d = 0$ and there is no degradation of the material stiffness. When $d = 1$ the material is completely damaged and the effective-stress drops to zero.

$$E'/E_0 \approx D'/D_0 = (1-d) \quad [6a]$$

The incremental plastic strain includes all irreversible deformations including brittle microcracking damage. Decomposing the total strain into elastic, ε^e , and plastic, ε^p , strain components ($\varepsilon = \varepsilon^e + \varepsilon^p$) gives the stress-strain relationship:

$$\sigma = (1-d)D_0(\varepsilon - \varepsilon^p) \quad [6b]$$

An important difference between the present model and those previously described is that the elastic-plastic constitutive response is decoupled from damage evolution (Lee and Fenves, 1998). That is, the effective-stress concept is used to degrade the elastic stiffness, which in turn controls the shape of the yield surface (discussed later on). However, the damage parameter evolves separately as a function of plastic strain, and is tracked separately for tension and compression damage. The result is that the material retains directional strength depending on how it is deformed. For example, a region containing microcracks oriented normal to the loading direction is very strong in compression, but weak in tension. Whereas d can be approximated from discrete populations using the fracture density function, it is described in the constitutive

equations as evolution of the dissipation potential, $d = d(\kappa_\varkappa)$. Damage evolution is thereby coupled with plastic strain evolution:

$$\kappa_\varkappa = 1/g_\varkappa \int_0^{\varepsilon_p} \sigma_\varkappa (\varepsilon_p) d\varepsilon_p \quad [7a]$$

$$g_\varkappa = 1/g_\varkappa \int_\infty^0 \sigma_\varkappa (\varepsilon_p) d\varepsilon_p \quad [7b]$$

To distinguish mode I and II damage, damage dissipation κ_\varkappa is defined in compression or tension, $\varkappa = t$ or c (Lee and Fenves, 1998). The term g_\varkappa is the normalized dissipated energy during microcracking, and is set in the uniaxial stress state. Because we are working within the continuum framework, g_\varkappa reflects normalization of the energy released during compressive or tensile fracturing (defined by fracture mechanics theory) G_\varkappa , by a localization size l_\varkappa (Lubliner et al. 1989; Lee and Fenves, 1998):

$$g_\varkappa = G_\varkappa / l_\varkappa \quad [7c]$$

The value of l_\varkappa is an “objective value” or “assumed as a material property” (Lee and Fenves, 1998), but for our purposes automatically appears as an element regularization parameter in Abaqus. There is flexibility in the Abaqus software to implement the damage parameter by specifying d as a function of plastic strain during uniaxial loading (Fig. 2.6), on a load-displacement curve (Rice, 1968), or directly by specifying the fracture energy G_f in compression or tension. The finite element implementation permits simulation of fracture propagation based on the equivalent crack concept, which states that there exists a length-scaled damage zone that is thermodynamically equivalent to a crack and vice versa (see Appendix A; Mazars and Pijadier-Cabot,

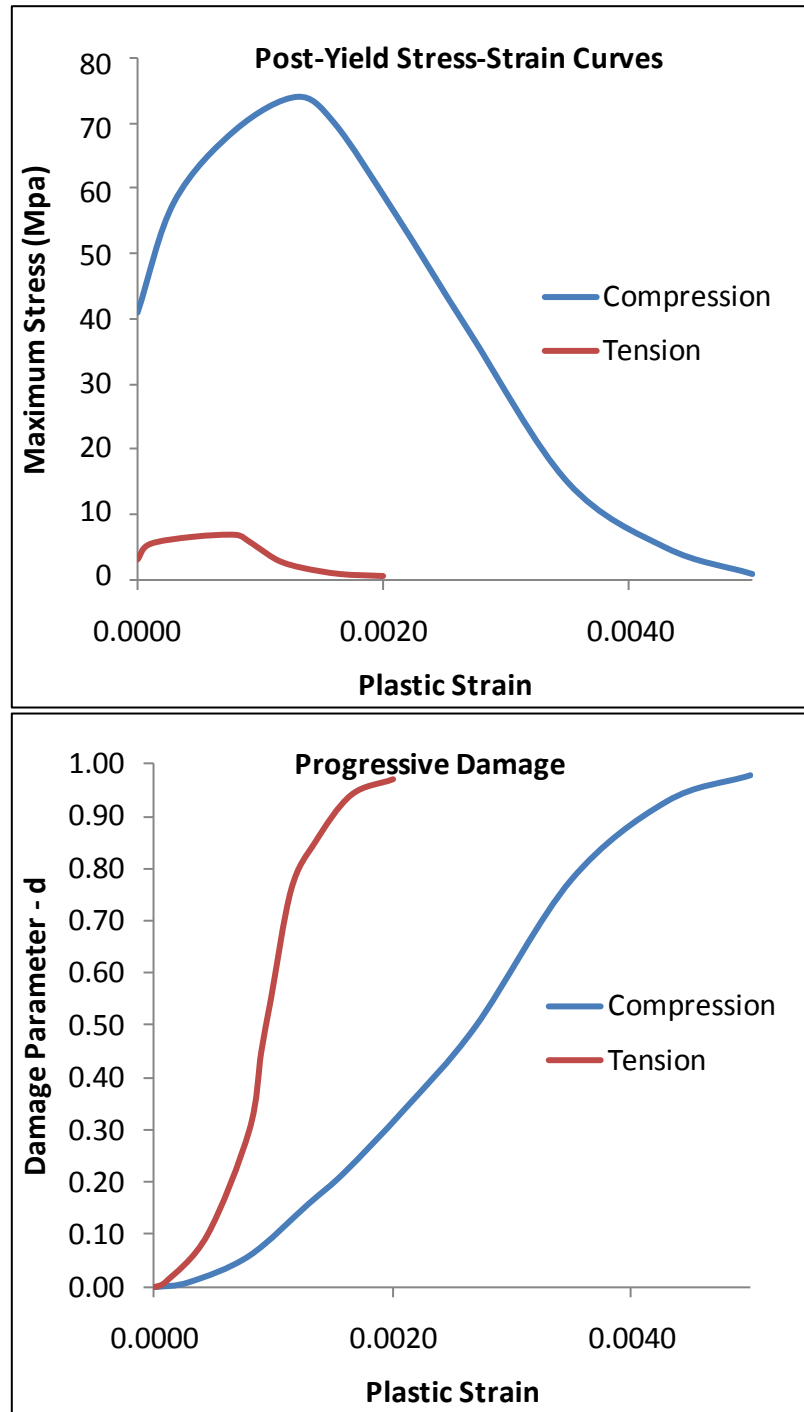


Figure 2.6. The presently derived post-yield curves for plastic strain (top) and damage (bottom) evolution used in the FE rheology defined in the uniaxial stress state. These parameters were entered directly into Abaqus' material model. The values for tension (red) and compression (blue) are based on experimental data for Berea sandstone. The material is about 10 times stronger in compression..

1996). Using this approach, a discrete fracture is represented by an equivalent fracture zone - a path of elements that are completely damaged and have no strength.

FINITE ELEMENT SIMULATIONS

Our approach to the adaptation of rock mechanics data of a “typical” reservoir rock into the damage model of the finite element program Abaqus includes the following steps: (1) Acquisition of experimental data of the relevant rock and deformation conditions. (2) Conversion of the experimental data into input material parameters used in Abaqus; we used the material “Concrete Damage Plasticity” (Abaqus Manual). (3) Creating a FE model for the laboratory configuration. (4) Calibrations by iterative model simulations and adjustment of material parameters to match the lab results (forward modeling). (5) Application of the calibrated material to other model configurations and geologic analysis.

To calibrate the material parameters we performed benchmark simulations of rock mechanics experiments with Berea sandstone under two different configurations (Weinberger et al., 1994; Ramsey and Chester, 2004; Bobich, 2005). We chose experimental configurations that may induce tensile failure under confining pressure, which is likely to represent subsurface conditions. We attempted to accurately calibrate the critical features of stress-strain relations: (1) onset of inelasticity, (2) strain hardening, (3) ultimate strength, (4) strain softening and brittle failure, and (5) post-failure finite strain. The benchmark models are at 1:1 scale to the laboratory tests, with only slight changes to the load rates to improve computational efficiency. The laboratory and finite element configurations are described below. As the mechanical

properties of Berea sandstone are well documented (Table 1), and fall within typical ranges of many reservoir rock types, we think that it is possible to adjust the damage rheology derived here to other lithologies. Petrophysically, Berea sandstone consists of medium grained, well sorted, subangular quartz (80%), feldspar (5%), clay (8%), and calcite (6%), and porosity is 19% (Hart and Wang, 1995).

FOUR-POINT BEAM BENDING

Weinberger et al. (1994) deformed samples of Berea sandstone, Indiana limestone, and Tennessee sandstone in a pressurized, four-point beam device under confining pressures of 5-50 MPa (Fig. 2.7). The four-point configuration was designed to induce near-uniform tension across the top-center of the beam and was dimensioned to minimize interference between the lower two fixed points. Rectangular samples (see Fig. 2.10 for dimensions) were jacketed with polyolefin tubing and loaded in a servo-controlled 138 MPa pressure vessel. An internal load cell monitored the amount of axial load, P , applied to the outermost points located on the top of the beam. Beam parallel strains were measured with strain gauges mounted on the top and bottom. The resultant tension and compression stresses in the beam were calculated after Yokoyama (1988). Results appear in Fig. 2.7.

TRIAXIAL EXTENSION OF DOG-BONE SHAPED SAMPLES

Ramsey and Chester (2004) and Bobich (2005) deformed dog-bone shaped samples of Carrara marble and Berea sandstone under confining pressure in order to study the transition from extension fracture to shear fracture with increasing compressive stress. The dog-bone shape with a large-notch cut radius was designed to

produce uniform tensile stress conditions at the center of the sample (Fig. 2.8). Dimensions are shown in Fig. 2.11. The pressure apparatus consisted of a latex inner jacket encasing the rock sample, plasticene-modeling clay along the neck portion to transmit confining pressure uniformly, and a polyolefin outer jacket in contact with the pressurized fluid. Pistons at the top and bottom of the sample moved simultaneously while recording axial force, axial displacement, and confining pressure (A. Kronenberg, 2008, personal communication). The experiments recorded acoustic emissions using a piezoelectric transducer attached to the top piston.

FINITE ELEMENT MODELS

We created 3D finite element models (Fig. 2.10 and 2.11) at the dimensions of the laboratory tests, and meshed with 8-node linear hexahedral elements with mesh density increasing in the regions with high strain. In the beam experiment, we used an axis of symmetry at the center to model half of the beam in order to reduce computational costs. The axial load points consisting of the four rigid pins (beam) and rigid platens (dog-bone) were modeled using 3D rigid elements and low-friction master-slave penalty contacts. Loading occurred in two steps. First, confining pressure, P_c , was established on all free surfaces, and was held constant during the simulations. In a second step, piston motion was simulated by applying a constant-velocity boundary condition to the appropriate rigid surfaces. For the beam, the top-outer pin was lowered at a constant velocity of 0.5 mm/s while holding the bottom-inner pin fixed. For the dog-bone sample, axial pressure was removed and the two pistons retracted at a rate of 0.2 mm/s while maintaining constant P_c . These applied load rates are about ten times faster than those of the physical experiments and were

used to reduce simulation time. Based on calculations that the ratio of kinetic energy to total system energy was very low ($\sim 1:20$), we concluded that higher load rate did not adversely introduce inertial effects. We also ran a few tests at slower strain rates with no effect on the results.

We used the explicit dynamic solver of Abaqus that is well suited for extreme non-linearity such as strain localization or contact. At the expense of a small stable time increment, the simulation continues during extensive propagation of damage. The implicit solutions had difficulty converging during strain softening and terminated shortly after failure. Mesh dependence can be an issue in continuum damage simulations and we experimented with several different meshing schemes and found that variations in the mesh density did not significantly affect the global solution (e.g., the stress-strain curve). Capturing the localized damage pattern necessary to discern individual fractures required a finer mesh density with elements on the scale of a few mm. Damage localization patterns were generally consistent for similarly sized and patterned meshes, though the specific fracture geometry varied somewhat. It should be noted that damage solutions derived from damage energy dissipation are determined by the elemental constitutive behavior rather than from decohesion of two discrete fracture surfaces, as in classical fracture mechanics. This method has particular value in larger-scale problems where modeling discrete surfaces is less relevant than capturing regions of intense strain localization, such as shear zones or fracture swarms. Moreover, the present approach lends well to modeling the interaction between zones of damage, with implications for fracture segmentation and branching, a subject we explore in Chapter 3.

Table 2.1 Material Parameters for Berea Sandstone

Sources	1,2,3,4,5
Composition	quartz (80%), feldspar (5%), calcite (6%), clay
Density	2100
E (Gpa)	19.3 - 27.5
ν	0.17 - 0.34
UCS Damage Onset Stress (MPa)	41-58
UCS Damage Onset Strain(MPa)	0.003 - 0.0035
UCS Fail Stress (MPa)	71.3 - 74
UCS Fail Strain (MPa)	0.0045
UTS Damage Onset Stress (MPa)	3.2-8.6
UTS Damage Onset Strain(MPa)	0.0007 - 0.0012
UTS Fail Stress (MPa)	3.8-9.8
UTS Fail Strain (MPa)	0.0015-0.002

1. Katz and Reches (2004) 2. Bobich (2005); Ramsey and Chester (2004) 3. Weinberger et al. (2000) 4. Eberhardt (1998) 5. Hart and Wang (1995)

**Table 2.2 Model Parameters
For Berea Sandstone Rheology**

Density	2100
E (GPa)	20.2
ν	0.27
Ψ	15
ecc.	0.1
fc0/fb0	1.16
K	0.66
viscos.	0

E = Young's modulus; ν = Poisson's ratio;

UCS = uniaxial compressive strength, UTS = uniaxial tensile strength

Ψ = dilation angle; ecc. = flow potential eccentricity; fc0/fb0 = ratio uniaxial to biaxial compressive yield stress; K = ratio of the second stress invariant on the tensile meridian to that on the compressive meridian; viscos. = viscous regularization parameter.

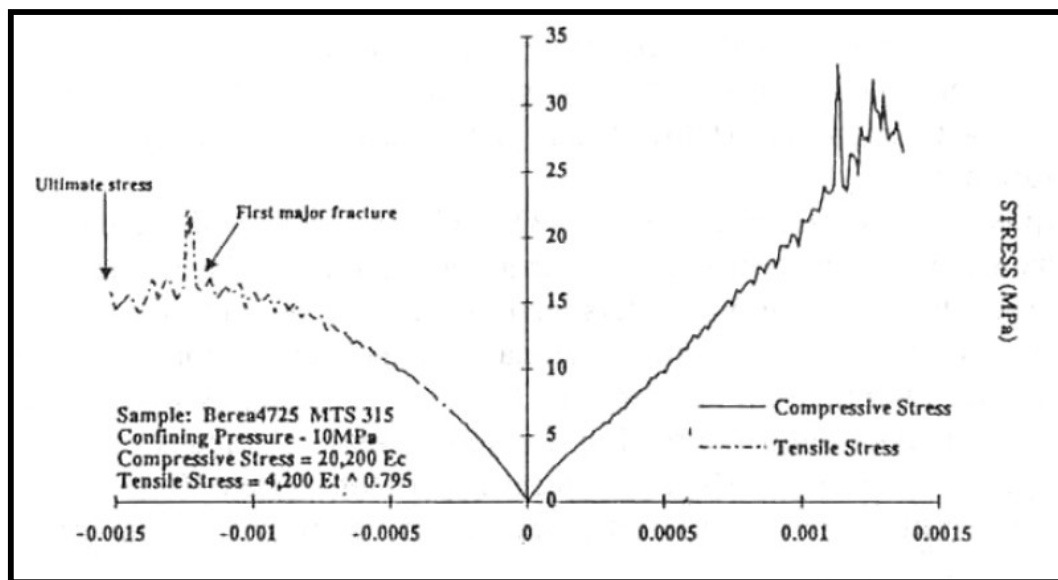
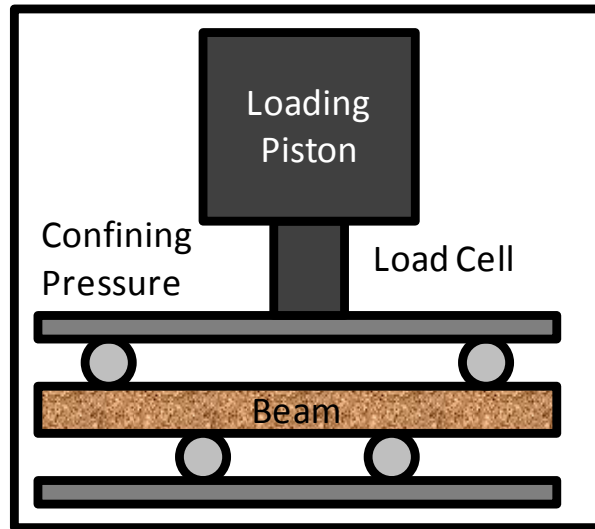
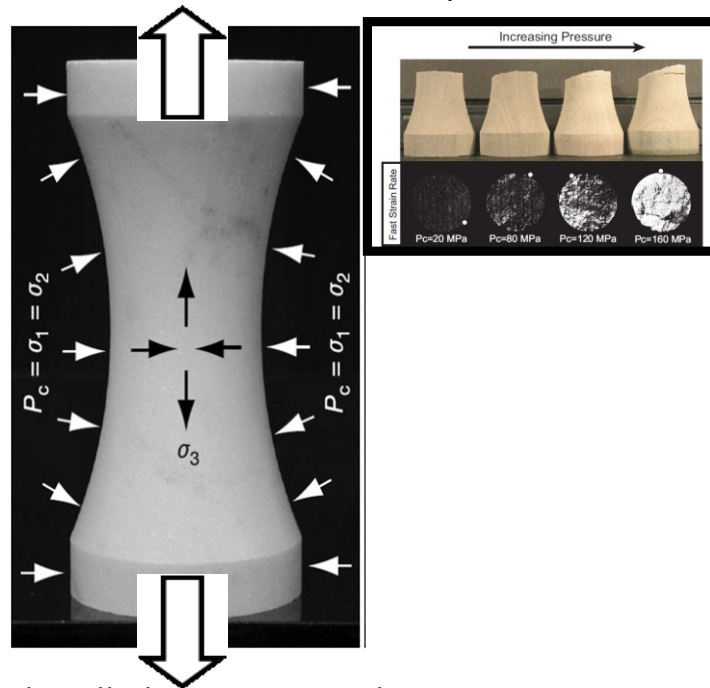


Figure 2.7. Four point beam experimental configuration of Weinberger et al. (2000). For the model dimensions see Figure 2.10. Confining pressure is applied to the entire sample. Loading of the piston induces tension in the upper center of the beam and compression in the lower center. The results for Berea sandstone, confining pressure 10 MPa, are shown at bottom. The sharp peaks were interpreted as fracturing events.

Piston retracted at constant velocity



Thick-walled pressure vessel

Dog-bone Extension

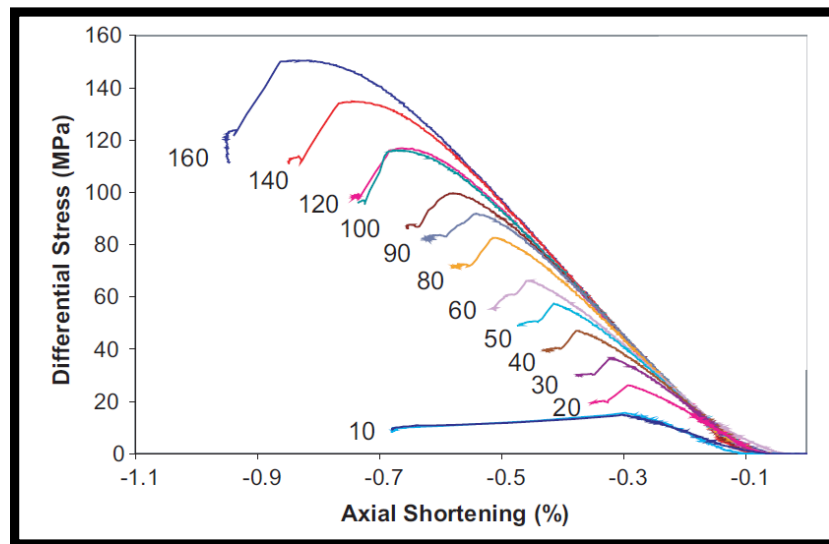
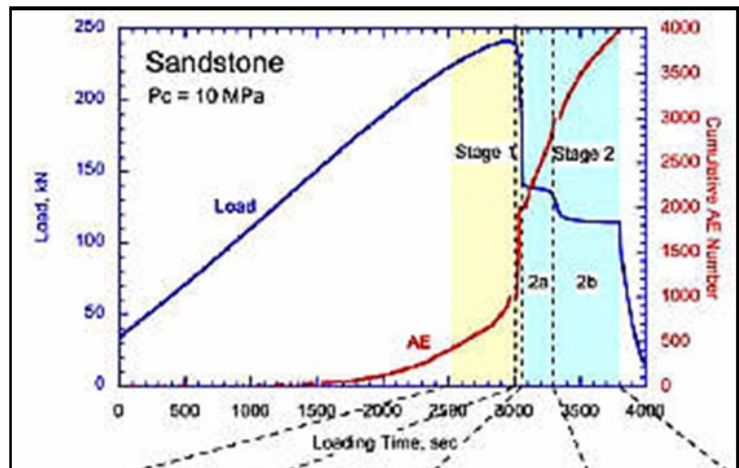


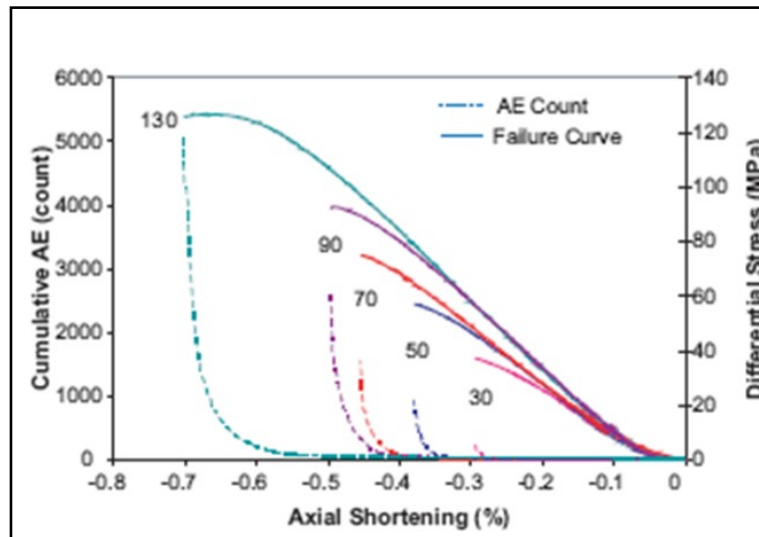
Figure 2.8. Dogbone extension experimental configuration of Bobich (2005) and Ramsey and Chester (2006). The geometry of the sample allows for tensile failure in the center as the upper and lower pistons are retracted. The experiments were designed to capture the transitional behavior from pure tensile to mixed-mode failure (inset). The results for a range of confining pressures are shown at bottom.

Compression Damage



Stanchits and Dresen, 2003

Tension Damage



Bobich, 2005

Figure 2.9. Experimental results for damage evolution in compression (top) and tension (bottom). In both cases damage is recorded by the cumulative acoustic emissions count. Damage increases slowly at first, rapidly increases at the point of yielding, and continues to accumulate during strain softening.

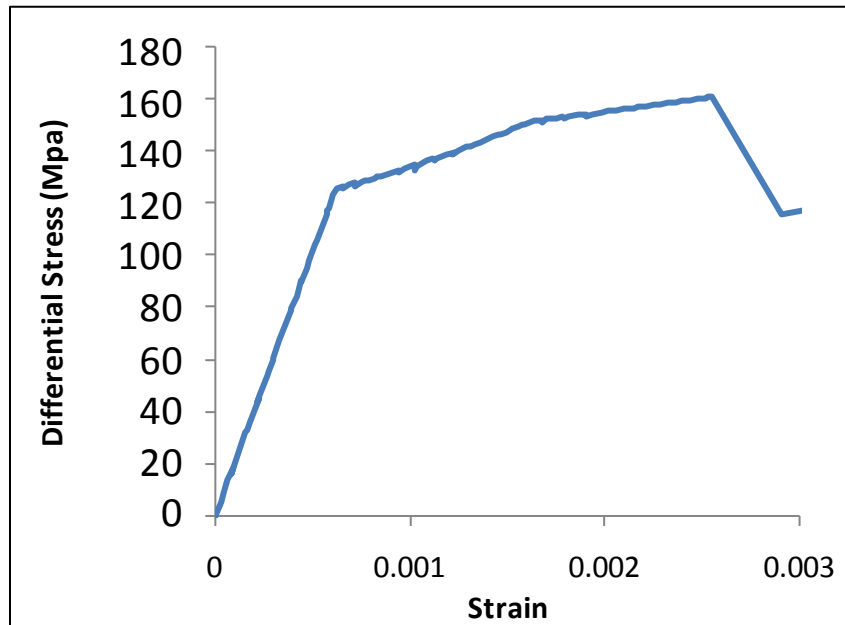
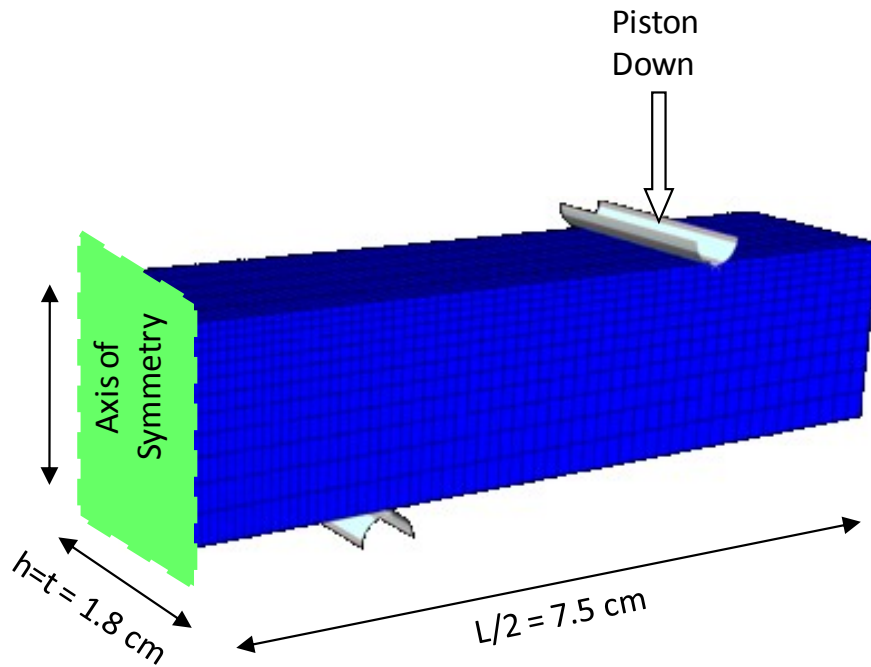


Figure 2.10. 3D finite element model of the four point beam configuration, with mesh and dimensions shown. Confining pressure is applied to all free surfaces. The beam is modeled in symmetry, so the far left end of the model is the true center of the beam. Arrows indicate applied confining pressure and the movement of the piston. The lower pin is fixed. The simulated results for the tensile part of the beam are shown at bottom.

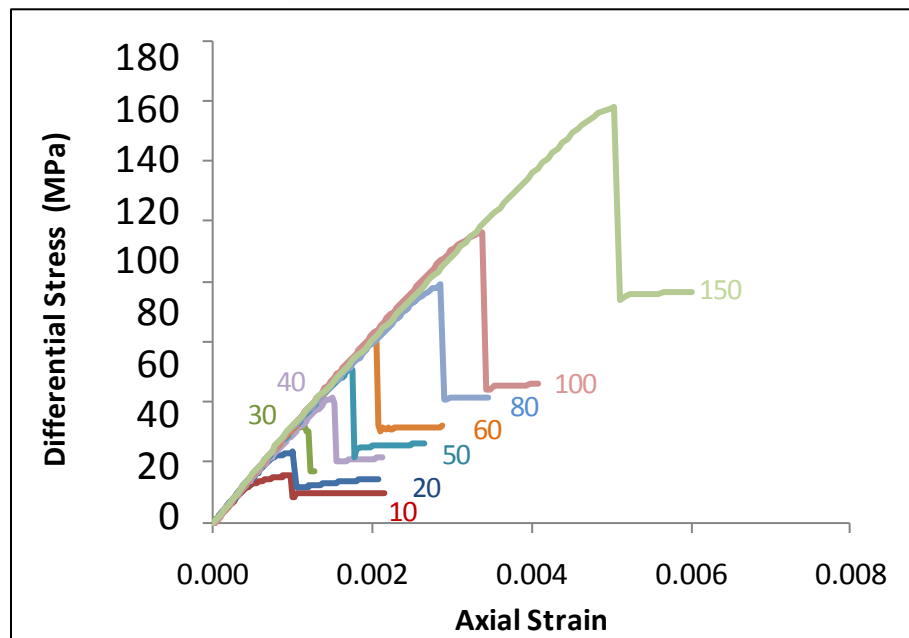
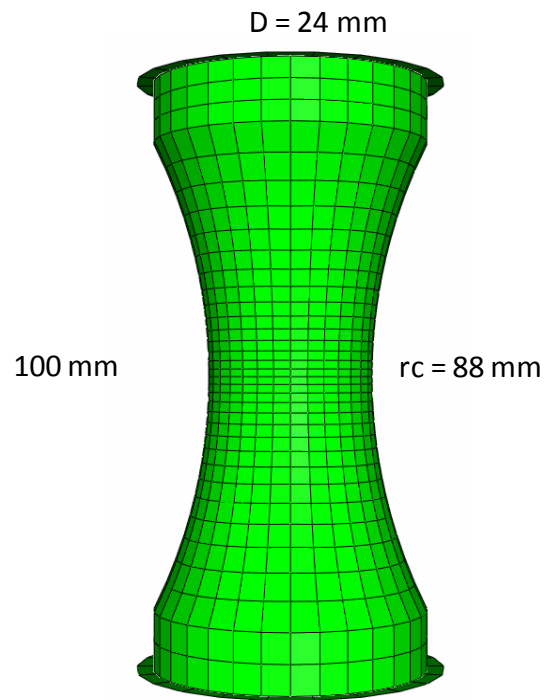


Figure 2.11. 3D finite element model of the dogbone configuration, with mesh and dimensions shown. Confining pressure is applied to all of the free surfaces. Both the upper and lower platen are rigid, frictional contacts and retract equally. The simulated results at the center of the sample are shown at right for several confining pressures.

CONSTITUTIVE MODEL

For our simulations, we use a constitutive model based on modifications of classical Mohr-Coulomb plasticity (Lubliner et al., 1989; Lee and Fenves, 1998; Abaqus). The model incorporates a pressure dependent yield criteria, a plastic flow rule, hardening rule, and an evolving stress function to model damage. More details of the plasticity rules appear in the above citations. In the “plastic-damage” model, plastic dissipation in compression and tension define a damage parameter, which scales the isotropic elastic stiffness matrix using the effective-stress approach (see Eq 6a, 6b). Because the model scales macroscopic deformation to plastic strain (Lee and Fenves, 1998), calibrating material parameters with experimental results is straightforward. The combination of strain softening and plastic-damage permits simulation of extreme localized weakening – where fractures or fracture zones (depending on the fineness of the finite element mesh) occur where material degrades to zero strength.

Mohr-Coulomb Yield Surface

The onset of yielding that occurs at the brittle ductile transition in rocks is typically pressure dependent (Murrell, 1965; Brace et al., 1966; Jaeger and Cook, 1976), defined by relating the shear and normal stress across a plane by the function:

$$F = c + \mu\sigma_n \quad [8a]$$

where $\mu = \tan(\phi)$ give the coefficient of friction and friction angle, and c is the cohesion. Byerlee showed experimentally that a value of $\mu = 0.6 - 0.85$ was a property intrinsic to most upper crustal rocks. The Mohr-Coulomb (MC) criterion assumes that failure does not depend on the intermediate principal stress, and thus can be written as:

$$\sigma_1 = c + q\sigma_3 \quad [8b]$$

$$q = [\mu_i^2 + 1]^{1/2} + \mu_i = \tan^2(\pi/4 + \phi/2) \quad [8c]$$

where σ_1 and σ_3 are the maximum and minimum principal stress. Equations 8b and 8c were used to model failure for several rock types (Colmenares and Zoback, 2002; Descamps and Tshibangu, 2007). In three-dimensional principal stress space (Fig. 2.12a), the MC criterion forms an irregular hexagonal cone centered about the hydrostatic axis, σ_0 :

$$\sigma_0 = 1/3(\sigma_1 + \sigma_2 + \sigma_3) \quad [9a]$$

The hydrostatic mean stress (or pressure, $\sigma_0 = p$) describes a lithostatic state of stress that increases proportionately with depth. The mean value is convenient because the three principal stresses are typically not equal (Turcotte and Schubert, 2002). The radius of the cone normal to the σ_0 axis defines the octahedral shear stress τ_{oct} , which rotates about the Lode angle θ (Fig. 2.12a), and takes the general form:

$$\tau_{oct} = 1/3[(\sigma_1 - \sigma_2)^2 + (\sigma_2 - \sigma_3)^2 + (\sigma_3 - \sigma_1)^2]^{1/2} \quad [9b]$$

The octahedral shear stress is a form of the deviatoric stress, where the mean stress is subtracted from the normal stress components (Turcotte and Schubert, 2002). In the MC model, τ_{oct} has a maximum and minimum value in the triaxial stress states. With rotation about the hydrostatic axis, τ_{oct} decreases linearly from the compressive to tensile meridians. τ_{oct} reaches a maximum for triaxial stress states along the compressive meridian ('C.M.', Fig. 2.12a), $\sigma_1 > \sigma_2 = \sigma_3$, at $\theta = \pi/6$. The hydrostatic stress then resolves to (following Descamps et al., 2007):

$$\sigma_{0C} = 1/3(\sigma_1 + 2\sigma_3) \quad [9c]$$

Solving for σ_1 and σ_3 and substituting into [9b] yields the triaxial octahedral shear stress in the compressive meridian:

$$\tau_{\text{octC}} = \sqrt{2} [(\sigma_{\text{oct}}(q-1) + c)/(2+q)] \quad [9d]$$

Similarly, τ_{oct} reaches a minimum along the tensile meridian ($\sigma_1 = \sigma_2 > \sigma_3$) ('T.M.', Fig. 11a) at $\theta = -\pi/6$. Giving:

$$\sigma_{0T} = 1/3(2\sigma_1 + \sigma_3) \quad [9e]$$

$$\tau_{\text{octT}} = \sqrt{2} [(\sigma_{\text{oct}}(q-1) + c)/(2+q)] \quad [9f]$$

Although the MC yield function has been widely used to analyze rock failure, the assumption that the intermediate principal stress is insignificant is only partially valid. Mogi (1967) points out that the MC predictions more closely match actual failure response in brittle rocks and for stress states having relatively lower values of the intermediate principal stress. Following in this direction, statistical evaluations of rock failure criteria show that some rock types (e.g., Shirahama sandstone, Yuubari shale) fail independently of the intermediate principal stress and can be approximated by MC, whereas others (e.g., Dunham dolomite, Solenhofen limestone) are highly σ_2 dependent and significantly deviate from MC (Colmenares and Zoback, 2002).

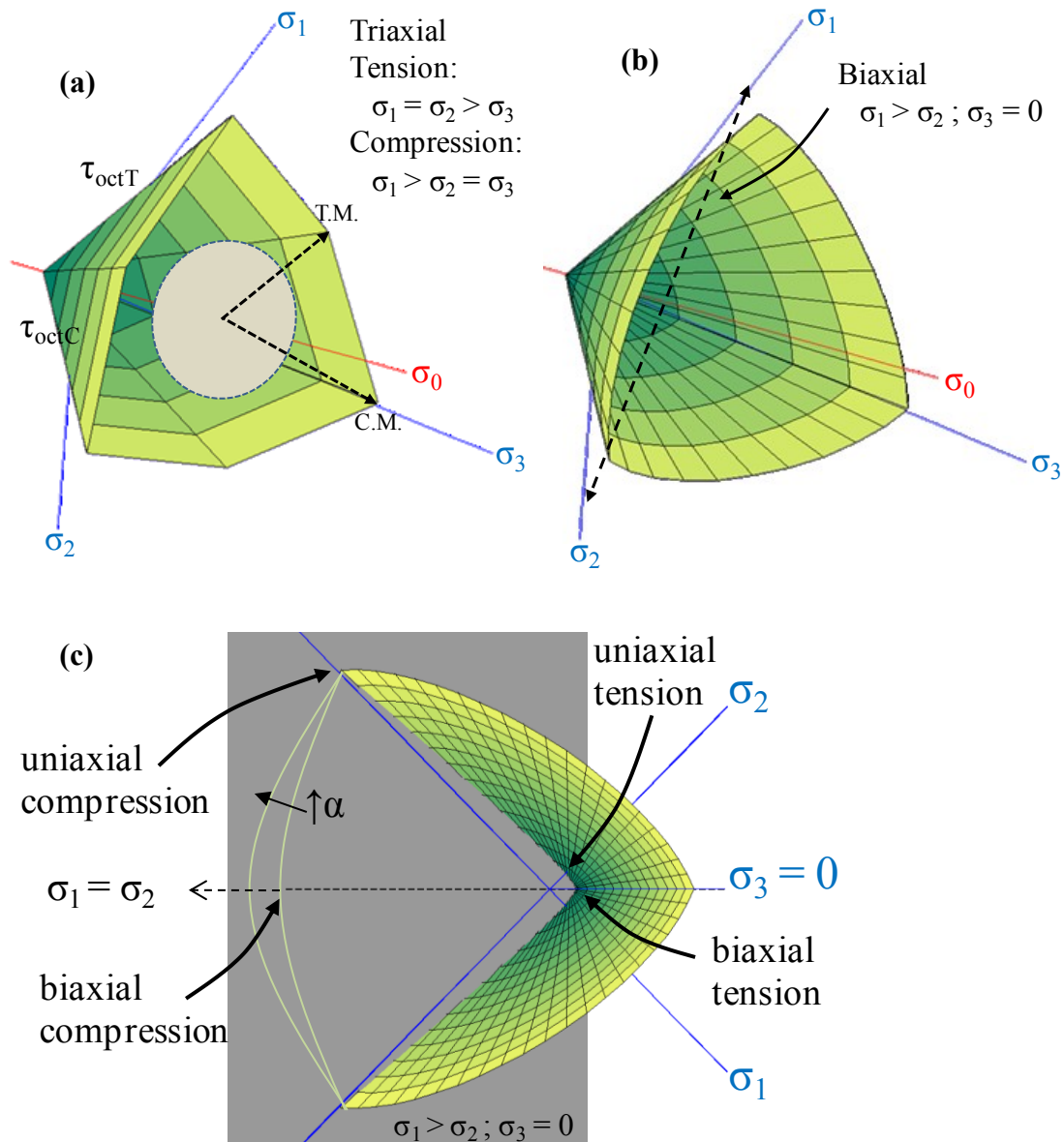


Figure 2.12. Yield surfaces plotted in principal stress space and centered around the hydrostatic stress axis, σ_0 . (a) Mohr-Coulomb yield surface showing tensile and compressive meridians (T.M. and C.M), defined by the octahedral shear stresses τ , and the lode angle (θ). (b) Barcelona yield surface, the curvature is adjusted to range between minimum dependence on the intermediate principal stress (e.g., Mohr-Coulomb) or full dependence (e.g., Drucker-Prager – a circular cone). The biaxial stress state is labeled and graphed in (c). The uniaxial yield parameters for the model UCS and UTS are labeled as well as the biaxial strengths.

Drucker-Prager Yield Surface

By assuming that the yield surface is fully dependent on the intermediate principal stress we establish τ_{oct} to be constant for all rotations of θ . Thus, we arrive at the Drucker-Prager (DP) criterion, where the shape of the yield surface is a perfect cone that opens with increasing σ_0 . The DP failure surface is a pressure-dependent variation on the von Mises criterion, and is given by:

$$J_2^{1/2} = k + 3\alpha I_1 \quad [10a]$$

where α and k are material constants, and the stress invariants I and the invariants of the stress deviator tensor J are:

$$I_1 = \sigma_1 + \sigma_2 + \sigma_3, \quad [11a]$$

$$J_2 = 3\sigma_0 - I_2, \quad [11b]$$

$$I_2 = \sigma_1\sigma_2 + \sigma_2\sigma_3 + \sigma_3\sigma_1 \quad [11c]$$

The radius of the DP cone can be set so that in the octahedral plane the circle circumscribes or inscribes the MC limits. For triaxial stress states, the DP criteria will typically either over-predict the tensile failure limit (circumscribed), or under-predict the compressive failure limit (inscribed). For conditions of plane stress, the circumscribed DP surface closely matches MC, whereas for plane strain the inscribed surface closely matches MC. In general, the Drucker-Prager criterion may be appropriate for modeling the upper and lower bounds of rock strength; however, rock strength is typically overestimated (Colmenares and Zoback, 2002).

Modified “Barcelona” Yield Surface

For our models, we use the modified yield surface proposed by Lubliner et al. (1989), which combines positive features of both the MC and DP models. Figure 2.12b shows the “Barcelona model” yield surface. The DP surface (Equation 10a) fits within the form:

$$F(\sigma) = 1/(1-\alpha)[(3J_2)^{1/2} + \alpha I_1] \quad [12a]$$

By assigning two additional parameters $\beta\langle\sigma_{\max}\rangle$ and $\gamma\langle\sigma_{\max}\rangle$ to [12a] the DP circle can be modified to reduce the dependence of the intermediate principal stress and establish tensile and compressive meridians. Thus, the form presented by Lubliner et al. (1989) and Lee and Fenves (1998):

$$F(\sigma) = 1/(1-\alpha)[(3J_2)^{1/2} + \alpha I_1 + \beta\langle\sigma_{\max}\rangle - \gamma\langle-\sigma_{\max}\rangle] \quad [12b]$$

where (Abaqus Manual)

$$\alpha = [(\sigma_{b0}-\sigma_{c0})-1]/[(2\sigma_{b0}-2\sigma_{c0}) -1]; 0 \leq \alpha \leq 0.5 \quad [12c]$$

$$\beta = [\sigma_{c0}/\sigma_{t0}](\alpha-1) - (1+\alpha) \quad [12d]$$

$$\gamma = 3(1 - K_c)/(2K_c - 1); 0.5 < K_c \leq 1.0 \quad [12e]$$

The uniaxial compressive and tensile yield strength are given by σ_{c0} and σ_{t0} and can be taken directly from experimental data. The biaxial tensile strength σ_{b0} is around 1.3% less than the uniaxial tensile strength (Lee and Fenves, 1998), yielding typical values of $0.08 \leq \alpha \leq 0.12$ and $1.10 \leq \beta \leq 1.16$ (Lubliner et al., 1989). K_c is the ratio of the length of the tensile to compressive meridians for a given pressure, i.e. controlling the dependence on σ_2 . For $K_c = 1$, β and γ drop out leaving the original DP function:

$$K_c = (\sqrt{J_2})_{TM}/(\sqrt{J_2})_{CM} \text{ at a given } I_1 \quad [12f]$$

This constitutive model has a few useful qualities for our purposes. First, it accommodates a broad range of rock behavior that was previously modeled by MC or DP failure. The form of the yield surface is familiar and flexible, and derives from standard plastic theory (Lubliner, et al., 1989). Second, in modeling new rock types from experimental data, it is convenient to use uniaxial failure and stress-strain data for calibrations. In reservoir applications, limited availability of rock core and restrictions on resources and time can make it difficult to calibrate a material model using a complete set of triaxial data; however, uniaxial compression tests are usually available. In limiting cases, one can apply the general observation that the tensile strength is 8-10 times less than compressive strength (Jaeger and Cook, 1976). Finally, the model is currently implemented in the commercial finite element software Abaqus, which can be used for a wide range of geologic problems.

MATERIAL PARAMETERS FOR NUMERICAL SIMULATIONS

Table 2.1 lists the range of stress-strain values from experiments on Berea sandstone. Table 2.2 lists the parameters used in the finite element models. Intermediate points on the strain hardening and damage curves (Fig. 2.6) were obtained by calibrating the benchmark model parameters against laboratory results (Figs. 2.7-2.12). We use a quasi-sinusoidal curve for damage-strain evolution based on Eberhardt (1998) and Bobich (2005). We assume a constant dilation angle of 15° . Other Abaqus parameters are a K_c value of 0.66 (see Eq. 12f), indicating minimal dependence on the intermediate principal stress, as well as the default value for the ratio of initial equibiaxial to uniaxial compressive yield stress, $fb_0/fb_c = 1.16$ (see Eq. 12c), which contributes to the shape of the yield surface (Fig. 2.12b).

RESULTS OF SIMULATIONS

We ran numerous simulations on the beam and dogbone configurations to calibrate the material parameters and model the stages of deformation observed experimentally for Berea sandstone. We calculated a variety of stress-strain curves across the top-center of the beam and in the central portion of the dogbone configuration using averaged element integration points values. When a reasonable ‘fit’ to the data was determined, we ran an additional refined simulation on the beam model for 10 MPa confining pressure, and on the dogbone model for $P_c = 10, 20, 30, 40, 50, 60, 80, 100, 150$ MPa. A ‘good fit’ in the simulations captures the essential stages of deformation corresponding to hardening, failure, and softening, and at values lying within the ranges observed experimentally (Fig. 2.7-2.9, Table 2.1). In comparison with Berea sandstone experiments, the simulated rheology slightly under-predicts non-linearity associated with strain hardening (Fig. 2.10, 2.11). We think that this is not a central limitation of the model, and that it can be eliminated by further refining the plastic parameters.

ONSET OF PLASTIC YIELDING

The initial linear portions of the curves reflect the Young’s Modulus of the undamaged material (Fig. 2.10, 2.11). The elastic stage accounts for the initial 0.0004-0.001 strain at low confining pressure, $P_c = 10-30$ MPa, which increases linearly to 0.0045 at $P_c = 150$ MPa. Fitting a linear trend line to the points at plastic onset gives the relationship $\epsilon_{EY} = (P_c + 3.8 \times 10^6) / 3.4 \times 10^{10}$. This equation approximates the elastic strain limit as a function of P_c , where ϵ_{EY} represents the elastic yield strain and P_c is the confining pressure.

STRAIN HARDENING

For $P_c < 30$ MPa strain hardening is pervasive and accounts for up to 50% of pre-strain failure, displayed as the broad “hump” on the stress-strain curve in Fig. 2.10.

For $P_c = 30-60$ MPa, strain hardening is greatly reduced and the “hump” essentially disappears. With increasing $P_c = 60-150$ MPa, strain hardening gradually increases to around 10% of the total pre-failure strain. Strain at ultimate failure occurs at 0.001 for $P_c < 30$ MPa, increasing to 0.005 at 150 MPa.

YIELD STRESS

Consistent with the yield surface definition (Eq. 12b), the ultimate yield stress increases linearly with confining pressure, i.e., constant friction angle. Failure occurs in the regions where stress is locally least compressive: under local tension for low confining pressure $P_c > 20$ MPa and under local compression for $P_c < 20$ MPa. The pressure to yield strain relationship can again be fit to a linear trend line by $\varepsilon_{UY} = (P_c + 3.5 \times 10^6) / 3.1 \times 10^{10}$, where ε_{UY} is the ultimate yield strain.

SOFTENING AND FINITE STRAIN

Following macroscopic failure at the ultimate yield stress-strain, there is an immediate stress drop, followed by constant stress deformation. The plastic parameters determine the character of the stress drop, where a more rounded peak and shallower post-failure slope reflects a more ductile behavior and a sharper peak and steep slope indicates brittle behavior. We found that increasing strain softening and the rate and magnitude of damage accumulation contributed to the brittle behavior observed experimentally. We also improved brittleness by using non-associated plastic

flow: i.e., decreasing the dilation angle ψ to 15° (e.g., Alejano, 2005), resulting in an additional stress drop of 1-2 MPa.

STRESS PATH

We plotted the stress paths (Harrison and Hudson, 2003) for the dog-bone simulations in order to understand the variations in magnitude of the stress tensor components during progressive deformation. Fig. 2.13 shows the incremental change in pressure stress $p' = 1/3(\sigma_1 + \sigma_2 + \sigma_3)$ versus deviatoric stress, $q = [1/2(\sigma_1 - \sigma_2)^2 + 1/2(\sigma_2 - \sigma_3)^2 + 1/2(\sigma_1 - \sigma_3)^2]^{1/2}$ for $P_c = 10-150$ MPa. All simulations begin at a hydrostatic stress state ($q = 0$). Retracting the pistons decreases p' and increases q along a constant, linear path during elastic deformation. The onset of strain hardening, plasticity, and damage causes the stress path to curve to the left as deviatoric stress decreases relative to pressure change.

DAMAGE PROPAGATION

The distribution of damage in the simulations shows good agreement with experimental observations. Figure 2.14 and 2.15 show contour plots of the tensile damage parameter, d_t , for the two simulated configurations. Damage initiates in a broad region corresponding to maximum strain, located just off center at the top of the beam. An explanation for this offset from center is apparent from plotting maximum curvature d^2y/dx^2 (solid lines) at several stages of deformation along the length of the beam (Fig. 2.16). Fig. 2.16 shows that the top-center region is not quite uniformly strained, and that curvature occurs about 2 cm from beam center, due to the lower fixed-points. Damage initiates (contours in Fig. 2.14, dashed lines in Fig. 2.16) at 3.5

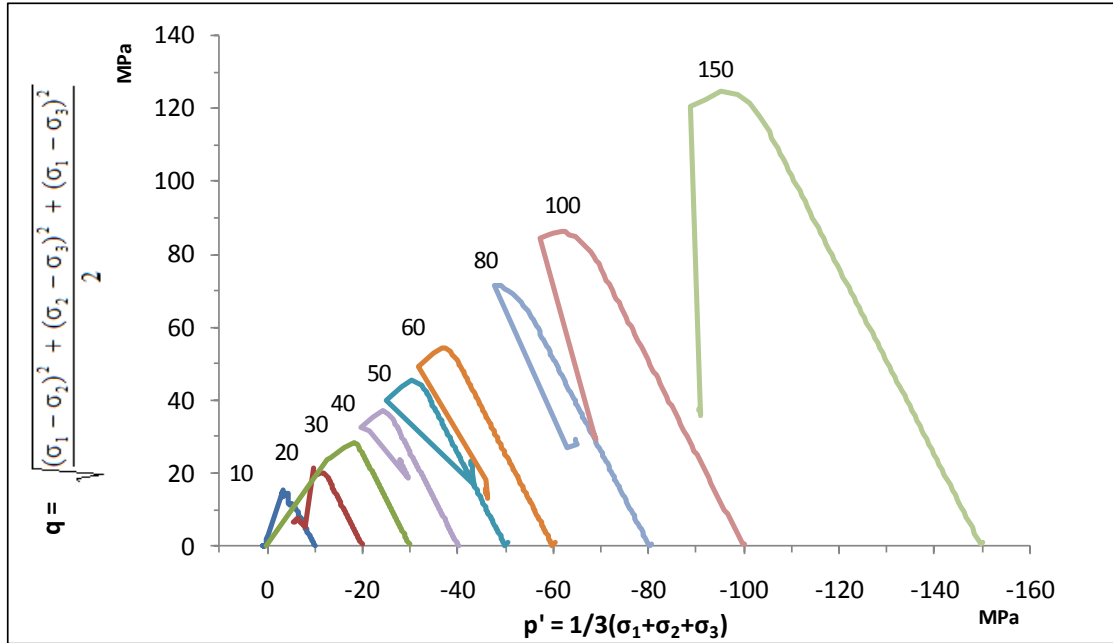


Figure 2.13. Stress paths plotted in p' - q space for the dogbone configuration. All tests begin at $q = 0$ and increase in q while decreasing in p' during elastic deformation (straight line). During plastic yielding (curved) q drops relative to p' . Failure occurs upon intersection with the yield surface (not plotted).

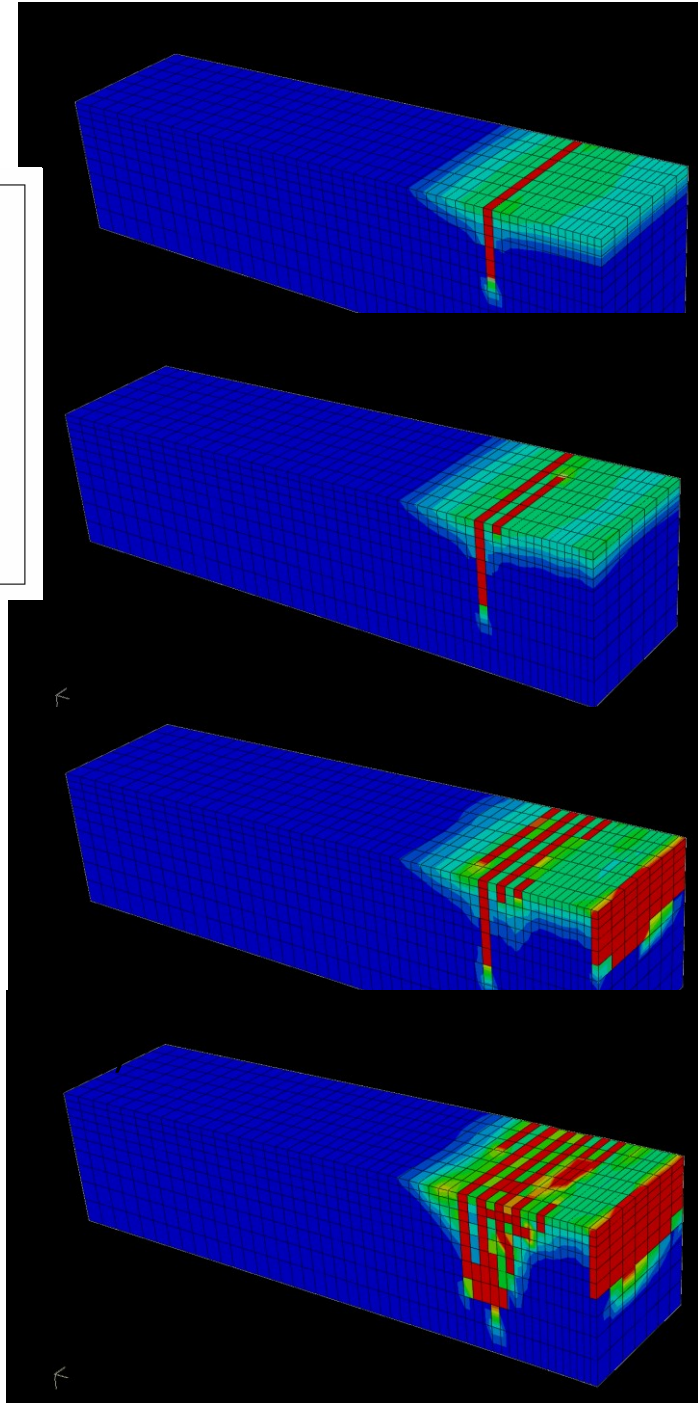
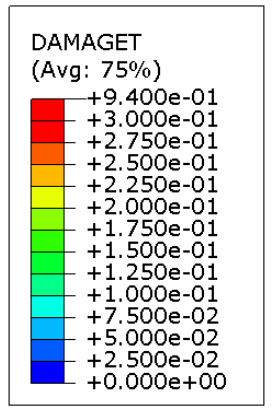


Figure 2.14. Contour plots of the tensile damage parameter for the four point beam configuration at four stages of deformation (a-d). Half of the beam is shown due to symmetry – the center is at the right. Blue is undamaged material, warm colors represent increasing damage. Red reflects an equivalent fracture zone with fully degraded stiffness. Several distinct main fracture paths are interpreted as forming within a pervasive zone of damage.

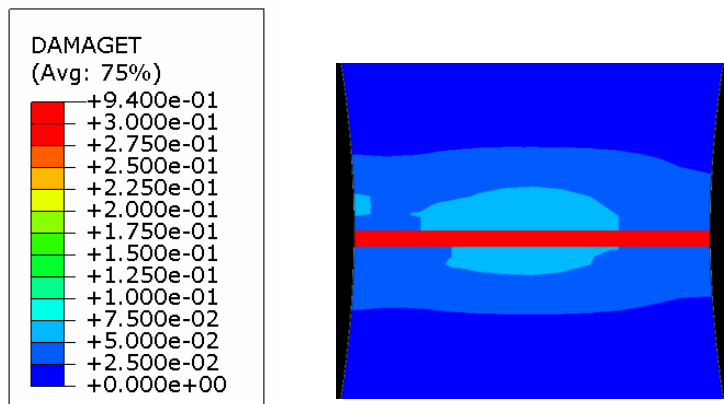


Figure 2.15. Contour plots of tensile damage for the dogbone setup with 10MPa confining pressure. Area shown is zoomed in at the center of the sample.

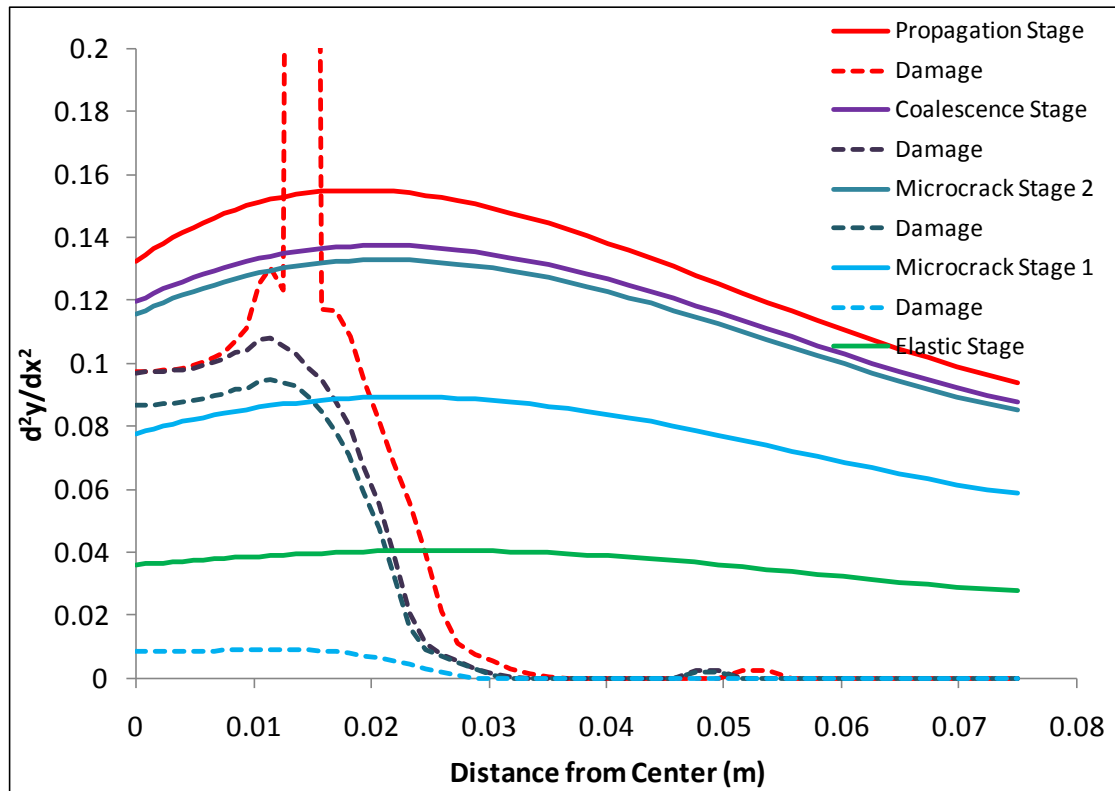


Figure 2.16. Curvature (solid lines) and damage (dashed lines) versus distance from the center of the beam at several stages of deformation, with interpreted micromechanical process. Damage accumulates in the areas of maximum curvature and localizes in a narrow equivalent fracture zone.

cm from the beam center and increases non-linearly towards the region of maximum curvature, reaching a maximum value of 1 at about 1.5 cm. Prior to first fracture, damage in the top-center of the beam increases to a value of 0.1, corresponding to 10% stiffness reduction. Multiple fractures form in regions of 15-20% stiffness reduction.

DISCUSSION

Elastic Limit: The elastic strain limit for many brittle rocks is less than 1% under typical reservoir conditions. The simulations indicate that Berea sandstone begins to deform inelastically as early as 0.1% strain under 30 MPa confining pressure. In zones of damage, particularly near fractures, the elastic Young's modulus needs to be replaced by the deformation modulus, which predicts the rock behavior in a more meaningful way.

Stiffness Reduction: Strain hardening begins at the onset of inelasticity and reflects decreasing stiffness. While the degree of strain hardening varies from rock to rock, the hardening stage may account for as much as 50% pre-failure strain. Our simulations match experimental results and show stiffness reduction of 10-15% prior to fracture formation for sandstone, and in compression and tension. Fractured zones displayed stiffness reduction of 20% or more.

Finite Deformation: In the simulations, post-failure strain is localized along planes of damage, and the macroscopic residual stress is essentially constant. Leading up to failure the pattern of strain becomes increasingly begins to localize. Fully failed and partially damaged regions contain heterogeneously distributed material properties.

With continued deformation, localized zones of failure function as if they were a new set of boundary conditions. The similar behavior is likely to occur in a sequence of rock layers in a geologic setting, albeit with more factors to consider.

SUMMARY

ROLE OF ROCK RHEOLOGY IN FRACTURED RESERVOIR ANALYSES

Intensely nonlinear processes control the development of fractured rocks, reflecting complex dynamical and strain-history dependent mechanical behavior. Necessarily, the same applies to fractured reservoirs since it is from within the mechanical framework that the pattern of natural fractures emerges. Often, the fracture architecture of a reservoir is simulated by overlaying stochastic models extrapolated from limited data sets onto kinematic reconstructions. This geometric/statistical approach cannot explain the mechanical development of natural fracture patterns (e.g., Nelson, 2001). Thus, it is our aim to advance the tools required to analyze the complex mechanics during progressive deformation and fracturing. The models presented here do not represent a particular geologic setting, rather they reflect upper crust conditions for realistic rock behavior.

Our goal was to develop a realistic rheologic model to implement in finite element simulations for the development of reservoir structures. A requisite for our modeling was to use readily available rock mechanics data and commercial finite element software – we used Abaqus/Explicit. The modeled rock rheology is elastic-plastic-damage and includes pressure dependent yield criteria, stiffness degradation, and fracturing via a continuum damage approach. We used the stress-strain character from

rock mechanics experiments of Berea sandstone to calibrate the numerical rheology, and successfully matched results for the main stages of deformation. This suggests that the material is now ready for implementation in a range of geologic problems. In Chapter 3 we apply the rheology to investigate the damage morphology, dynamical characteristics, and tectonic controls on hydraulic fracture propagation.

REFERENCES

- Ashby, M.F. and S.D. Hallam, S.D., 1986, The failure of brittle solids containing small cracks under compressive states. *Acta Metallurgica.*, v. 34, no. 3, p. 497–510
- Backers, T., Stanchits, S., and Dresen, G., 2005, Tensile fracture propagation and acoustic emission activity in sandstone: The effect of loading rate. *International Journal of Rock Mechanics and Mining Sciences*, v. 42, no. 7-8, p. 1,094-1,101.
- Barenblatt, G.I., 1962, Mathematical theory of equilibrium cracks in brittle fracture. *Advances in Applied Mechanics*, v. 7, p. 55-129.
- Bazant, Z.P. and Oh., B., 1983, Crack band theory for fracture of concrete. *RILEM Materials and Structures*, v. 16, p. 155-177.
- Brace, W.F., Paulding, B.W., Jr., and Scholz, C., 1966, Dilatancy in the fracture of crystalline rocks. *Journal of Geophysical Research*, v. 71, p. 3,939-3,956.
- Bobich, J.K., 2005, Experimental analysis of the extension to shear fracture transition in Berea sandstone. Master's Thesis, Texas A&M University, College Station, 52 p.
- Budiansky, B.R.J., and O'Connell, R.J., 1976, Elastic moduli of a cracked solid, *International Journal of Solids and Structures*, v. 12, p. 81-97.
- Colmenares, L.B. and Zoback, M.D., 2002, A statistical evaluation of intact rock failure criteria constrained by polyaxial test data for five different rocks. *International Journal of Rock Mechanics and Mining Sciences*, v. 39, p. 695-729.
- Chen, Z.H., Tham, L.G., Yeung, M.R., and Xie, H., 2006, Confinement effects for damage and failure of brittle rocks. *International Journal of Rock Mechanics and Mining Sciences*, v. 43, p. 1,262-1,269.

- Davis, P.M., and Knopoff, L., 1995, The elastic modulus of media containing strongly interacting antiplane cracks. *Journal of Geophysical Research*, v. 100, p. 18,235-18,258.
- De Borst, R. and Nauta, P., 1985, Non-orthogonal cracks in a smeared finite element model. *Engineering Computing*, v. 2, p. 35-46.
- Descamps, F. and Tshibangu, J.P., 2007, *Oil and Gas Science and Technology – Rev. IFP*, v. 62, no. 5, p. 683-694.
- Eberhardt, E., 1998, Brittle rock fracture and progressive damage in uniaxial compression. Doctoral Dissertation, University of Saskatchewan, Saskatoon, 334 p.
- Fish, J. and Belytchko, T., 2007, *A first course in finite elements*, Wiley, West Sussex, England, 336 p.
- Griffith, A.A., 1920, The phenomena of rupture and flow in solids. *Philosophical Transactions of the Royal Society, London*, v. A221, p. 163.
- Hamiel, Y., Lyakhovskly, V., and Agnon, A., 2004, Coupled evolution of damage and porosity in poroelastic media: theory and applications to deformation of porous rocks. *International Journal of Geophysics*, v. 156, p. 701-713.
- Handin, J. and Hager, R.V., 1957, Experimental deformation of sedimentary rocks under confining pressure: Tests at room temperature on dry samples. *Bulletin of the American Association of Petroleum Geologists*, v. 41, p. 1-50.
- Jaeger, J.C. and Cook, N.G.W., 1976, *Fundamentals of rock mechanics*, 2nd edition, Chapman & Hall, London.
- Johnson, P.A., Rasolofosaon, P.N.J., 1996, Nonlinear elasticity and stress-induced anisotropy in rock. *Journal of Geophysical Research*, v. 101, p. 3,113-3,124.
- Kachanov, L.M., 1958, On the time to rupture under creep conditions. *Izv. Akad. Nauk., USSR, Otd. Tekhn., Nauk*, v. 8, no. 1, p. 26-31.
- Kachanov, L.M., 1992, Effective elastic properties of cracked solids; critical review of some basic concepts. *Applied Mechanics Reviews*, v. 45, no. 8, p. 304-335.

- Kachanov, L.M., 2007, On the effective elastic properties of cracked solids – editor’s comments. *International Journal of Fracture*, v. 146, no. 4, p. 295-299.
- Katz, O. and Reches, Z., 2004, Microfracturing, damage, and failure of brittle granites. *Journal of Geophysical Research*, v. 109, B01206.
- Lee, J. and Fenves, G.L., 1998, Plastic-Damage model for cyclic loading of concrete structures. *Journal of Engineering Mechanics*, v. 124, p. 892-900.
- Lockner, D.A., Byerlee, J.D., Ponomarev, A., and Sidorin, A., 1992, Observations of quasistatic fault growth from acoustic emissions. In, *Fault mechanics and transport properties of rocks – A festschrift in honor of W.F. Brace*, *International Geophysics*, v. 51, p. 3-31.
- Lyakhovskiy, V., Reches, Z., Weinberger, R., and Scott, T.E., 1997, Non-linear elastic behavior of damaged rocks. *Geophysics Journal International*, v. 130, p. 157-166.
- Lublinter, J., Oliver, J., Oller, S. and Onate, E., 1989, A plastic-damage model for concrete. *International Journal of Solids and Structures*, v. 25, no. 3, p. 299-326.
- Mazars, J., 1986, A description of micro and macro-scale damage of concrete structure. *Journal of Engineering Fracture Mechanics*, v. 25, p. 729-737.
- Mazars, J. and Pijaudier-Cabot, G., 1996, From damage to fracture mechanics and conversely: a combined approach, *International Journal of Solids and Structures*, v. 33, p. 3,327-3,342.
- Mogi, K., 1973, Rock Fracture. *Annual Review of Earth and Planetary Sciences*, v. 1, p. 63.
- Murrell, S.A.F., 1965, The effect of triaxial stress systems on the strength of rocks at atmospheric temperatures. *Geophysical Journal of the Royal Astronomical Society*, v. 10, p. 231-281.
- Nelson, R.A., 2001, *Geologic analysis of naturally fractured reservoirs*. Gulf Professional Publishing, 2nd edition, 332 p.
- Nur, A., 1975, A note on the constitutive law for dilatancy. *Pure and Applied Geophysics*, v. 113, no. 1, p. 197-206.

- Ramsey, J.M. and Chester, F.M., 2004, Hybrid fracture and the transition from extension fracture to shear fracture. *Nature*, v. 428, p. 63-66.
- Reches, Z. and Lockner, D., 1994, Nucleation and growth of faults in brittle rocks. *Journal of Geophysical Research*, v. 99, no. B9, p. 18,159-18,173.
- Reches, Z., Schubert, G., and Anderson, C., 1994, Modeling of periodic great earthquakes on the San Andreas fault: Effects of nonlinear crustal rheology. *Journal of Geophysical Research*, v. 99, no. B11, p. 21,983-22,000.
- Rice, J.R., 1968, A path independent integral and the approximate analysis of strain concentration by notches and cracks. *Journal of Applied Mechanics*, v. 35, p. 379-386.
- Rice, J.R., 1975, On the stability of dilatants hardening for saturated rock masses. *Journal of Geophysical Research*, v. 80, p. 1,531-1,536
- Segall, P., and Pollard, D.D., 1983, Joint formation in granitic rock of the Sierra Nevada, *Geological Society of America Bulletin*, v. 94, p. 563-575.
- Stanchits, S., and Dresen, G., 2003, Separation of tensile and shear cracks based on acoustic emission analysis of rock fracture. *International Symposium Non-Destructive Testing in Civil Engineering (NDT-CE 2003)*, 107 p.
- Steinmann, P., Miehe, C., and Stein, E., Comparison of different finite deformation inelastic damage models within multiplicative elastoplasticity for ductile materials. *Computational Mechanics*, v. 13, p. 458-474.
- Thompson, R.M., 1986, Physics of fracture. *Solid State Physics*, v. 39, p. 1-130.
- Turcotte, D.L. and Schubert, G., 2001, *Geodynamics*, Cambridge University Press, 2nd edition, 528 p.
- Walsh, J.B. and Brace, W.F., 1964, A fracture criterion for brittle anisotropic rock. *Journal of Geophysical Research*, v. 69, no. 3, p. 449-456.
- Walsh, J.B., 1965, The effect of cracks on the compressibility of rock. *Journal of Geophysical Research*, v. 70, no. 2, p. 381-389.

Weinberger, R., Reches, Z., Eidelman, A., and Scott, T.E., 1994, Tensile properties of rocks in four-point beam tests under confining pressure. In Nelson, P.P. and Laubach, S.E., eds., Rock mechanics models and measurements: challenges from industry; proceedings of the 1st North American Rock Mechanics Symposium, the University of Texas at Austin, 1994, Rotterdam, Brookfield, VT, 1155 p.

APPENDIX A: FRACTURE ENERGY EQUIVALENCE

A brief point of clarity is helpful regarding fracturing from a classical fracture mechanics theory compared with the continuum damage method used here. The fracture mechanics approach (Griffith, 1920) and subsequent refinements (e.g., Barenblatt, 1962; also see Chapter 3) are useful for describing the growth of discrete cracks propagating from initial flaws. Continuum damage theory is well suited when describing the global, averaged behavior of fracture networks (e.g., smeared crack models [Bazant and Oh, 1983; de Borst and Nauta, 1985; Mazars and Pijaudier-Cabot, 1989] or locally, the evolution of microcracks (e.g., Steinmann et al., 1994; Mazars and Gilles Pijaudier-Cabot, 1996). The present work fits the latter perfectly, but expands to model discrete fracture growth in Chapter 3). Thus, it is important to note that the two theories are equivalent thermodynamically according to the equivalent crack concept (Mazars and Pijaudier-Cabot, 1996), which manifests in the normalized dissipated energy term g_d . Namely, there exists a damage zone that is equivalent to a discrete fracture and vice versa. The energy consumed by forming all of the microcracks in a volume is equivalent to decohesion of singular cracks with surface area A_d :

$$\int_V -Y \dot{\mathbf{d}} dV = -G \dot{A}_d \quad [13a]$$

where Y is the damage energy release rate, $\dot{\mathbf{d}}$ is the damage parameter increment, and $-G = G_f$ is the fracture energy release rate. On the left side the damaged area (or volume) is calculated directly using the energy density function. Following Mazars (1986), an equivalent crack A_e is attained from equation 13a:

$$Ae = \frac{\int_V \int_0^{D(x)} -Y d d x}{Gf} \quad [13b]$$

where $dd(x)$ represents evolution of the damage at a point, x . The total damaged area then reflects the summation of the area comprising all equivalent cracks over a volume V , which is the definition of the energy density function, ρ . This equivalence relates continuum and discrete fracture theory, but also offers a means for comparison between numerically predicted damage and the damage observed in experiments and quantified using other stiffness reduction models.

CHAPTER III

MORPHOLOGY AND DYNAMICAL ANALYSIS OF TRANSIENT HYDRAULIC FRACTURE PROPAGATION IN A ROCK LAYER WITH DAMAGE

RHEOLOGY

ABSTRACT

Finite element simulations are used to study hydraulic fracture propagation in a rock layer with damage rheology. Field and experimental observations indicate that non-uniform loading conditions and local heterogeneity precludes planar mode I growth and may lead to irregular propagation paths. Analytical hydrofracturing models usually consider an elastic host rock and produce idealized fracture geometries. The present approach begins with a simple configuration, but simulates transient, complex propagation in a rock with the elastic-plastic-damage rheology developed in Chapter 2. The present FE model simulates layer-scale propagation of a hydrofracture segment located away from near-borehole effects. A short injection period and fluid lag conditions are considered. The configuration is for a 0.30 m tall vertical hydrofracture embedded in a 3 m wide by 2.3 m tall layer. Vertical and horizontal tectonic loads of 50 MPa and 10-45 MPa are established, and internal fracture pressure of 10 MPa/s is then applied. The results indicate that high tectonic stress ratio requires low injection pressure and creates long hydrofractures with little fracture connectivity. Low tectonic stress ratio requires high injection pressure and creates high connectivity with short fracture segments. We simulated the dynamical growth of build-up periods during strain hardening and ruptures during brittle failure.

Unstable ruptures create larger, irregular damage patterns with multiple branches and segments.

INTRODUCTION

Hydraulic fracturing is a common technique used in low permeability reservoirs to create new fracture volume and stimulate fluid flow. Hydrofrac operations involve injecting highly pressurized slurries of water with sand or gel into perforations in the wellbore. Hydrofracturing also occurs naturally during the emplacement of dikes and sills (Pollard, 1978). Hubbert and Willis (1957) developed the basic model for hydraulic fracturing. They derived the state of stress at the wellbore and presented a solution for propagating a hydrofrac in a direction normal to the minimum principal regional stress. Haimson and Fairhurst (1967) extended the solution to solve for the size and shape of an idealized hydrofracture in a homogeneous elastic rock. This approach however, does not consider realistic rheology and it cannot explain the complex and non-idealized morphologies that occur in rock layers. For example, observations from excavated hydrofractures (Elder, 1977), laboratory induced hydrofractures (Wu, 2006; Ishida et al., 2004) and outcrops of dikes (Baer et al., 1994; Weinberger et al., 2000) suggest that idealized fracture patterns rarely occur under field conditions. Attempts to explain complex hydrofracture behavior include consideration of mechanical interactions (Delaney and Pollard, 1982; Sim, 2004), inelastic rock rheology (Papanastasiou, 1997; Lyakhovskiy et al., 1997; Weinberger et al., 2000; van Dam et al., 2002; also see Chapter 2), and detailed injection properties (e.g., Desroches, et al., 1994; Ishida et al., 2004).

We address the problem by using the finite element (FE) method , and effective computational technique to simulate complicated mechanical problems. The FE simulations of this paper demonstrate that the idealized hydraulic fractures predicted by the basic models occur under a limited range of field conditions. The simulations indicate that under typical reservoir conditions, complex fracture morphology is likely, even when the initial configuration is simple.

While the present analysis starts with a 2D model similarly to Hubbert and Willis (1957) and Haimson and Fairhurst (1967), it differs from the classical approach in three main points. (1) The rheology of the host rock is elastic-plastic-damage. In Chapter 2 we demonstrated that a finite element continuum damage rheology can faithfully approximate the finite stress-strain and brittle failure character of Berea sandstone in rock mechanics experiments. The present models implement this rheology. Fracture propagation is determined by the constitutive behavior of the rock, which permits simulation of failure independent of a crack-tip or decohesive zone. (2) We use a dynamic solution technique in order to simulate transient propagation. We investigate the processes of fracture arrest, rupture, branching, and segmentation. (3) We explore the effects of the loading conditions on the propagation morphology. The area of investigation of the simulations is limited to a single layer. This enables us to focus on the effect of the internal pressure and tectonic stress-state, which ultimately drive propagation, while maintaining the resolution in sufficient detail to characterize local complexity and interactions that occur within the layer. It is likely that the response within a single, simple layer reflects the least complex behavior to be expected in the reservoir.

The first portion of the paper describes key observations of hydraulic fracture complexity from the field and laboratory experiments. Next, the FE configurations are presented. The second part of the paper is presents the simulation results, in particular: (1) Main morphological features; (2) Fracture arrest and rupture; (3) Branching and segmentation; and (4) Loading conditions. Lastly, we discuss implications for fracture velocity and stability and approaches to control hydrofrac propagation.

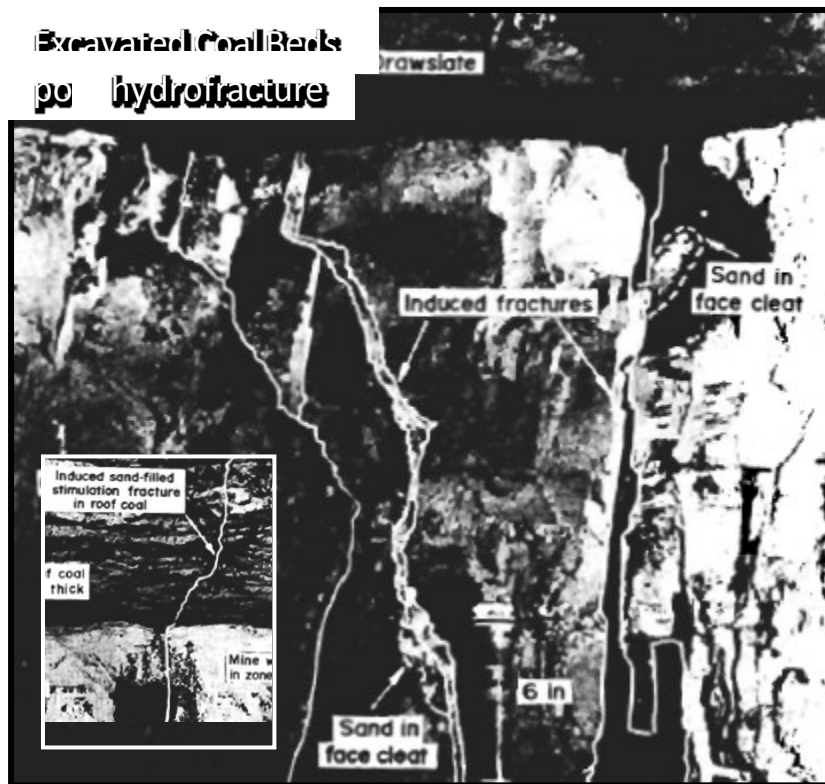
COMPLEX HYDRAULIC FRACTURES

FIELD OBSERVATIONS

Observation of hydraulic fractures in the subsurface is possible by employing multiple techniques (e.g., Mahrer, 1999). For example, the timing, spatial location, and interpreted source mechanisms of microseismic events reveal that the propagation path often conforms to the preexisting structure. In the Barnett Shale, Fort Worth Basin, TX, microseismic events “clouds” are diffuse and spherical, elongated and planar, or highly asymmetric depending on the state of stress and proximity to folds, faults, and karst structures (Busetti and Reches, 2007; Roth and Thompson, 2009; see Chapter 4). The fracturing mechanisms also conform to the local structure. For instance, high-energy microshear events induced during hydraulic fracturing were recorded in the compressive jogs of natural fracture corridors in the Carthage Cotton Valley Gas Field, Texas (Rutledge et al., 2004). Pre- and post-injection borehole image logs and cored intervals also suggest that in structurally complex areas multiple hydrofractures are more likely to propagate (Warpinski et al., 1993; Fast et al., 1994; Sim, 2004).

Though uncommon, there are a few instances of post-injection excavations. Excellent exposures were obtained following water and propping-sand treatments at depths of ~200m in two active coal mines in Pennsylvania and Illinois (Elder, 1977). Excavations revealed curved and zig-zag hydrofracture propagation paths, irregular aperture profiles, branching and linking segments, and terminations at layer contacts (Fig. 3.1). Detailed mapping revealed that the propagation paths conformed to the local structure. For instance, in one location a maximum pressure of 11.7 MPa was achieved and created a 1.3 to 6.4 cm wide sub-vertical fracture that was mapped for 20 feet propagating in the direction of the coal butt cleat (the non-systematic fracture orientation). In another location, a single sub-vertical fracture was mapped for 127 m. The fracture followed a path sub-parallel to the axis of a small anticlinal fold on the flank of the coal basin.

Dike formation is analogous to manmade hydrofracture operations (Pollard, 1978). Field exposures of dike segments are particularly helpful in understanding hydrofracture formation since the intruded, damaged host rock, the induced fracture pattern, and remnants of the injection fluid are often preserved. Arrays of en echelon dikes in sandstone, Maktesh Ramon, Israel, displayed stepped segments and continuous linked segments (Baer and Reches, 1991). The points of intersection for the segments were located within local zones of damage comprised of net-like patterns of deformation bands or in bridged zones showing evidence for pervasive shear deformation (Baer and Reches, 1991; Weinberger et al., 2000). Dike patterns near Timna Mountain, Israel, revealed subvertical contact structures and subhorizontal



Bureau of Mines, 1977

Figure 3.1. Photograph of induced hydrofractures (white) in an excavated coal mine. In the main picture the fractures terminate against the overlying rock strata. The propagation paths are complex and non-planar. In the inset picture the fractures are planar in the lower layer but not in the overlying coal layer. The field of view is about 1m. After Elder (1977).

steps, as well as interacting segment boundaries, ridges, and grooves (Baer et al., 1994). In some locations, variations in dike thickness correlated better to the local segment attitude than with the regional setting (the overall dike length). The authors concluded that both the preexisting dike segments and the regional state of stress controlled the dike pattern.

LABORATORY EXPERIMENTS

Experiments confirm that a state of high differential stress may enhance, redirect or completely suppress hydrofracture propagation. In rocks, such variations may be due to layering effects, preexisting discontinuities, local material heterogeneity, or by the presence of the hydrofracture itself. For example, Zhou et al. (2008) conducted experiments on a fabricated sand-cement block loaded in a true-triaxial machine to test the effect of the tectonic stress state on hydrofracture propagation and interaction with a preexisting fracture. In the normal stress regime ($S_v \gg S_{Hmax} \gg S_{hmin}$; ratio = 6.7:4.3-2.6:1), a vertically propagating hydrofracture was simple, straight and planar. The path was mostly undisturbed by a preexisting fracture with a high intersection angle 90° and arrested at a low intersection angle 30° . However, in a strike-slip regime ($S_{Hmax} > S_v > S_{hmin}$; ratio = 3:4:2) the propagation path was very sensitive to preexisting fractures at any angle of intersection (Fig. 3.2). In this case, the path was tortuous and the rotation angle ranged from $20-60^\circ$.

Tortuous propagation and segmentation of the fracture front is understood to relate to mixed-mode (I + III) loading, an observation explained by theory (Rice, 1968) and

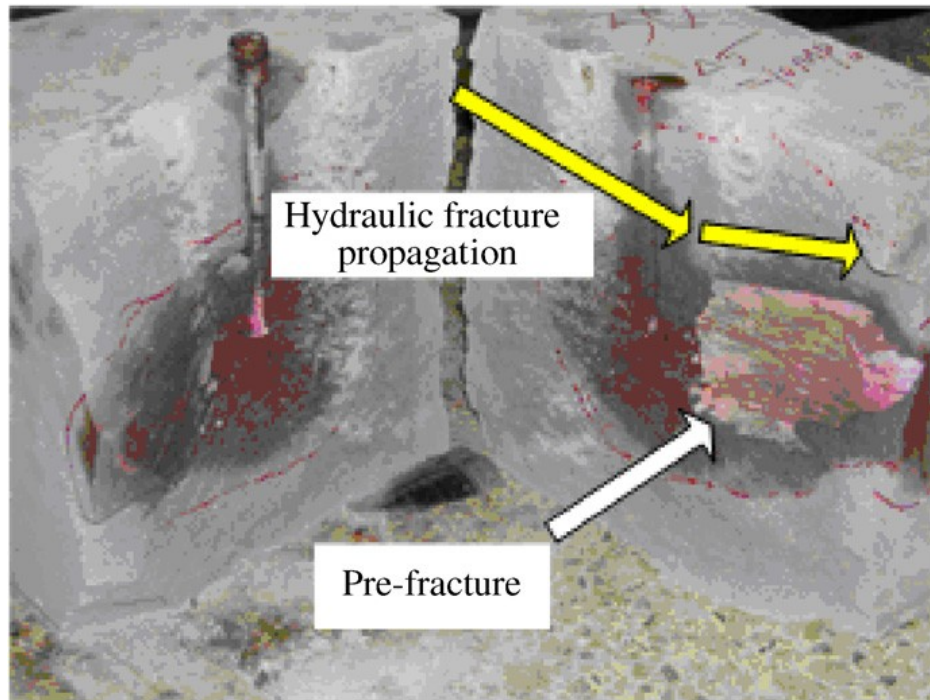


Figure 3.2. Photograph of laboratory induced hydrofracture. The propagation path first is along the direction of the maximum principal stress before bending towards the preexisting fracture. Continued propagation is from the tip of the preexisting fracture (after Zhou et al. 2008).

confirmed in experiments (Cooke and Pollard, 1996). Hydraulic fracturing experiments in PMMA (Wu, 2006) revealed that complex fracturing could be induced by injecting fluid into an initial planar, circular fracture, if only a small amount of torque was applied to the sample. Complex “flower petal” and en echelon structures with multiple twisting segments deviating up to 18° out of plane were created (Fig. 3.3) under a stress state with a shear component of only a few percent ($K_{III}/K_I = 1-10\%$).

In addition to the effects of the external loading, which reflect the conditions in the local geologic structure, experiments show that loading within the injection fractures affects complex fracture growth. Ishida et al. (2004) found that hydrofractures generated from injecting viscous oils into samples of granite created thick planar cracks with few branches, whereas water generated thin and wavelike fractures with many branches. By monitoring fault plane solutions from acoustic emission events, it was found that shear mechanisms were more dominant in forming the complex fractures.

The field observations and experimental results consistently reveal that there is a limited range of loading and geologic conditions under which the classical mode I hydraulic fractures form. It is more common that under reservoir conditions, non-idealized hydrofractures with irregular propagation paths form. The influence of local shear stress due to non-uniform loading conditions and inhomogeneity within the layer preclude simple growth in most cases. However, to produce complex morphologies, it is not necessary to begin with innumerable heterogeneities. As we will demonstrate later on, fracture complexity can develop naturally when the propagation model is able

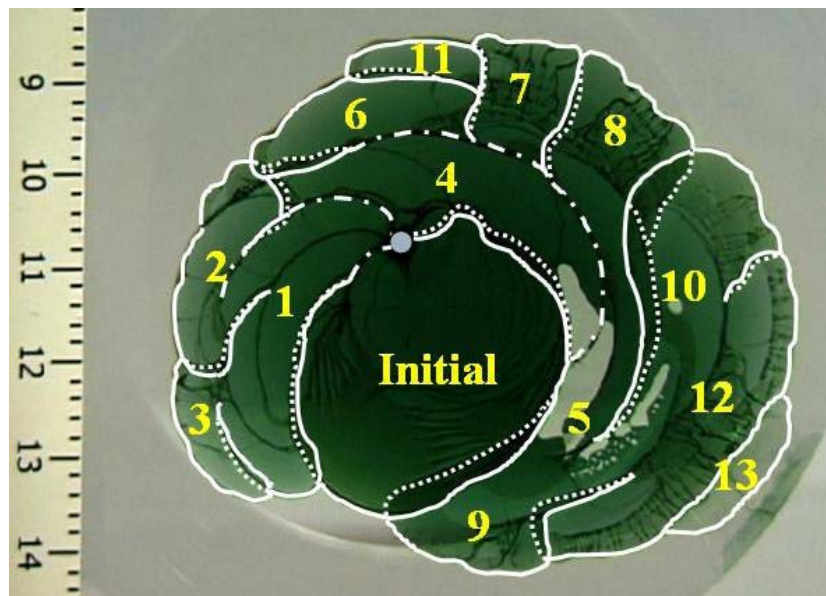
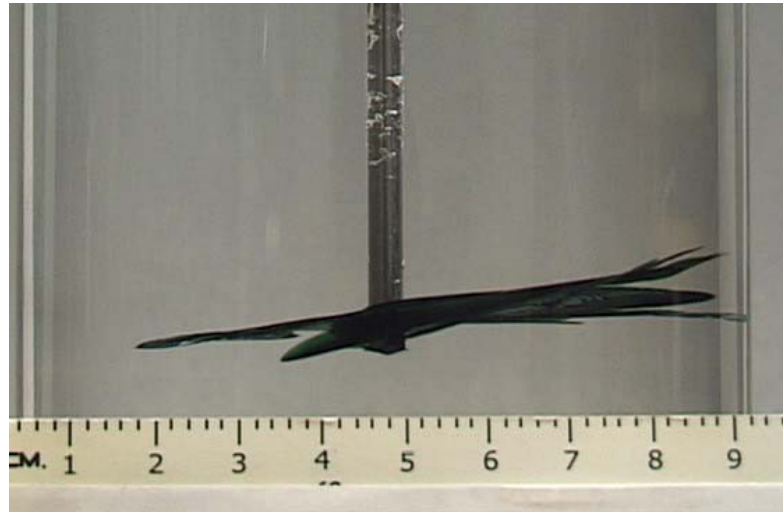


Figure 3.3. Laboratory induced hydrofracture in PMMA. Numerous out-of-plane segments develop (side view - top) with a shear component to loading of only a few percent. The growth sequence is not uniform (top view –bottom) and the resulting pattern is a complex “flower petal” with asymmetric lobes (Wu, 2006).

to “see” and respond to the intrinsic non-uniformity in the stress field. Mathematically, this requires the use of non-local stress-strain solutions – in the FE models we accomplish this using a continuum damage approach. We now move forward and review the fundamental mechanics needed to model simple and complex fracture propagation.

FE MODELING

MODELING APPROACH

In the introduction, we identified three distinct features of the present models: the implementation of an elastic-plastic-damage rheology, the use of a dynamic solution technique, and the emphasis on local damage characterization. In Chapter 2, we developed the theoretical background and described the calibration of the FE continuum damage scheme in detail. Here, we will not address it any further with the exception of outlining the damage and fracture energy formulation and the relevance of the approach to the current problem – in Appendix A. Appendix B outlines the explicit finite element technique and the time-integration scheme.

To solve the problem we use the explicit dynamic capabilities of the finite element code Abaqus/Explicit. FE is well suited to solve for non-linear constitutive behavior, finite strain, and time-dependent deformation, and it is straightforward to implement many of the boundary conditions involved in the classical hydraulic fracturing problem. The explicit solution technique handles finite strain well, which permits carrying out the simulations beyond brittle-failure, a feature necessary to model arbitrary propagation. In addition, it allows us to investigate the dynamical fracturing

response, the results of which we compare with laboratory and field observations.

Appendices A and B contain short reviews of the FE continuum damage scheme and the explicit/dynamic procedure.

CONFIGURATION

The scenario considered is for a single hydrofracture segment that has already propagated vertically through the reservoir some distance, has just cut through a ductile sandstone layer, and is now about to propagate upward through a thick layer of brittle sandstone (Fig. 3.4). The analyzed area is sufficiently far from the wellbore.

The tectonic stress states are for normal faulting conditions ($\sigma_v \geq \sigma_{Hmax} \geq \sigma_{hmin}$). The FE model is for 2D plane-strain, and the layer dimensions are 3 m wide by 2.3 m tall.

The overall model dimensions are large enough to negate adverse boundary effects within the area of interest in the center of the layer. The upper 2 m is homogeneous and contains elastic-plastic-damage material. The lower 0.3 m is elastic-plastic and contains a thin, vertical crack in the center.

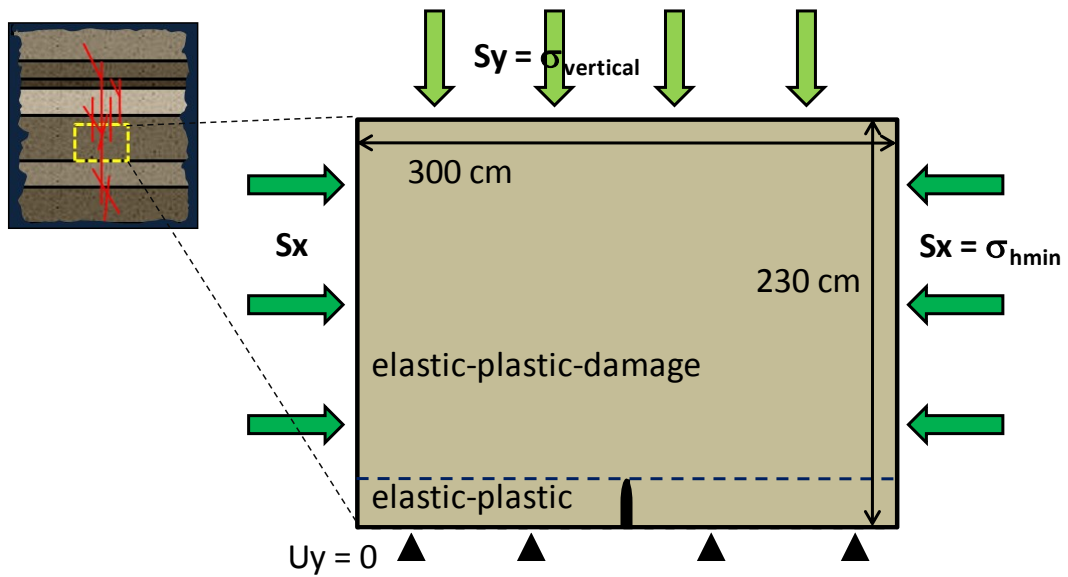


Figure 3.4. Finite element model configuration (right). Insert: schematic of the geologic scenario showing a set of horizontal layers at a distance from the wellbore, and for a single hydrofracture segment propagating through the reservoir and into a sandstone layer. Tectonic loads S_x and S_y are applied to the sides and internal pressure is applied in the preexisting thin, vertical crack.

CONSTITUTIVE MODEL

The rock material is elastic-plastic-damage with pressure dependant yielding, strain hardening and softening, and strain-based damage evolution in compression and tension, calibrated to rock mechanics experimental data for Berea sandstone. The material model is implemented in Abaqus as ‘Concrete Damage Plasticity’. Chapter 2 describes the constitutive model as well as the calibration procedure. The yield surface is based on the Barcelona model (Lubliner et al., 1989) (Fig. 3.5a), and is derived from the concepts of Mohr-Coulomb plasticity and is an adaptation of the Drucker-Prager cone-shaped yield surface to include the effect of the intermediate principal stress. We set the parameters so that a curved yield surface circumscribes an irregular three-dimensional hexagon with tensile and compressive meridians (similar to Mohr-Coulomb), and has limited dependence on the intermediate principal stress (Fig. 3.5a). Damage and fracture propagation are simulated using the continuum damage concept (Chapter 2). Two damage parameters for tension and compression evolve independently to capture both mode I and II/III failure (Lee and Fenves, 1998). Post-failure strain softening coupled with nonlinear damage evolution permit extreme damage localization (Fig. 3.5b, 3.5c). The robustness of the post-failure definition compares to that used in the crack-tip region of decohesive models (or in the enhanced elements in XFE) that are based on load-displacement criteria and strain-based cohesion degradation. In our simulations, the resolution of the damage zone equivalent to a discrete crack is determined by the coarseness of the FE mesh; an area of damage localization is the width of a single element, or 1-2 mm.

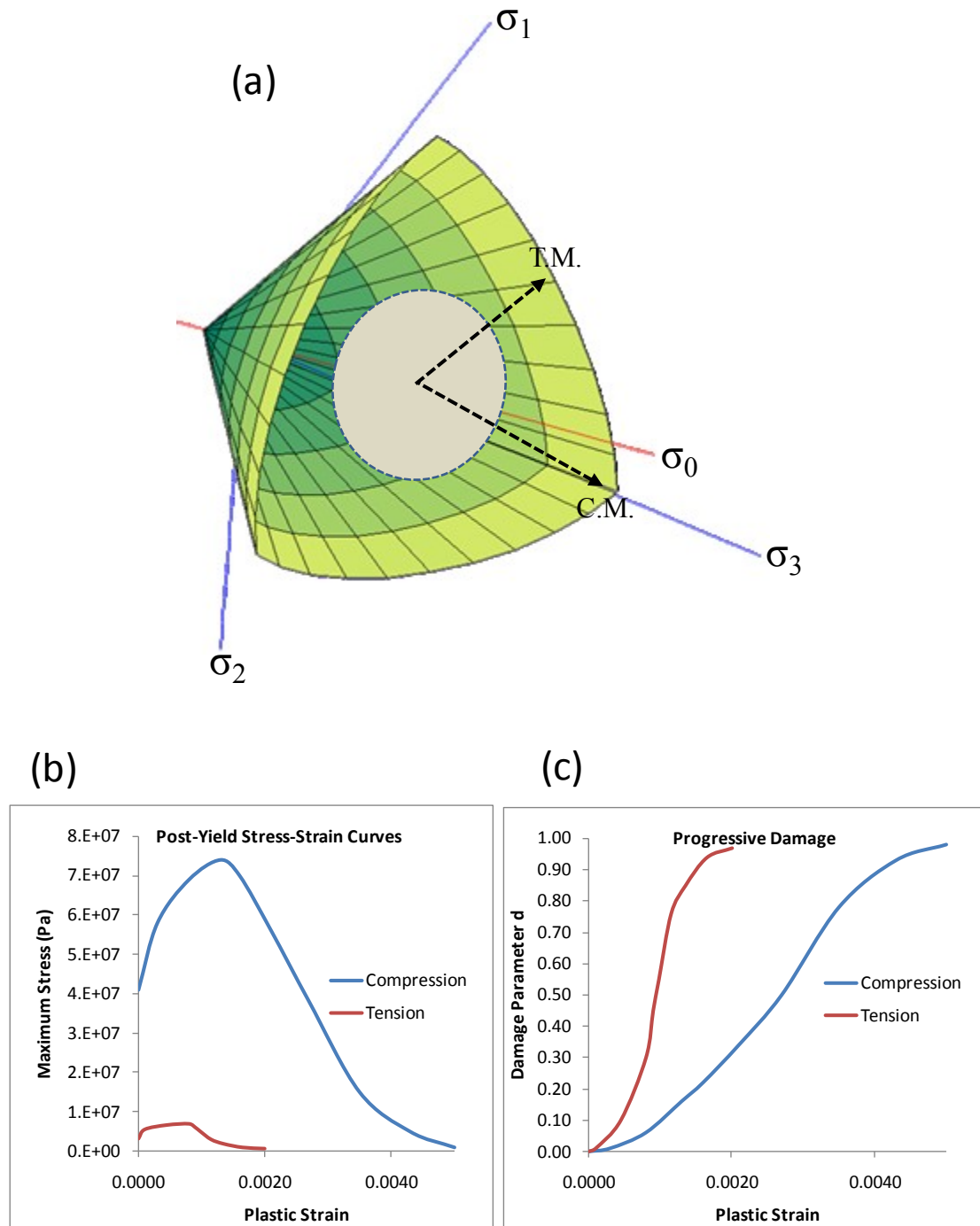


Figure 3.5. Constitutive model for the FE damage rheology. (a) Barcelona yield surface in principal stress space and centered about the hydrostatic axis, showing tensile and compressive meridians (T.M. and C.M.). (b) Strain hardening and softening curve for tension and compression and (c) evolution of the damage

LOADING PROCEDURE

The values for the tectonic stresses and injection pressure are based on field data and operational data from fluid injections in the Barnett Shale (Devon Energy, personal communication) and are typical for many hydraulically fractured reservoirs. Table 3.1 is a summary of the simulated cases. Constant pressure S_x and S_y are applied to the top and sides of the block to simulate the minimum horizontal stress and overburden, respectively, while the base is fixed in the y-direction. Pressure P_f is applied to the sides of the internal crack to simulate fluid injection. For all models the vertical stress is constant at $S_y = 50$ MPa, equivalent to a reservoir depth of about 6600 feet. The horizontal stress varies in each simulation from $S_x = 10$ MPa to 45 MPa. Loading occurs by first establishing S_x and S_y and gravity, and then by applying the internal crack pressure in two steps. First, P_f increases from 0 to $S_x + 5$ MPa, which is slightly below the breakdown pressure for the rock layer. Then, P_f increases until either total failure of the layer occurs or to twice the value of S_x . For both steps, the internal crack pressure P_f increases linearly with time at a rate of 10 MPa/s. This rate is about 10 times faster than the increase in bottom hole pressure recorded during the seconds immediately preceding the break down pressure for wells in the Barnett Shale (Devon Energy, personal communication).

The models simulate a single phase of “dry” propagation, with internal loading based on fluid lag conditions. No fluid penetrates through the fracture walls, into the crack-tip region, or ahead of the crack. These conditions of a local impermeable zone of microcracking ahead of the crack, and the advancing fluid front subsequently penetrating into the dry fracture tip are consistent with the results of various

Table 3.1. Summary of Simulations

Test	Load Configuration				Damage Distribution		
	Tectonic State of Stress (Mpa)		Rate of Extension (mm/s)	Internal Pressure Distribution	Pattern of Main Fracture Path	Pattern of Damage	Shape l/w ratio
	Sx	Sy	dx/2		(d > 0.5)	(0.01 < d < 0.1)	(d ≈ 0.01)
1	0	0	0.5	N/A	long, straight	parallel, symmetric	7.0
2	0	0	0.25	N/A	long, straight	parallel, symmetric	4.8
3	0	0	0.15	N/A	long, straight	parallel, slightly wavy	5.9
4	0	0	0.075	N/A	long, straight	parallel, wavy	4.8
1	10.0	50	N/A	Uniform	complex, long	pervasive, bifurcated	0.8 - 1.2
2	12.5	50	N/A	Uniform	complex, long	pervasive, bifurcated	0.7 - 1.4
3	15.0	50	N/A	Uniform	complex, long	pervasive	0.8 - 2.0
4	17.5	50	N/A	Uniform	complex, long	pervasive, bifurcated	0.7 - 1.5
5	20.0	50	N/A	Uniform	complex, short	pervasive, asymmetric	0.6 - 1.7
6	22.5	50	N/A	Uniform	complex, short	pervasive, symmetric	0.5 - 1.6
7	25.0	50	N/A	Uniform	long, straight	tear drop tip	2.2
8	30.0	50	N/A	Uniform	long, straight	small tear drop tip	3.1
9	35.0	50	N/A	Uniform	long, straight	small tear drop tip	4.2
10	40.0	50	N/A	Uniform	simple, short branches	asymmetric bridging	2.6
11	45.0	50	N/A	Uniform	complex, short	pervasive, irregular	0.3 - 0.4
12	10.0	50	N/A	Non-Linear	complex, long	pervasive, bifurcated	0.9 - 1.3
13	12.5	50	N/A	Non-Linear	complex, long	pervasive, bifurcated	0.6 - 1.2
14	15.0	50	N/A	Non-Linear	complex, long	pervasive, bifurcated	0.6 - 1.2
15	17.5	50	N/A	Non-Linear	complex, long	pervasive, bridging	1.4
16	20.0	50	N/A	Non-Linear	complex, long	asymmetric bridging	2.1
17	22.5	50	N/A	Non-Linear	long linking segments	symmetric bridging	N/A
18	25.0	50	N/A	Non-Linear	long linking segments	symmetric bridging	1.8
19	30.0	50	N/A	Non-Linear	long, straight	tear drop tip	2.8
20	35.0	50	N/A	Non-Linear	long, straight	tear drop tip	3.1
21	40.0	50	N/A	Non-Linear	simple, short branches	asymmetric bridging	2.6
22	45.0	50	N/A	Non-Linear	complex, short	pervasive, lateral	0.5

experiments, especially in the case of viscous fluids (e.g. Van Dam et al., 1999). In the experiments of Ishida et al. (2004), whether viscous oil or water was used significantly affected the shear distribution and the hydrofracture pattern. The pressure distribution within a crack can be approximated by:

$$dp/dx = 12\mu q/w^3 \quad [9]$$

where dp/dx is the pressure drop along the crack, μ is the viscosity, q is the flow rate, and w is the maximum aperture. Internal pressure distribution is applied according to two end-member conditions. Case 1 is for a uniform pressure distribution $dp/dx = 0$. In case 2, a non-linear pressure distribution (Fig. 3.6a) is applied. Figure 3.6b shows the effect of each of the two cases on the resulting crack profile during pressurization.

DATA OUTPUT

The subsequent discussion and figures quantify the amount of damage using the damage parameter d , which was discussed in Chapter 2. Unless otherwise specified, d reflects the combined damage from tension and compression and is equal to the local stiffness degradation (for example, $d = 0.9$ means 90% of the original stiffness has been lost). The parameter $d = 0$ is for undamaged rock, $d \sim 0.4$ coincides with the ultimate stress limit and is generally understood to reflect the stage when microcracks have coalesced to form macroscopic fractures, and $d = 1$ represents a pervasively damaged, completely failed region of rock with stiffness = 0. During the propagation periods of the simulations, field variable output requests were made every 0.001s, and data for various energy variables for the entire system were recorded at 200 equal intervals.

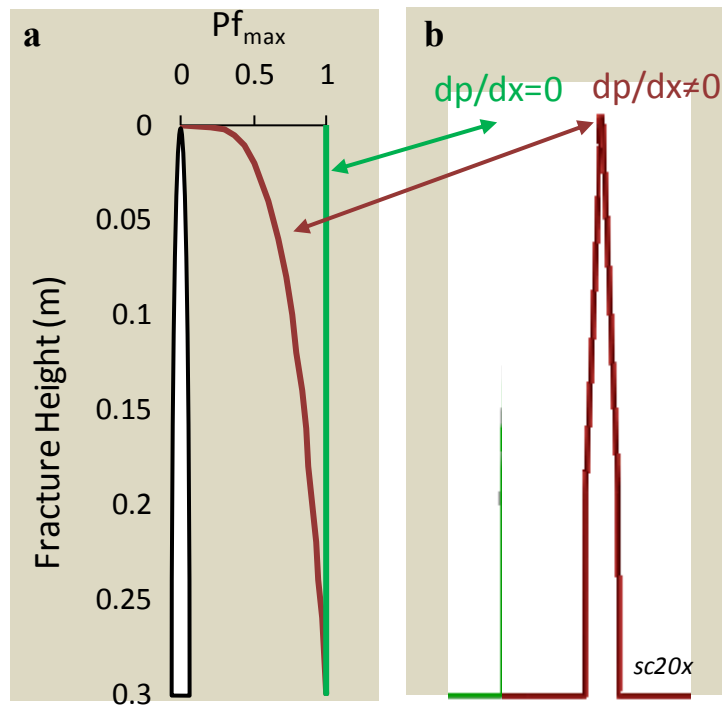


Figure 3.6. Pressure loading conditions. (a) Uniform (green) or distributed (red) pressure is applied to the inside of the initial vertical fracture. (b) The resulting aperture profile for the two loading conditions. Note the geometry is exaggerated by a factor of 20. The uniform pressure creates a quasi-elliptical profile, whereas the distributed pressure yields a more cusped fracture.

RESULTS: SIMULATION OF PROPAGATION DYNAMICS

A total of 22 successful simulations were run by increasing the internal pressure, P_f , in the initial crack while holding the tectonic stresses S_x and S_y constant. Additionally, four simulations were conducted for tectonic extension only ($S_y = P_f = 0$; $\epsilon_x > 0$) to explore the dynamical sensitivity of the FE models. The test configurations are listed in Table 3.1. We start by (1) describing a typical propagation sequence and reviewing the main features of the simulations and explaining the associated terminology, using the extension tests for reference. Next, (2) for both the simple extension and hydrofracture scenarios we describe the geometry and evolution of fracture arrest and rupture patterns. These topics are closely coupled to fracture velocity and stability and carry significant implications for interpreting complex fracturing. Therefore, some discussion about the character and conditions that determine the dynamical response is included. We then (3) address segmentation and branching features, which are not limited to but appear dominantly in the hydrofracture simulations. Finally, (4) we look at the role of three primary field conditions on damage evolution and fracture propagation, starting with tectonic loading and fluid pressure, followed by the results of varying the fluid pressure distribution in the initial crack.

It is important to clarify that the constitutive behavior for the modeled elastic-plastic-damage rheology is strain rate independent by definition. Thus, the observed dynamical effects are solely related to the kinetic response due to loading and failure. It will become evident that the intrinsic complexity of dynamical propagation in a

nonlinear medium has the potential to generate complex fracturing even under very simple loading and geometric configurations.

MAIN FEATURES

Figure 3.7 shows the progressive damage pattern at three time intervals for extension test 1 and at a late stage for test 4 (see Table 3.1). At the start of initial extension, two symmetric, least-compressive stress lobes form at the tip of the initial fracture. With continued extension, the lobes become increasingly tensile and the size of the tensile domain gradually widens ahead of the fracture. When the plastic yield limit is reached, quasi-symmetric lobes of damage begin to form within the tensile region ahead of the crack-tip. A damaged region of magnitude $0.001 < d < 0.0001$ grows to 150 x 100 mm, widest in the direction of the minimum horizontal stress, (note, ~100 x 60 mm for the hydrofrac cases). This broad, weak *damage front* precedes the propagating crack-tip, migrating upward with continued extension, and leaves behind a swath of microcracks henceforth referred to as the *damage corridor*. In the center of the damage corridor, damage quickly intensifies and localizes within a narrow zone ~10-20 mm wide (1 element width) with $d = 0.99$; interpreted as the *equivalent fracture zone* which we will also refer to as the *main fracture path* (Fig 3.7a, $t = 0.2670$ s). The main fracture path continues to grow in a series of *build-up and release periods*. The build-up periods widen and intensify the damage corridor at the current crack-tip location. The release periods extend the length of the damage corridor and the main fracture path (*note, we use the dimensions height and length interchangeably: though designation of the axes as S_v and S_{hmin} is geologically convenient, S_y and S_x are nonetheless arbitrary). A release period begins as a *rupture*

and concludes as an *arrest*. Prolonged lateral damage intensification without upward propagation results in the formation of *potential branch sites*. If the main fracture path subsequently propagates forward, the potential branches may either propagate as *active branches*, or terminate, leaving behind one or more *failed branches* (Fig. 3.7b, $t = 0.2870\text{s}$). Failed branches are recognized as lobes of damage extending obliquely from the main fracture path. Active branches may eventually reconnect with the main path. The overlapping of closely spaced failed branches creates the net effect of an intensified damage corridor, where $d = 0.01$ to 0.05 (Fig. 3.7b). *Fracture segments* are disconnected branches that form out of sequence from the main fracture path and may be isolated, connected by bridges of damage, or be completely linked (Fig. 3.7c, $t = 0.3700\text{s}$).

FRACTURE ARREST AND RUPTURE

The main features described above are produced in all simulations; however, the local morphology and the growth process vary significantly between tests. We will first summarize the arrest and rupture character for the extension tests before proceeding to the hydrofracture scenario. The purpose for this is two-fold. First, the dynamical features exhibited in the hydrofracture scenario are clearer following a review of the simpler case. Second, it is important to show that even small changes to the model compound over time. In the extension case, the only load change is the strain rate, and yet the resulting growth process and morphology is distinct for each case.

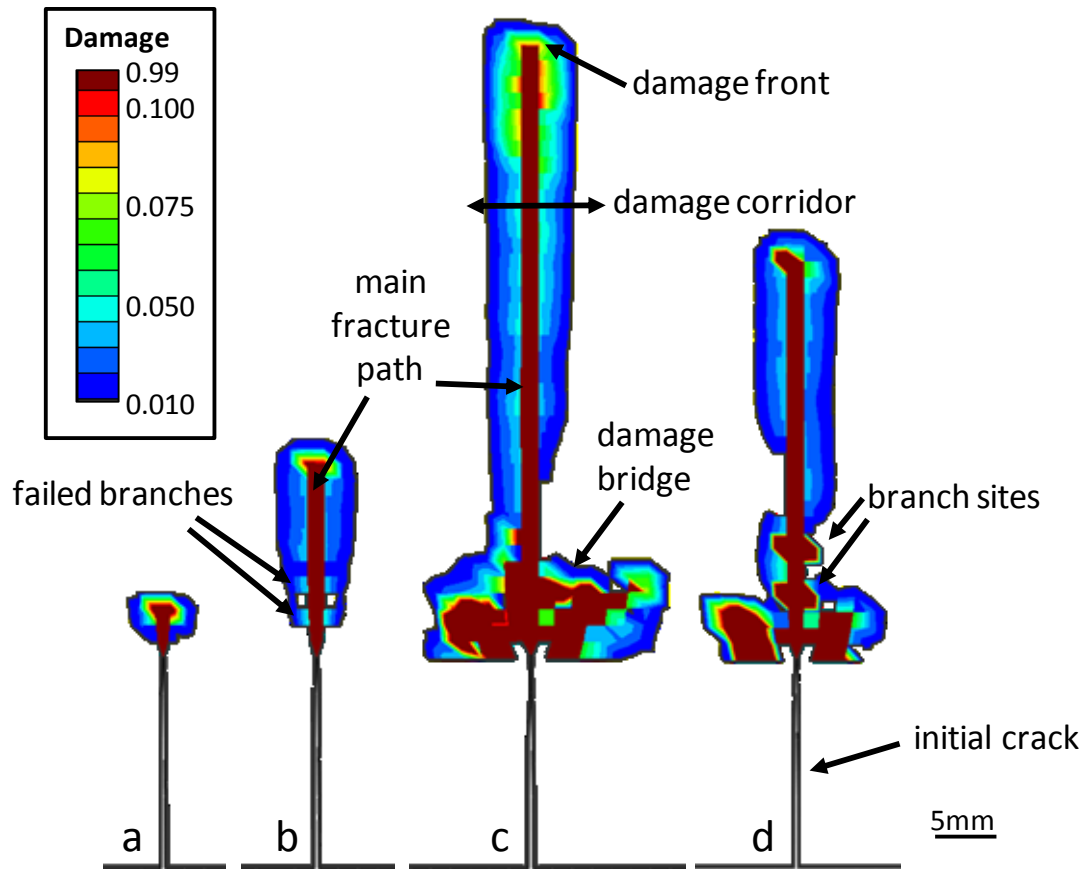


Figure 3.7a. Damage contour plot showing the main morphological features. The damage pattern is shown at three time intervals for the 0.5 mm/s extension test (a-c) and at a late stage for the 0.075 mm/s test (d). The initial crack is 30 cm long. Color scale reflects intensity of damage by microcracking. The dark red is interpreted as the main fracture path, where damage has completely localized and there is zero stiffness. Several key features are identified on the plots (see text).

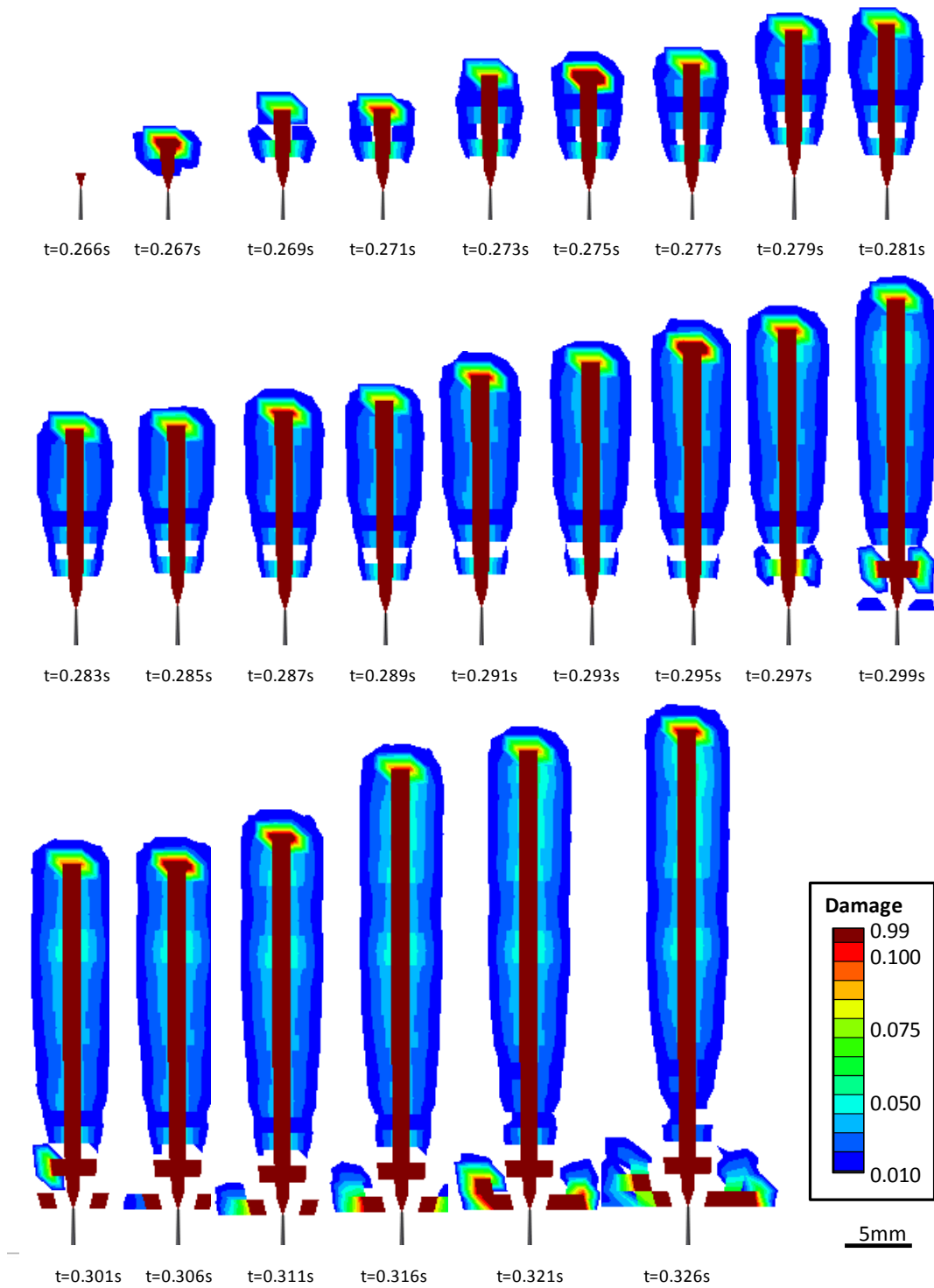


Figure 3.7b. Time-sequence damage contour plots showing evolution of the main morphological features for the 0.5 mm/s extension test (plots a-c in Fig. 3.7a). Time increment is 0.002s seconds except the last few frames which are at 0.005 second intervals.

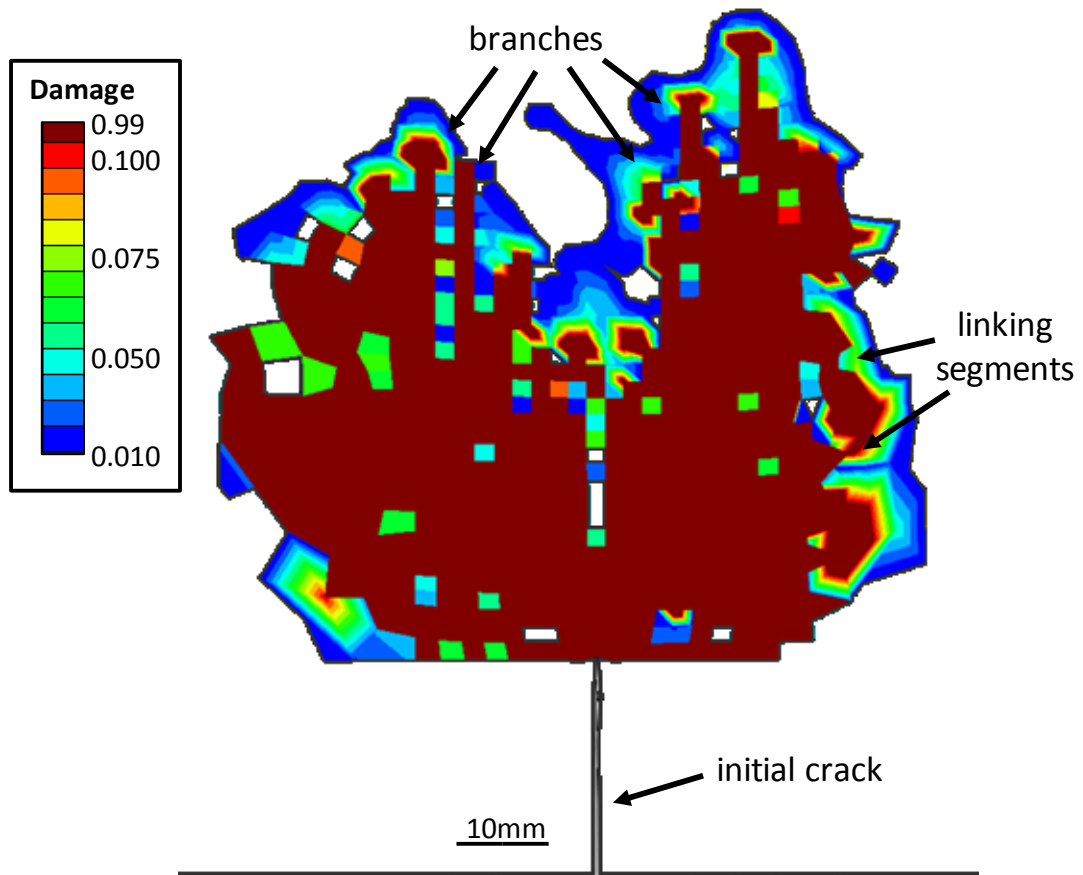


Figure 3.8a. An example of a complex hydrofracture formed under a state of high differential stress. The pattern shows no distinct main fracture path, displays multiple branches and linking segments, and the overall damage distribution is pervasive.

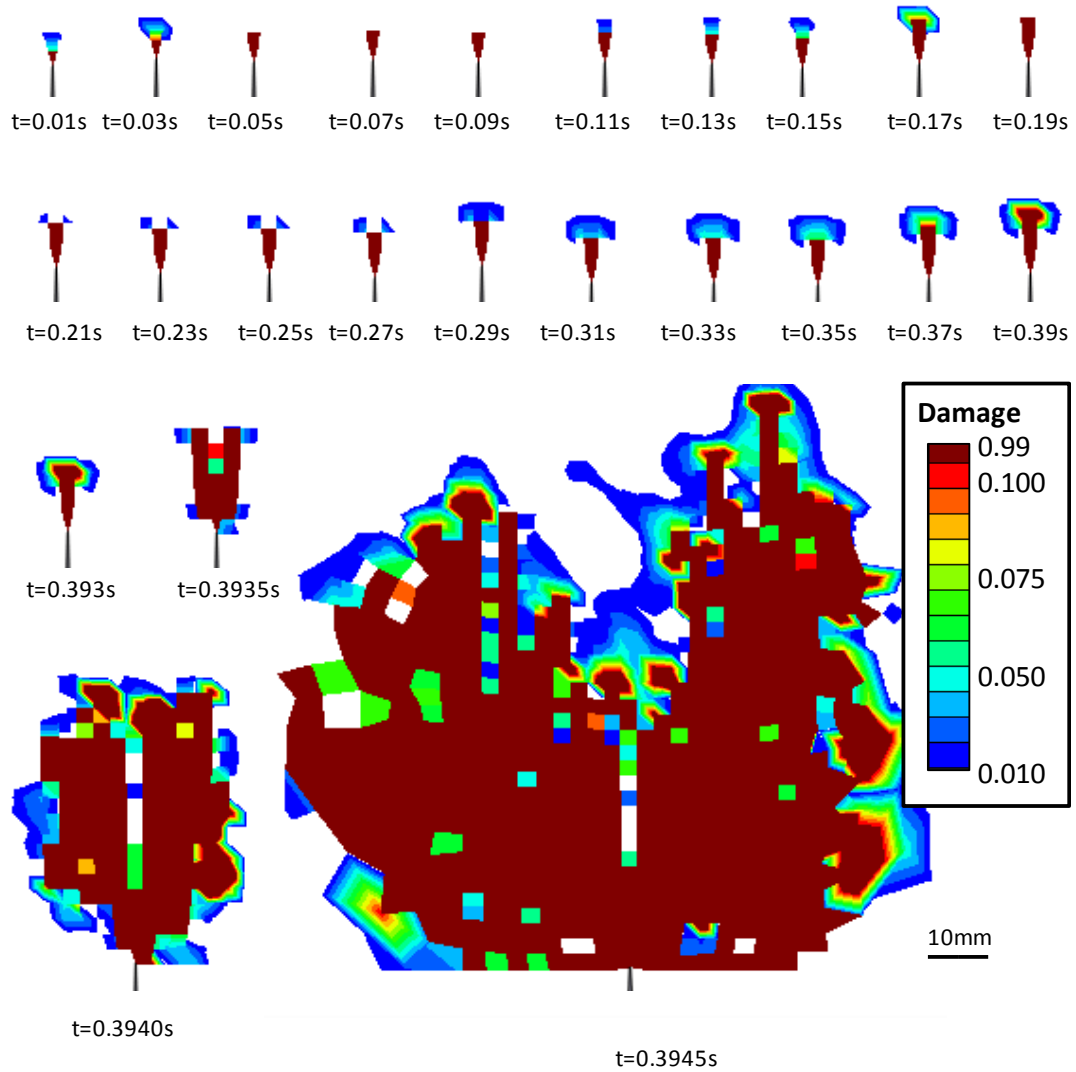


Figure 3.8b. Time-sequence damage contour plots showing evolution of the main morphological features for a very high differential stress tectonic regime ($S_x = 10$ Mpa, $S_y = 50$ Mpa) in Figure 3.8a. The time increment of each frame is 0.02 seconds in the early frames during the slow, stable build-up period. The later frames during the major unstable rupturing are captured at 0.0005 second intervals.

Scenario 1: Simple Extension with Variable Strain Rate

The loading scenario for extension only (see Fig. 3.7, Table 3.1) is a typical configuration used in fracture mechanics to study fracture stability and velocity. The rate of applied displacement at each side ($dx/2$) for tests 1-4 is 0.5 mm/s, 0.25 mm/s, 0.15 mm/s, and 0.075 mm/s, respectively. For tests 1-3 damage propagation initiates at $dx = 0.267$ mm. In test 4 damage initiates at $dx = 0.138$. Each of the damage patterns consist of a long main fracture path (600-1100 mm) within a subparallel damage corridor ($0.01 < d < 0.05$) about 100 mm wide. Two broad lobes ($0.001 < d < 0.05$) extend from the damage corridor, widening to about 250 mm near the fracture tip.

(i) The two faster extension rates produce a more continuous propagation pattern where the build-up and release periods occur in regular spacing along the fracture path and at regular time intervals. (1) 0.5 mm/s (Fig. 3.7a [t=0.3700]): The main fracture path grows continuously by consecutive arrests and ruptures. A series of failed branches grow perpendicular to the main path beginning at fracture length ~ 50 mm, spaced regularly every 20 mm. The damage zone for each failed branch extends about 45 mm long, and transitions with length along the main path from distinct to overlapping. The overall damage pattern is symmetric until damage surrounding the initial crack-tip becomes pervasive and then the pattern becomes slightly wavy. (2) 0.25 mm/s: A small damage cloud initially develops at the crack tip and then ruptures at $dx = 0.267$ mm creating a broad damage zone ($0.3 > d > 0.9$) about 70 mm long and 80 mm wide. Following this initial event, the fracture grows similarly to the 0.5 mm/s test: straight and continuously, with close, regularly spaced failed branches.

(ii) The two slower rates produce irregular, punctuated growth and the damage distribution is wavy (e.g., Fig. 3.7d). (3) 0.15 mm/s: A small damage cloud forms at the crack-tip and then initial propagation occurs as series of short ruptures: ~20 mm in 0.001s followed by a series of longer ruptures ranging from 45 to 183 mm long, the duration of each is 0.001s. The main fracture path is straight. Asymmetric and irregularly spaced failed branches expand during prolonged arrest periods and create local zones of higher damage intensity. The overall damage corridor is irregular and slightly wavy. (4) 0.075 mm/s (Fig. 3.7d t=1.853]: A small damage cloud forms at the crack-tip at $dx = 0.138$ mm, followed by a 20 mm long segment that develops two 46 mm wide, failed branches in a 0.017s build-up period. A 0.001s rupture produces another set of branches and lengthens the fracture path 114 mm. Immediately following, a 0.001s rupture creates a 412 mm long segment as well as complex damage pattern surrounding the initial crack-tip. A few short ruptures lengthen the main path 68 mm, intensifying the damage zone around the initial crack-tip. The overall damage pattern is asymmetric and wavy.

Scenario 2: Internal Pressurization with Constant Strain Rate

The loading scenario is for initial tectonic loading followed by internal pressurization of the preexisting vertical crack (Table 3.1). A total of 22 tests were conducted, 11 each for the uniform and nonlinear pressure distribution – the differences between those two cases will be discussed later on. We first focus on the features associated with changing S_x , and using the uniform pressure distribution for reference. Note that for all tests $S_y = 50$ MPa. The internal pressure increases linearly

with time from 0 MPa until total failure or up to $P_f = 2S_x$. The results of four tests are highlighted here: $S_x = 17.5, 25, 35,$ and 45 MPa.

(i) Tests with relatively high differential stress (large ratio S_y/S_x) produce long, upward propagating fracture paths. Under a state of high differential stress, the development of asymmetric build-up sites leads to branching and long segments (e.g., Fig. 3.8). Under a state of moderate differential stress (e.g., inset in Fig. 3.9b), build-up sites are more symmetric and increasingly overlap with crack extension. Active branches reconnect with the main fracture path and the damage pattern is teardrop or mushroom shaped. (1) $S_x = 17.5 \text{ MPa}$: A continuous 70mm long segment propagates from the initial crack-tip up to $P_f = 28.6$ MPa. Consecutive arrests and ruptures form a series of overlapping failed branches and a 125mm wide by 200 mm long damage corridor extending from the original crack-tip. At $P_f = 38.6$ MPa a 20 mm left-stepping jog forms and links with the damage front to produce a vertical 70mm segment and an asymmetric x-shaped damage pattern. At $P_f = 39.5$ MPa a right stepping jog forms from the previous bend, grows parallel the left segment, and then both segments link along the main fracture path. With continued pressure, damage clouds accumulate at the leading fracture front as well as at the outer bends of both segments. At $P_f = 42.95$ MPa, two broad, butterfly-shaped ruptures quickly grow diagonally from the damage corridor and within 0.01s the entire layer fails. (2) $S_x = 25 \text{ MPa}$: At the initial fracture tip, a leftward asymmetric damage cloud develops continuously beginning at $P_f = 35.75$ MPa, and then at $P_f = 36.15$ MPa begins to fill in on the right side, resulting in a 65 mm wide by 46mm long T-shaped main fracture path. A build-up period from $37.05 < P_f < 38.45$ ensues before rupturing vertically from the center intersection

point. The main fracture path grows 30 mm and its damage cloud forms a bridge first with the left branch, followed by a build-up period from $40.3 < P_f < 41.8$ MPa, and then a bridge forms with the right branch. Two branches fill in where the damage bridges connect to the main segment, creating a slightly asymmetric 118 mm wide by 92mm long net-like damage corridor. Subsequent failed branches with a spacing that decreases with continued propagation from 20 mm to less than 10 mm apart form due to continued build-up and release periods. The result is a roughly symmetric, elongated teardrop shaped damage corridor that encloses the straight, main fracture path. At $P_f = 61.8$ MPa, at a main fracture path length of 230mm, branches at the damage front split the main path into vertical 69 mm long left stepping and 46mm long right stepping segments.

(ii) Tests with relatively low differential stress (small ratio of S_x/S_y) vary significantly. Regions under a state of moderate differential stress display continuous, uniform propagation by repeating arrest and rupture patterns and symmetric damage corridors (e.g., inset in Fig. 3.9a). A low differential stress state produces short, irregular fractures that form during irregular, asymmetric development of lateral branches. Continued growth occurs by pervasive infill damage, bridging, and multiple contemporaneous ruptures. There is no distinct main fracture path. (3) $S_x = 35$ MPa: A left branch begins to form at the initial fracture tip at $P_f = 51.75$ MPa followed by right branch at the tip at $P_f = 52.1$ MPa. A build-up period fills in the associated damage clouds asymmetrically until the damage corridor ($d > 0.001$) is comprised of two crack-perpendicular damage lobes. After build-up to a width of 109mm, the branches fail and at $P_f = 56.3$ MPa the main fracture path propagates upward 23 mm.

As the vertical damage front intensifies, a damage bridge links the main path with the left branch. A forward rupture at $P_f = 61.4$ MPa extends the main fracture another 25mm and the new damage front begins to bridge with both the previous left and right failed branches, forming a net-like damage pattern within the fracture corridor. The fracture path continues to extend according to a forward rupture, left bridge, right bridge, build-up, and forward rupture sequence. The initial spacing of the failed branches is 46 mm and then with continued propagation decreases to less than 20mm. The final pattern is a straight 183 mm main fracture path within a symmetric, 123 mm wide upside-down teardrop shaped damage corridor ($d > 0.001$) containing several distinct lateral failed branches. At the end of the simulation, $P_f = 80$ MPa, the damage at the tip of the fracture path begins to accumulate slightly asymmetrically in the up-left direction. (4) $S_x = 45$ MPa: At $P_f = 56.3$ MPa damage begins to form to the immediate diagonal up-left of the initial fracture tip, and propagates continuously to the left for a length of 45 mm. A build-period follows, forming a 64 mm wide by 70 mm long cloud of damage ($d > 0.001$) to the left of the crack-tip, and bounded below by the elastic-plastic layer boundary. A 10 mm long leftward rupture occurs at $P_f = 60.2$ MPa followed by a build-up period. The left branch does not increase in size but the damage increases to $d = 0.1$, then at $P_f = 64.9$ MPa damage accumulation shifts to the immediate forward-right of the first branch point, at a main fracture path length of 47 mm. At $P_f = 66.8$ MPa the damage accumulation shifts to the lower right of the right-hand branch site, and then at $P_f = 67.25$ MPa the lower-right branch builds a damage cloud to the right while contemporaneously, the first far left branch propagates a damage cloud upward, forming 69 mm long vertical segment. Continued

damage intensifies the segments and links the various segments forming an irregularly shaped, 138 mm wide by 92 mm long cloud of damage ($d > 0.001$). At $P_f = 73.1$ MPa a broad, irregular rupture composed of several branches and an intense broad damage cloud ($d > 0.9$) propagates to the left 230 mm wide by 180 mm tall and to the right 430 mm wide by 360 mm tall. Continued pressurization up to $P_f = 90$ MPa is entirely accommodated within the damage region, which intensifies but does not continue to expand.

FRACTURE MORPHOLOGY: BRANCHING AND SEGMENTATION

We found that branching and segmentation occur during complex, transient propagation beginning from both simple and complex load configurations. By reducing the differential stress during the pressurization simulations, the features become increasingly dominant. We now take a closer look at branching and segmentation by concentrating on two pressurization cases that resulted in different fracture patterns: a state of high differential stress produced simple fracturing (Fig. 3.9a) and moderate differential stress produced complex fracturing (Fig. 3.9b). Simple, in-plane fracture growth developed self-similarly over time. That is, damage evolution at early stages of growth is the same as during later stages. As shown in Figure 3.9a, each region of rock within the main fracture path, quantified now by the values at the integration points of individual elements, evolves from intact to completely damaged (x-axis, $0 > d > 1$) nearly identically. In contrast, complex fracture growth (Fig. 3.9b) developed uniquely over time or according to position along the main fracture path. Note in Figure 3.9b that the elements in the straight portion of the fracture path develop as in the simple case, but approaching the branch sites and in the later

(a) Simple Fracture

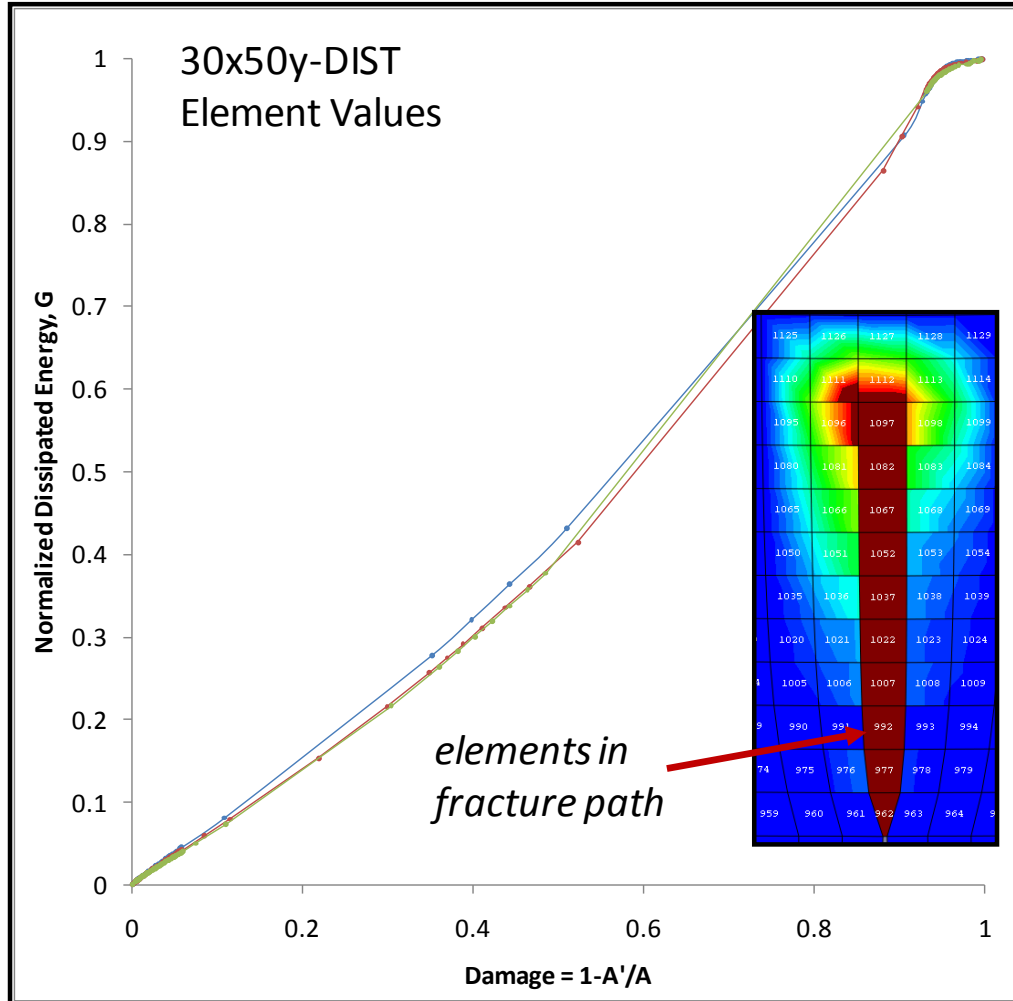


Figure 3.9. Evolution of the damage parameter (x-axis) versus normalized dissipated damage energy (y-axis). Each line represents an element in the main fracture path. The steeper the slope the more unstable the propagation. The small dots reflect equal 0.001s time intervals. Closely spaced dots indicate slow propagation, widely spaced dots are periods of fast propagation. (a) A simple fracture pattern – the fracture develops uniformly at all stages of growth. (b) See next page. (c) See next page.

(b) Complex Fracture

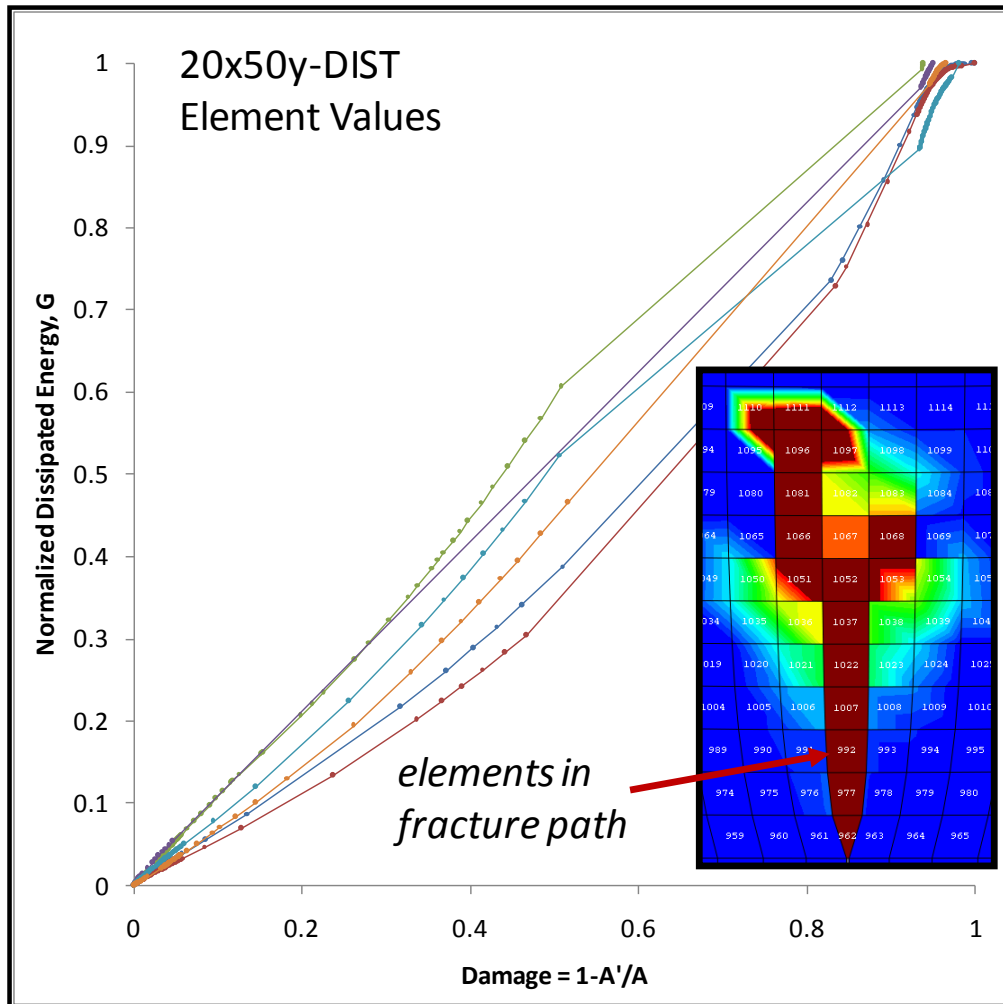


Figure 3.9 - continued. Evolution of the damage parameter (x-axis) versus normalized dissipated damage energy (y-axis). Each line represents an element in the main fracture path. The steeper the slope the more unstable the propagation. The small dots reflect equal 0.001s time intervals. Closely spaced dots indicate slow propagation, widely spaced dots are periods of fast propagation. (a) See previous page. (b) A complex fracture pattern – earlier stages are more stable (lower curves) than later stages (top curves). Late stage instability is associated with segmentation and branching. (c) See next page.

(c) Multiple Growth and Arrest Periods

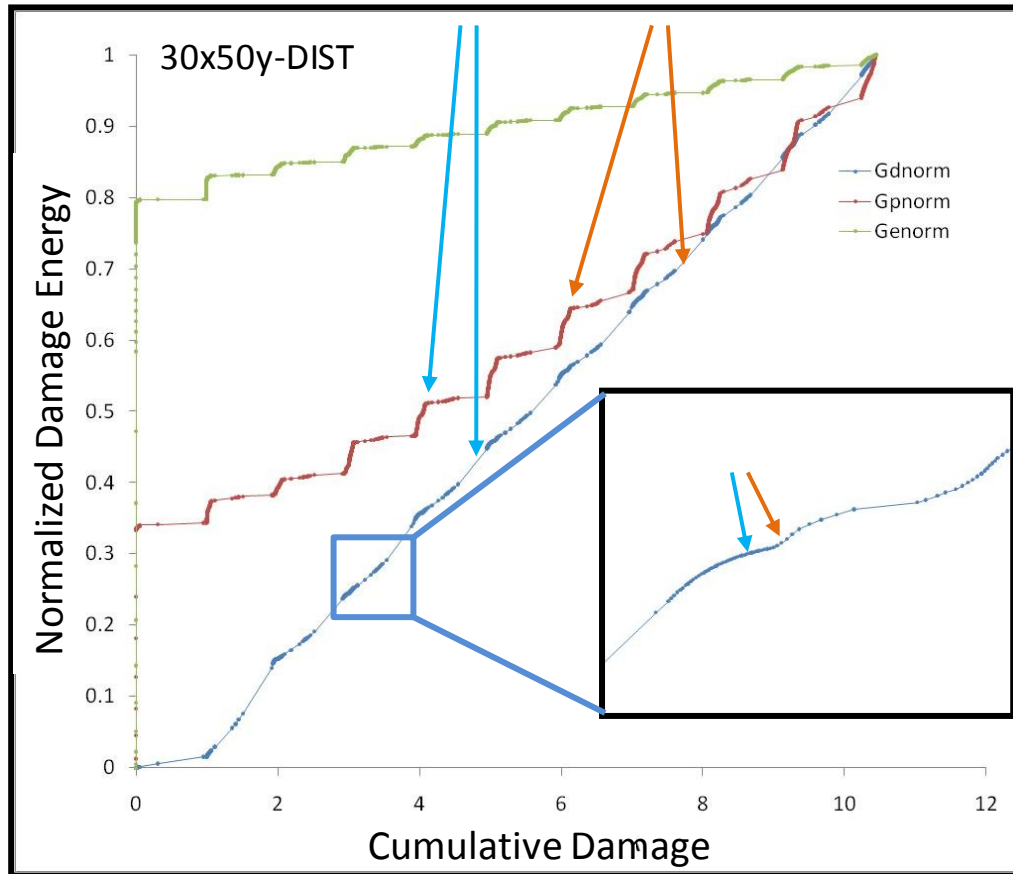


Figure 3.9 - continued. Evolution of the damage parameter (x-axis) versus normalized dissipated damage energy (y-axis). The lines are for elastic (green), plastic (red), and damage (blue) dissipated energy. Inset is a close up of rupture-arrest period. The steeper the slope the more unstable the propagation. The small dots reflect equal 0.001s time intervals. Closely spaced dots indicate slow propagation, widely spaced dots are periods of fast propagation. (a) See previous page. (b) See previous page. (c) Cumulative (global) pattern shows stair-stepping pattern indicating build-up and release periods, reflective of stable or unstable fracture growth and related to local dynamical behavior.

segments, the evolution deviates more and more from uniform. Steepening of energy-damage slope in the branches reveals that damage in the out-of-plane segments progresses more unstably than in the in-plane segments.

The sequential evolution of elemental damage also varies between the two cases and is displayed in Figure 3.10a and 3.10b. For the simple case (Fig. 3.10a), regions of rock in the main damage path initiate and evolve in sequence, and the timing between rupture events is uniform – the fracture grows continuously by uniform rupture and arrest events. For the complex case (Fig. 3.10b), damage develops out of sequence and multiple segments initiate and grow contemporaneously. This out of sequence growth has an adverse affect on local stability, as we discuss later.

CONDITIONS CONTROLLING PROPAGATION

We now return to the effect of the loading conditions on the overall accumulation of damage. We now use the convention of normalized fluid pressure and normalized tectonic stress. We have chosen the q - p' convention, where q is the deviatoric stress and p' is the pressure stress. Thus:

$$\text{Net } P/q = (P - S_3) / (S_1 - S_3) \quad (\text{normalized fluid pressure}) \quad [16a]$$

$$q/p' = (S_1 - S_3) / ([S_1 + 2S_3] / 3) \quad (\text{normalized tectonic stress}) \quad [16b]$$

where $P = P_f$ is the internal pressure for the crack, $S_1 = S_y$ is the maximum principal stress, $S_3 = S_x$ is the minimum principal stress, and $(P - S_3)$ is the net pressure. The amount of damage is quantified by the total damage accumulated in the entire layer. In the previous section we used cumulative damage to explain the process of damage evolution and here we apply the total damage to serve as a proxy for fracture

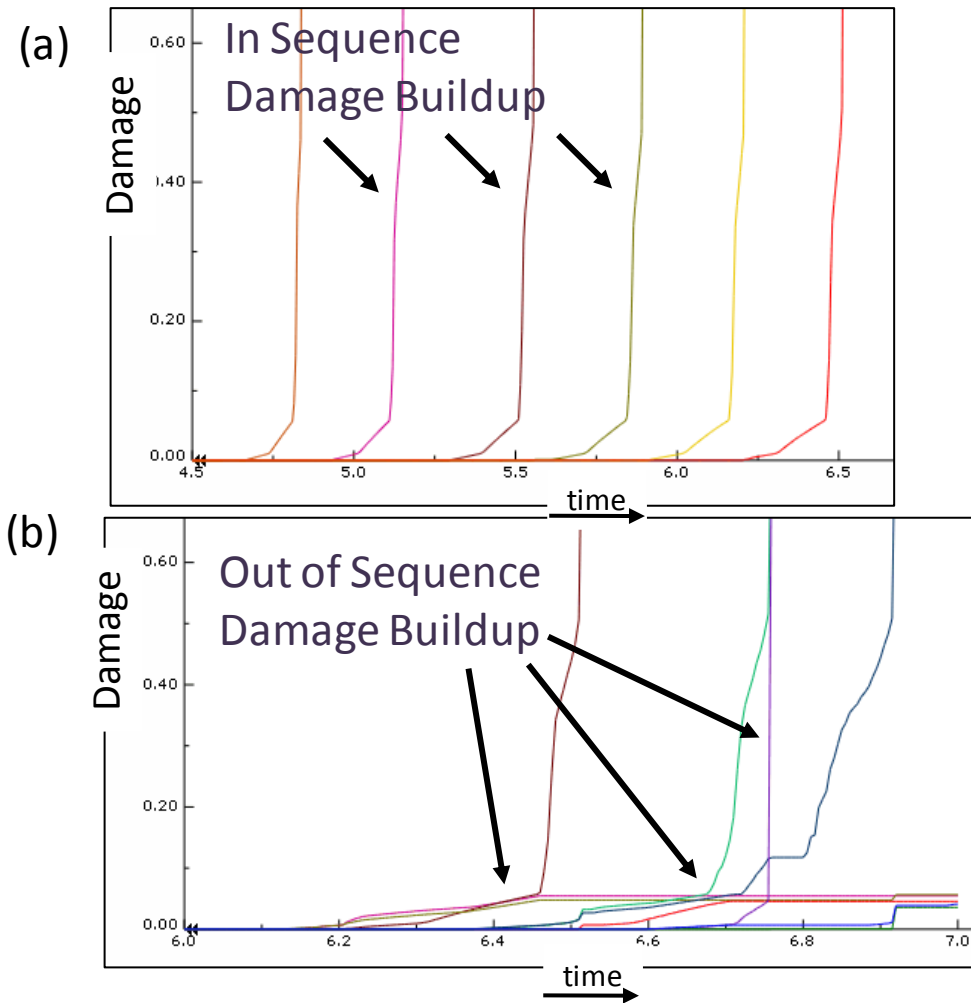


Figure 3.10. Sequence of damage build-up in the main fracture path, corresponding the elements in figures 3.9a and 3.9b. (a) For the simple case, the main fracture path grows uniformly and in sequence. (b) For the complex case, multiple regions of rock are damaged contemporaneously, leading to non-uniform segmentation and complex damage patterns.

connectivity (note, not fluid conductivity). A practical point to the assumption is that the total amount of damage approximates the *minimum* total damaged area. In the FE scheme, damage is distributed by elements, and the elements are capped at a value of $d = 1$. For example, $d_{\text{tot}} = 10$ reflects the equivalent of 10 completely damaged elements, here equal to about 0.005 m^2 . The actual interconnected damaged area tends to be about twice the minimum. Small elemental values (i.e., $d < 0.1$) that model the onset of microcracking but do not imply microscale linkage will not significantly contribute to the total damage.

Tectonic Load and Fluid Pressure

Figure 3.11 is a compilation of 11 tests run with a continuous pressure distribution in the initial fracture. For reference, the black dashed box marks the range of tectonic stresses for a “typical field” and injection pressures for “normal operating conditions” based on data from about a dozen wells in the Barnett Shale. The curved boundary extending from the top left to bottom right is the damage cut-off point $d_{\text{tot}} = 12$.

For all tectonic stress ratios, the total damage accumulates nonlinearly with increasing injection pressure and in steps that reflect the build-up and rupture periods (Fig. 3.9c). The steps decrease in amplitude (color contours, Fig. 3.11) and increase in duration with decreasing tectonic stress ratio. The steps increase in frequency for intermediate tectonic stress ratios (e.g., the smoother color transitions at $0.4 < q/p' < 0.8$).

For tests with tectonic stress ratios above ~ 0.8 , the area to the right of the cut-off are for injection pressures that resulted in rapid failure of the layer. Simulations with tectonic stress ratios between about 0.2 and 0.8 did not run to total failure. At the

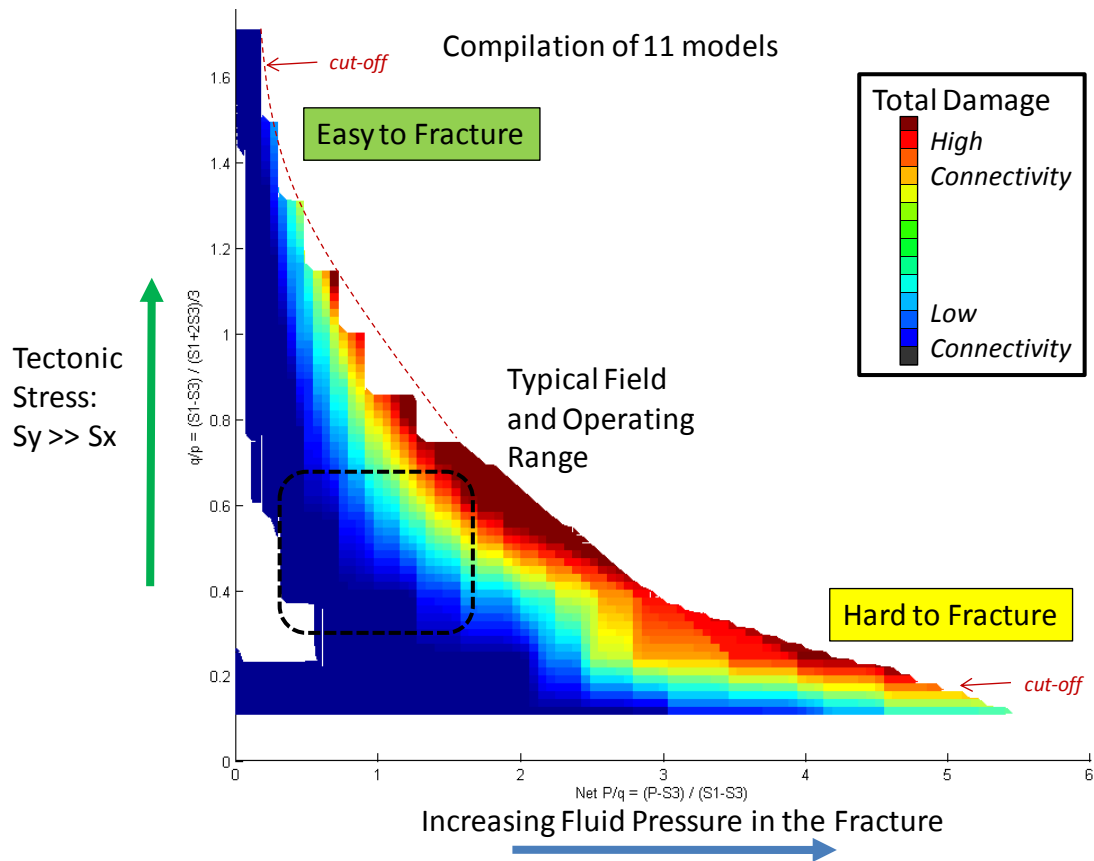


Figure 3.11. Contour map showing the effect the loading conditions on cumulative damage evolution. The operator typically controls the fluid pressure (x-axis) for a given tectonic stress state (y-axis). Warm colors indicate high damage and also suggests greater fracture connectivity (see text). The curved right-hand boundary (cut-off at $d_{tot} = 12$) reflects the pressure needed to induce total failure of the layer. Layers under high tectonic stress are easy to fracture but create little damage. In areas of low tectonic stress a lot of damage develops but high fluid pressure is required to initiate fracturing.

lowest stress ratios ($q/p' < \sim 0.2$) pressures in the cut-off area led to failure of the initial fracture wall and shear failure at the layer boundary. The models with high tectonic stress ratio require little injection pressure to induce complete failure of the layer (Net $P/q > 1$), and can be thought of as “easy to fracture”. However, very little damage accumulates prior to total failure of the layer, suggesting limited fracture connectivity apart from the main fracture path. The models with low tectonic stress ratio require a lot of injection pressure to induce complete failure of the layer (Net $P/q > 3$) and are “hard to fracture”. In this case, prior to layer failure more damage accumulates, suggesting high fracture connectivity.

Pressure Distribution

Both the onset of damage accumulation and the point of total layer failure for the non-linear pressure distribution occur at a higher injection pressure than for the uniform distribution (Fig. 3.12a, 3.12b). The effect is more pronounced as the tectonic stress ratio decreases. Consequently, it is more difficult to induce and propagate fractures in the non-uniform pressure case. The damage patterns for the non-linear pressure tests are roughly similar to the uniform ones; however, there are slight morphological differences that expose a subtle shift in the damage mechanism. In the simulations, a uniform internal pressure slightly decreases the spacing and increases the intensity of the build-up periods, which we saw are responsible for the development out-of-plane segments and failed and active branches. The phenomena is more clearly seen by plotting the ratio of shear damage to tension damage for both load cases as shown in Figures 3.12a and 3.12b. Especially for moderate differential stress states ($0.4 > q/p' > 0.8$) (also see Fig. 3.16, 3.17 – stress path), the uniform pressure distribution produces

a higher proportion of shear damage, whereas the damage in the non-linear distribution is more tensile. The explanation is that the uniform pressure distribution creates an elliptical fracture profile with a more blunt fracture tip, whereas the shape is cusped and the tip sharp for the non-linear case (Fig. 3.6). Blunting of the crack tip is a distinct departure from the theoretical Irwin-type crack that assumes the tips are atomically sharp. Two sources of rounding have been posed (e.g., Lawn 1993): (1) stress-enhanced dissolution and (2) shear induced plasticity. Clearly, the former mechanism does not apply here; however, the latter is consistent with the results of the FE simulations. It is important to note that although the mixed-mode component arising from the difference in pressure distribution is small, it is not negligible, as various rock mechanics experiments have demonstrated. While capturing accurate crack-tip geometry would require much finer FE meshing (we do not purport crack-tip scale resolution here), the sensitivity of the results to the shear contribution is at a similar level as micromechanical experiments:

(1) That pressure distribution affects the fracture development is consistent with Ishida et al. (2004), whose experiments we referenced earlier: hydrofractures generated from injecting viscous oils created planar cracks with few branches, whereas water generated wavelike fractures with many branches. As in equation [9], the pressure drop associated with water or light-sand injection is much less than if the fluid contains coarse sand proppant or gel, or as in the extreme case, is magma.

(2) The idealized uniform pressure condition introduces a shear component at the crack-tip, which, when accommodated inelastically, promulgates deviation from mode I behavior. The experiments of Wu (2006) demonstrated that even just a few percent

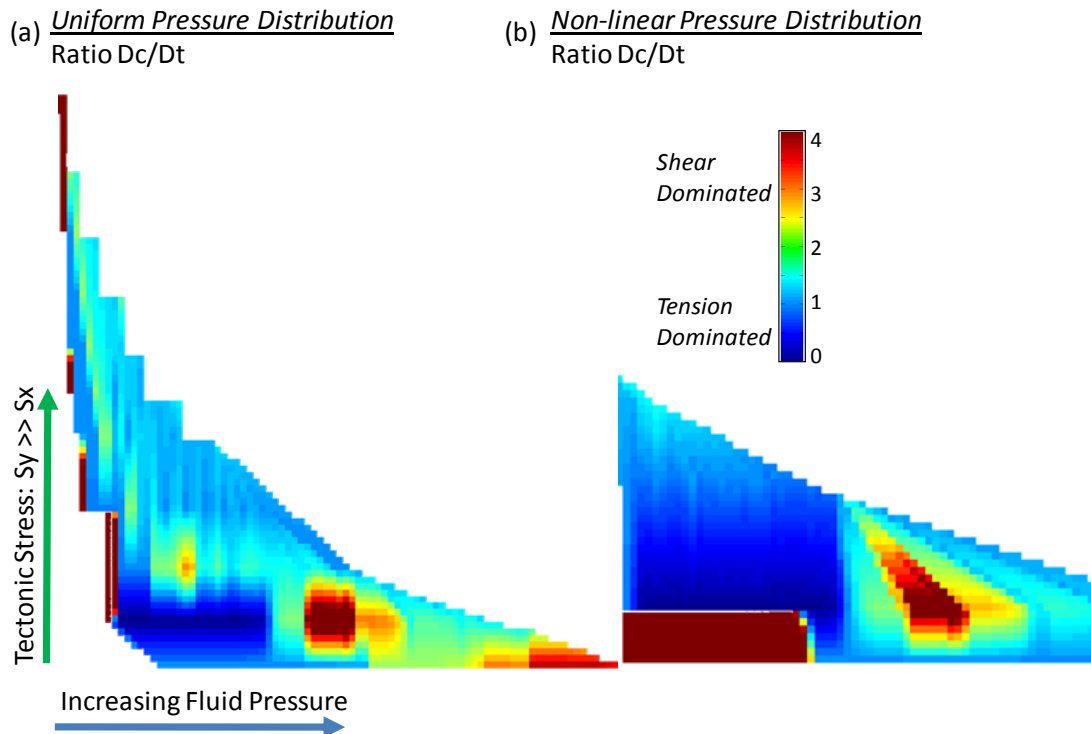


Figure 3.12. Contour plots of the ratio of damage in compression to damage in tension for all 22 hydrofracture simulations. Warm colors indicate a shear dominated failure and cool colors tensile failure. For the uniform pressure distribution (a) failure has both a shear and tensile component. For the non-linearly distributed pressure tests (b) the tensile component dominates. Also in (b) the pressure required to induce damage and total layer failure is higher than in (a).

shear component lead to complex fracturing. Fluid penetration into and reactivation of even weakly developed failed branches would certainly have an even greater impact.

(3) One last consideration is that unlike in our homogenous matrix, in a granular material, grain size has a non-linear affect on fracturing. For example, a model proposed by Horii and Nemat-Nasser (1986) predicts that the stress ratio σ_3/σ_1 at the brittle-plastic transition scales with the square root of the grain size. Experimental results by Fredrich et al. (1990) concluded that the prediction holds if the square of the ratio of the mode I fracture toughness to the plastic yield stress in shear scales with the grain size. In other words, it is possible that between layers or even within the same layer of a given rock type, a finely grained zone will fail in shear more readily and a coarser zone would be weaker in tension. In such cases, the effect of the internal pressure distribution would be enhanced.

SYNTHESIS AND INTERPRETATION

SCENARIO 1: IMPLICATIONS FOR FRACTURE VELOCITY AND STABILITY

Whether simple or complex, the dynamical interchange between build-up periods and ruptures relates to how the rock locally progresses through the typical stages of deformation (i.e., elasticity, strain hardening, yielding, and strain softening, see Chapter 2). In addition to loading conditions, the constitutive behavior dictates how energy builds up and releases since the area under the stress-strain curve reflects the stored energy and the area under the load-displacement curve, defining damage evolution for the material, reflects the dissipated fracture energy. When the work applied to the system is accommodated elastically, no damage accumulates and no

energy is dissipated by microfracturing. The inverse is true when work is accommodated inelastically. In typical rocks (including the modeled Berea sandstone rheology), damage accumulates slowly relative to the plastic strain during initial yielding, speeds up approaching the ultimate yield, and accumulates rapidly during brittle failure. The actual amount of energy released by microcracking depends on a few factors. (1) If energy dissipates by plasticity and damage as quickly as it builds, the ruptures will be energetically small. If energy builds more rapidly than it dissipates, the ruptures will be energetically large. (2) An undamaged material can store more energy than one with degraded stiffness due to damage. Unless a well-developed damage network is optimally oriented, the tendency for high-energy release may increase as multiple regions cumulatively “lock-up” prior to release. (3) Velocity and inertial effects, in the system as a whole or locally, contribute to the release of stored kinetic energy during yielding. Figure 3.9a displays an example of this damage-energy interaction for a moderate differential stress load case that produces continuous, simple propagation. The cumulative global pattern (Fig. 3.9c) shows a series of stair stepping events reflecting arrest-rupture periods where intervals when energy dissipates relatively more slowly than damage accumulates reflect build-up periods, and intervals when energy dissipates more quickly than damage reflect rupture events. Energy jumps are associated with high velocity ruptures that manifest as a short burst of damage – note the steep slopes develop over a few time-points (each small dot is a 0.001s increment) whereas the shallowly sloped growth periods comprise many time-points. The behavior is consistent for the macroscopic rupture-arrest pattern, but also holds locally as shown by the zoomed-in inset.

Figure 3.13a and 3.13b (blue lines) show the half-width displacement for the initial crack versus time in two extension tests ($P_f = 0$), where the slope reflects the rate of crack dilation. A steep slope coincides with a period of rapid extension – i.e., the work applied to the system is accommodated by crack development. A shallow slope reflects slow extension, and a flat or negative slope reflects a build-up period – the work applied is accommodated by damage accumulation. The two fastest extension rates (e.g., test 1, Fig. 3.13a) display constant-increase growth periods comprised of several small ruptures with few significant build-up periods. Note in Figures 3.13a and 3.13b that each rupture event is associated with a 10-50 μm jump in crack half-width followed by an immediate rebound. In the two slower extension tests (e.g., test 4, Fig. 3.13b), propagation is punctuated and nearly all of the fracture path growth occurs from a short sequence of ruptures.

The results may seem counter-intuitive; however, they indicate a crucial dynamical effect that is also present but obscured in the hydraulic fracturing tests ($P_f > 0$). The difference between the continuous (more stable) and punctuated (less stable) growth patterns may be explained by the kinetic response to yielding. In the simulations, major rupture events are associated with a jump in kinetic energy of about 5-50 J (red lines, Fig. 3.13a and 3.13b). The small early ruptures sourcing from the initial crack-tip are about 5 J for the fast load rates (Fig. 3.13a) and 0.5 J for the slow rates (Fig. 3.13b). Because the initial rupture events for the faster load rates fail more energetically, the resulting damage cloud extends further than the slower, more stable tests. Thus, the potential branches initiate, but only weakly develop and then are bypassed as consecutive ruptures extend with the propagating damage front. In other

words, the forward propagation of pre-rupture damage preconditions the region ahead of the main fracture path, reducing the tendency for subsequent large, unstable ruptures. Conversely, the slower load rates effectively damp the early kinetic oscillations due to yielding. Thus, a product of the more stable early ruptures is that the damage accumulated during the first build-up periods is more localized, leading to the build-up of more strongly developed sets of failed branches. This early complex pattern accommodates strain within a few out-of-plane damage branches and their associated damage clouds, and thus, no clear damage preconditioning occurs ahead of the main fracture path. Consequently, despite the more stable load rate, the formation of out-of-plane damage during the slowly advancing build-up periods increases the tendency for overall instability. Subsequent ruptures are more unstable, punctuated, and the resulting damage corridor is more complex and irregular.

SCENARIO 2: IMPLICATIONS FOR FRACTURE VELOCITY AND STABILITY

Referring again to the plot in Figure 3.9b, comparison of the local, elemental damage evolution provides clues for the conditions that reduce stability during complex fracturing (Fig. 3.14). The lower curves are the values for elements in the straight portion of the fracture path ('s'). In this region, damage initiates slowly (Fig. 3.14a, 'S') and then builds up ('B') more stably (shallower slope) until yielding occurs at around $d = 0.5$ ('R'). The unstable rupture occurs until arrest at $d = 0.8$, at which point evolution slows and stabilizes – the damage transfers to a new region of rock which stabilizes the growth. The upper curves are for the complex portion of the fracture path ('C' - also Fig. 3.14b). The build-up period occurs at the same point as before; however, more out-of-plane the segment is, the steeper the slope becomes.

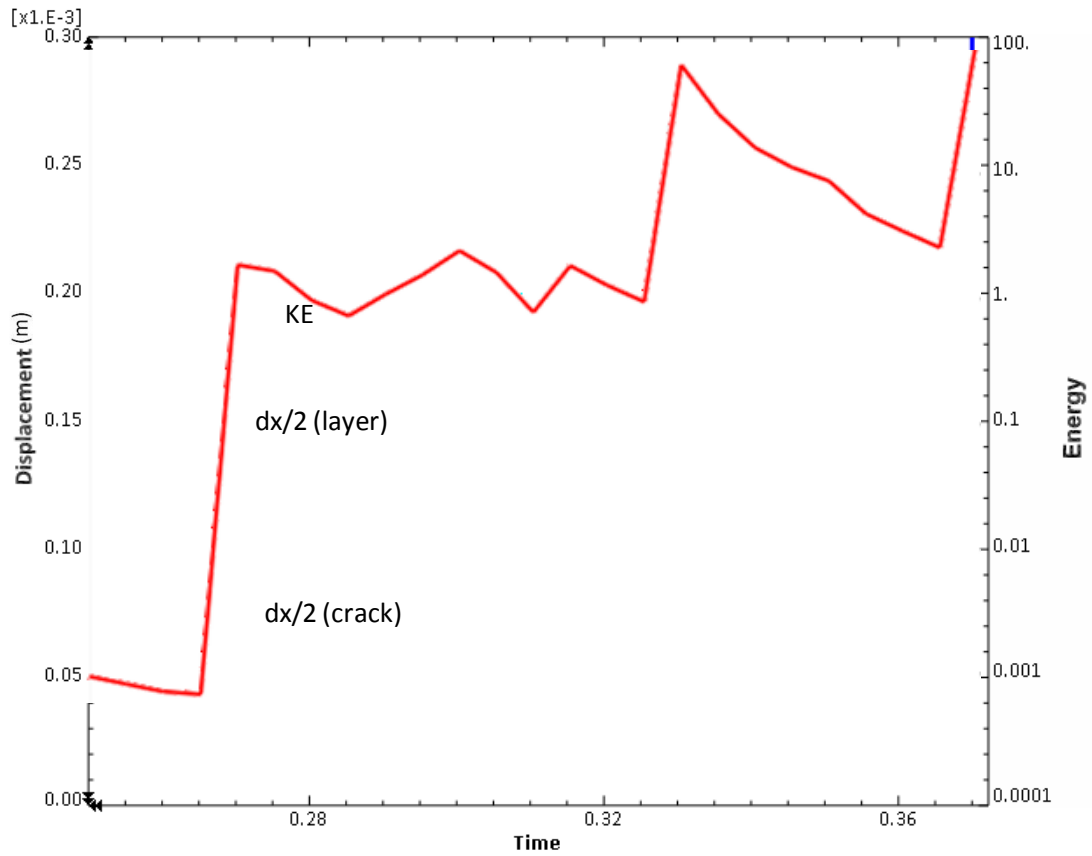


Figure 3.13a. Crack half-width displacement (blue) and kinetic energy (red) for extension test 1. The dashed black line indicates the half-displacement for the layer. Small jumps in displacement indicate rupture events. Following the initial rupture event, there is a spike in kinetic energy and the crack grows continuously.

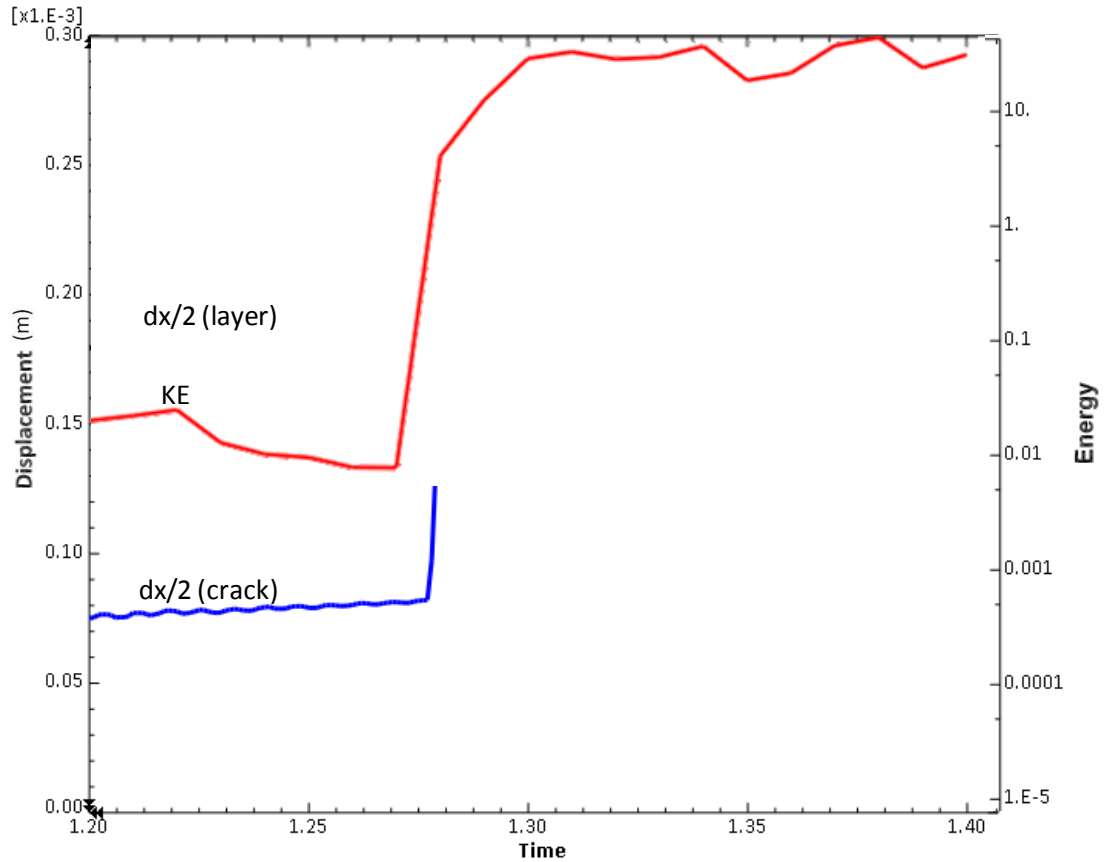


Figure 3.13b. Crack half-width displacement (blue) and kinetic energy (red) for extension test 3. The dashed black line indicates the half-displacement for the layer. Small jumps in displacement indicate rupture events. Kinetic energy associated with the initial rupture event is relatively damped compared to fig. 13a. There are a series of large, fast rupture events that comprise the bulk of the main fracture path growth.

The explanation is simply that the shear component to propagation increases when the crack deviates from mode I propagation, and since the shear strength of the rock material is higher than the tensile strength more energy can accumulate prior to failure. Following the rupture event, there is no return to stability – damage transfers to another region of rock, however, the new region does not stabilize the growth because it has already been weakened by previous build-up or rupture events. We can think of the zone of damage transference as analogous to the shielding zone ahead of the crack-tip from fracture mechanics theory. Unstable propagation occurs when the incremental damage energy (dG) per crack length (dC) exceeds the strength contribution from the shielding region (dR) ahead of the crack (Lawn, 1993):

$$dG/dC > dR/dC \quad (\text{unstable}) \quad [17a]$$

$$dG/dC < dR/dC \quad (\text{stable}) \quad [17b]$$

In other words, transference of propagation into a damage-weakened location is less stable than into an intact region. We saw from the descriptions of fracture morphology that the size of the damage cloud was proportional to the size of the kinetic energy contribution. In the same way, moving from the lower curves in figures 3.14a and 3.14b to the upper curves, the increase in energy dissipated due to damage during build-ups corresponds to broadening of the associated damage clouds. While transference between adjacent localized zones is still unstable, the ruptures paths are spatially constrained. A broad zone of transference is less constrained in two ways: (1) by distance – the amount of lengthening during a rupture event reflects the distribution of damage into which it propagates; and (2) by angle – the likelihood for out-of-plane growth increase since there are a wider range of ‘favorable’ locations in which to

propagate. Associated with this is less likelihood to self-correct the propagation path back in plane once it has branched or a segment has formed.

In comparison with the extension-only tests, the loss of stability here relates to the inability to precondition the fracture path effectively. In both load scenarios, the active damage transfers to new regions of rock ahead of the fracture path, which lowers the right-hand term of equations [17a] and [17b]. However, the effect of preconditioning in the stably propagating extension tests was that the stored energy was periodically released into the preceding zones of weakness and the fracture path continuously extended through a series of short unstable ruptures, thus the left hand term of equations [17a] and [17b] remained relatively small. Local preconditioning also occurred in branches and fracture segments during the internal pressurization tests; however, irregularity in the damage pattern contributed to inefficient links between zones of damage transference, resulting in larger build-up periods and more unstable ruptures.

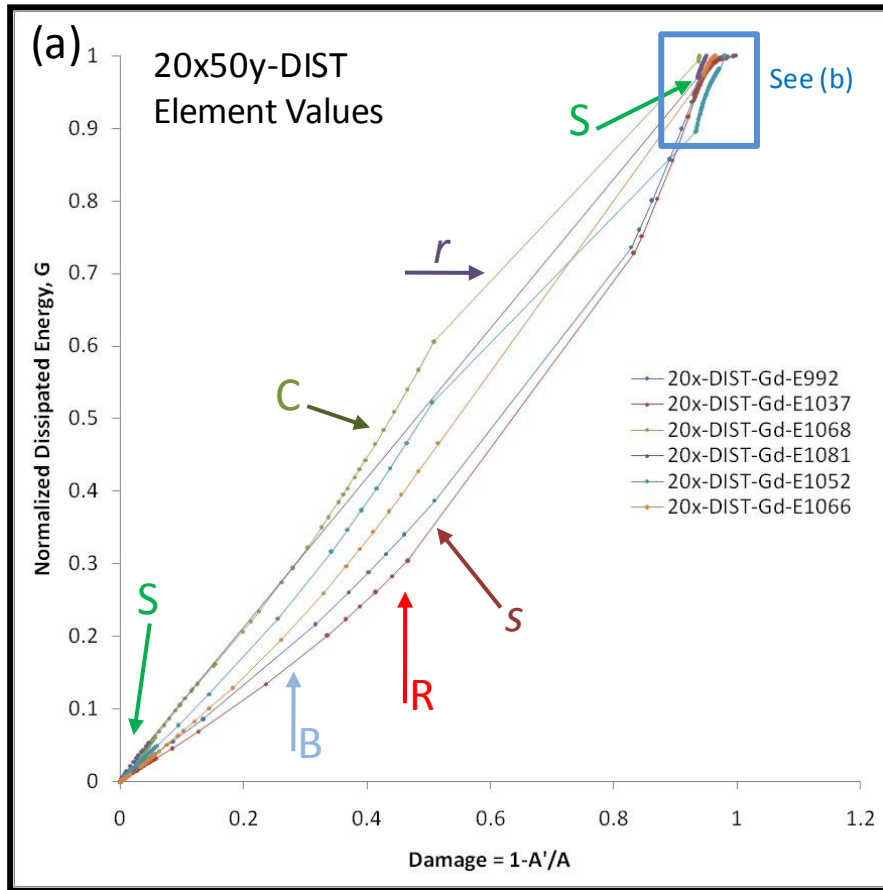


Figure 3.14. Changes in stability are displayed by plotting the variation in damage evolution along the fracture path. (a) element damage evolution. (b) See next page.

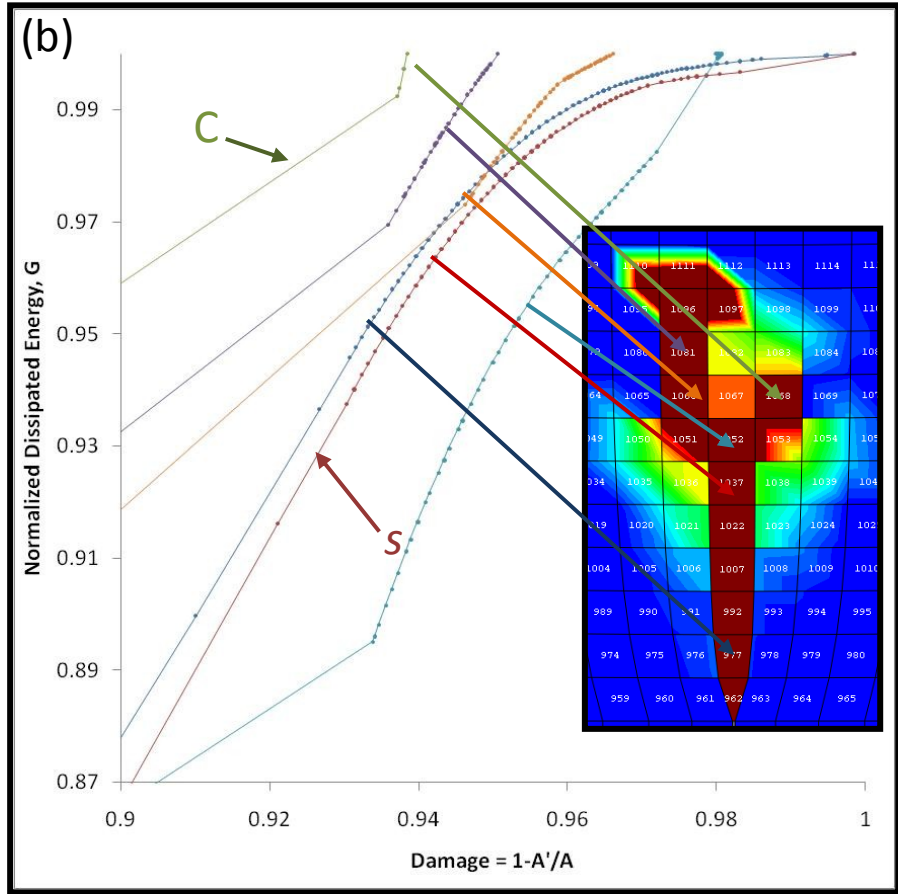


Figure 3.14 - continued. Changes in stability are displayed by plotting the variation in damage evolution along the fracture path. (a) See previous page. (b) zoomed in area of blue box associated with damage transference from one element to another. The curves are connected to the appropriate element by the long arrows. Several features are identified (see text): S – intervals of slow growth. B – stable build-up period. R – initiate of rupture. r – rapid growth period. s – simple, straight portion of the fracture path. C – complex portion of the fracture path.

CONTROLLING HYDROFRACTURE PROPAGATION: STRESS PATH ANALYSIS

We plotted the stress paths for the four load configurations described earlier ($S_x = 17.5, 25, 35, 45$ MPa) (Figures 3.15a and 3.15b). The locations for stress path recording, relative to the initial crack tip, are for an “in-plane” region, $x = 0$ and $y = 100$ mm (red arrow, Fig. 3.15a) and an “out-of-plane” region adjacent to the main fracture path at $x = -50$ mm and $y = 100$ mm (orange arrow, Fig. 3.15b). The path from tectonic loading (not shown) culminates in the initial stress state (far right); the path from internal pressurization advances to the left with time/pressure. Upon intersection with the element’s yield envelope (not plotted), the path either terminates, moves downward along the yield surface according to the plasticity rule, or fluctuates depending on the local stress. The stress path plots are referenced here in summarizing some of the overall effects of load conditions on hydraulic fracturing:

(1) Tectonic conditions determine the general propensity to fracture. The local stress state establishes how close the material at a given location is to the yield surface. The high stress ratios are already close to failure and require very little injection pressure. For the low stress ratios, significant pressurization is required to overcome the local stress field. It is also important to note that the local stress state is not necessarily the same as the regional one due to the effects of stress amplification (e.g., at the initial crack-tip). For instance, in the $S_x = 45$ MPa tests, for the in-plane location $p' = 73.9$ MPa and $q = 10.0$ MPa versus $p' = 72.5$ MPa and $q = 15.3$ MPa for the out-of-plane location.

(2) The internal pressure, which should be normalized to the state of local stress, facilitates stress evolution. The stress path at each location of rock conforms to a

family of curves that steepens for high stress ratios and inverts for very low stress ratios. For the out-of-plane location, the average pre-failure change in q is 20-30 MPa, for the in-plane location q varies 3-5 MPa. Low differential stress states are not optimal for tensile fracturing and the stress path takes an indirect route. It should be noted that in all cases a straight line from the initial state to the yield surface does not approximate the stress path.

(3) Regions within the in-plane zone (in the main fracture path) predominantly fail due to reduction of the hydrostatic pressure. On a Mohr-circle diagram, this is seen as a circle of nearly constant diameter moving to the left until intersecting the failure envelope, an effect common during elevated pore pressure. This suggests that failure is mostly tensile with minor shear contribution.

(4) Regions within the out-of-plane zone (away from the main fracture path), but still within its area of influence, fail via increased differential stress and pressure reduction. This is reflected on a Mohr-plot as a circle that intersects the failure envelope by both size increase and shift toward low normal stress. This path is consistent with normal faulting conditions, and explains the proclivity for microseismic shear events associated with hydrofracture propagation.

(5) The effect due to changing the internal pressure distribution decreases with tectonic stress ratio and increases adjacent to the main fracture path. For a nearly homogenous stress state and a uniform pressure distribution, the stress path for the in-plane region of rock shifts to become influenced more by the differential stress.

Moreover, for these conditions the stress paths for in-plane and out-of-plane

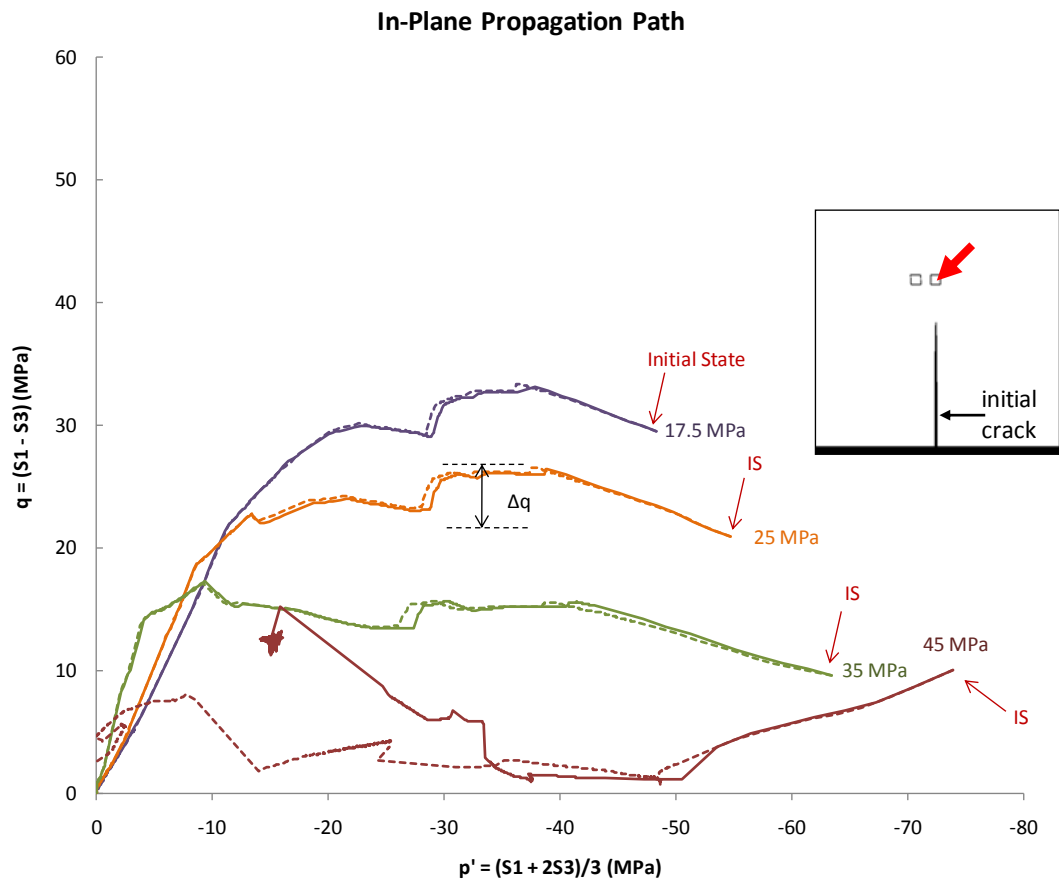


Figure 3.15a. Stress path for a region in-plane to the main fracture path (inset, red arrow), plotted for four tectonic stress states ($S_y = 50$ MPa, S_x as shown). Solid lines are for tests with a uniform pressure distribution, dashed for the nonlinear distribution. The initial state of stress for the region is at the far right of the curves. With internal pressurization and as damage advances, the local stress changes for the region and the stress path follows the curve to the left. Failure occurs when the path intersects the yield surface (not plotted).

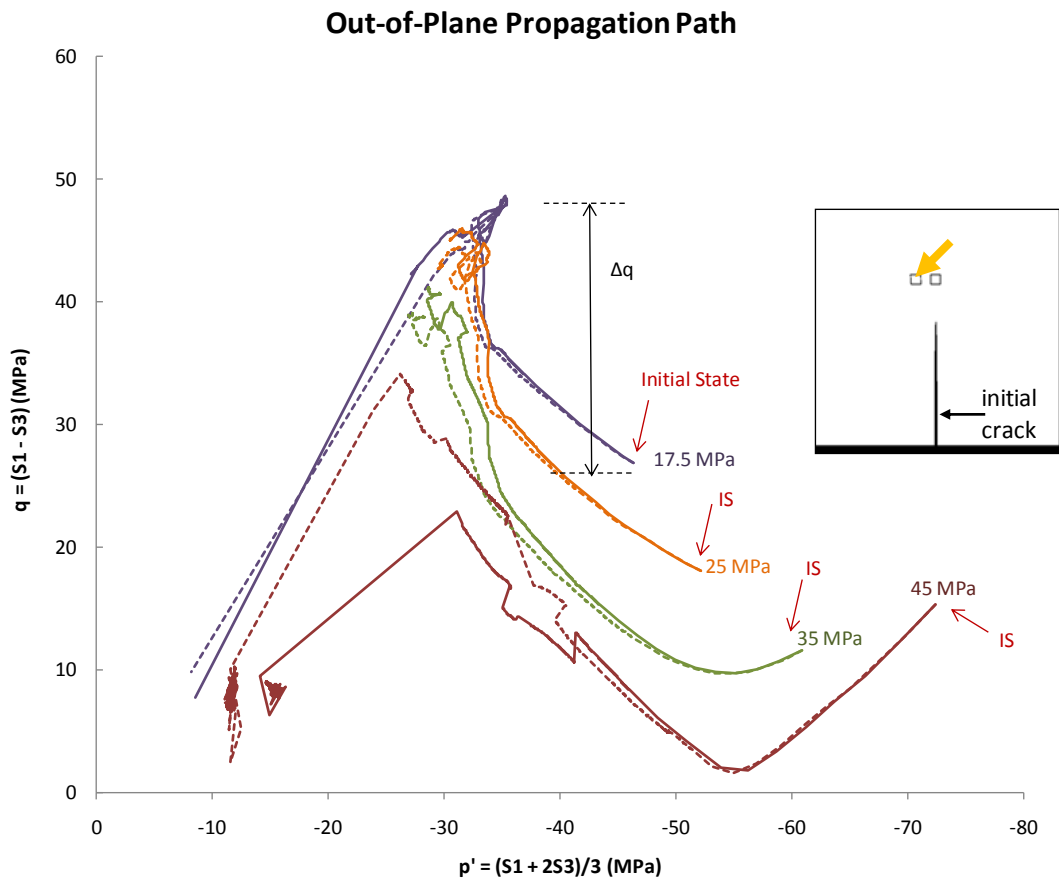


Figure 3.15b. Stress path for a region out-of-plane to the main fracture path (inset, orange arrow), plotted for four tectonic stress states ($S_y = 50$ MPa, S_x as shown). Solid lines are for tests with a uniform pressure distribution, dashed for the nonlinear distribution. The initial state of stress for the region is at the far right of the curves. With internal pressurization and as damage advances, the local stress changes for the region and the stress path follows the curve to the left. Failure occurs when the path intersects the yield surface (not plotted).

propagation are quite similar. This suggests that in very weakly tectonically stressed areas, mixed-mode fracturing is most likely unless very viscous fluids are used.

APPLICATIONS

Field Observations of Propagation Dynamics

Fractographic features on joints (Fig. 3.16) have been widely used to interpret the growth history and paleostress conditions during their formation. For example, smooth, lobed patterns displayed on joint surfaces have been associated with slow, subcritical propagation, whereas branching, segmentation (Fig. 3.17), and rough plumose patterns were linked to fast, transitional regime propagation (Sagy et al., 2001; Engelder, 2004). Variations in the waviness of the markings as well as well defined arrest lines and rupture boundaries are understood to reflect velocity changes and a discontinuous growth rate. Stair stepping and twisting hackles and fringes (refer to the classical diagram in Hodgson, 1961), are attributed to joint propagation under mixed-mode loading (Younes and Engelder, 1999; Belayneh, 2004). It is possible that the FE simulations represent a vertical 2D transect of these types of features, taken normal to the crack-surface. If so, the solutions serve as an example of quantitative analysis of the associated micro-mechanical processes at a resolution that is difficult to achieve experimentally.

Hydrofracturing

The results of our analysis can be used as a predicative tool for hydrofracturing operations as shown in detail in Chapter 4. If the local state of stress is known, we can see two immediate applications: it is possible to estimate the minimum fluid pressure

necessary to induce damage and fracture propagation and the relative degree of fracture connectivity. Conversely, if the hydrofracture pattern is known, such as from microseismic events maps, the local stress state and the qualities of the injection can be inferred for particular structural domains. We demonstrate these options by considering three general cases.

(1) In a state of high differential stress, new fractures form at $P_f = 20\text{-}40$ MPa (2,900-5,800 psi). The fractures are long and complex, forming numerous branches and linking segments, which increase the fracture connectivity. Because this state of stress is highly conducive to hydrofracture propagation, the tendency is for the network to conform to the tectonically stressed structural domains. The result is redirection away from the orientation of the far-field stress without significantly increasing the fluid pressure.

(2) For moderate differential stress states new fractures form at $P_f = 40\text{-}70$ MPa (5,800-10,100 psi). Fractures are straight, planar, and develop uniformly according to a repeating arrest and rupture pattern. In order to create complexity: (a) the fluid pressure must be significantly increased in order to intensify the rupture events, thus expanding the size of the damage front out-of-plane and triggering local instability, or (b) the fluid viscosity must be reduced to amplify the inelastic shear component at the crack tip.

(3) For a state of low differential stress new fractures form at $P_f = 70\text{-}90$ MPa (10,100-13,000 psi). Fractures are short and growth is unstable, resulting in a pervasive damage network comprised of numerous linking segments. The high pressures that are required may be difficult to achieve in practice, and may be

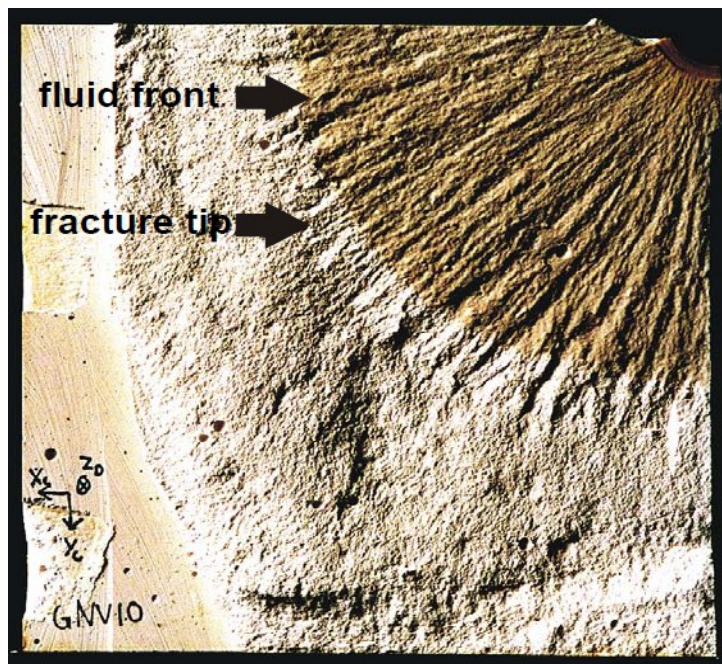
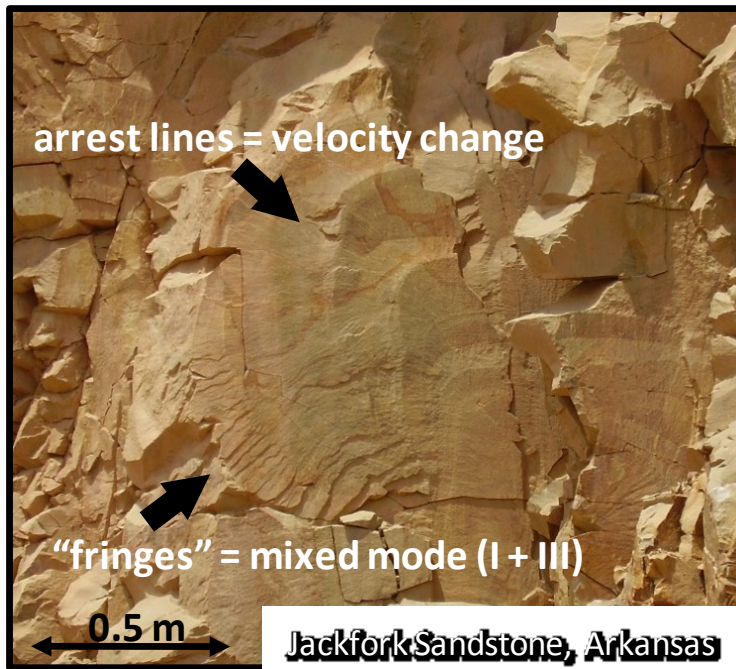


Figure 3.16. Photographs of morphological features preserved on joint surfaces. Top: plumose markings, arrest lines and fringes from a Jackfork sandstone quarry in Arkansas. Bottom: grooved fracture surface and fluid lag region from laboratory hydrofracturing experiments (Papanastasiou, 2002)



Jackfork Sandstone, Ouachitas, Arkansas



Carmel Fm. Limestone, Cedar Mountain, Utah

Figure 3.17. Photographs of branching (left) and segmented fractures (right) in outcrop.

preempted by some combination of unstable failure of the fracture walls and shear failure at the crack-tip. If this stress-state is encountered near the borehole, it is possible that the network would spread to the nearest favorable stress field – the well path - rather than propagating distally into the reservoir. Some degree of control can be regained if the injection fluids are viscous; however, complex fracture patterns and high fracture connectivity are expected. In Chapter 4 we more rigorously apply such predictions to hydraulic fracturing operations in the Barnett Shale.

SUMMARY

We developed finite element simulations of hydraulic fracture propagation and analyzed dynamical propagation. The main results are outlined below.

(1) The state of stress determines how close the rock layer is to failure. Under high differential stress hydrofracturing is easy with likelihood of little fracture connectivity. Under low differential stress high connectivity is created, but the fractures are short and high injection pressures are required. Because the local stress conditions change during hydrofracturing, the remote stress state should be augmented to include local stress evolution – this is shown here by plotting the stress-path. Regions of rock directly ahead of the fracture path fail by pressure reduction and are dominated by tensile fractures, whereas areas oblique to the main path fail by mixed stress with both tensile and shear fractures.

(2) During complex fracturing, out-of-plane damage builds up more intensely and leads to a higher shear contribution. A uniform internal pressure distribution creates a more elliptical crack shape and increases the shear contribution at the crack tip - this

effect is more pronounced for low tectonic stress ratios. A non-uniform distribution results in a more cusped-shaped crack and reflects a profile expected for a viscous injecting fluid. Although the latter condition is more conducive to stable mode I fracturing, the pressure drop requires higher injection pressure to initiate fracturing than in the uniform case.

(3) Transient fracture propagation occurs as the energy stored from applied loading is locally accommodated and released by damage and fracturing over short time periods. A strain-rate independent rheology still elicits a dynamical fracturing response. Build-up periods occur during strain hardening and result in widening and intensification of the damage front. Release periods occur during brittle failure and extend the main fracture path into the induced zone of damage.

(4) Small dynamical variations are a sufficient catalyst for unstable propagation. Unstable ruptures create larger, irregular damage patterns. The intensity and spacing of the ruptures dictates the character of the propagating damage front. Two scenarios are observed: (a) stable propagation via short, controlled ruptures occurs when the damage is spatially constrained so that it preconditions the potential fracture path for subsequent propagation, or (b) unstable propagation happens if the zones of damage transference are non-ideally linked and build-up periods and ruptures occur out of sequence.

(5) The idealized, simple hydrofracture shape can be produced in a layer given the specific conditions that the material is homogeneous and lies within a state of moderate differential stress and that a viscous injecting fluid is used. However, such conditions are difficult to sustain over a distance and in time. The simulations agree

with field observations and laboratory experiments and indicate that a complex, damaged hydrofracture network should be expected in the reservoir.

REFERENCES

- Baer, G., Beyth, M., and Reches, Z., 1994, Dikes emplaced into fractured basement, Timna igneous complex, Israel. *Journal of Geophysical Research*, v. 99, no. B12, p. 24,039-24,050.
- Baer, G., and Reches, Z., 1991, Mechanics of emplacement and tectonic implications of the Ramon dike systems, Israel. *Journal of Geophysical Research*, v. 96, no. B7, p. 11,895-11,910.
- Bazant, Z.P., 1986, Mechanics of distributed cracking. *Applied Mechanics Reviews*, American Society of Mechanical Engineers, v. 39, p. 675-705.
- Belayhneh, M., 2004, Palaeostress orientation inferred from surface morphology of joints on the southern margin of the Bristol Channel Basin, UK, in Cosgrove, J.W. and Engelder, T., 2004, eds., *The initiation, propagation, and arrest of joints and other fractures*, Geological Society, London, Special Publications, v. 231, p. 243-255.
- Busetti, S. and Reches, Z., 2007, Formation of network fractures during hydraulic fracturing of the Barnett Shale, a tight gas shale with preexisting fractures. *Eos Trans. of the American Geophysical Union*, v. 88, no. 52, Fall Meet. Suppl., Abstract T42C-04.
- Cooke, M.L. and Pollard, D.D., 1996, Fracture propagation paths under mixed mode loading within rectangular blocks of polymethacrylate. *Journal of Geophysical Research*, v. 101, no. B2, p. 3,387-3,400.
- De Borst, R., and Nauta, P., 1985, Non-orthogonal cracks in a smeared finite element model. *Engineering Computing*, v. 117, p. 35-46.
- Desroches, J., Detourney, E., Lenoach, B., Papanastasiou, P., Pearson, J.R.A., Thiercelin, M., and Cheng, A., 1994, The crack tip region in hydraulic fracturing. *Royal Society (London), Proceedings, Series A – Mathematical and Physical Sciences*, v. 447, no. 1929, p. 39-48.

- Elder, C.H., 1977, Effects of hydraulic stimulation on coalbeds and associated strata. United States Department of the Interior, Bureau of Mines, Report of Investigations 8260, 20 p.
- Engelder, T., 2004, Tectonic implications drawn from differences in the surface morphology on two joint sets in the Appalachian Valley and Ridge, Virginia. *Geology*, v. 32, no.5, p. 413-416.
- Fast, R.E., Murer, A.S., and Timmer, R.S., Description and analysis of cored hydraulic fractures – Lost Hills Field, Kern County, California. *Society of Petroleum Engineers Production and Facilities*, v. 9, no. 2, p. 107-114.
- Fish, J. and Belytchko, T., 2007, *A first course in finite elements*, Wiley, West Sussex, England, 336 p.
- Fredrich, J.T., Evans, B., and Wong, T., 1990. Effect of grain size on brittle and semibrittle strength: Implications for micromechanical modeling of failure in compression. *Journal of Geophysical Research*, v. 95, no. B7, p. 10,907-10,920.
- Haimson, B. and Fairhurst, C., 1967, Initiation and extension of hydraulic fractures in rocks. *Society of Petroleum Engineers Journal*, p. 310-318.
- Hart D.J. and Wang, H.F., 1995, Laboratory measurements of a complete set of poroelastic moduli for Berea sandstone and Indiana limestone. *Journal of Geophysical Research*, v. 100, no. B9, p. 17,741-17,751.
- Hodgson, A.R., 1961, Classification of structures on joint surfaces, *American Journal of Science*, v. 259, p. 493-502.
- Horii, H. and Nemat-Nasser, S., 1986, Brittle failure in compression: Splitting, faulting and brittle-ductile transition. *Philosophical Transactions of the Royal Society*, v. 319, no. 1549, p. 337-374.
- Hubbert, M. K. and Willis, D.G., 1957, Mechanics of hydraulic fracturing. *Transactions of the American Institute of Mining, Metallurgical, and Petroleum Engineers* 210, p. 153-68.
- Ishida, T., Chen, Q., Yoshiaki, M., and Roegiers, J.C., 2004. Influence of viscosity on the hydraulic fracturing mechanism. *Journal of Energy Resources Technology*, v. 126, p. 190-200.

- Lawn, B., 1993, Fracture of brittle solids – second edition. Cambridge University Press, 378 p.
- Lee, J. and Fenves, G.L., 1998, Plastic-Damage model for cyclic loading of concrete structures. *Journal of Engineering Mechanics*, v. 124, p. 892-900.
- Lublinter, J., Oliver, J., Oller, S. and Onate, E., 1989, A plastic-damage model for concrete. *International Journal of Solids and Structures*, v. 25, no. 3, p. 299-326.
- Lyakhovskiy, V., Reches, Z., Weinberger, R., and Scott, T.E., 1997, Non-linear elastic behavior of damaged rocks. *Geophysics Journal International*, v. 130, p. 157-166.
- Mahrer, K.D., 1999, A review and perspective on far-field hydraulic fracture geometry studies. *Journal of Petroleum Science and Engineering*, v. 24, no. 1, p. 13-28.
- Mazars, J. and Pijaudier-Cabot, G., 1996, From damage to fracture mechanics and conversely: a combined approach, *International Journal of Solids and Structures*, v. 33, p. 3,327-3,342.
- Papanastasiou, P., 1997, The influence of plasticity in hydraulic fracturing. *International Journal of Fracture*, v. 84, p. 61-97.
- Pollard, D.D., 1978, Forms of hydraulic fractures as deduced from field studies of sheet intrusions. *Proceedings of 19th U.S. Rock Mechanics Symposium*, v.1, no. 19, p.1-9.
- Reddy, J.N., 2004, Introduction to the finite element method. McGraw-Hill, 912 p.
- Reddy, J.N., 2007, An introduction to nonlinear finite element analysis. Oxford University Press, New York, 463 p.
- Rice, J.R., 1968, A path independent integral and the approximate analysis of strain concentration by notches and cracks. *Journal of Applied Mechanics*, v. 35, p. 379-386.
- Roth, M. and Thompson, A., 2009, Fracture interpretation in the Barnett Shale using macro and microseismic data. *First Break*, v.27, no.4.
- Rutledge, J.T., Phillips, W.S., and Mayerhofer, M.J., 2004, Faulting induced by forced fluid injection and fluid flow forced by faulting: An interpretation of hydraulic-

- fracture microseismicity, Carthage Cotton Valley Gas Field, Texas. *Bulletin of the Seismological Society of America*, v. 94, no.5, p. 1,817-1,830.
- Sagy, A., Reches, Z., and Roman, I., 2001, Dynamic fracturing of rock fragmentation and joint density: Field and experimental observations. *Journal of Structural Geology*, v. 23, p. 1223-1239.
- Sim, Y., 2004, Mechanics of complex hydraulic fractures in the Earth's crust. Doctoral Dissertation, Georgia Institute of Technology, Atlanta, Georgia, 324 p.
- Van Dam, C.J., De Pater, C.J., and Romijn, R., 1999, Reopening of dynamic fractures in laboratory experiments, In *International Congress on Rock Mechanics*, Paris, II, p. 792-794.
- Van Dam, D.B., Papanastasiou, P., and de Pater, C.J., 2002, Impact of rock plasticity on hydraulic fracture propagation and closure. *Society of Petroleum Engineers Production and Facilities*, v. 17, no. 3, p. 149-159.
- Warpinski, N.R., Lorenz, J.C., Branagan, P.T., Myal, F.R., and Gall, B.L., 1993, Examination of a cored hydrofracture in a deep gas well. *Society of Petroleum Engineers Production and Facilities*, v. 8, no. 3, p. 150-158.
- Weinberger, R., Lyakhovsky, V., Baer, G., and Agnon, A., 2000. Damage zones around en echelon dike segments in porous sandstone. *Journal of Geophysical Research*, v. 105, no. B2, p. 3,115-3,133.
- Wu, R., 2006, Some fundamental mechanisms of hydraulic fracturing. Doctoral Dissertation, Georgia Institute of Technology, Atlanta, Georgia, 280 p.
- Younes, A.I. and Engelder, T., 1999, Fringe cracks: Key structures for the interpretation of the progressive Alleghanian deformation of the Appalachian plateau. *Geological Society of America Bulletin*, v. 111, no. 2, p. 219-239.
- Zhou, J., Chen, M., Jin, Y., and Zhang, G., 2008. Analysis of fracture propagation behavior and fracture geometry using a tri-axial fracturing system in naturally fractured reservoirs. *International Journal of Rock Mechanics and Mining Science*, v. 45, no. 7, p. 1,143-1,152.

APPENDIX A: FE CONTINUUM DAMAGE MODEL

Our models implement a finite element damage scheme (de Borst and Nauta, 1985; Bazant, 1986) developed by Lubliner (1989) and later modified by Lee and Fenves (1998) to include cyclic loading, and compressive and tensile behavior. The material model is included in ABAQUS as “Concrete Damage Plasticity”. Note that here only a few salient points of the scheme are covered - the reader should refer to Chapter 2 for a more comprehensive explanation. The material elastic properties D , and effective stress σ , in the host medium depend on the amount of damage accumulated through microcracking in compression and tension (Lee and Fenves, 1998):

$$D=D(\kappa) = 1 - (1-D_t)(1-D_c) \quad [18a]$$

$$\sigma = (1-D)\sigma; \sigma = (1-D)E_0:(\varepsilon - \varepsilon^p) \quad [18b]$$

where κ is the damage variable, and ε^p is the scalar plastic strain. Damage increase due to microcracking is proportionate to the dissipated fracture energy density, G , normalized over a localization zone with a characteristic length, l :

$$\kappa_\chi = 1/g_\chi \int_0^{\varepsilon^p} (\sigma_\chi) d\varepsilon^p \quad [19a]$$

$$g_\chi = \int_0^\infty (\sigma_\chi)(\varepsilon^p) d\varepsilon^p \quad [19b]$$

$$g_\chi = G_\chi/l_\chi \quad [19c]$$

The normalized fracture energy in equation [19b] is analogous to the energy definition for the shielding zone of the cohesive crack model, with the exception that the constitutive relationship in [19b] is based on plastic damage theory (see Lubliner, 1989). This scheme is useful in our investigations for a few reasons. First, as we have previously discussed, the continuum damage approach permits the entire model to be

assigned a constitutive properties representative of reservoir rock. Thus, the limitations of the crack-tip approaches are overcome. Extension of the near crack-tip behavior of cohesion models to regions outside of the frontal zones permits use of the same model to describe the initiation of tectonically induced failure, propagation of multiple cracks, and self-interaction. Second, because the underlying damage model is compatible with fracture mechanics theory, many of the same interpretation techniques are possible. Specifically, we have compared how energy is dissipated in the system for different loading conditions. Third, the finite element implementation permits simulation of fracture propagation based on the equivalent crack concept, which states that there exists a length-scaled damage zone that is thermodynamically equivalent to a crack and vice versa. For a more thorough discussion on the equivalence of fracture and damage energy, refer to Mazars and Pijaudier-Cabot (1996). A discrete fracture is represented by a path of elements that are completely damaged and have no strength. Finally, we are able to use the Abaqus software to model the rheology as well as to solve the complex mechanics involved in transient, non-linear propagation. We chose a widely used commercial FE code for a number of practical reasons, in particular, that the software interface did not require additional programming or the use of other add-ons, and a number of Abaqus help resources and professional publications are available online.

APPENDIX B: EXPLICIT DYNAMIC FE SOLUTION

To solve the problem, we use the explicit dynamic FE procedure of ABAQUS/Explicit. The explicit technique is popular for solving a diverse range of non-linear dynamics problems in science and engineering. The technique incrementally solves for the transient, physical behavior of the problem, and is designed to handle extreme, local instability. Thus, it is well suited to simulate transient propagation of damage and complex fracture morphologies. A brief discussion follows on the explicit technique as applied in Abaqus (see Abaqus Theory Manual). For the general concepts of FE, we refer the reader to Fish and Belytchko (2007) and Reddy (2004, 2007).

The basic finite element procedure for structural analysis is to find an approximate discretized solution for $u(x)$ for the differential equation (here shown in 1D for clarity):

$$-d/dx[a(du/dx)] + cu - f = 0 \text{ for } 0 < x < L \quad [20]$$

Equation [20] is simply Hooke's law in differential form, where $a = a(x)$ reflects the material property (e.g., $a = EA$, Young's modulus x area), $b = b(x)$ is an environmental variable, for instance a penalty constraint, and $\varepsilon = du/dx$. A series of mathematical operations allows [20] to be recast in algebraic form in terms of matrix coefficients:

$$\mathbf{K}u - F = 0 \quad [21]$$

The coefficient \mathbf{K} is referred to as the stiffness matrix, u is the displacement vector, and F is the external force vector. The global \mathbf{K} contains the material properties and

shape functions (linear or quadratic) assembled over the entire mesh. The implicit FE technique (e.g., Abaqus/Standard) formulates \mathbf{K}_{ij}^e for each element in order to assemble the global matrix \mathbf{K} , which is then inverted to find the nodal displacement values $\{u\}$. For non-linear problems, the computation must be divided into many “solution-time” increments, and for each increment, it may take several iterations to converge upon a stable solution. If there are large changes in material properties, numerous evolving contacts, or extreme deformations, it may be impossible to achieve convergence. Alternatively, the explicit procedure solves [20] using sufficiently small “physical-time” increments on an element-by-element basis, and consequently does not require full matrix inversion and iterative convergence. The procedure is based on integrating the equations of motion ($F = ma$) and thus considers dynamical effects.

Modification of equation [21] yields:

$$\mathbf{M}\ddot{\mathbf{u}} + \mathbf{K}\mathbf{u} - \mathbf{F} = 0 \quad [22]$$

\mathbf{M} is the diagonal mass matrix and $\ddot{\mathbf{u}}$ is the acceleration vector. The size of the stable time increment is determined by the characteristic element dimension L_e and the smallest dilatational wave speed of the material c_d for all elements in the mesh.

$$\Delta t = \min(L_e/c_d) \quad [23a]$$

$$c_d = [(\lambda+2\mu)/\rho]^{1/2} \quad [23b]$$

where λ and μ are effective Lamé’s constants and ρ is the density of the material. In short, small elements, high material stiffness, low material density, and large applied loads reduce numerical stability, decrease the time increment, and increase the

computation time. The equations of motion are solved using a time integration scheme, where i is the time increment:

$$\int_{t_i}^{t_{i+1}} F(t)dt = [(1-\theta)F_i + \theta F_{i+1}]\Delta t \quad [24a]$$

Abaqus/Explicit uses a central difference rule ($\theta = 1/2$) so that the equations of motion become:

$$u^{(i+1)} = u^{(i)} + \Delta t^{(i+1)}\dot{u}^{(i+1/2)}, \quad [24b]$$

$$\dot{u}^{(i+1/2)} = \dot{u}^{(i-1/2)} + 1/2[\Delta t^{(i+1)} + \Delta t^{(i)}]\ddot{u}^{(i)}, \quad [24c]$$

$$\ddot{u}^{(i)} = \mathbf{M}^{-1}(F^{(i)} - \mathbf{K}u^{(i)}) \quad [24d]$$

The solution for each increment is achieved by using $u^{(i)}$ and $\dot{u}^{(i)}$ at the state of the previous increment to invert the diagonal mass matrix in [24d] at the beginning of the subsequent increment in order to compute the accelerations $\ddot{u}^{(i+1)}$. Integrating twice gives the primary displacement variables at the nodes of each element for the current time increment. Abaqus' post-processor then uses the nodal displacements to compute the secondary variables, i.e. stress and strain, at a single integration point in each element. The shape functions interpolate the values within each element. It is important to remind that in the present models for the elastic-plastic-damage material, the parameter a in equation [20] is a function that varies spatially and evolves over time depending on plastic strain, such that $\mathbf{K} = f[u_{ij}(t), \varepsilon^p(t)]$. Based on the plastic strain at each increment, the damage parameters in tension and compression are then calculated and are used to update the material stiffness and the shape of the yield surface for each element.

CHAPTER IV

MECHANICAL ANALYSIS OF HYDRAULIC FRACTURING IN THE BARNETT SHALE, FORT WORTH BASIN, TEXAS

ABSTRACT

The success of hydraulic fracturing in Barnett Shale wells depends on the local state of stress and the qualities of the injection. An effective operation reactivates natural fractures and propagates new fractures that together connect the wellbore to the reservoir. This study is a mechanical analysis of hydrofracturing in Barnett Shale wells that combines field data with numerical and analytical models.

The state of stress is determined for 13 hydrofrac stages in three horizontal wells and in 22 pump-in intervals in four vertical wells. These stress data are (1) used to predict natural fracture reaction by shear-slip and dilation, and (2) applied to finite element simulations developed in Chapter 4 to model hydrofracture propagation and the induced fracture pattern. The models indicate that injection under a state of low differential stress is more likely to produce short, complex hydrofracture segments with high connectivity, but require high fluid pressure P_f , and to expand the network distally, $P_f > \sigma_2$ is required. Injection under a state of high differential stress produces long branching hydrofracture segments with diversion into preexisting zones of weakness. In this case, to induce a spherical volume, P_f sufficient to activate fractures perpendicular to the σ_1 - σ_2 ($\sim S_v$ - S_{Hmax}) plane is required. The models' predictions are compared with pressure-time logs and microseismic event distribution maps and show

good agreement. Most wells in the study are in weakly tectonically stressed regions and rely on sustaining high net P_f to create volume and develop complexity.

INTRODUCTION

The Barnett Shale of the Fort Worth Basin, Texas, is a 26.2 tcf unconventional gas field that requires artificial stimulation to produce. The reservoir consists of Mississippian-age sequences of heterogeneous mudstone (Singh, 2008) with extremely low matrix permeability (e.g., 100-100 nano-Darcy) (Mayerhofer et al., 2006). It lies below the Pennsylvanian Marble Falls limestone and unconformably sits above heavily karstified Ordovician carbonates. In the core area to the northeast, the underlying layers are of the Viola Group; in the expansion areas to the southwest the lower Barnett Shale contacts the water-bearing Ellenberger Group (Fig. 4.1). The presence of local flexures, faults, and other collapse-related structures extending from the Ellenberger carbonates (Hardage et al., 1996) often diverts hydrofracture growth away from the orientation of the regional stress field (Browning, 2006; Roth and Thompson, 2009) and contributes to unique stimulation response from each hydrofracture stage. It is now widely recognized throughout the Barnett Shale that the local structure and its state of stress affects the hydrofracture pattern. This has caused many operators to reconsider the basic design of drilling wells normal to the maximum horizontal stress S_{Hmax} and injecting into equally spaced perforation intervals and instead, to develop more case-specific treatment plans.

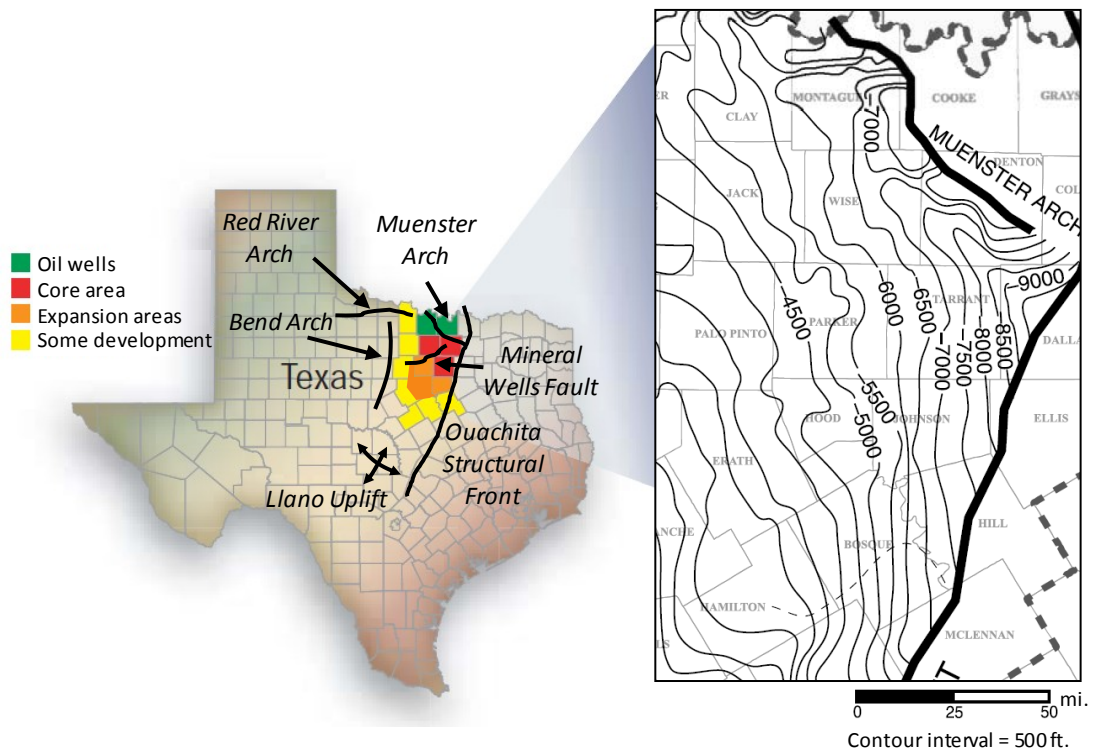


Figure 4.1. Map of the Barnett Shale play and major structural features. The present study focuses on the southwest expansion areas, colored in orange. The zoomed in area (right) shows the structural contours for the top of the Ellenberger carbonates and shows a gentle northeast dipping trend of the basin. Modified after Johnson (2004) and Pollastro et al. (2007).

The practice of characterizing the local state of stress in the Barnett Shale in order to model hydrofracture development was inferred in the net pressure calculations of Fischer et al. (2005). However, the early stress estimates in the Barnett Shale were primarily designed for drilling operations. Since then, the use of more sophisticated techniques such as pump-in tests and borehole sonic tools has become more common in designing treatment plans (e.g., Daniels et al., 2007) and the complete state of stress can be characterized. There have also been efforts to improve the understanding of the role of preexisting fractures. For example, Gale et al. (2007) studied natural fractures in cores of Barnett Shale and concluded that preferential reactivation of the preexisting fracture network could affect hydrofracture stimulations by redirecting fluid flow. In this case, the local state of stress and the injection qualities control whether natural fractures are induced to slip in shear, to dilate, or to propagate as hydrofractures. Our goal is to build on this progress and investigate how the state of stress in the Barnett Shale affects hydrofracture formation away from the wellbore.

We use two mechanical models. (1) An analytical model for fracture dilation (Busetti and Reches, 2007; after Baer et al., 1994; Jolly and Sanderson, 1997) is applied to investigate the conditions for natural fracture reactivation by shear-slip and tensile dilation. (2) A finite element model that we developed to study complex hydraulic fracturing (Chapter 4) is used to investigate the conditions for hydrofracture propagation and the expected pattern of the induced fracture network. Our goal here is to extend these idealized models to field scale with use real reservoir data. When information on the state of stress is available, the models predict the conditions for and

pattern of the hydrofractures. Conversely, when the patterns are known in the field, the models provide an estimate for the state of stress.

In the first part, the mechanical basis for the two models is outlined. In the second part, we discuss the application of the models to the Barnett Shale stress data. We compare the models' solutions with the simulated pattern for microseismic events for one well and the pressure-time logs for the associated hydrofracture treatments as well as few other pump-in tests. We focus on a selection of data from the Barnett Shale wells, most of which are in the southwest expansion areas of the field (Fig. 4.1).

PART I: MECHANICAL MODELS FOR HYDRAULIC FRACTURING

ANALYTICAL MODEL FOR REACTIVATION OF NATURAL FRACTURES

To solve for the tectonic stress and fracture fluid pressure needed to reactivate natural fractures, we implement an analytical model developed by Delaney et al. (1986) and then extended by Baer et al. (1994). These works were designed to estimate the 3D stress state during dike emplacement into fractured host rock. The model represents three principal stresses, σ_1 , σ_2 , and σ_3 , and the internal fluid pressure P_f by two normalized parameters: tectonic stress ratio Φ and normalized driving pressure R .

$$\Phi = (\sigma_2 - \sigma_3) / (\sigma_1 - \sigma_3) \quad [1a]$$

$$R = (P_f - \sigma_3) / (\sigma_1 - \sigma_3) \quad [1b]$$

The model assumes that preexisting fractures dilate when the internal pressure P_f is larger than the normal stress across them, determined by the inclination with respect to the principal stress axes, θ . Thus, the directional cosines $N_1 = \cos\theta_1$, $N_2 = \cos\theta_2$, and $N_3 = \cos\theta_3$ characterize the relationship with the far-field normal stress σ_n across the fracture (Jaeger and Cook, 1979, p. 27):

$$\sigma_n = \sigma_1 N_1^2 + \sigma_2 N_2^2 + \sigma_3 N_3^2 \quad [2]$$

Baer et al. (1994) used the general relations of $N_1^2 + N_2^2 + N_3^2 = 1$ and combined [1a] and [1b] with [2], yielding the relationship $(1/R)N_1^2 + (\Phi/R)N_2^2 \geq 1$. This form is presented on a stereographic projection with the principal stresses as the axes (Fig. 4.2). The range of orientations of dilating fractures (red lines) are reflected by $2\theta_w$ and $2\theta_L$, the width and length of the dilating fracture populations on the stereonet. The

range of fracture azimuths that can be dilated for a given Φ and R is $2\theta_L$ (the angular distance from σ_2 to σ_3) and the range of dips $2\theta_w$ (the angular distance from σ_1 to σ_3).

This solution works for values of $P_f < \sigma_2$. Jolly and Sanderson (1997) presented an alternative method to solving the relationship using a 3D Mohr diagram that also is valid for values of $P_f > \sigma_2$. The model then indicates the following relationships.

For $P_f < \sigma_2$

$$\Phi = \cos^2\theta_2 / \cos^2\theta_1 = \sin^2\theta_w / \sin^2\theta_L \quad [3a]$$

$$R = \cos^2\theta_2 = \sin^2\theta_w \quad [3b]$$

For $P_f > \sigma_2$

$$\Phi = 1 - \sin^2\theta_2 / \sin^2\theta_3 = 1 - \cos^2\theta_w / \cos^2\theta_3 \quad [3c]$$

$$R = \cos^2\theta_2 = \sin^2\theta_w \quad [3d]$$

The graphical approach (Fig. 4.3a, 4.3b, 4.3c) reveals that $2\theta_1 = 2(90 - \theta_L)$ is the counter-clockwise angle on the $\sigma_2 - \sigma_3$ circle (blue), beginning at σ_2 and ending at the point on the circle where $\sigma_n = P_f$. Likewise, $2\theta_2 = 2(90 - \theta_w)$ is the counter-clockwise angle on the $\sigma_1 - \sigma_3$ circle (red), beginning at σ_1 and ending at the point on its circle where $\sigma_n = P_f$. For the case of $\sigma_3 < P_f < \sigma_2$ (Fig. 4.3a) a range of fracture azimuths in the $\sigma_2 - \sigma_3$ plane dilate, indicated by the blue shaded area, fewer dips in the $\sigma_1 - \sigma_3$ plane are dilated (red shaded area), and no fractures dilate in the $\sigma_2 - \sigma_3$ plane (green circle). For this case, fractures oriented perpendicular to σ_1 are not dilated (e.g., if $\sigma_1 = S_v$, then horizontal fractures remain closed). For the case of $\sigma_2 < P_f < \sigma_1$ (Fig. 4.3b), all azimuths dilate (P_f encompasses the blue circle), a large range of dips dilate (red

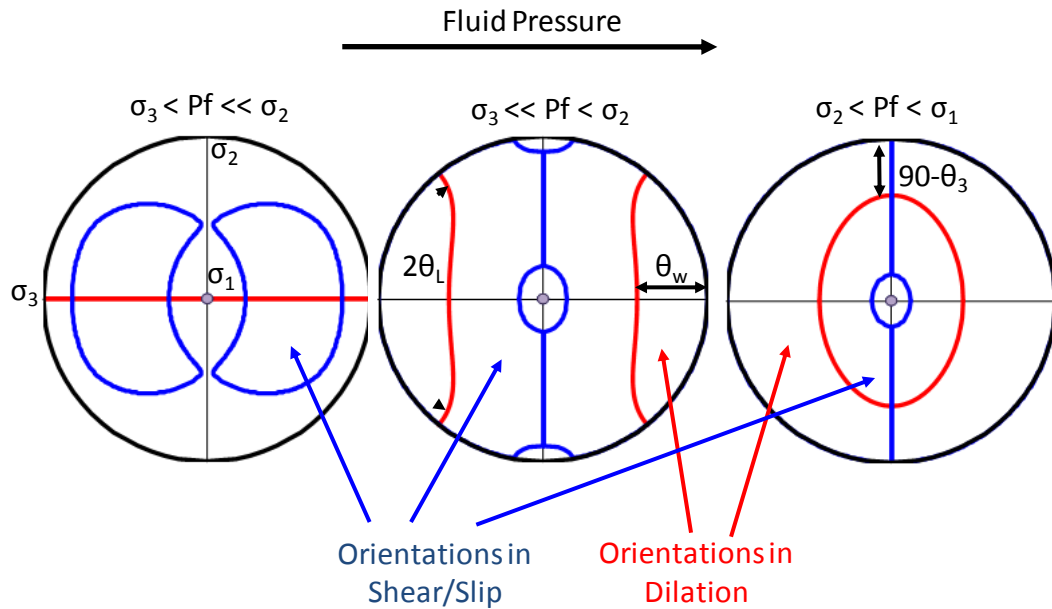


Figure 4.2. Stereographic projection showing the calculated limits for the range of poles to fracture orientations that can be reactivated by dilation (red) or shear-slip (blue) relative to the tectonic state of stress and for three stages of increasing fluid pressure. For $\sigma_3 < Pf \ll \sigma_2$ (left) two groups of fracture orientations can be reactivated in shear-slip, but no dilation is possible. For $\sigma_3 \ll Pf < \sigma_2$ (center) most orientations can slip and two groups of fractures oriented parallel to σ_3 can be dilated. For $\sigma_2 < Pf < \sigma_1$ (right) a wide range of fractures can slip and dilate.

(3a) Dilation of Preexisting Fractures $\sigma_2 > P_f > \sigma_3$

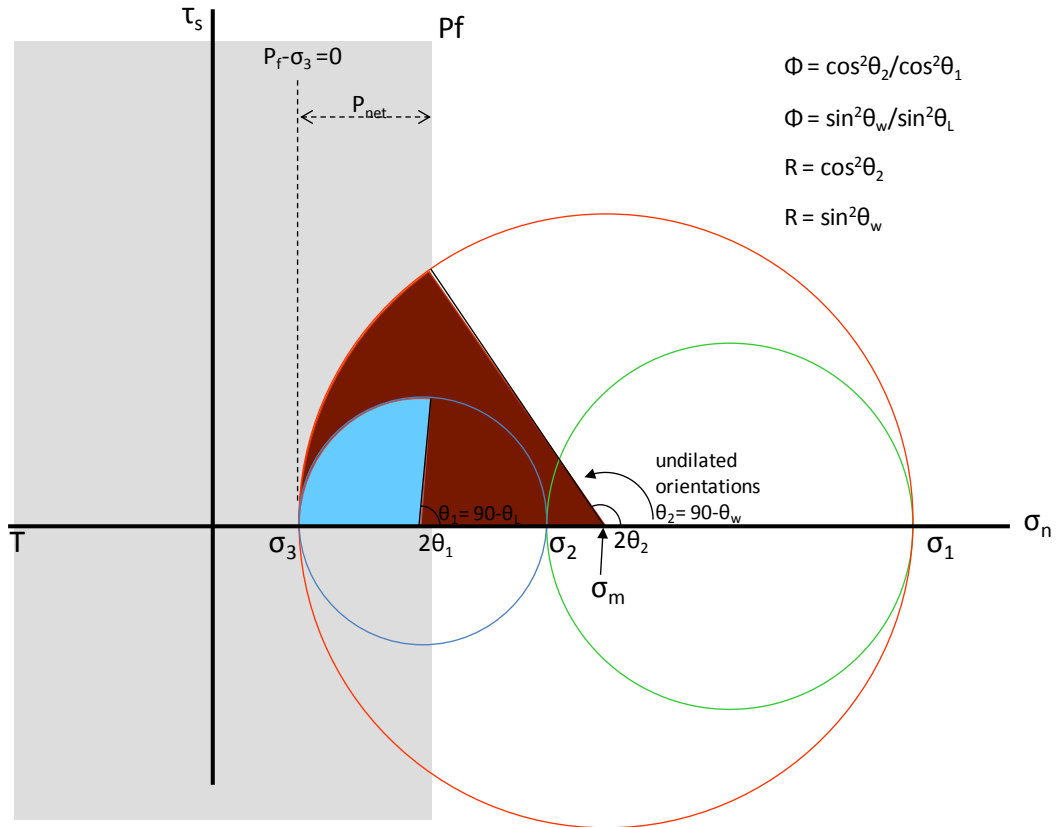


Figure 4.3. Mohr-circle plots showing the reactivation conditions for fractures in dilation (a and b) and in shear (c). Colored shaded areas correspond to reactivated fracture orientations in the associated principal stress plane. See text for explanation of parameters. Modified after Jolly and Sanderson (1997) and McKeagney et al. (2004).

(3b) Dilation of Preexisting Fractures $\sigma_1 > P_f > \sigma_2$

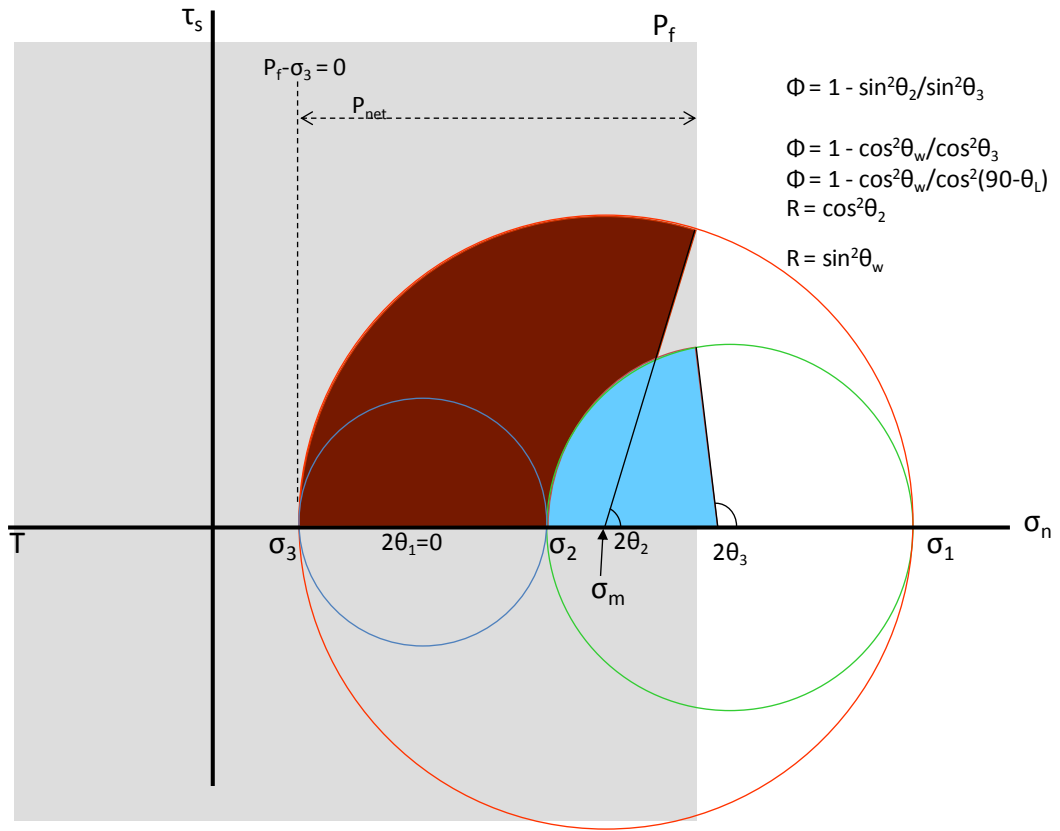


Figure 4.3. Mohr-circle plots showing the reactivation conditions for fractures in dilation (a and b) and in shear (c). Colored shaded areas correspond to reactivated fracture orientations in the associated principal stress plane. See text for explanation of parameters. Modified after Jolly and Sanderson (1997) and McKeagney et al. (2004).

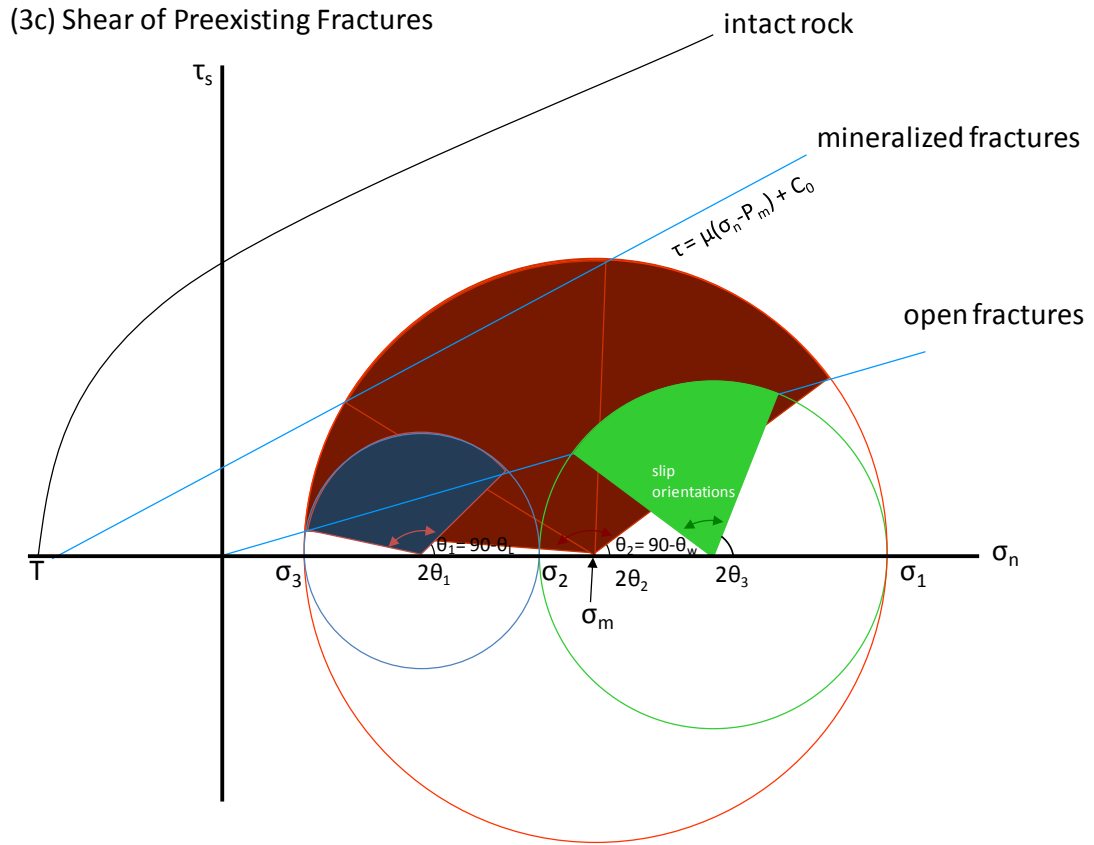


Figure 4.3. Mohr-circle plots showing the reactivation conditions for fractures in dilation (a and b) and in shear (c). Colored shaded areas correspond to reactivated fracture orientations in the associated principal stress plane. See text for explanation of parameters. Modified after Jolly and Sanderson (1997) and McKeagney et al. (2004).

shaded area) and orientations close to perpendicular to σ_1 are now capable of dilation. For a given value Φ and R , any fracture in the shaded areas may also propagate if additional fluid pressure equal to the tensile strength of the rock is achieved.

Expansion to Model Shear and Dilation Limits

To solve for reactivated fracture orientations from each hydrofrac stage of Barnett Shale wells, we implemented the model graphically using the 3D Mohr circle approach (e.g., Jolly and Sanderson, 1997; McKeagney et al., 2004). On 3D Mohr circles, points defining each circle are solved in τ - σ_n coordinates and plotted as x-y values. The centers of the circles are the corresponding mean stresses which shift left or right depending on the fluid pressure: $\sigma_{\text{effective}} = (\sigma_n - P_f)$. The angles θ_1 , θ_2 , and θ_3 are solved by calculating the points of intersection of a vertical line fixed at $P_f - \sigma_3$ with each of the circles (note, intersection occurs with circle σ_1 - σ_3 and either σ_2 - σ_3 or σ_1 - σ_2 , but not both). The criteria for dilation must be met before propagation can occur, however, failure by shear slip along preexisting fractures that serve as planes of weakness occurs earlier than dilation. To solve for fracture orientations that would slip in shear, we also plotted a Mohr-Coulomb failure surface with no cohesion (Fig. 4.3c). The intersection of this failure line with each circle can be solved in the same manner as before to yield $\theta_{1\tau}$, $\theta_{2\tau}$, and $\theta_{3\tau}$. For both dilation and shear, we use the 3D Mohr diagram to plot the limit of θ_1 , θ_2 , and θ_3 on a stereonet. The procedure involves using Mohr circle deconstruction techniques for a general 3D state of stress to convert the points of intersection for the vertical line defining dilation or the inclined line for shear into directional cosines, and then to translate those into strike and dip notation. An

Excel spreadsheet (after C.R. Stanley) was modified to plot the points on a stereonet with the principal stresses as the axes.

One feature of the fracture reactivation model that should be mentioned here is the ability to solve for a missing component of the stress tensor if the others are known and data on the tensile fracture population is available. We could not complete the method on the wells in our study, but the approach of Baer et al. (1994) for dike intrusions can be adapted for reservoir applications as follows. (1) Compile the orientations of the drilling induced fractures for the desired interval from image logs and plot them on a stereonet to determine θ_w and θ_L . Solve equations [3a] and [3b] to find the value of Φ and R . Depending on which additional stress data is available, the values of σ_1 , σ_2 , and σ_3 are constrained by solving [1a] and [1b]. The injection pressure P_f reflects the fluid pressure or mud weight during drilling responsible for the induced tensile fractures. If the fracture population is of tensile fractures induced during hydrofracturing (i.g., post-injection image logs), then P_f is the maximum bottom-hole treatment pressure from pressure-time logs. Thus, depending on which data is available, the reactivation model can be used to determine (1) S_{hmin} prior to the hydraulic treatments if S_{Hmax} is available, e.g., from sonic data; (2) S_{Hmax} after the injections if S_{hmin} is determined from the initial ISIP.

FE MODEL FOR FRACTURE PROPAGATION

We also apply Barnett Shale stress data to a finite element model presented in Chapter 3 to explore whether the injection pressures and tectonic stress conditions could develop simple or complex hydrofracture patterns. The model also indicates the

relative fracture connectivity to be expected under given local stress conditions. By using the explicit dynamic capabilities of the program Abaqus we were able to simulate layer-scale transient damage propagation ahead of a pressurized hydrofracture segment based on a real-time loading scenario. It is likely that the response within a single, simple layer reflects the least complex behavior to be expected in the reservoir and thus can be used to approximate the shape of the stimulation patterns observed in the field.

MODEL CONFIGURATION

The model configuration (Fig. 4.4) is for an initial fracture embedded in a layer with elastic-plastic rheology and its propagation into a 2m thick layer with elastic-plastic-damage rheology, calibrated to the properties of Berea Sandstone determined from rock mechanics experiments (Chapter 3). The material model uses strain-based damage evolution, where a continuum damage scheme is used to simulate fracturing. Damage is calculated as the local stiffness degradation and ranges from 0 to 1, where $d = 0.9$ means 90% of the original stiffness has been lost. The parameter $d = 0$ for undamaged rock, $d \sim 0.4$ coincides with the ultimate stress limit and is generally understood to reflect the stage when microcracks have coalesced to form macroscopic fractures, and $d = 1$ represents a pervasively damaged, completely failed region of rock with stiffness = 0. The stress-strain properties of Berea Sandstone serve as a proxy to the behavior of reservoir rocks, and specifically, they lie within the range of those measured experimentally for members of the siliceous mudstone lithofacies of the Barnett Shale (proprietary data). The assumption is likely to be valid for simulated conditions of “dry propagation” and a “fluid lag region” where no fluid penetrates into

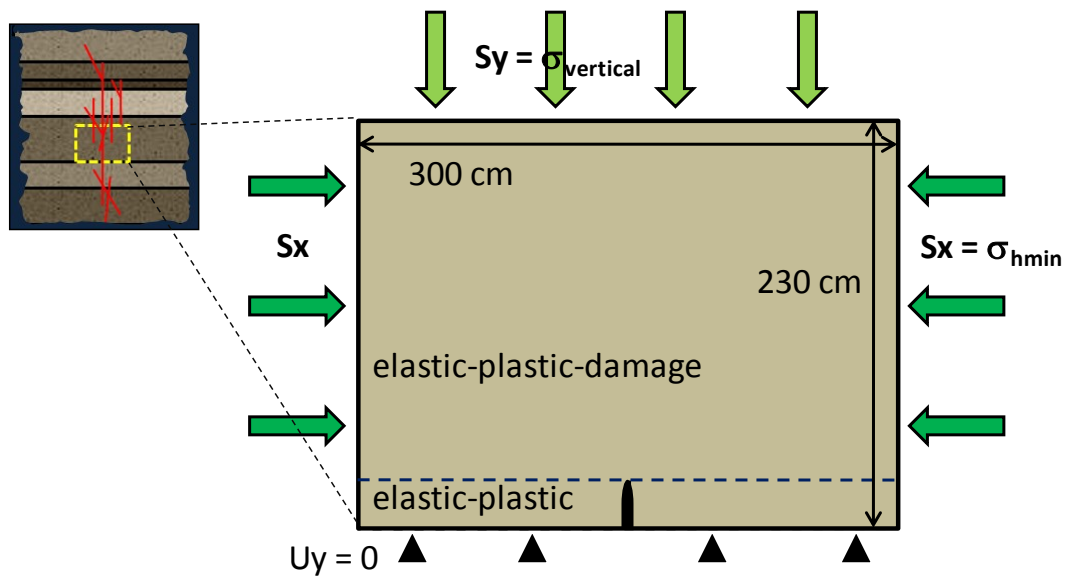


Figure 4.4. Finite element model configuration (right) and schematic of the geologic scenario (left) for a single hydrofracture segment propagating through the reservoir and into a sandstone layer. Tectonic loads S_x and S_y are applied to the sides and internal pressure is applied in the preexisting thin, vertical crack.

the fracture walls or into the crack-tip region ahead of the crack. In this case, consideration of the effective stresses rather than true stress accounts for pore pressure related to permeability differences.

The stress conditions are for plane strain and are based on the general conditions for hydrofracturing in the Barnett Shale. Two tectonic stresses are initially applied to the rock layers, $S_y = 50$ MPa (7252 psi) and $S_x = 10$ to 45 MPa (1450 to 6527 psi). If the conditions $S_y = S_v$ and $S_x = S_{hmin}$ are assumed, then the model simulates vertical up-section propagation. The internal crack pressure P_f increases linearly with time at a rate of 10 MPa/s (1450 psi/s). This rate is about 10 times faster than the increase in bottom hole pressure recorded during the seconds immediately preceding the break down pressure for wells in the Barnett Shale. The simulations considered the case of a uniform pressure distribution $dp/dx = 0$, and a non-linear pressure distribution. Based on the simulated results and experiments of Ishida et al. (2004), we found that the former case more closely reflected the conditions for a low-viscosity fluid such as in the slickwater treatments used in Barnett Shale operations, when no leak off occurs.

SOLUTION AND APPLICATION

The two aspects of the simulations we apply here are the comprehensive results from the diagram in Figures 4.5 and 4.6 and the simulated hydrofracture patterns. A short summary is provided here; for a detailed explanation refer to Chapter 3. The convention is for the normalized fluid pressure and normalized tectonic stress ratio in plane strain and based on the q - p' convention, where q is the deviatoric stress and p' is the pressure stress. Thus:

$$\text{Net } P/q = (P - S_3) / (S_1 - S_3) \quad (\text{normalized fluid pressure}) \quad [4a]$$

$$q/p' = (S_1 - S_3) / ([S_1 + 2S_3] / 3) \quad (\text{normalized tectonic stress}) \quad [4b]$$

where $P = P_f$ is the internal pressure for the crack, $S_1 \approx S_y$ is the maximum principal stress, $S_3 \approx S_x$ is the minimum principal stress, and $(P - S_3)$ is the net pressure.

CONDITIONS FOR PROPAGATION

Figure 4.6 is a compilation of 11 simulations run with a continuous pressure distribution in the initial fracture. The color scale reflects the cumulative amount of damage in the layer. The contours are based on the pressure-dependent yield parameters for Berea Sandstone (red dashed lines in Fig. 4.6) (details in Busetti and Reches, in prep), so that for weaker lithologies such as clay-rich shale units the warm colors shift to the left (grey dashed lines), whereas for stronger rocks like the Ellenberger carbonates the colors shift to the right. The curved boundary extending from the top left to bottom right is the damage cut-off point, or the limit at which the induced fracture has completely propagated through the layer (*note, because of the ‘dry’ propagation criteria this boundary reflects the extreme case that the fracture front fully precedes the fluid-front within the layer). For units more brittle than Berea Sandstone, the cut-off shifts to the left (i.e., easier to fracture, but with less pervasive damage) and for units more ductile the cut-off shifts to the right. Injection stages with high tectonic stress ratio require low injection pressure to induce complete failure of the layer ($\text{Net } P/q > 1$), and are considered “easy to fracture”. However, little damage accumulates prior to total failure of the layer, suggesting limited fracture connectivity apart from the main fracture path. Hydrofrac operations under low tectonic stress ratio

require a lot of injection pressure to induce complete failure of the layer ($\text{Net } P/q > 3$) and are “hard to fracture”. In this case, prior to total failure more damage accumulates, suggesting high fracture connectivity within the layer.

HYDROFRACTURE COMPLEXITY

The simulations (Fig. 4.5 and 4.6) indicate that (1) in a state of high differential stress, new fractures form at $P_f = 20\text{-}40$ MPa (2,900-5,800 psi). The fractures are long and complex, forming numerous branches and linking segments, which increase the fracture connectivity. Because this state of stress is highly conducive to hydrofracture propagation, the tendency is for the network to conform to the tectonically stressed structural domains. The result is redirection away from the orientation of the far-field stress without significantly increasing the fluid pressure. (2) In a state of moderate differential stress new fractures form at $P_f = 40\text{-}70$ MPa (5,800-10,100 psi). Fractures are straight, planar, and develop uniformly according to a repeating arrest and rupture pattern. In order to create complexity: (a) the fluid pressure must be significantly increased in order to intensify the rupture events, thus expanding the size of the damage front out-of-plane and triggering local instability, or (b) the fluid viscosity must be reduced to amplify the inelastic shear component at the crack tip. (3) For a state of low differential stress new fractures form at $P_f = 70\text{-}90$ MPa (10,100-13,000 psi). Fractures are short and growth is unstable, resulting in a pervasive damage network comprised of numerous linking segments. The high pressures that are required may be difficult to achieve in practice, and may be preempted by some combination of unstable failure of the fracture walls and shear failure at the crack-tip. If this stress-state is encountered near the borehole, it is possible that the network

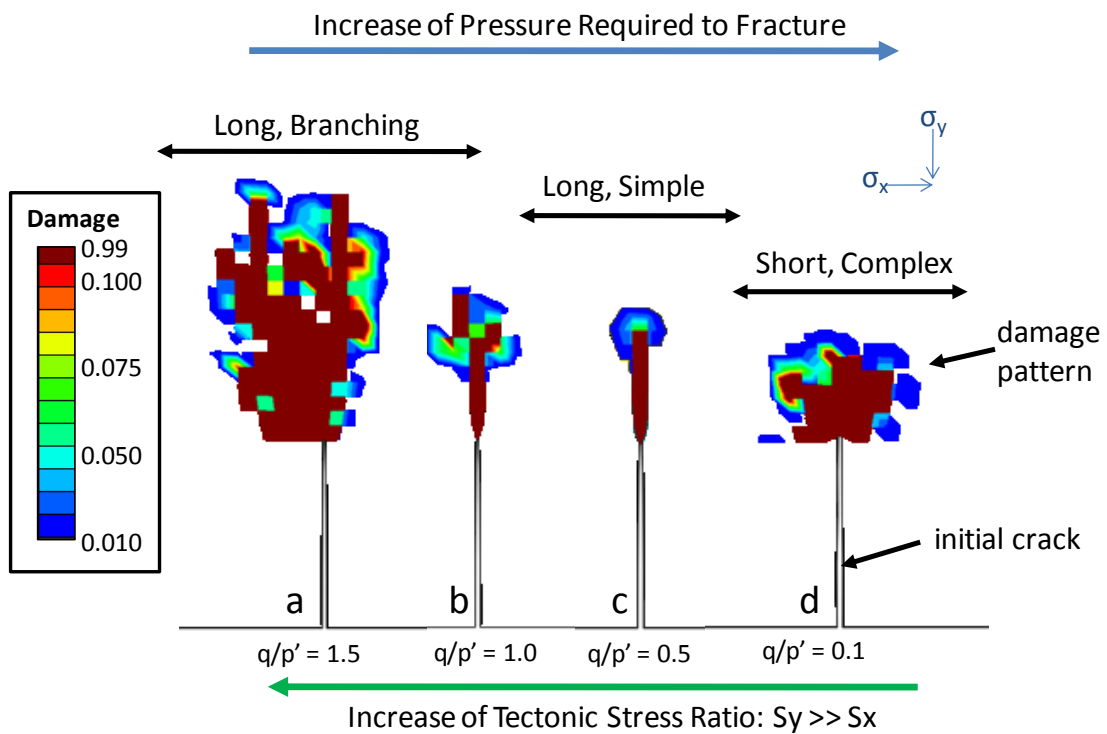


Figure 4.5. Simulation results showing hydrofracture shapes formed under a range of stress regimes: (left) high differential stress, (center) moderate differential stress, and (right) low differential stress. The length of the initial fracture (black outline) is 30 cm. Dark red indicates pervasively damaged regions (2-3mm quad-elements) with total stiffness degradation, and are mechanically equivalent to a discrete fracture. Cool to warm colors indicate progressive microcracking and stiffness degradation, where orange-red colors reflect early stage microcrack linkage and macro-fracture formation. The outer patterns (very high or very low differential stress) show complex segments with no distinct main fracture path, displays multiple branches and linking segments, and the overall damage distribution is pervasive. The inner patterns (moderate differential stress) are simple segments with narrow, symmetric zones of damage that extend uniformly over time.

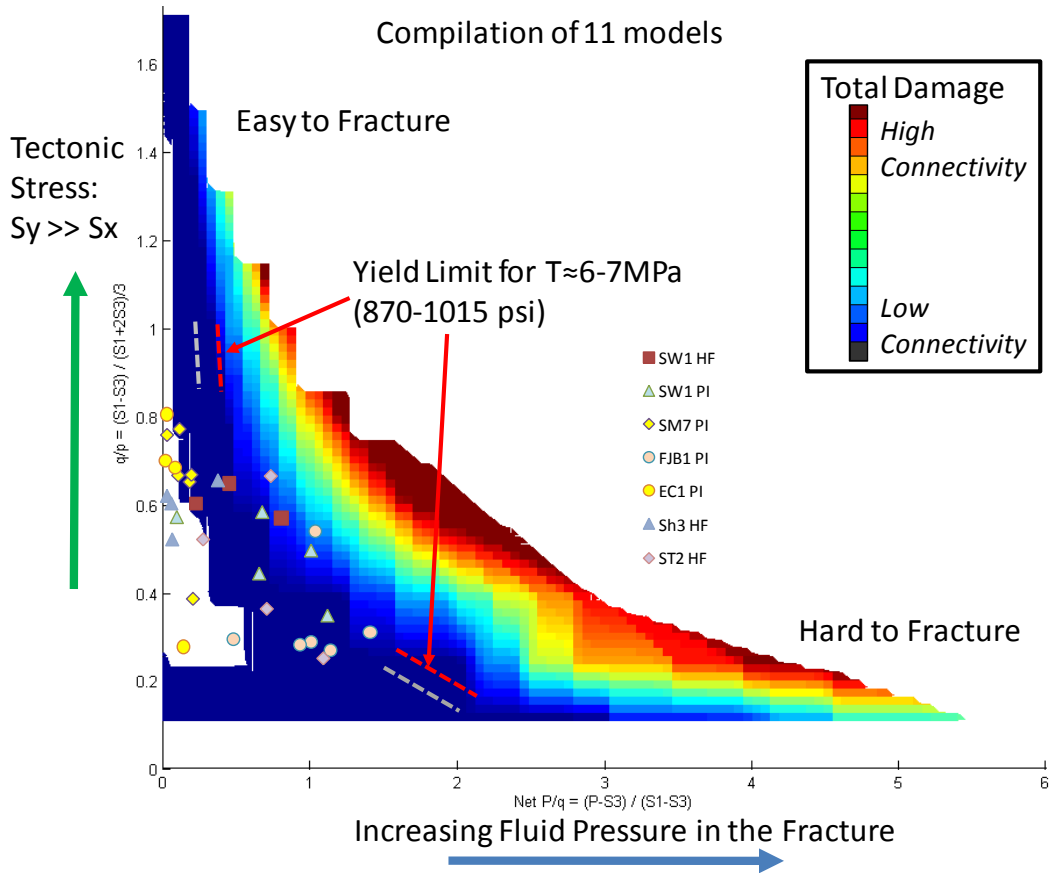


Figure 4.6. Contour map showing the effect of loading conditions on cumulative damage evolution. The operator typically controls the fluid pressure (x-axis) for a given tectonic stress state (y-axis). Warm colors indicate high damage and also suggests greater fracture connectivity (see text). The curved right-hand boundary reflects the pressure needed to induce total failure of the layer. Layers under high tectonic stress are easy to fracture but create little damage. In areas of low tectonic stress a lot of damage develops but high fluid pressure is required to initiate fracturing.

would spread to the nearest favorable stress field – the well path - rather than propagating distally into the reservoir. Some degree of control can be regained if the injection fluids are viscous; however, complex fracture patterns and high fracture connectivity are expected.

PART II: APPLICATION OF THE MODELS TO BARNETT SHALE STRESS DATA

RESERVOIR/GEOLOGIC SETTING

STRUCTURAL GEOLOGY OF THE FORT WORTH BASIN

Regional and Local Structures

The Fort Worth basin is a north-south elongated foreland basin that formed in front of the Ouachita thrust belt during the Late Paleozoic (Walper, 1982). The basin is bound on all sides by gentle arches (Fig. 4.1), the most dominant being the Bend Arch to the west, a broad north-plunging flexure and structural high thought to have formed as a hinge-line during late Mississippian subsidence and when the basin tilted westward during the late Paleozoic (Pollastro et al., 2007). The gently dipping ($2-3^\circ$) regional structural dip is to the northeast and coincides with thickening of the Barnett Shale from the Llano Uplift where the Barnett Shale is 30-50 feet thick to the Muenster Arch where thickness reaches a maximum of 1000 feet . Throughout the field, there are a number of minor southwest-northeast trending high-angle normal faults and graben structures and north-south trending faults associated with development of the Mineral Wells fault system in the northeast or the Ouachita structural front to the east (Fig. 4.1) (Pollastro et al., 2007; also see Simon, 2005). Some of these faults were periodically reactivated and may be basement related (Montgomery et al., 2005). The most dominant features in the field are the small flexures and fault and fracture corridors related to karst collapse in the underlying Ordovician Ellenberger Group that pervade the Mississippian to middle Ordovician strata (Hardage, 1996), also see (1) below.

Stress State

Along the vertical and horizontal well paths throughout the field, and especially in the present study area, where reservoir thickness decreases to 300-500 feet, we observed fluctuations in the direction and magnitude of the local stress field. The influence of the regional structure on the current state of stress is less clear to the north and west of the basin in the 'oil window' where reservoir quality is poor and to the east where the higher depths and maturity levels contribute to difficult economics (Montgomery et al., 2005).

The local variations in the stress field can be attributed to:

(1) The presence of collapse-related flexures and fault and fracture corridors (Fig. 4.7). Seismic interpretation of karst related fault and fracture corridors in the Ellenberger horizon in the southwestern expansion area (Baruch, 2009) indicates the presence of two dominant sets of lineaments (1: NNW; 2: NNE) spaced >100 feet to 1000 feet apart that source from the carbonate units and extend upward, in some cases past the overlying Marble Falls. The sub-vertical corridors form a coalescent rectilinear network of synformal sags that overly collapsed paleocaves (Loucks, 1999; McDonnell et al., 2007; Baruch, 2009), some of which may be related to basement-fault reactivation (Elibiju et al., 2008). Comparison of macro- and microseismic data indicates that the semi-circular fault systems surrounding the collapse zones are a major cause of hydrofracture diversion (Roth and Thompson, 2009).

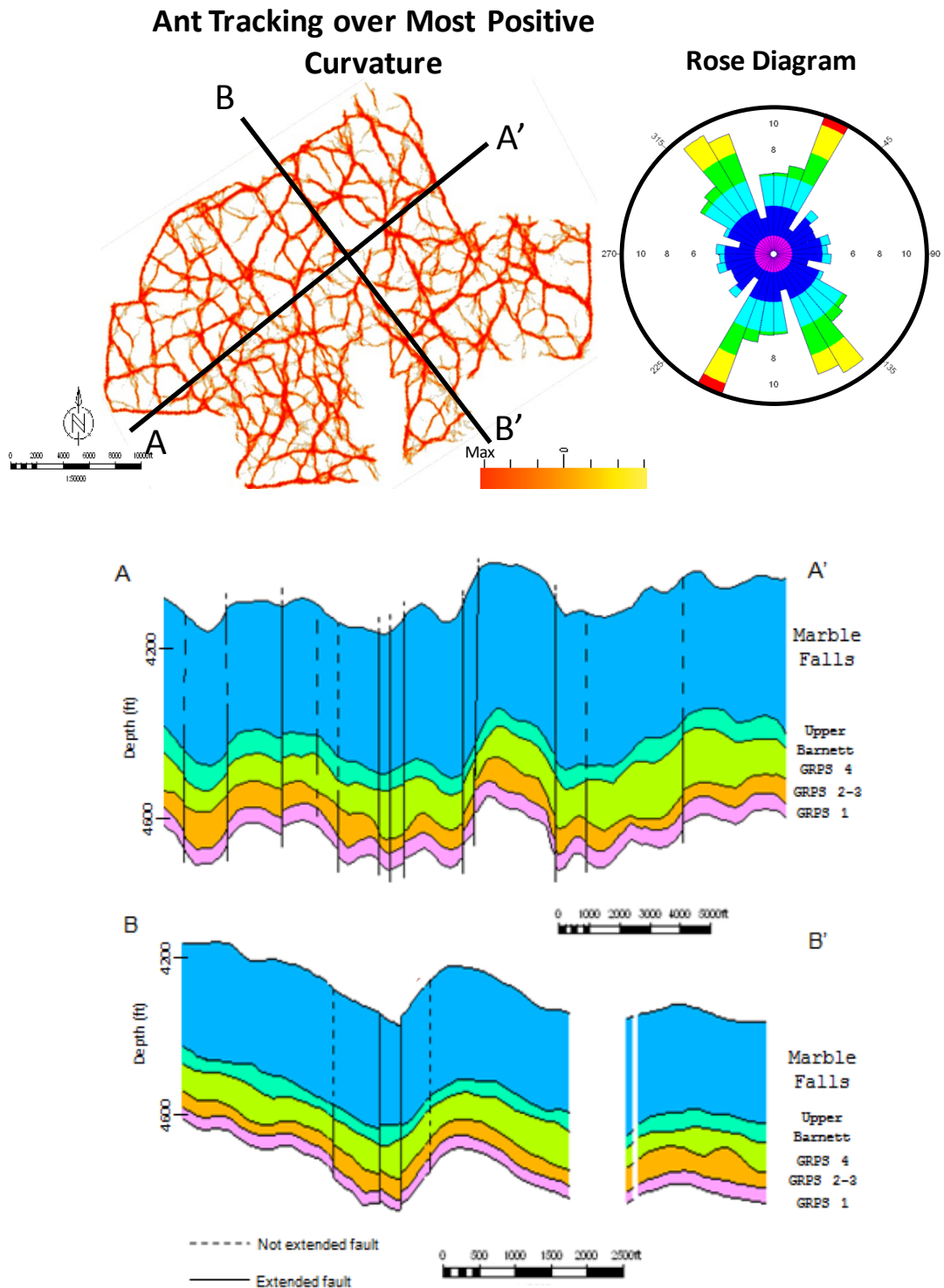


Figure 4.7. Seismic structural interpretations of collapse-related flexures and fracture corridors in the present study area of the Barnett Shale (Modified after Baruch, 2009). (Top): Horizon slice through the most positive curvature along the Ellenberger, and the associated rose diagram for the mapped lineations. (Bottom): seismic cross sections along the major (A-A') and intermediate (B-B') axes of the karst features.

(2) Lithologic variations that induce stress amplification. Stress rotation and tensile stress amplification have been associated with stiffness contrasts in rock layers (e.g., Reches, 1998). Proprietary rock mechanics data for uniaxial and triaxial tests indicate that the Young's modulus and compressive and tensile failure strengths varies significantly within the Barnett Shale units. At least nine lithofacies were identified from core (Singh, 2008): (a) siliceous non-calcareous mudstone, (b) siliceous calcareous mudstone, (c) micrite/limy mudstone, (d) bottom-current calcareous deposit, (e) reworked shelly deposit, (f) silty-shaly (wavy) interlaminated deposit, (g) phosphatic deposit, (h) dolomitic mudstone, and (i) concretions. Core, borehole image log, and gamma ray logs suggest that the mechanical thickness (the thicknesses of stratigraphically sequential units with similar mechanical properties) in some cases extends to a maximum of 10-20 feet, but is typically less than a few feet.

(3) Over-pressurization and pore pressure variations. Areas with elevated pore pressure exhibit principal stresses that are closer in magnitude, are more prone to faulting under small stress differences, and more easily transition between modes of failure (Zoback et al., 2003). Estimates of the pore pressure based on the initial formation pressure during pump-in tests for study wells in the southwest expansion areas indicate a range of 0.489-0.524 psi/ft, which is consistent with the value of 0.52 psi/ft reported for the Barnett Shale in Montgomery et al. (2005). Propagation of the hydrofractures into a structural domain with reduced pore pressure could affect which natural fractures reactivate and change the mode of fracture propagation, potentially with a loss of complexity.

HYDRAULIC FRACTURING OPERATIONS

Pump-in Tests in Vertical Wells

Pump-in tests were conducted to evaluate the stress and failure response to controlled injections in multiple mechanical or stratigraphic formation intervals in the vertical pilot holes. The four wells we studied (see Table 4.1 and Figs. 4.8 and 4.9) began with initial shut-in tests to qualitatively gauge the permeability - packers were initially inflated to between 100-400 psi above the formation pressure and then allowed to leak-off. Several injection cycles were then run at each interval. The cycles consist of pressurization by applying a constant RPM from the pumps until the peak pressure is achieved followed by continued pumping for an additional minute, after which the interval is sealed and the pressure drop occurs naturally. For several intervals intermediate 'rebound tests' were conducted by closing the test interval and monitoring the rise in pressure in order to verify that fluid is not bypassing into the borehole (i.e., Haimson and Cornet, 2003). The total pumping time for each interval is 1-3 hours.

Hydrofrac Stages in Horizontal Wells

Three typical hydrofracture stages are shown in Figures 4.10-4.12. The actual injection parameters vary for each stage and in each well, but for the typical injection in the studied wells each treatment consists of 4 or 5 stages along the wellbore, each involving pumping 300,000 to 1,000,000 gallons of water with 100 mesh and 40/70 sand into 12-24 0.42 inch diameter perforations spaced at 6 shots per foot.

Table 4.1. Stress data for Barnett Shale Wells

Well	Type	Formation	S_v	S_{Hmax}		S_{Hmin}			T Pump-In Test	Pf Max Pressure	Tectonic Stress		Fluid P1 R or Net P/q
			ρ Log	Sonic Log	Pump-In Test	Sonic Log	Pump-In Test	ISIP			Φ	q/p'	
SW1	HF Stage #1	Barnett	6495	3826				3736		4368	0.03	0.59	0.23
	HF Stage #2	Barnett	6463	3748				3568		4879	0.06	0.64	0.45
	HF Stage #3	Barnett	6425	3727				3876		5900	0.06	0.56	0.81
	HF Stage #4	Barnett	6377	3698				4017		2801	0.12	0.56	-0.33
	Pump-In #1	Ellenberger	6682	5155	N/A	4850	N/A			6900	0.17	0.34	1.12
	Pump-In #2	Ellenberger	6612	4593	4717	4027	3865	3988	1787	5727	0.31	0.57	0.68
	Pump-In #3	Barnett	6510	4253	4760	5003	3845		234	4112	0.34	0.56	0.10
	Pump-In #4	Barnett	6541	4127	5764	4589	4345	4536	1393	5789	0.65	0.43	0.66
	Pump-In #5	Barnett	6376	4046	3888	3783	3310	3155		3234	0.19	0.71	-0.02
	Pump-In #6	Marble Falls	6255	3960	N/A	4194	N/A			6274	0.10	0.49	1.01
SM7	Pump-In #1	Barnett	7399	4195	4679	4175	4013		274	4361	0.20	0.66	0.10
	Pump-In #2	Ellenberger	7532	4943	4547	4869	4140		177	4752	0.12	0.64	0.18
	Pump-In #3	Ellenberger	7532	4943	4234	4869	4080			4745	0.04	0.66	0.19
	Pump-In #4	Ellenberger	7553	5098	6522	4781	5290			5749	0.54	0.37	0.20
	Pump-In #5	Barnett	7304	4204	3943	4370	3603		251	4017	0.09	0.77	0.11
	Pump-In #6	Barnett	7220	4121	3999	4000	3605			3702	0.11	0.75	0.03
FJB1	Pump-In #3	Barnett	5268		5619		4289		110	4928	0.74	0.28	0.48
	Pump-In #6	Barnett	5405		5377		4225		555	5571	0.98	0.26	1.14
	Pump-In #11	Barnett	5411		4551		4151			5424	0.32	0.28	1.01
	Pump-In #12	Barnett	5335		4272		4009			5877	0.20	0.30	1.41
	Pump-In #13	Barnett	5335		3423		3250			5411	0.08	0.53	1.04
	Pump-In #14	Barnett	5198		4845		4018			5119	0.70	0.27	0.93
EC1	Pump-In #1	Barnett	8272		4188		3964			4082	0.05	0.80	0.03
	Pump-In #2	Barnett	8284		5014		4367		1125	4445	0.17	0.69	0.02
	Pump-In #7	Ellenberger	8339		9220		6470			6730	1.47	0.26	0.14
	Pump-In #9	Barnett	8042		4767		4298			4625	0.13	0.68	0.09
Sh3	HF Stage #1	Barnett	8359	5696				5178		5375	0.16	0.51	0.06
	HF Stage #2	Barnett	8278	5421				4689		4783	0.20	0.61	0.03
	HF Stage #3	Barnett	8064	4639				4639		4830	0.00	0.59	0.06
	HF Stage #4	Barnett	7719	4440				4235		5538	0.06	0.65	0.37
ST2	HF Stage #1	Barnett	5693	3126				3091		5010	0.01	0.66	0.74
	HF Stage #2	Barnett	5695	4492				4077		5226	0.26	0.35	0.71
	HF Stage #3	Barnett	5697	3905				3526		4130	0.17	0.51	0.28
	HF Stage #4	Barnett	5709	5760				5330		5137	1.13	0.07	-0.51
	HF Stage #5	Barnett	5725	4832				4557		5835	0.24	0.24	1.09

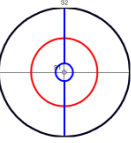
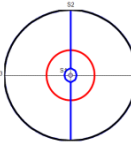
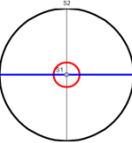
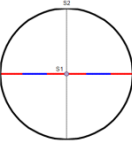
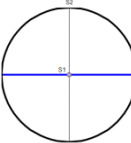
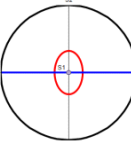
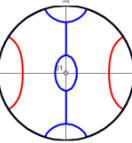
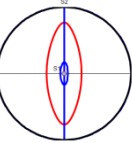
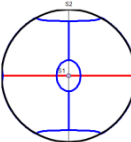
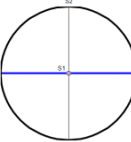



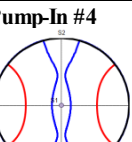


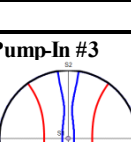
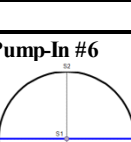
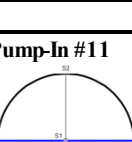
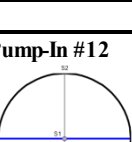
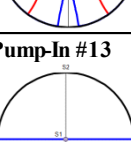
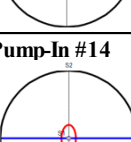
SW1 HF Stage #1 Dilation — θ_w 28.6 θ_L 90 90-03 26.8 	SW1 HF Stage #2 Dilation — θ_w 42.3 θ_L 90 90-03 40.2 	SW1 HF Stage #3 Dilation — θ_w 63 θ_L 90 90-03 63.8 	SW1 HF Stage #4 Dilation — θ_w 0 θ_L 0 90-03 0 
SW1 Pump-In #1 Dilation — θ_w 90 θ_L 90 90-03 90 	SW1 Pump-In #2 Dilation — θ_w 60.9 θ_L 90 90-03 46.9 	SW1 Pump-In #3 Dilation — θ_w 18.5 θ_L 32.7 90-03 0 	SW1 Pump-In #4 Dilation — θ_w 54.2 θ_L 90 90-03 10.3 
SW1 Pump-In #5 Dilation — θ_w 0 θ_L 0 90-03 0 	SW1 Pump-In #6 Dilation — θ_w 90 θ_L 90 90-03 90 		
SM7 Pump-In #1 Dilation — θ_w 18.7 θ_L 46.3 90-03 0 	SM7 Pump-In #2 Dilation — θ_w 25.1 θ_L 90 90-03 15.2 	SM7 Pump-In #3 Dilation — θ_w 26 θ_L 90 90-03 23.2 	SM7 Pump-In #4 Dilation — θ_w 26.8 θ_L 37.6 90-03 0 
SM7 Pump-In #5 Dilation — θ_w 19.5 θ_L 90 90-03 8.5 	SM7 Pump-In #6 Dilation — θ_w 9.4 θ_L 29.7 90-03 0 		
FJB1 Pump-In #3 Dilation — θ_w 43.9 θ_L 53.9 90-03 0 	FJB1 Pump-In #6 Dilation — θ_w 90 θ_L 90 90-03 90 	FJB1 Pump-In #11 Dilation — θ_w 90 θ_L 90 90-03 90 	FJB1 Pump-In #12 Dilation — θ_w 90 θ_L 90 90-03 90 
FJB1 Pump-In #13 Dilation — θ_w 90 θ_L 90 90-03 90 	FJB1 Pump-In #14 Dilation — θ_w 75 θ_L 90 90-03 61.8 		

Table 4.2. Results of fracture reactivation model predictions for several pump-in tests and hydrofracture stages, based on the stress data in Table 4.1.

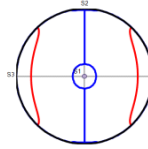
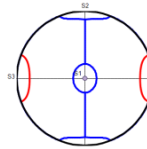
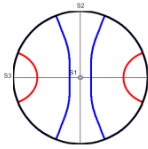
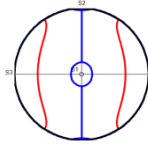
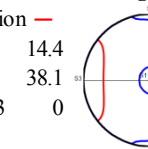
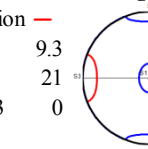
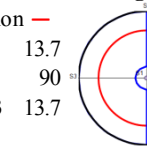
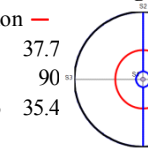
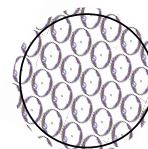
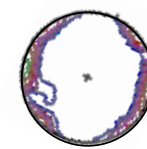
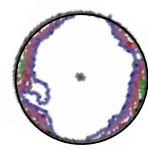
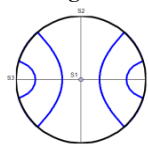
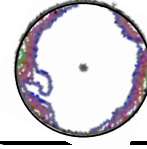
EC1 Pump-In #1 Dilation — θ_w 9.5 θ_L 46.5 90-03 0		EC1 Pump-In #2 Dilation — θ_w 8.1 θ_L 20.3 90-03 0		EC1 Pump-In #7 Dilation — θ_w 17.9 θ_L 21.9 90-03 0		EC1 Pump-In #9 Dilation — θ_w 17.2 θ_L 56.6 90-03 0	
Sh3 HF Stage #1 Dilation — θ_w 14.4 θ_L 38.1 90-03 0		Sh3 HF Stage #2 Dilation — θ_w 9.3 θ_L 21 90-03 0		Sh3 HF Stage #3 Dilation — θ_w 13.7 θ_L 90 90-03 13.7		Sh3 HF Stage #4 Dilation — θ_w 37.7 θ_L 90 90-03 35.4	
ST2 HF Stage #1 Dilation — θ_w 59.2 θ_L 90 90-03 58.5		ST2 HF Stage #2 Dilation — θ_w 57.4 θ_L 90 90-03 51.4		ST2 HF Stage #3 Dilation — θ_w 31.8 θ_L 90 90-03 20.3		ST2 HF Stage #4 Dilation — θ_w 0 θ_L 0 90-03 0	
ST2 HF Stage #4 Dilation — θ_w 90 θ_L 90 90-03 90							

Table 4.2 - continued. Results of fracture reactivation model predictions for several pump-in tests and hydrofracture stages, based on the stress data in Table 4.1.

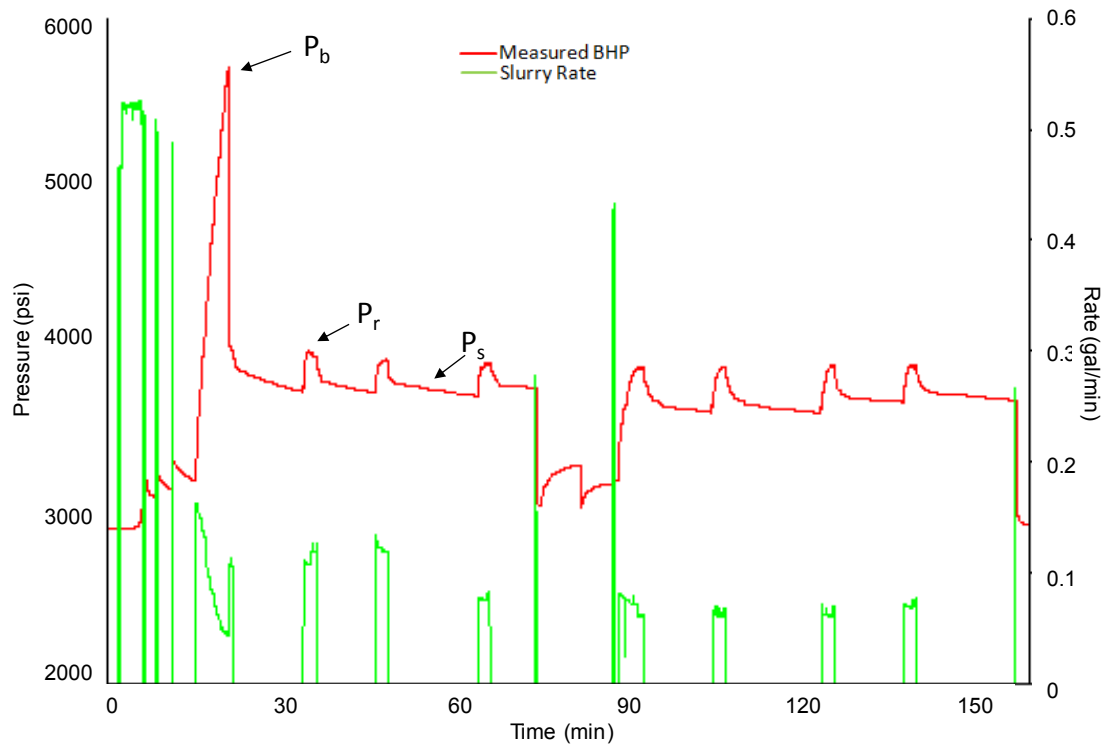


Figure 4.8. Pump-in test for well SW1-MDT2. The breakdown pressure P_b , shut-in pressure P_s , and reactivation pressure P_r are indicated.

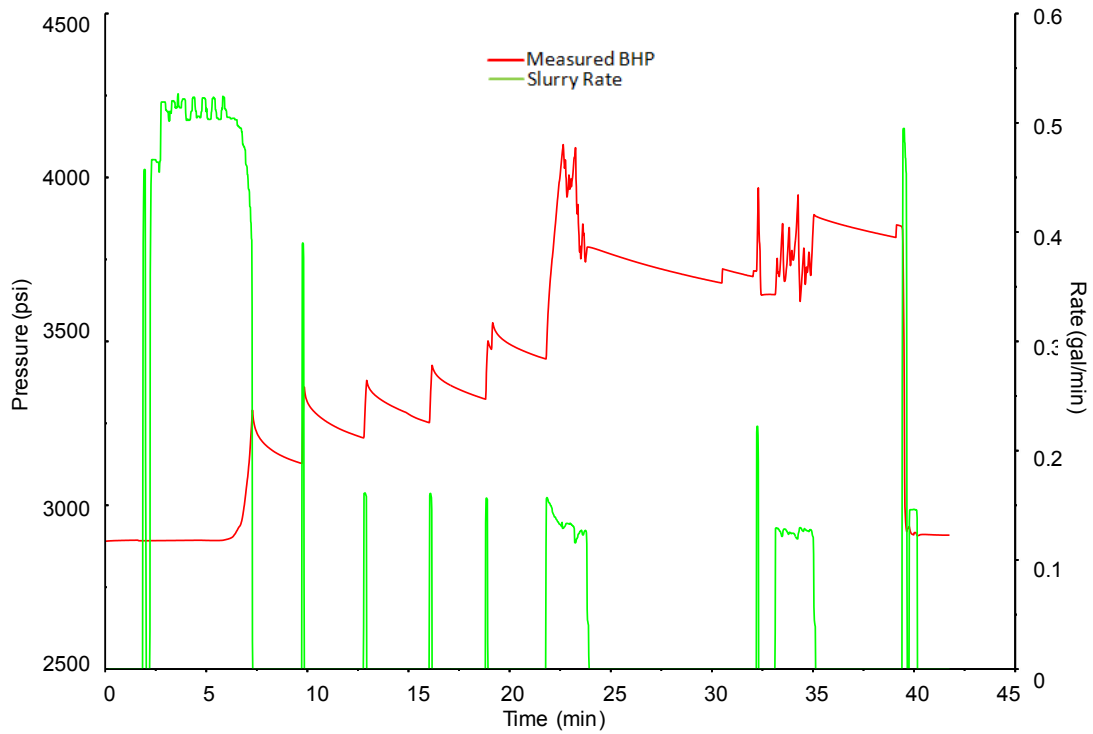


Figure 4.9. Pump-in test for well SW1-MDT3

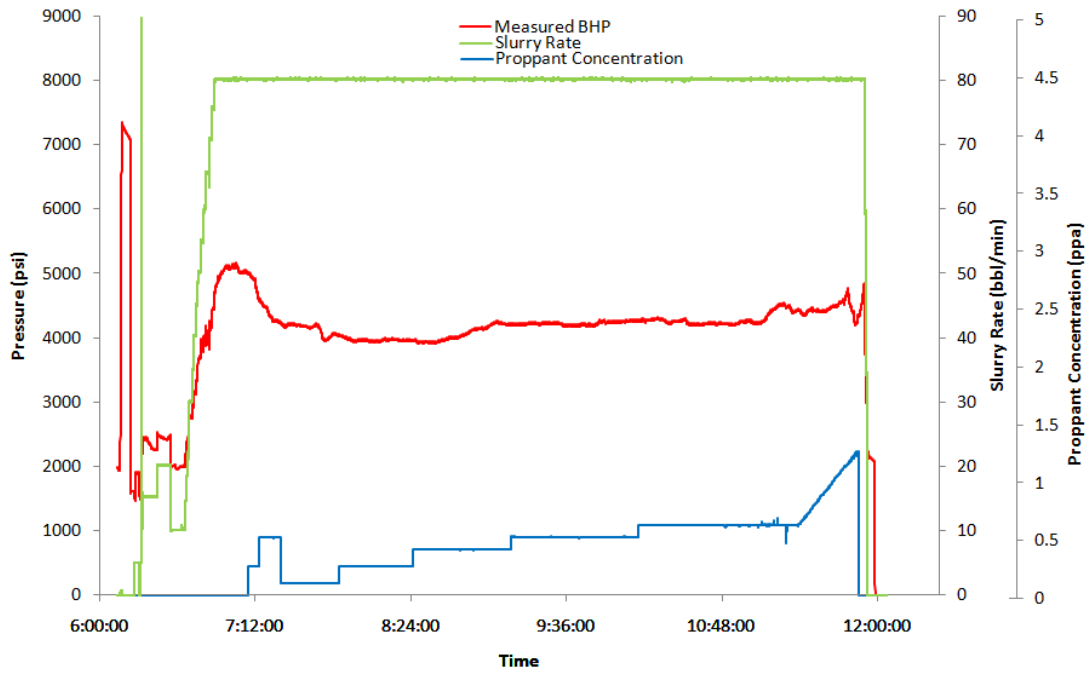


Figure 4.10. Hydrofracture stage 2 for well Sh3

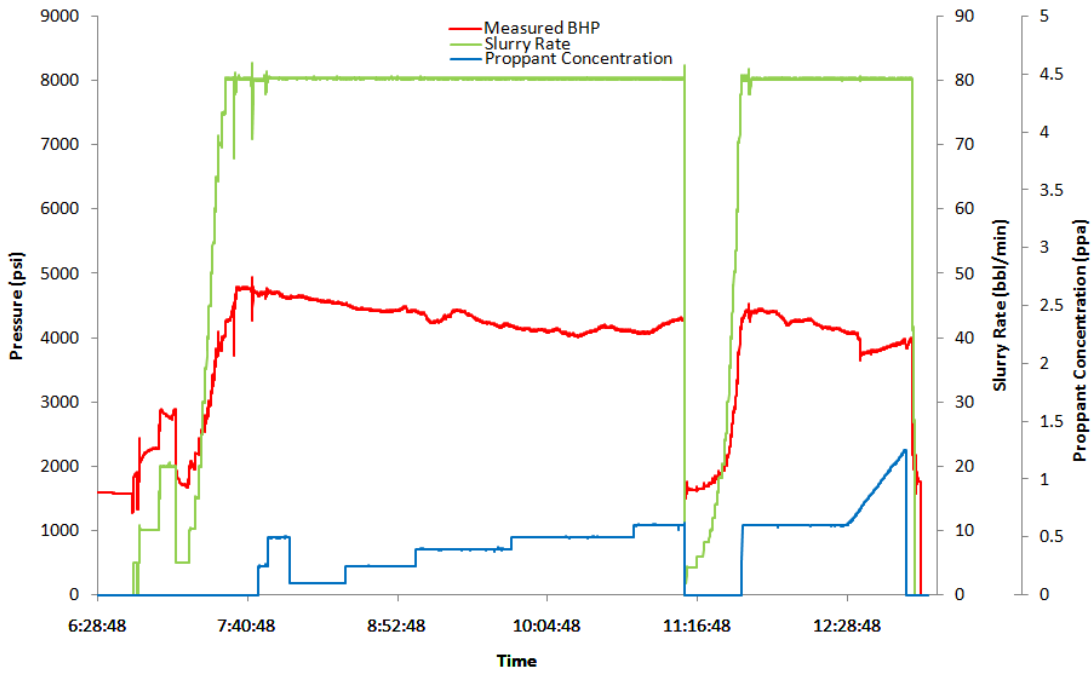


Figure 4.11. Hydrofracture stage 3 for well Sh3

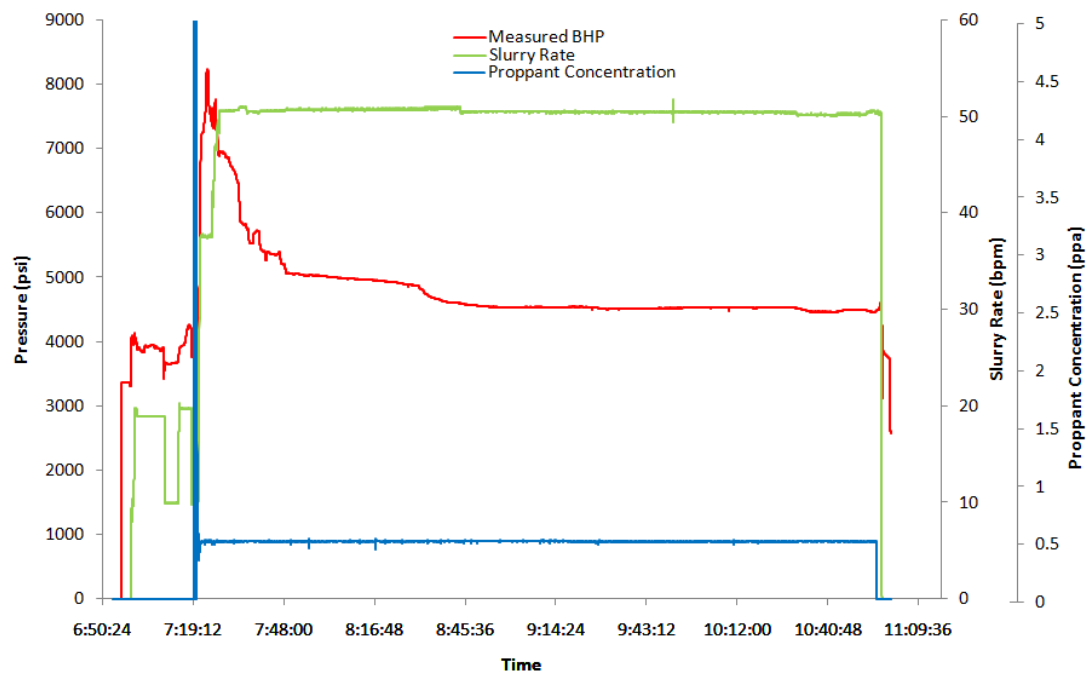


Figure 4.12. Hydrofracture stage 3 for well SW1

Pumping is at an average rate of 45-80 bbl/min and a full stage lasts from 1-4 hours. In order to maintain pressure away from the borehole, the slurry rate is typically held constant while gradually increasing the proppant concentration and there are no intermediate shut-ins. In the absence of reliable and repeated shut-in decline curves, the initial instantaneous shut-in pressure (ISIP) is taken to determine the value of S_{hmin} . For several injections, there is a distinct breakdown pressure event P_b , but the shut-in pressure P_s and reopening pressure P_r typically do not appear. A typical injection stage in the Barnett Shale wells contains a steep pressure rise with a large peak and steep decline if P_b is met, or a medium size peak and gradual decline if failure occurs prior to meeting P_b (i.e., fault or fracture reactivation), followed by a long flattening pressure curve. Though not applied in the wells in this study, recent techniques such as increasing flow rate and adding fibrous proppant to temporarily clog open conduits have been implemented in an attempt to build net pressure.

PRESENT GEOMECHANICAL ANALYSIS

DETERMINATION OF THE STATE OF STRESS

We used log data to determine the stress state for 13 hydrofrac stages in three horizontal wells. From the studied wells: (1) $\sigma_1 \approx S_v$, calculated from overburden at the depth of fluid penetration; (2) $\sigma_2 \approx S_{Hmax}$, from the inversion of borehole sonic data; and (3) $\sigma_3 \approx S_{hmin}$, calculated from instantaneous bottom-hole shut-in pressure from pressure-time curves, where $S_{hmin} = ISIP + 0.433z$, where 0.433 is the constant hydrostatic gradient for fresh water in psi/ft, and z is the depth in feet. We also determined the state of stress in 22 intervals in four vertical wells following the

procedures of Haimson and Cornet (2003) and Zoback et al. (2003). The results are summarized in Table 4.1. The solution for the state of stress around a vertical wellbore is used to determine S_{Hmax} from pump-in test data:

$$S_{Hmax} - P_0 = 3(S_{hmin} - P_0) - (P_r - P_0) \quad [5a]$$

where S_{Hmax} and S_{hmin} are the maximum and minimum horizontal stresses, P_0 is the pore (or borehole) pressure, and P_r is the fracture reopening pressure.

In some intervals, it is possible to solve for the tensile strength using the form:

$$S_{Hmax} - P_0 = T + 3(S_{hmin} - P_0) - (P_b - P_0) \quad [5b]$$

where T is the tensile strength and P_b is the breakdown pressure. From proprietary rock mechanics data, we expect the tensile strength to be at least a few MPa in the shale strata, e.g., 1-3 MPa (145-435 psi), some of the more siliceous intervals may be slightly higher than that, and greater than 10 MPa (1450 psi) in the limestone and dolomite units of the Ellenberger. Intervals where a reasonable value for P_b is not met indicate (a) leakage at the packers, (b) redirection of flow back along the wellbore, or (c) reactivation of a preexisting fracture or faults rather than formation of a new fracture. The value of S_{hmin} is taken as the point of departure from the tangent to the downward portion of the curve for the pressure-drop following the breakdown pressure. For P_b we used the largest peak of the first cycle., which flattens sub-horizontally at the shut-in pressure, P_s . For P_r we used the average pressure value of the small peaks subsequent to P_b . P_0 was approximated by the initial formation pressure - the constant pressure value at the beginning of the tests prior to the first set of leak-offs.

HYDRAULIC FRACTURING IN THE BARNETT SHALE

Shape of the Hydrofracture Network

We begin by looking at the macroscopic geometry of the hydrofracture network, typically revealed by the distribution of microseismic events (see Busetti and Reches, 2007; Daniels et al., 2007). The analytical model described above predicts the fracture orientations that are favorable for reactivation and overall shape of the stimulation volume. The model shows that under high tectonic stresses ($\uparrow\Phi$) reactivation is restricted to a limited range of preferentially oriented fractures ($\downarrow\theta_L$). Thus, stimulation is enhanced in the direction of the far-field S_{Hmax} and is suppressed in the direction of S_{hmin} . The limited range of dips that can be reactivated ensures that the zone of stimulation is vertically centered about the S_v axis. This prediction is further supported by the FE simulated hydrofracture damage patterns for high q/p' stress ratios (Fig. 4.5), where stress heterogeneity in the σ_1 - σ_3 plane produces a damage corridor parallel to the σ_1 axis. Thus, the reactivation calculations and FE models predict that at sites of high differential stress ($S_{Hmax} \gg S_{hmin}$ or $S_v \gg S_{horiz.}$), the shape of the zone of stimulation is a prolate spheroid, elongated in the direction of the far field maximum stress.

We now examine field data. Two examples are shown in Figure 4.13 for the microseismic events locations for hydrofrac stages #1 and #2 in well Sh3. In the horizontal plane, the stimulated volumes are more densely clustered in a direction elongated in the direction of S_{Hmax} , coinciding with the tectonic stress ratios of $\Phi = 0.16$ and 0.20 . For each of the four stages the q/p' ratio is similar (0.51, 0.61, 0.59, 0.65) indicating the difference in the narrower patterns in the S_v - S_{hmin} plane of stages

#1 and #2 versus the wider zone in #3 and #4 (Fig. 4.13) relates to the pressure of the injection. Daniels et al. (2007) associated the poor injection response in stage #2 to a combination of higher stressed rock and having only two of three perforation clusters active during pumping – this interpretation is consistent with the lower R value. Stage #2 was the least pressurized, $R_{\max} = 0.03$, and displays the smallest number of events, mostly contained in the Lower Barnett strata, about 100 feet from the wellbore.

The reactivation solutions for both stages #1 and #2 (upper part of Fig. 4.13) indicate that the injection pressure was insufficient to dilate any fractures in the S_v - S_{hmin} plane ($90-\theta_3 = 0^\circ$), which is reflected by narrow microseismic events clouds. In contrast, for stages #3 and #4, $\Phi = 0.00$ and 0.06 and the microseismic event patterns in the horizontal plane are more diffuse and spherical. In the vertical plane, the patterns are also diffuse – we attribute this to the higher injection pressures. For example, stage #4 was the most pressurized, $R_{\max} = 0.37$, and displays a large number of events that are widely distributed over 500 feet vertically into the Marble Falls and laterally over 1000 feet into the formation. The reactivation solutions for stages #3 and #4 indicate that a wider range of dips could have been reactivated: $90-\theta_3 = \pm 13.7^\circ$ and $\pm 35.4^\circ$, respectively. Considering all of the injection data from Table 4.1, it is likely that for most horizontal lengths of the same well, the driving pressure has a greater influence than the variability of q/p' in stimulating the S_v - S_{hmin} plane. R is still the most important factor for stimulation in the S_{Hmax} - S_{hmin} plane; though because there is typically more variability in Φ than in q/p' in the Barnett Shale wells, stress homogeneity in the S_{Hmax} - S_{hmin} plane is expected to contribute more to a diffuse pattern than homogeneity in the S_v - S_{hmin} plane.

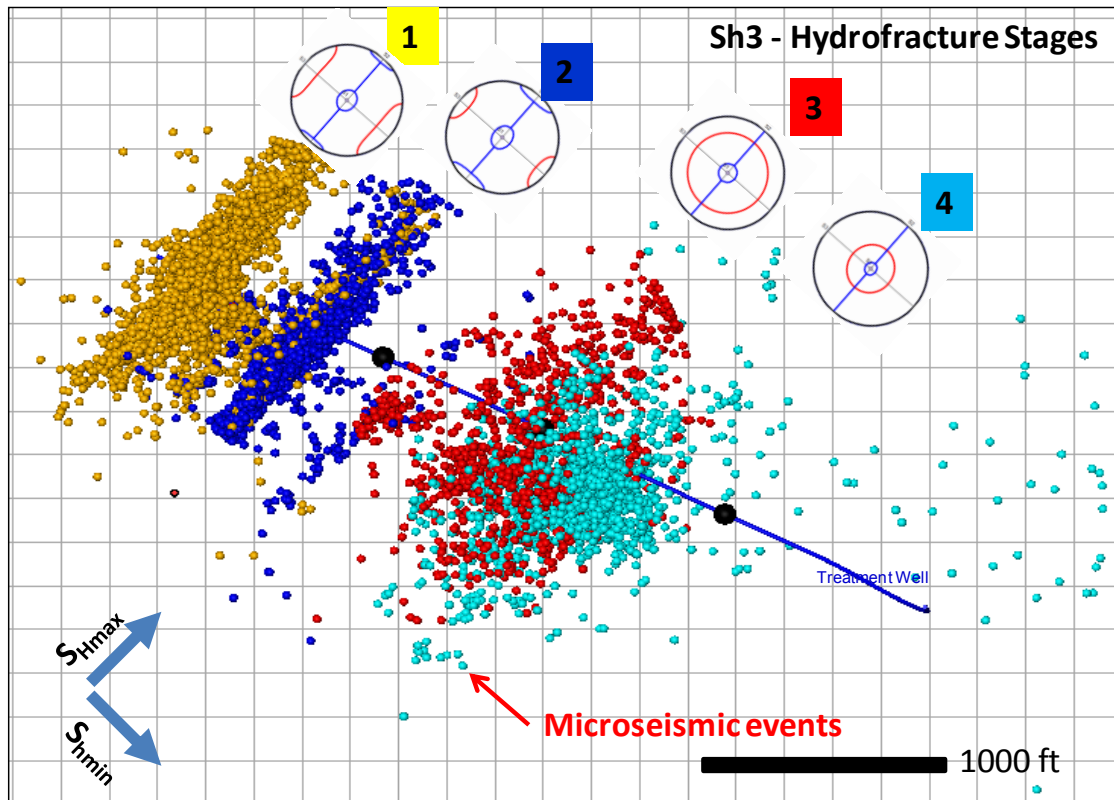


Figure 4.13. Map view of distribution of monitored microseismic events (colored dots) for four hydrofracture stages in a horizontal well (blue line), Barnett Shale (modified from Daniels et al., 2007). The stereonet inserts (rotated to match the near-field stress orientations) show (color zoning of the normal to the predicted dilated fractures), the model predictions of the 3D fracture dilation model for each of the stages. Data and model predictions for each stage are given in Tables 1 and 2. Note that the model predicts that stage 1 and 2 will have restricted zones of stimulation (color-shaded regions) which agrees with narrow, elongated fields of microseismic events of the corresponding color. The model predicts wide strike coverage in stage 3 and wide strike and dip in stage 4, which is demonstrated by the broader microseismic zones.

Hydrofracture Complexity

We developed plots of cumulative damage to display the nature of the induced hydrofracture network (Fig. 4.14 and 4.15). These plots are based on FE simulations and several Barnett Shale wells - comparison indicates the following points. First, simulated cumulative damage and microseismic event counts appear to be analogous. Second, the y-axes in both plots reflect the volume increase in the fracture network. In the FE model (Fig. 4.14), the pressure increase along the initial fracture profile varies linearly with time and is equivalent to a linear fluid volume increase. While direct comparison of the y-values in Figures 4.14 and 4.15 is not possible, a qualitative comparison of the relative position and slopes of the curves can provide insight into the active mechanisms in the field cases.

FE Simulations: Under a moderate differential stress, the FE simulations produced uniform, stable propagation, resulting in long, symmetric damage corridors. In this case, the energy added to the system is incrementally accommodated by small, regularly spaced arrests and ruptures in the direction of the maximum stress. The preferential stress direction constrains the propagation of damage to directly ahead of the pressure front (i.e., a limited θ_L range in the reactivation model), into which the hydrofracture stably extends. This is shown in Figure 4.5c, and was produced for values of $q/p' \approx 0.5$. Under lower differential stress ($q/p' < 0.5$), the simulations created short, irregular fractures (Fig. 4.5d). This case reflects a wide range of θ_L , however, because there is no preferred propagation direction (i.e., a well-defined S_{hmin}), the energy added to the system builds during prolonged arrests (asymmetric damage build-up periods), leading to the development of complex growth in the form of lateral

branches, damage bridges, and linking segments. For states of higher differential stress ($q/p' > 0.5$), although the direction of propagation is strongly constrained (low θ_L), the damage front ahead of the crack-tip intensifies. This creates a heterogeneous zone of weakness into which the fracture unstably extends (Fig. 4.5b).

These processes can be applied to several simulations in the tectonic stress ranges of the Barnett Shale wells. The top-left of Figure 4.14 is equivalent to the lower portion of Figure 4.6 (steepening curves = “hard to fracture”) – the bottom right of Figure 4.14 is equivalent to the upper portion of Figure 4.6 (flattening curves = “easy to fracture”). The stair-steps reflect the cumulative arrest-rupture behavior for the entire layer in each simulation, where vertical periods of increased pressure without damage indicate “build-up” periods and horizontal periods indicate “release” periods. Note that for low values of q/p' (e.g., < 0.2) the behavior is more irregular. Also plotted on Figure 4.14 is the cumulative damage curve for $q/p' = 0.8$ for the pressurization scenario $dp/dx \neq 0$. This case simulates internal pressure loss in the hydrofracture. Note that for the same tectonic conditions (q/p') and the same injection pressure (Net P/q), the damage curve shifts to the left when fluid pressure drops within the fracture. The cumulative damage log for pressure loss more closely matches the case for moderate differential stress ($\sim q/p' = 0.5$) with no pressure loss.

To summarize, the simulations indicate that (a) lower differential stress states shift the cumulative damage curves to the upper-left whereas higher differential stress states are to the lower-right; and (b) internal pressure loss shifts the cumulative damage curves to the left, whereas net pressure build shifts the curves to the right. We interpret that gradual steepening of the curve will occur when fluid is lost into the formation

from the fracture walls (reduced damage) and/or when the zone of stimulation intersects a more uniformly stressed zone (more pressure is required to induce damage). Similarly, gradual flattening of the curve should occur when fluid pressure builds in the fracture network (increased damage) and/or when the zone of stimulation extends into a more tectonically stressed zone, (less pressure is required to induce damage).

Field Analysis: The simulated results in Figure 4.14 can be compared to the field data analysis of Figure 4.15. Daniels et al. (2007) used a proprietary algorithm for the estimated stimulated volume (ESV) to interpret the diffuse microseismic patterns and the net pressure build recorded in stages #3 and #4 of well Sh3 as indicators for propagation of a complex hydrofracture system. ESV vs. microseismic events count for hydrofrac stages in well Sh3 are plotted in Figure 4.15. ESV is an estimate of the volume of rock that was infiltrated and pressurized during the injection. The algorithm weights the density (or magnitude of the moments) of microseismic events within a given cell size and then calculates the volume by drawing boxes around the event clusters (J. Daniels, 2009, personal communication). For all of the hydrofrac stages in Sh3, the flow rate was held constant at 80 bbl/min (e.g., Fig. 4.10-4.12). Thus, the vertical stair-steps in figure 15 reflect periods where fluid penetrates new volumes of rock (expanding ESV boxes) at a greater rate than there is infill of induced shear-slip or propagation seismic events. The horizontal steps indicate small volumetric expansion but a high amount of internal damage. Both are required for effective stimulation.

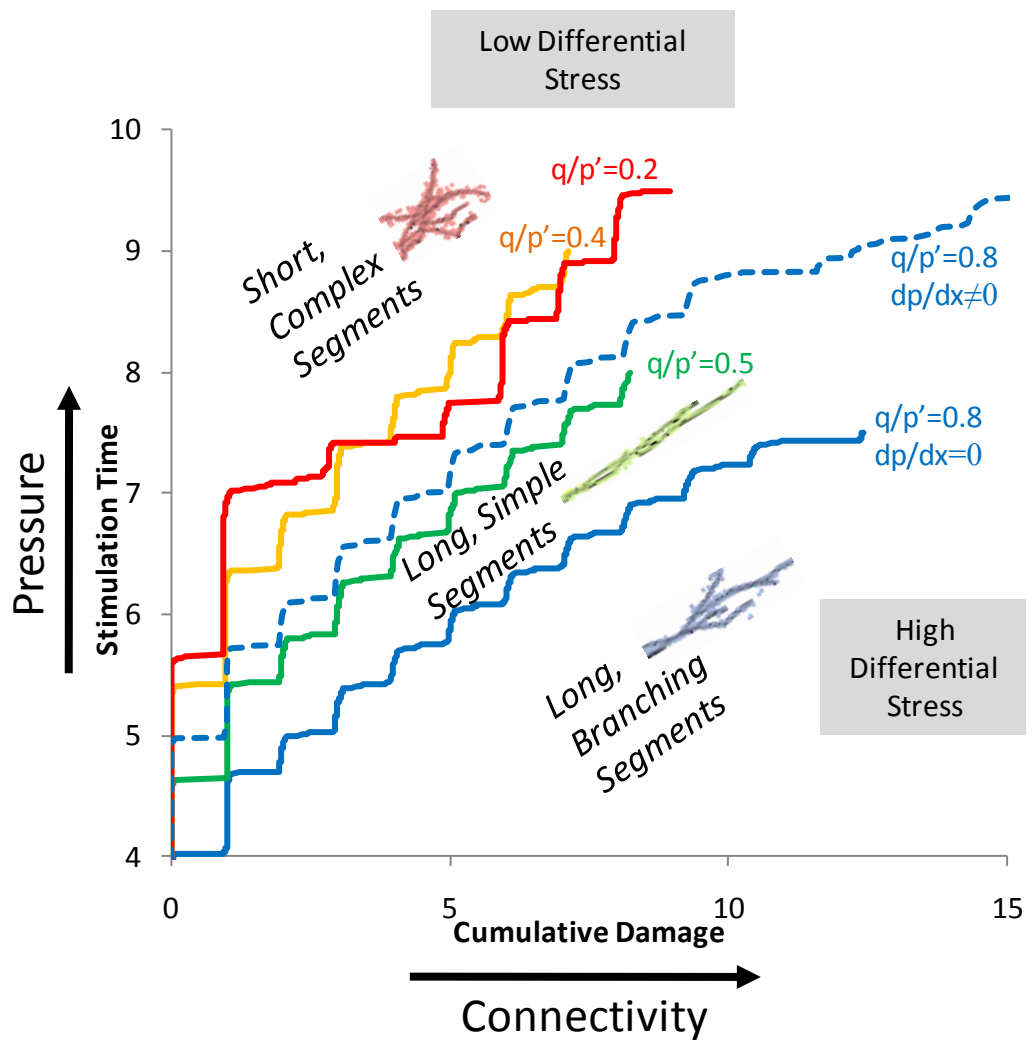


Figure 4.14. Cumulative damage vs. simulation time from FE simulations. Solid lines reflect damage curves for the tectonic stress ratios for the case of uniform pressure distribution. Dashed line is for a case of pressure drop ($dp/dx \neq 0$) in the initial fracture. Stair-steps reflect arrest and rupture periods. The sketched fracture geometries are generalized from the simulated patterns, for example Figure 4.5.

Barnett Shale Hydrofrac Well

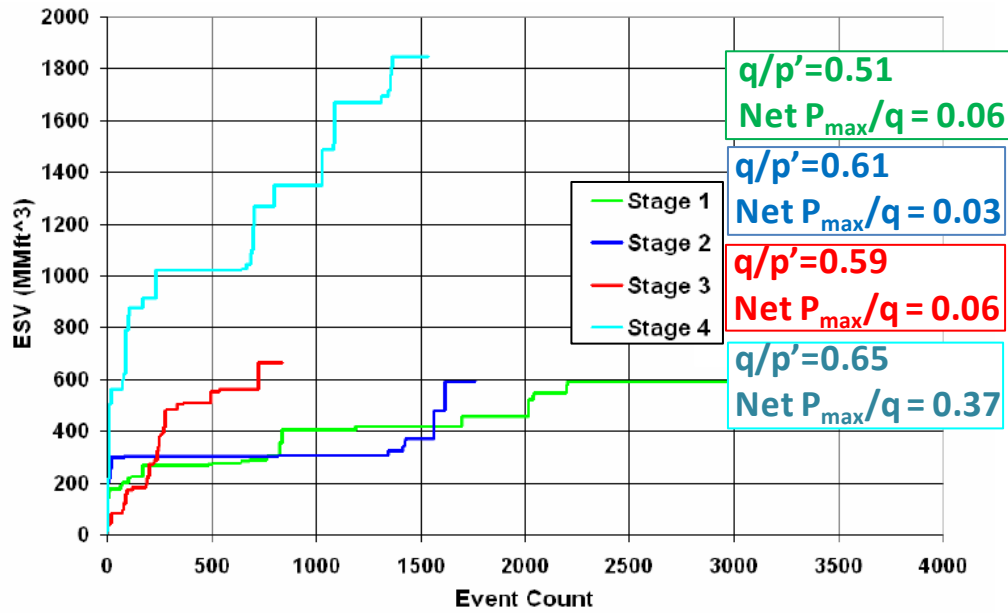


Figure 4.15. Microseismic event count vs. Estimated Stimulation Volume for well Sh3 (modified after Daniels et al. 2007). The four hydrofrac stages are plotted along with the respective stress data (see Table 4.1).

The authors provided a few observations from the ESV logs. (1) Continual growth of ESV versus time indicates a continued growth in fracture dimensions. (2) Large ESV without generating events probably reflects stimulation of an existing fracture network. (3) Net-pressure build is proportional to ESV and is indicative of creating a more complex fracture network. For instance, in a separate well, use of fiber-based diversion resulted in a net-pressure build (~250 psi), a larger stimulation zone, and an increased number of microseismic events.

Synthesis and Interpretation: From field data for well Sh3, the most complex and diffuse hydrofracture stage was #4, followed by #3, in the upper left of Figure 4.15. The least complex were stages #1 and #2 in the lower right. The high pressure achieved in stage #4 distinguishes it from the other stages. Although a large volume of rock was infiltrated, the high pressure and diffuse spherical pattern suggests that the hydrofracture network was not diverted by a preexisting fault or fracture corridor. Similar stress conditions and a similar microseismic pattern for stage #3 suggests that new volume was stimulated with local complexity, but the lower value of R yielded the smaller ESV and event count. The curve for #3 is shifted to the left of #1 and #2 because of the higher Φ value, which is not reflected by the q/p' ratio. Stages #1 and #2 are also similar to one another. Daniels et al. (2007) identified that both stages #3 and #4 recorded a good build in net pressure over the injection period, whereas stages #1 and #2 recorded a negative pressure build. The limited growth of stage #2 is marked by a leftward shift in the curve beginning at the 1500 events mark. That the shift reflects a loss of pressure agrees with the interpretation that the abrupt drop in

events indicates diversion into a local preexisting fracture corridor. It is likely that though both stage #1 and #2 were in more tectonically stressed locations, the higher driving pressure in stage #1 was enough to break into a zone of weakness that was more favorable for propagation and diverted growth distally. With continued pumping, the stimulated volume expanded into the formation and up section, but with little added complexity. In stage #2, continued pumping re-stimulated the smaller volume and increased the local complexity of the network (e.g., upper-left shift), but without expanding it into the reservoir.

Conditions for Fracture Reactivation

We will now describe the solutions for fracture reactivation. First, the stress data for each well (Table 4.1) is substituted into the reactivation model (equations 3a-d) and the results are plotted on stereonets (Table 4.2). Following the conventions in Figure 4.2, the maximum principal stress σ_1 is in the center, σ_2 is at top and bottom, and σ_3 is at left and right. For most intervals, $\sigma_1 \approx S_v$, $\sigma_2 \approx S_{Hmax}$, and $\sigma_3 \approx S_{hmin}$. This is not the case in FJB1 pump-in #3, EC1 pump-in #7, or ST2 hydrofrac stage #4, where $\sigma_1 \approx S_{Hmax}$, $\sigma_2 \approx S_v$, and $\sigma_3 \approx S_{hmin}$. Natural fractures with orientation in the limits marked by the blue line can be reactivated by shear-slip. The Mohr-Coulomb criteria is for a friction angle of 25° and zero cohesion. The red line indicates the limits for dilation. The tensile limit is also set at zero, i.e., open or weak mineralized fractures. The injections in all cases, excluding SW1 hydrofrac stage #4, SW1 pump-in #5, and ST2 hydrofrac stage #4, generated sufficient pressurize to induce shear-slip reactivation on nearly all existing fracture orientations. The effectiveness of the injections to induce dilation varies greatly. For example, in well SM7 pump-in #1, a maximum pressure of

4361 psi was achieved, resulting in a normalized fluid pressure R of 0.10. The solution indicates that fractures with azimuths $\pm 46.3^\circ$ from the direction of $\sigma_2 \approx S_{Hmax}$ and dips $\pm 18.7^\circ$ from the direction of $\sigma_1 \approx S_v$ can be reactivated by dilation. On the other hand, fractures perpendicular to S_{Hmax} or S_v cannot be reactivated by shear-slip. For SM7 pump-in #2, $P_{fmax} = 4752$ psi, giving $R = 0.18$. In this case, all of the azimuths with dips less than $\pm 19.5^\circ$ from $\sigma_1 \approx S_v$ can be reactivated by dilation and only horizontal fractures do not slip in shear. Measured natural fracture data also can be plotted on the stereonet, rotated relative to the orientation of σ_1 for each interval. As an example, we plotted the natural fracture populations from image logs for each interval in well ST2 (bottom of Table 4.2). The dots mark the fracture strike-dip within each interval and the contours reflect the total population for the lateral length. There are two vertical sets oriented north-south (110°) and northwest-southeast (80°). Thus, for hydrofrac stages #1,2,3, and 5 of well ST2 the injection pressure was high enough to induce shear and dilation in all of the fractures orientations observed at the wellbore.

Conditions for Propagation

The in-situ stress data for all the wells are plotted on the cumulative diagram summarizing the results of the FE simulations (Fig. 4.6). The stress data lies on the lower-left corner of the figure for tectonic stress ratio $q/p' = 0.2-0.8$, indicating a weak to moderately stressed normal faulting regime. Consequently, some of the wells lie in the “hard to fracture” range where high injection pressure is required to fracture the rock and deviation along the wellbore or preexisting fracture corridors should be anticipated. In particular, at least 9 of the 14 pump-in tests in well FJB1 record high

fluid pressures sufficient to dilate most natural fracture orientations. However, for the tests, despite repeated fracture attempts in several injection cycles, the breakdown pressure was not reached. Most wells fall in the mid-range indicating that hydrofracture segments grow stably and uniformly with continuous pressurization. The implication is that as the fracture network expands the pressure must be continuously increased to overcome the pressure-drop in the formation unless the path of the injection fluid intersects a more tectonically stressed structural domain.

Reduction of the driving pressure over time relative to the local state of stress (R or Net P/q), would be seen as shrinking dilation limits in the reactivation model or as shifting to the left in the compiled FE diagram (Fig. 4.6). Such reduction leads to the loss of ability to create fracture complexity, to create new fractures, to propagate old fractures, or to reactivate the natural fractures. This gradual reduction is demonstrated in the pressure-time log for well SW1 hydrofrac stage #3 (Fig. 4.12). After the breakdown pressure is achieved, the pressure slowly drops as fluid penetrates into the formation. Note that the slurry rate remains constant while the proppant concentration only slightly increases over the total treatment time. In contrast, it is likely that the increased proppant concentrations in stages #2 and #3 of well Sh3 helped to compensate for the pressure drop within the formation.

We used the reactivation model to recalculate Sh3 hydrofrac stage #1, where the microseismic events extend upward to 1000 feet but the driving pressure is relatively low. Using a tensile strength of 1 MPa (145 psi), the range of azimuths and dips that can dilate *and* induce new fracture becomes $\theta_L = \pm 18.5^\circ$ and $\theta_w = \pm 7.3^\circ$. If T for the rock is $> 2\text{MPa}$ (290 psi), new fracturing could not occur in fractures of any

orientation. Propagation of the initially injected fractures would occur at a lower strength value, but this still reduces the range of orientations to a fraction of that calculated for dilation. This indicates that the majority of the microseismic events for Sh3 stage #1, especially those distant from the wellbore where a significant pressure-drop can be expected, are produced by shear-slip on preexisting fractures rather than dilation and propagation. Similar conclusions can be drawn for other marginally pressurized hydrofrac stages in the other wells.

Comparison with Pressure-Time Logs

We conclude with a closer examination of the pressure-time logs for two pump-in tests and two hydrofracture stages. Test intervals #2 and #3 from well SW1 are shown in Figures 4.8 and 4.9, hydrofracture stages #2 and 3 from Sh3 are in Figures 4.10 and 4.11 . Pressure-time logs for interval #2 of SW1 and hydrofracture stage #3 of Sh3 indicate that the breakdown pressure of the rock was achieved, resulting in new fracture propagation. The curve displays a clear breakdown pressure followed by a large pressure drop, representing the tensile strength of the rock plus the difference between the reopening and shut-in pressure ($P_r - P_s$). The slope immediately following the break down pressure is initially very steep and then gradually shallows as fluid infiltrates into the new fracture (Haimson and Cornet, 2003) and levels out at the shut-in pressure. Inspection of the pattern of the dilation and shear limits as well as the pressure-time curves for the pump-in tests with all of the hydrofrac stages suggests that new fracture propagation was achieved in hydrofrac stages 1, 2, 3, and 4 in well SW1, stages 1, 2, and 3 in well ST2, and stages 3 and 4 in well Sh3.

Conversely, the injection pressure in pump-in intervals #3 of well SW1 and hydrofracture stage #2 of well Sh3 dropped prior to the tensile failure limit. The initial peak is very weak and probably does not indicate the true break down pressure but rather reactivation of mineralized fractures, i.e., the fracture strength lower than the tensile strength of intact rock, or limited pressure build-up prior to reactivation of non-preferentially oriented natural fractures. The peaks from subsequent pumping cycles in SW1 interval #3 and attempted pressure build-ups in Sh3 stage #2 reflect the fracture reopening pressure and are not distinct from the initial pressure-drop event. This suggests that the fluid initially diverted into one or more preexisting zones of weakness that reactivated during each pumping cycle. Similar dilation and slip patterns are observed in stage 4 of well SW1 and stage 1 of well Sh3, suggesting that these hydrofrac stages primarily diverted fluid into the preexisting network and did not achieve pressures sufficient to propagate new hydrofractures. As discussed above, injection pressures below the failure limits of the rock does not mean that pressurized fluid is not penetrating through the formation. Sub-critical pressures may still induce shear-slip, dilation, and propagation through damaged rock (for example, where the current strength is less than the intact tensile strength).

SUMMARY

We used an analytical model for the conditions of fracture reactivation and a FE model simulating damage propagation to understand how the state of stress and the injection pressure affects hydrofracturing in the Barnett Shale. We applied several field techniques to discern the conditions for reactivation by shear-slip, dilation, and

for propagation, as well as to understand the complexity of the induced hydrofracture network. The main results are summarized below.

(1) Complex hydrofracturing in the Barnett Shale is best explained by transient propagation of damage and fractures and is characterized by (a) multiple interacting zones of damage in which fracture segments of varying length and pattern propagate, and (b) complex dynamical behavior, e.g., damage build-up periods, complex rupture, and segmentation. These features are effectively modeled using the elastic-plastic-damage rheology and an explicit/dynamic FE technique. The same results could not be attained by omitting damage or modeling growth quasi-statically.

(2) The shape of the hydrofracture network is determined by the local state of stress and the injection pressure. The higher the differential stress, the more elongated the stimulation volume in the direction of the maximum stresses, S_v and S_{Hmax} . For a low fluid pressure (R or $Net\ P/q \sim 0$), the stimulation volume remains fixed about the S_v - S_{Hmax} plane unless it diverts into a preexisting zone of weakness. For Barnett Shale wells in regions of higher differential stress, pressure sufficient to activate fractures perpendicular to the σ_1 - σ_2 plane ($90-\theta_3 > 0$) are required to create a spherical stimulation volume. A more uniform stress field easily produces a spherical shape, but pressure $> S_{Hmax}$ is required to expand the volume far into the reservoir.

(3) Stimulation follows a sequential path, based on increasing the normalized pressure (R or $Net\ P/q$): fluid penetration \rightarrow reactivation of preferred orientations under shear-slip \rightarrow reactivation of preferred orientations by dilation \rightarrow propagation of weak fractures of preferred orientations \rightarrow creation of new fractures from fresh host rock. In many of the pressure-time logs from the Barnett Shale wells, we were able to

distinguish the larger breakdown pressure from smaller fracture reopening pressure. Moderately sized peaks that do not match the expected tensile strength of the rocks (a few hundred psi for the shale layers versus over 1000 psi for the carbonates) likely reflect reactivation of non-preferentially oriented fracture corridors.

(4) Shear-slip microseismic events require much less fluid pressure than is needed to dilate and propagate old fractures or to create new ones. While slip events are an indicator of the overall dimensions of fluid penetration, which may be quite large, they are not a reliable indicator of network complexity. Instead, we recommend comparing the stress conditions and pressure-time logs with the two models described here. We worked through several examples, the most thorough being for the hydrofracture stages of well Sh3, and found a good match between the model solutions and the field data. The models show that injection into regions of low differential stress is more likely to produce short, complex hydrofracture segments with high connectivity, but high fluid pressure is required. Regions with high local differential stress are favorable for long branching hydrofracture segments and because fracturing is easy, there is a greater risk of diverting the network into a preexisting zone of weakness. Most of the Barnett Shale wells in this study fall somewhere in the middle, in moderately to weakly stressed regions, and are highly dependent on sustaining the driving pressure needed to create volume and develop complexity. This pressure is not an absolute value, but must be determined relative to the local stress conditions, which differ along the wellbore and at a distance into the reservoir.

REFERENCES

- Baer, G., and Reches, Z., 1991, Mechanics of emplacement and tectonic implications of the Ramon dike systems, Israel. *Journal of Geophysical Research*, v. 96, no. B7, p. 11,895-11,910.
- Baruch, E., 2009, Seismic sequence stratigraphy of the Barnett Shale, southwestern part of Fort Worth Basin, Texas. Master's thesis, University of Oklahoma, Norman, Oklahoma, 76 p.
- Browning, D., 2006, Investigating correlations between microseismic event data, seismic curvature, velocity anisotropy, and well production in the Barnett Shale, Fort Worth Basin, Texas. Master's thesis, University of Oklahoma, Norman, Oklahoma, 105 p.
- Buseti, S. and Reches, Z., 2007. Formation of network fractures during hydraulic fracturing of the Barnett Shale, a tight gas shale with preexisting fractures. *Eos Trans. AGU*, 88(52), Fall Meet. Suppl., Abstract T42C-04.
- Daniels, J., DeLay, K., Waters, G., LeCalvez, J., Lassek, J., and Bentley, D., 2007, Contacting more of the Barnett Shale through an integration of real-time microseismic monitoring, petrophysics and hydraulic fracture design. *Society of Petroleum Engineers 110562*, presented at the SPE ATCE, Anaheim, Oct. 12-14, 2007.
- Delaney, P.T., Pollard, D.D., Zioney, J.I., and McKee, E.H., 1986, Field relations between dikes and joints: Emplacement processes and paleostress analysis. *Journal of Geophysical Research*, v. 91, p. 4920-4938.
- Elebiju, O., Keller, G.R., and Marfurt, K.J., 2008, New structural mapping of basement features in the Fort Worth basin, Texas, using high-resolution aeromagnetic derivatives and Euler depth estimates. *Earth Scientist*, The University of Oklahoma, p. 46-48.
- Fisher, M.K., Wright, C.A., Davidson, B.M., Goodwin, A.K., Fielder, E.O., Buckler, W.S., and Steinsberger, N.P., 2005. Integrating fracture-mapping technologies to improve stimulations in the Barnett Shale. *Society of Petroleum Engineers Production and Facilities 77441*, p. 85-93.
- Gale, J.F.W., Reed, R.M., and Holder, J., 2007, Natural fractures in the Barnett Shale and their importance for hydraulic fracture treatments. *American Association of Petroleum Geologists Bulletin*, v. 91, No.4, p. 603-622.

- Haimson, B.C. and Cornet, F.H., 2003, ISRM Suggested methods for rock stress estimation – Part 3: hydraulic fracturing (HF) and/or hydraulic testing of pre-existing fractures (HTPF). *International Journal of Rock Mechanics and Mining Sciences*, v. 40, p. 1011-1020.
- Hardage, B.A., Carr, D.L., Lancaster, D.E., Simmons, J.L., Elphick, R.Y., Pendleton, V.M., and Johns, R.A., 1996, 3-D seismic evidence of the effects of carbonate karst collapse on overlying clastic stratigraphy and reservoir compartmentalization. *Geophysics*, v. 61, no. 5, p. 1336-1350.
- Ishida, T., Chen, Q., Yoshiaki, M., and Roegiers, J.C., 2004. Influence of viscosity on the hydraulic fracturing mechanism. *Journal of Energy Resources Technology*, v. 126, p. 190-200.
- Jaeger, J.C. and Cook, N.G.W., 1979, *Fundamentals of Rock Mechanics*, Chapman and Hall, London, 593 p.
- Jolly, R.J.H. and Sanderson, D.J., 1997, A Mohr circle construction for the opening of pre-existing fracture. *Journal of Structural Geology*, v. 19, no. 6, p. 887-892.
- Loucks, R.G., 1999, Paleocave carbonate reservoirs: origins, burial-depth modifications, spatial complexity, and reservoir implications. *American Association of Petroleum Geologists Bulletin*, v. 83, p. 1795-1834.
- Mayerhofer, M.J., Lolon, E.P., and Youngblood, J.E., Heinze, J.R., 2006, Integration of microseismic fracture mapping results with numerical fracture network production modeling in the Barnett Shale. Society of Petroleum Engineers 102103, presented at the SPE ATCE, San Antonio, Sept. 24-27, 2006.
- McDonnell, A., Loucks, R.G., and Dooley, T., 2007, Quantifying the origin and geometry of circular sag structures in northern Fort Worth Basin, Texas: paleocave collapse, pull-apart fault systems, or hydrothermal alteration? *American Association of Petroleum Geologists Bulletin*, v. 91, no. 9, p. 1295-1318.
- McKeagney, C.J., Boulter, C.A., Jolly, R.J.H., and Foster, R.P., 2004, 3-D Mohr circle analysis of vein opening, Indarama lode-gold deposit, Zimbabwe: implications for exploration., *Journal of Structural Geology*, v. 26, p. 1275-1291.
- Montgomery, S.L., Jarvie, D.M., Bowker, K.A., and Pollastro, R.M., 2005, *Mississippian Barnett Shale, Fort Worth Basin, north-central Texas: Gas-shale play*

- with multi-trillion cubic foot potential. American Association of Petroleum Geologists Bulletin, v. 89, no. 2, p. 155-175.
- Pollastro, R.M., Jarvie, D.M., Hill, R.J., and Adams, C.W., 2007, Geologic framework of the Mississippian Barnett Shale, Barnett-Paleozoic total petroleum system, Bend arch-Fort Worth Basin, Texas. American Association of Petroleum Geologists Bulletin, v. 91, no. 4, p. 405-436.
- Reches, Z., 1998, Tensile fracturing of stiff rock layers under triaxial compressive stress states. International Journal of Rock Mechanics and Mining Science, v. 35, no. 70, p. 4-7.
- Roth, M. and Thompson, A., 2009, Fracture interpretation in the Barnett Shale, using macro and microseismic data. First Break EAGE, v. 27, no. 4, 7 p.
- Simon, Y., 2005, Stress and fracture characterization in a shale reservoir, North Texas, using correlation between new seismic attributes and well data. Master's thesis, University of Oklahoma, Norman, Oklahoma, 84 p.
- Singh, P., 2008, Lithofacies and sequence stratigraphic framework of the Barnett Shale, Northeast Texas. Doctoral dissertation, University of Oklahoma, Norman, Oklahoma, 181 p.
- Walper, J.L., 1982, Plate tectonic evolution of the Fort Worth basin, in Martin, C.A., ed., Petroleum geology of the Fort Worth basin and Bend arch area. Dallas Geological Society, p. 237-251.
- Zoback, M.D., Barton, C.A., Brudy, M., Castillo, D.A., Finkbeiner, T., Grollimund, B.R., Moos, D.B., Peska, P., Ward, C.D., and Wiprut, D.J., 2003, Determination of stress orientation and magnitude in deep wells. International Journal of Rock Mechanics and Mining Sciences, v. 40, p. 1049-1076.

CHAPTER V

ZONES OF HIGH FRACTURE DENSITY IN LAYERED ROCKS

Chapter V covers a series of field investigations of sites with high fracture density (HFD) in layered rocks. We address that the growth mechanisms of tensile fractures within the pressure-shadow of neighboring fractures should be examined as a function of rock properties, layer and fracture dimensions, and properties of neighboring layers.

The field work was conducted in shallow marine carbonates of the Carmel Formation, Utah, and layered deepwater sandstones and shales of the Jackfork Group in Oklahoma and Arkansas. The Utah site is near Cedar Mountain, on the eastern margin of the San Raphael Swell, an asymmetric anticline associated with Laramide uplift. Here, limestone layers display extreme fracture density (Reches, 1998) in a gently deformed area. The Jackfork Group outcrops are located in the Ouachita Mountains, a clastic-dominated fold-thrust system in southeastern Oklahoma and southern Arkansas. The Pennsylvanian Jackfork Group serves as a significant natural gas reservoir (Montgomery, 1996). The Jackfork Group outcrops are well-established reservoir analogs (Slatt et al., 2000; Buseti, 2003). The exposures at two sandstone quarries offer excellent 3D exposure to the fractured layers, many of which display zoned HFD.

BACKGROUND

Zones of HFD can enhance or destroy porosity and permeability in hydrocarbon reservoirs, depending on the timing and conditions for fracturing (Hanks et al, 1997, 2004; Yose, 2001). Fracture clusters, including fault related fracture corridors

(Ozkaya et al., 2003) and deformation bands (Tindall 2003, 2006) increase the anisotropic permeability, and could lead to compartmentalization (Tindall, 2003). Fracture corridors could redirect fluid flow depending on their orientation and properties, to the benefit or detriment of the stimulation.

Factors Affecting Fracture Density

Role of Mechanical Stratigraphy

The presence of fractures is strongly controlled by the mechanical stratigraphy, specifically layer thickness, interaction between layers, and alternating lithologies (Fig. 5.1). A mechanical layer is assumed to behave uniformly, and typically is cut by particular fracture sets (Pollard and Segall, 1987). Many fractures terminate at the contacts between mechanical layers (Hodgson, 1961), reflecting a contrast in the properties between the layers (e.g., Underwood et al., 2003; Shackleton et al., 2005) or interlayer slip (e.g., Ji et al., 1998; Sagy and Reches, 2006). Layers can be delaminated when the shear stress along the contact exceeds its shear strength (Kelly and Tyson, 1965; Sagy and Reches, 2006). Fractures often terminate at the transition from a brittle layer into a ductile layer, which is less likely to fracture (Hobbs, 1967; Narr and Suppe, 1991; Rijken and Cook, 2001).

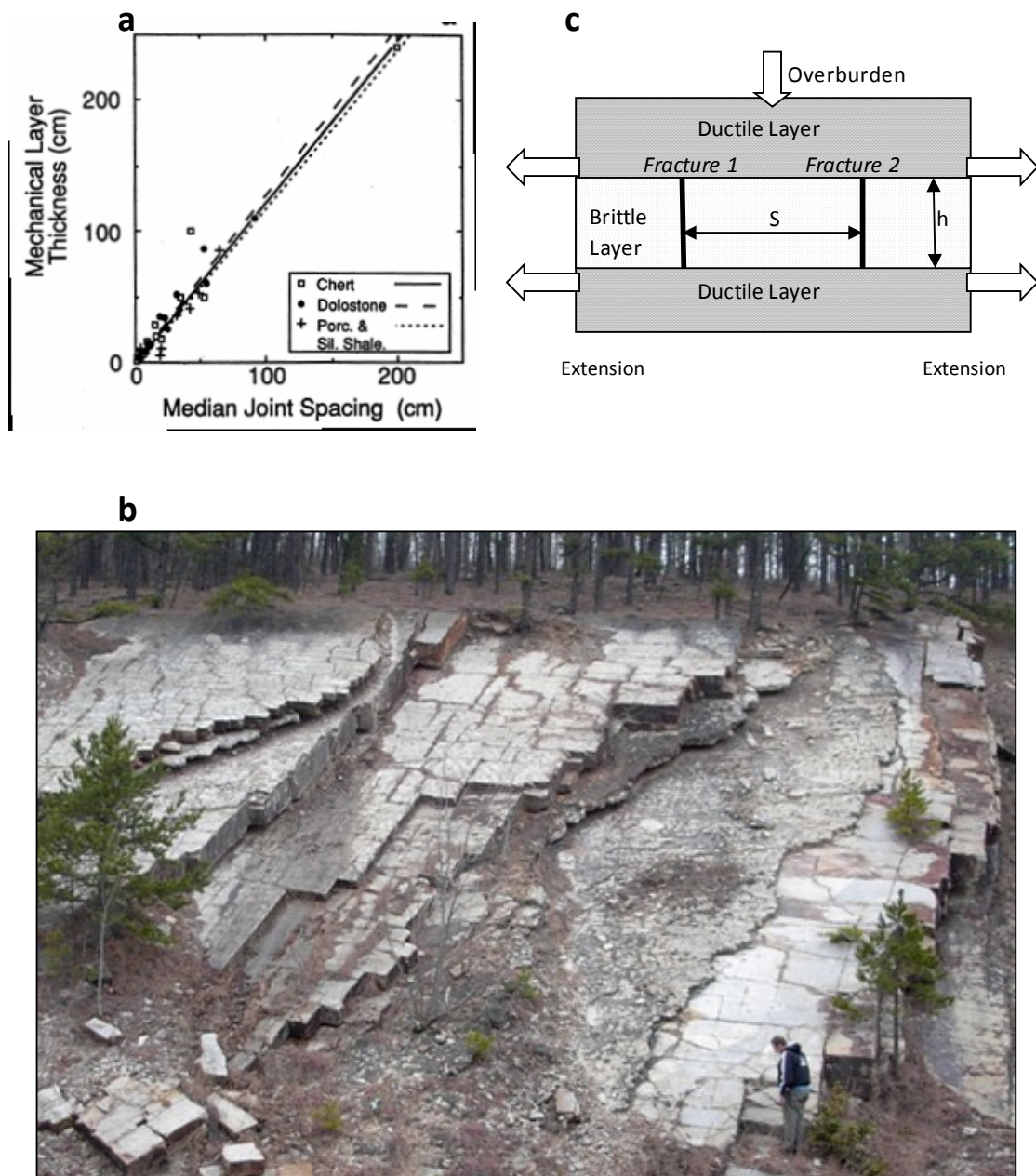


Figure 5.1. Relations between fracture spacing and layer thickness. (a) Fractures in three lithologies; note that spacing \approx thickness (Narr and Suppe, 1991). (b) Fractured sandstone layers of the Jackfork Group, Oklahoma; note “cubic” blocks that indicate spacing \approx thickness. (c) A two-dimensional section of a fractured brittle layer between two ductile layers; h - thickness of the brittle layer; S - spacing between fractures; arrows indicating remote extension.

Petrophysical/Rheologic Controls

Fracture density in layered rocks is also determined by the mechanical properties of the rock. Petrophysical properties that strengthen and embrittle rock layers are likely to increase the tendency to fracture (Nelson, 1985). These properties include brittle mineralogy, low porosity, fine grain size, thin mechanical layers, high competence, high strength, and homogeneous rock fabric (Laubach, 2003; Ehrenberg et al., 2006; Fredrick et al, 1993; Olsen, 2004). These properties are not mutually exclusive. For example, Katz et al. (2000) used the Schmidt Hammer to find that the rebound values correlate well with the Young's Modulus, porosity and uniaxial strength. Eberli et al. (2003) found that the sonic velocity in limestones is highest in low porosity rocks with rigid frame cementation (Fig. 5.2) (Eberli et al., 2003). Fracture density in a layered carbonate sequence systematically decreased as a function of mud and grain content (Di Naccio et al, 2005). We made similar observations in a layered sandstone sequence (see Jackfork content below).

Fracture Density in Rock Layers

Definitions for Fracture Density

Fracture density in a set is the inverse of fracture spacing, S , the fracture-normal distance between neighboring fractures in a given set (Fig. 5.1c). Density is frequently normalized by the layer thickness h . Ladeira and Price (1981) introduced the term $K = S/h$, and Gross (1993) used 'Fracture Spacing Ratio' $FSR = h/S$, where S is the mean (or median) spacing in the layer. Here D denotes the fracture density, where $D = S/h = 1/K = FSR$. The D parameter is a useful measure of the density because (1) the spacing of fractures in layered rocks is often linearly proportional to h (Fig. 5.3) (Narr

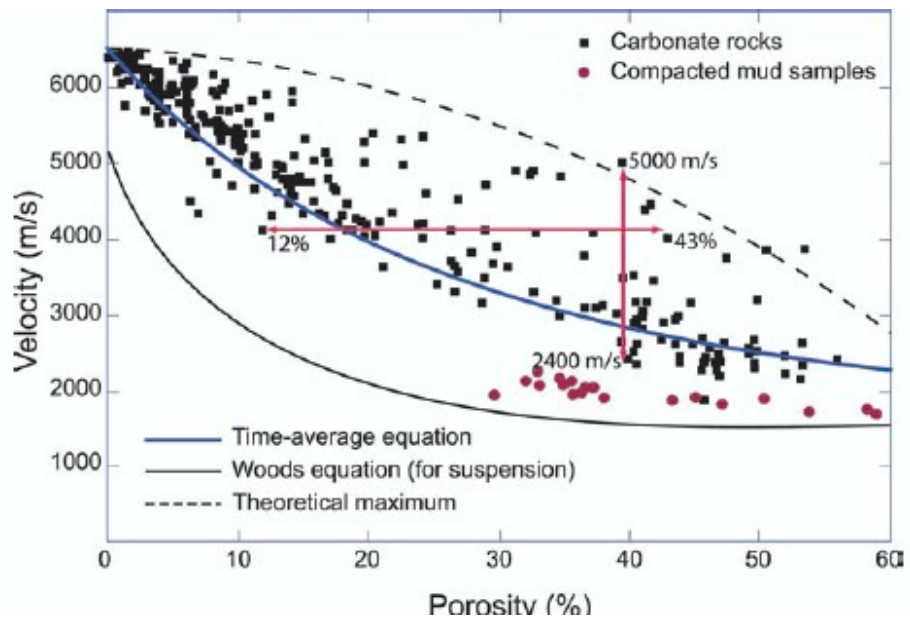


Figure 5.2. The relationships between V_p and porosity for two rock types. The velocity serves as a proxy for brittleness or rock strength (Eberli, et al, 2003).

and Suppe, 1991; Gross, 1993; Engelder et al., 1997; Ji et al., 1998); (2) most fracturing models for layered rocks predict linear relations between fracture spacing and layer thickness (Hobbs, 1967; Gross, 1993; Bai et al, 2000; Sagy and Reches, 2006).

Fracture Saturation

Brittle layers are first to fail by tensile fracturing in a brittle and ductile sequence subjected to extension. Upon failure, the tensile stresses near a newly formed fracture are relaxed forming a stress shadow within which the stresses are below the rock strength (e.g. Gross et al., 1995; Renshaw, 1997). Continuous extension builds up stress at a distance from the first fractures, and amplifies by transfer of extension from the ductile layers above and below the brittle one. New fractures continue to nucleate and propagate, infilling the rock mass and increasing the fracture density until the critical saturation stage where new fractures cease to form (Hobbs, 1967; Wu and Pollard, 1995). The various mechanical models of fracture saturation (Hobbs, 1967; Gross, 1993; Olson, 1993; Ji et al., 1998, Bai and Pollard, 2000; Germanovich and Dyskin, 2000) predict, in spite of their different assumptions, that $1.0 < D < 3.0$ (Sagy and Reches, 2006). This prediction is in general agreement with observations in many field areas where D is about 1 (Fig. 5.1b, 5.3a) (Narr and Suppe, 1991; Gross, 1993; Engelder et al., 1997; Ji et al., 1998; Busetti, 2003; Bai et al., 2000).

High-Fracture Density (HFD)

A comprehensive compilation of fracture density observations however, reveals a more complicated picture. Figure 5.3a displays D values from 0.1 to 35, well below and above $D=1.0-3.0$ predicted in the models. Three classes of fracture density can be

recognized (Fig. 5.3a,b): the unsaturated class with $D < 1.0$, saturated class with $D=1.0 - 3.0$, and supersaturated class with $D > 3.0$. A fourth class, the cluster class (Sagy et al., 2001; or swarm in Putot et al., 2001; or joint-zone in Rogers and Engelder, 2004) is displayed in Fig. 5.3b; this class has irregular intensity with local density of $D > 3.0$ and mean density of $D < 3.0$.

The common fracture models effectively explain unsaturated and saturated classes for fracture density (Bai and Pollard, 2000). Alternative mechanisms are required to explain the supersaturated class and the cluster class (Fig. 5.3b). The field studies below focus on the occurrence and development of these two classes, to which are henceforth referred to as zones of high-fracture-density (HFD) where $D > 3.0$. More specifically, the field work concentrates on three identified HFD groups, based on their distributions and described in the next section: (1) sets of subparallel and quasi-uniform HFD spacing; (2) clusters of local HFD within sets of typical density; and (3) multiple fractures with branches or splays that form 2D or 3D tree-like structures.

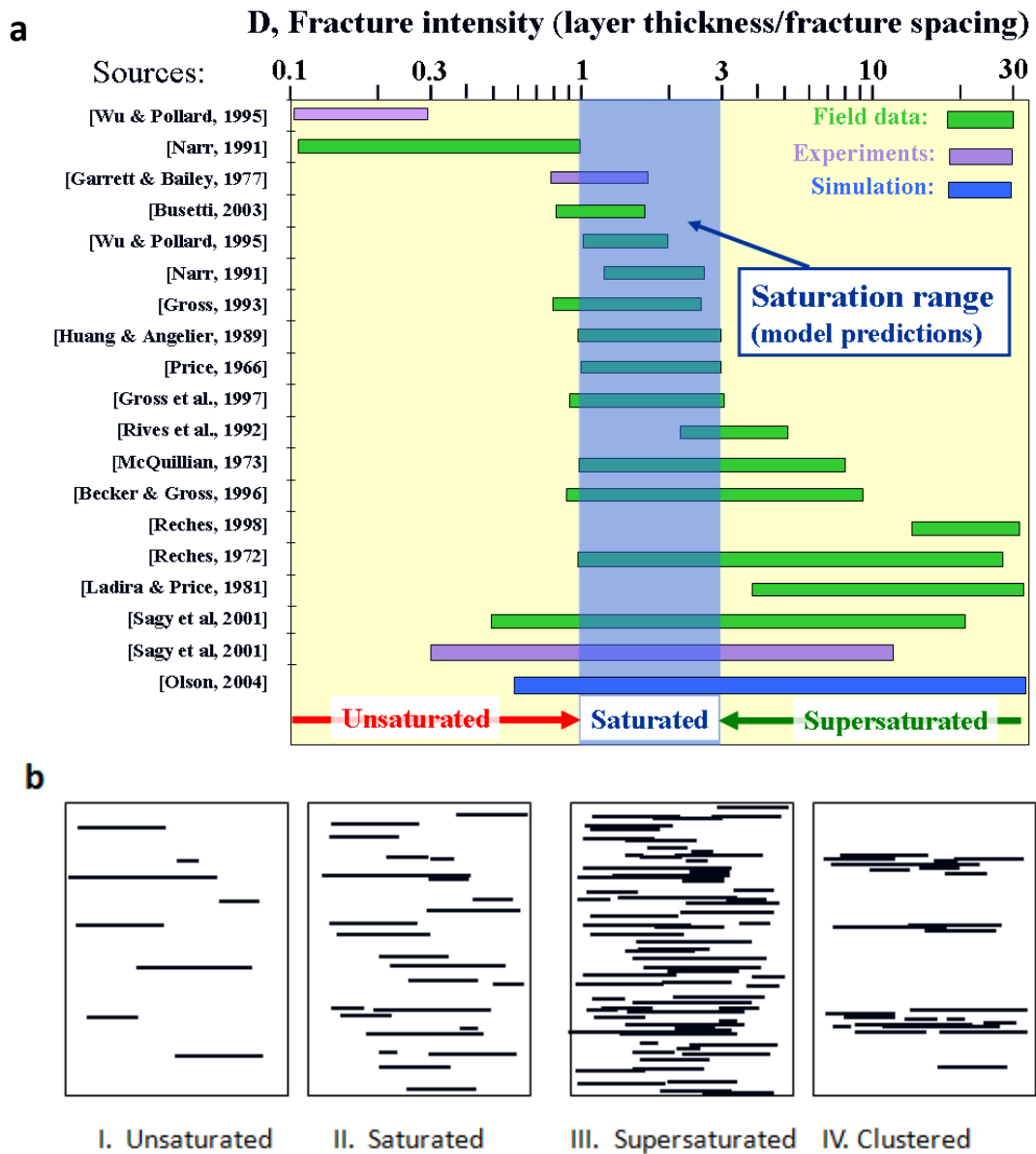


Figure 5.3. (a) Measured joint and fracture intensity in field and experiments. Dotted zone at $1.0 < D < 3.0$ is the range of intensities predicted by the models (see text). Studies are divided into three groups, with $D < 3$ for the undersaturated group, $1 < D < 3$ for the saturated group, and $D > 3$ for supersaturated cases (see text). [Data sources: 1. Wu and Pollard (1995); 2. Narr and Suppe (1991); 3. Garrett and Bailey (1977); 4. Ji et al. (1998); 5. Engelder et al. (1997); 6. Gross et al. (1995); 7. Wu and Pollard (1995); 8. Narr and Suppe (1991); 9. Gross (1993); 10. Huang and Angelier (1989); 11. Price (1966); 12. McQuillan (1973); 13. Becker and Gross (1996); 14. Reches (1998); 15. Reches (1972); 16. Ladeira and Price (1981); 17–18. Sagy et al. (2001)]. (b) A scheme of the unsaturated (I), saturated (II), supersaturated (III), and clustered (IV) classes. Modified after Sagy and Reches (2005).

Fracture Spacing Distributions

Several methods were presented to distinguish fracture spacing distributions and were applied to the Cedar Mountain and Jackfork sites. A general comparison of the classes is shown in the 1D spacing logs and histograms in Figures 5.4-5.8. Fractures with quasi-uniform spacing show a normal distribution, whereas clustered fractures suggest a Poisson distribution (Fig. 5.6). Branching fractures (Fig. 5.5c) are also often clustered (Fig. 5.5b, 5.6) and show a Poisson distribution (Fig. 5.7). However, because they are not parallel, spacing varies in the propagation direction (Fig. 5.8).

In addition to the spacing distributions generalized above, the discussions below reference the correlation coefficient of spacing C_v from Di Naccio et al., (2005) and lognormal, power-law, and exponential distributions as in Bonnet et al. (2001). (a) Lognormal distribution occurs when the spacing variable is defined by many independent variables, suggesting fracture nucleation and propagations are spatially and temporally random processes. (b) Exponential law distributions describe Poisson processes, where the spacing variable is spatially independent but has constant probability over time increments because a continuous process is followed.

Exponential distributions have been related to fracture growth resulting from uniform stress distribution and to early stage deformation, where fracture nucleation dominates over growth and coalescence processes (Bonnet et al., 2001). (c) Power law distributions describe systems that are scale invariant. Physically, this may describe the heterogeneity that exists between fracture length dimensions, causal stresses, and the intrinsic heterogeneity of earth materials. Deformation of the fractured system can

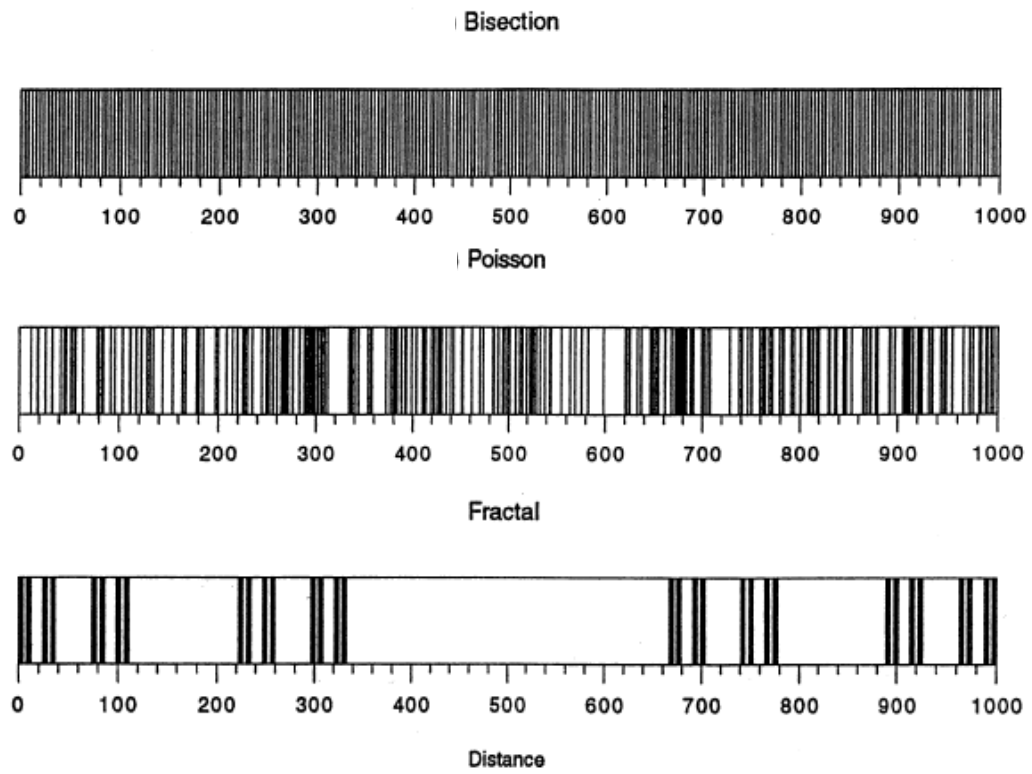
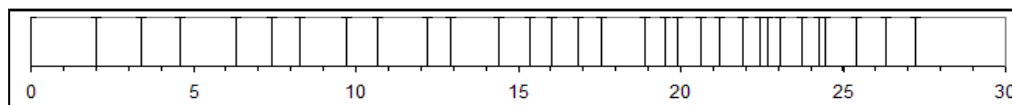
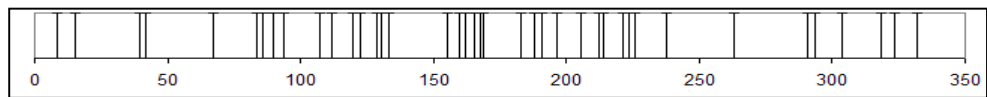
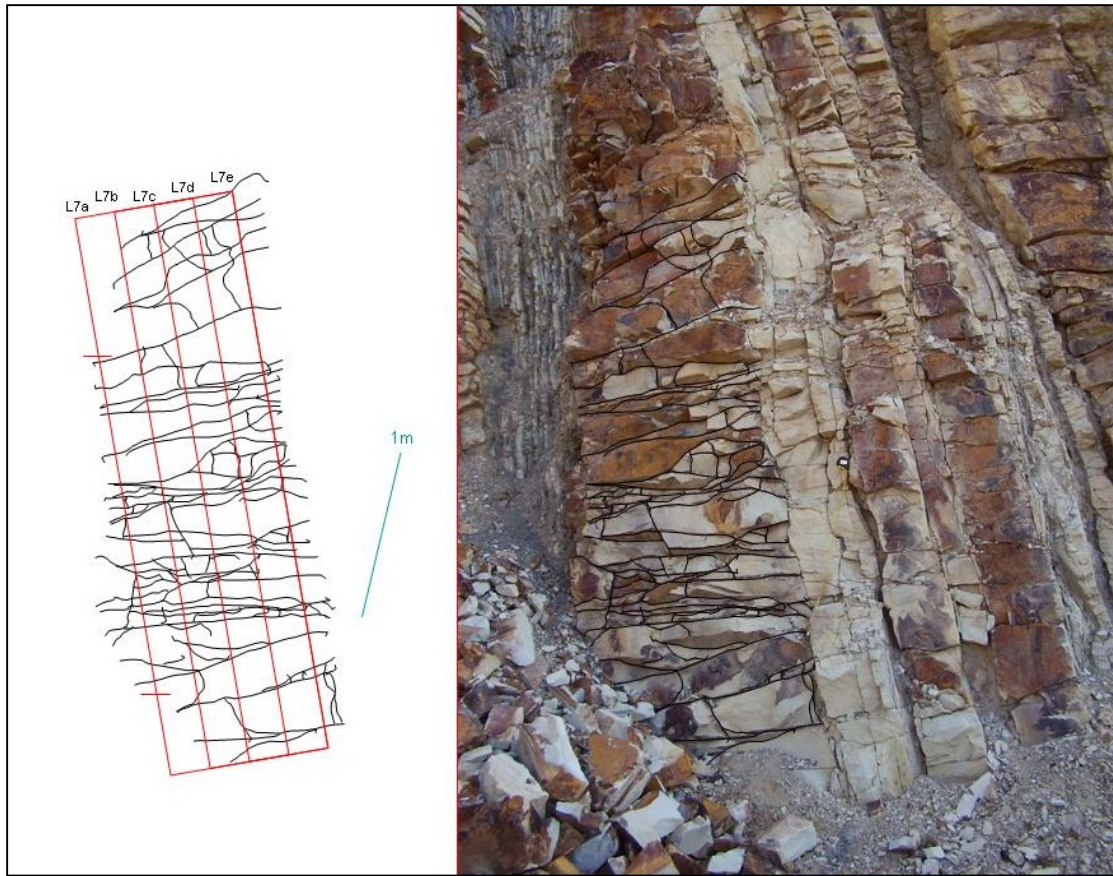


Figure 5.4. 1-D logs showing fracture spacing distribution along a single scan line. Above are theoretical distributions of fractures (modified after Gillespie et al., 1993).



Mean Spacing	STD DEV	Thickness/Spacing
0.89	0.44	28.0

Figure 5.5a. Quasi-uniform fracture distributions in rock layers with 1-D spacing logs and some statistical data. Histograms for the two layers are shown in Figure 5.6 and 5.7 (near Cedar Mountain, Utah).



Mean Spacing	STD DEV	Thickness/Spacing
9.27	7.25	12.9

Figure 5.5b. Clustered (b) fracture distributions in rock layers with 1-D spacing logs and some statistical data. Histograms for the layers are shown in Figures 5.6-5.8 (Jackfork sandstone at Kirby Quarry, AR).

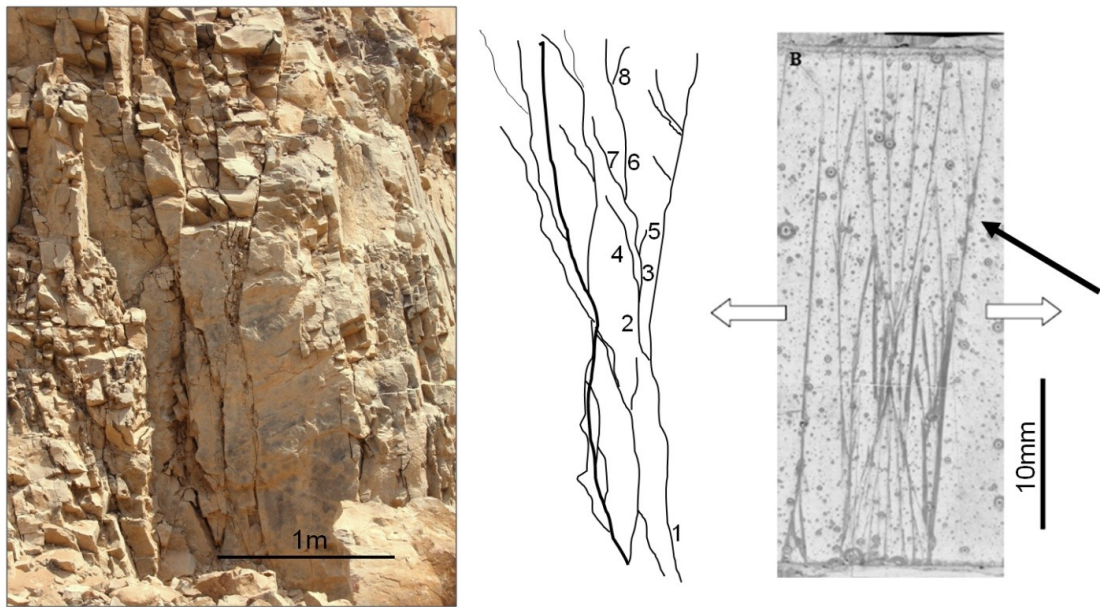


Figure 5.5c. Branching fractures in outcrop (left) are geometrically similar to experimental branching fractures (right) in an epoxy layer loaded in layer parallel extension (Sagy et al., 2001). The fracture map (center) is for the outcrop and reveal the hierarchy of branches. Field location is Jackfork sandstone at Sawyer Quarry, AR.

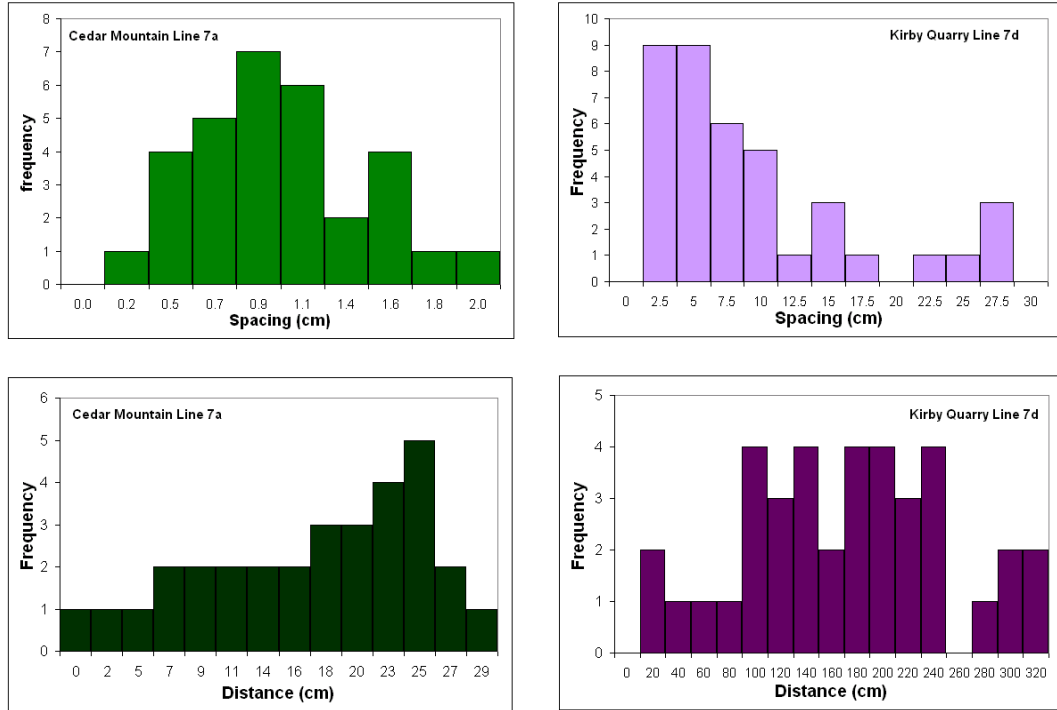


Figure 5.6. Histograms for measured fracture distributions from Figure. 5.5. Fractures with quasi-uniform spacing (Fig. 5.5a) show normal distribution (green), whereas clustered fractures (Fig. 5.5b) suggest a Poisson distribution (purple).

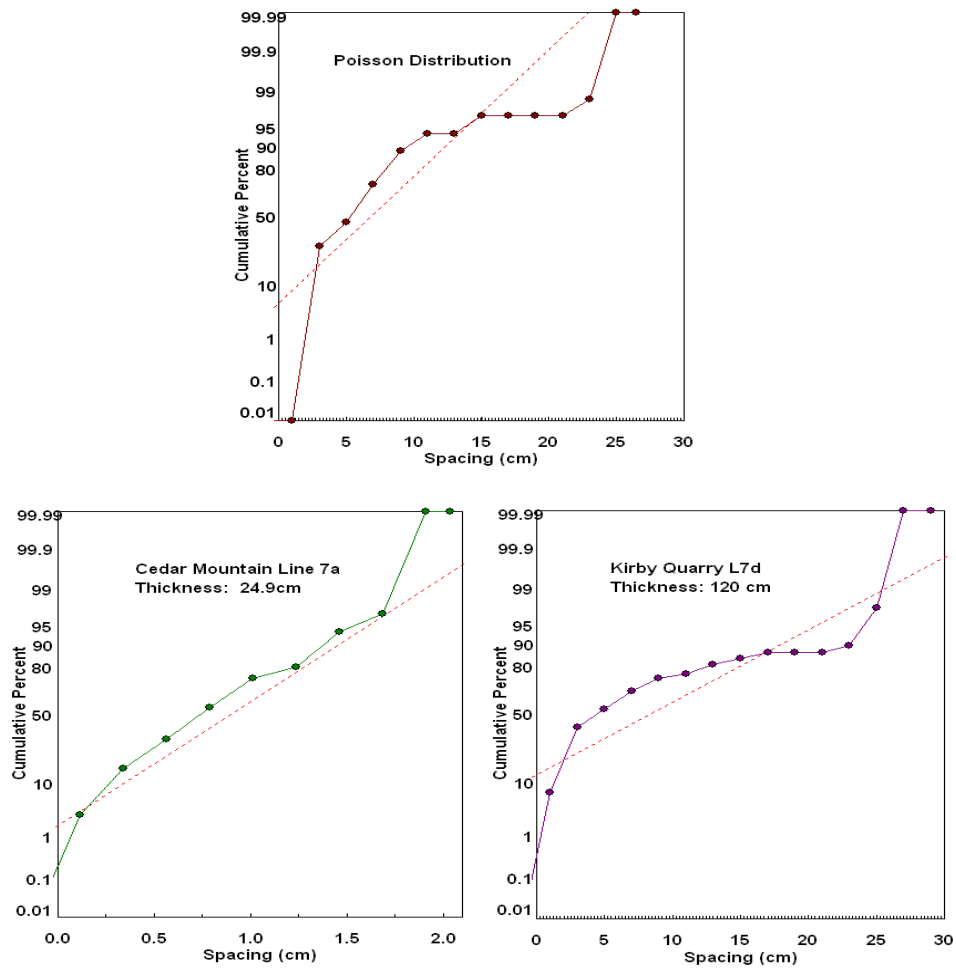


Figure 5.7. Cumulative distribution logs further demonstrate the deviation from the normal distribution (pink dashed line). The top plot is for the Poisson distribution, the other plots are for the 1-D spacing logs in Figure 5.5.

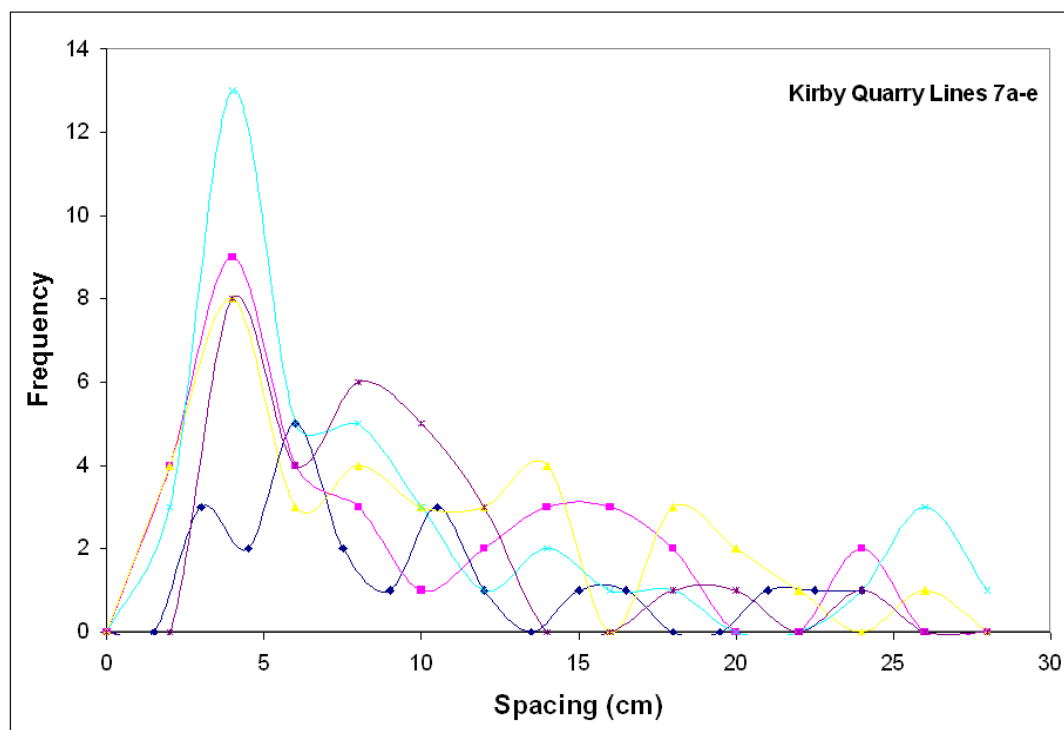


Figure 5.8. Histogram for scanlines 7a-7e for the fracture clusters in Figure 5.5b. The distribution also varies in the propagation direction for the branching clusters.

be interpreted as being increasingly localized as the exponent approaches 2, with the exponent 2 reflecting strain maturity (Bonnet et al., 2001).

FIELD STUDIES NEAR CEDAR MOUNTAIN, UTAH

Field Location

The study area is located east of the San Rafael Swell, which is 50 km wide and 125 km long, trends roughly north-south, and curves to the southwest on the southern end and to the northwest on the northern end (Fig. 5.9). Beds dip gently ($<10^\circ$) on the western margin of the swell and nearly 80° on the eastern monoclinical margin (Fischer and Christenson, 2004). The swell is presumably associated with basement faults that were active during Laramide shortening (Bump, 2000).

The Cedar Mountain area is faulted by normal faults that are continuous for a few kilometers with up to 38m of throw that exposes the upper Navajo Sandstone (Fig. 5.9) (Krantz, 1988; Maerton et al., 2001). The faults display a zig-zag pattern with four sets in orthorhombic symmetry that reflect a three dimensional strain field (Krantz, 1988). Fischer and Christensen (2004) showed regional variations of fracture characteristics while moving northward along the San Rafael monocline: fracture sets increase in number and complexity, fracture density increases $D\sim 1.0$ to $D\sim 1.7$, and fracture orientations rotate counterclockwise (from 157° to 115°).

Field Measurements

We studied fractures in subhorizontal, alternating layers of limestone, marl and shale of the lower Carmel Formation, Cedar Mountain, Utah (Fig. 5.9). Here, a few layers (8-71 cm thick) display high density (up to 30) of regularly spaced layer-

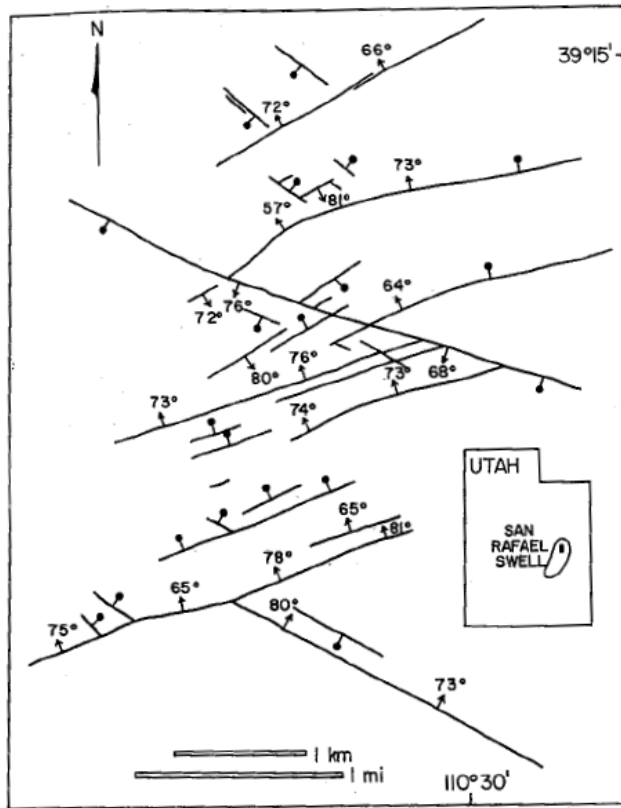
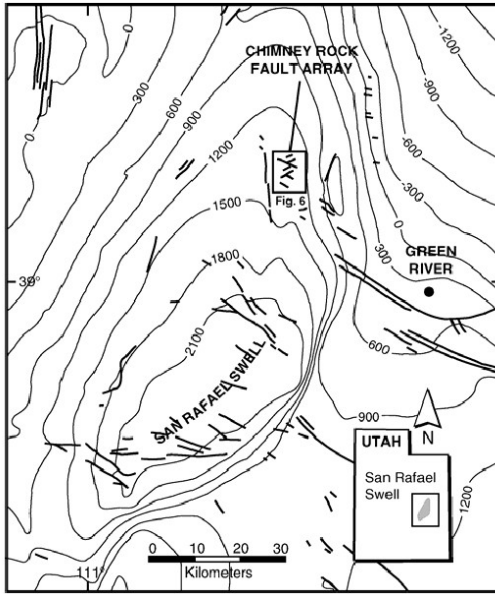


Figure 5.9. Location map of the study area close to Cedar Mountain, Utah. Top- regional structure of the San Rafael Swell showing counters in meter of Chinle Formation (Maerten and Pollard, 2001). Bottom- Simplified fault map of the study area (Krantz, 1988).

normal, layer-bound fractures. Locally, the dense fracturing forms paper-thin sheets bounded by fractures spaced at 2-3 mm (Fig. 5.5a). Many of the fractures display well-preserved plumose features (Fig. 5.10).

Stratigraphic Section

The studied outcrops are of the Carmel Formation, consisting of 30-80 m of marginal marine sediments including colored siltstone, shale, sandstone, gypsum and marine limestone, deposited during the middle Jurassic (Cashion, 1967). This formation extends across Utah and Arizona, and lies between Navajo Sandstone and Entrada Sandstone within the San Rafael Group (O'Sullivan, 2000).

We measured a 13 meter thick stratigraphic section of the lower Carmel Formation; this stage included only lithological description and gamma ray logging (Fig. 5.11). Two of the limestone beds display extreme HFD. One HFD layer is 46 cm thick, dark gray, fine grained sparitic limestone; it is bounded below by fine grained limestone, and above by silty limestone. The second HFD layer is 71 cm thick, massively bedded, gray, fine grained limestone with filled veins and stylolites; this layer is bounded below by chalky limestone, and above by limey siltstone. The gamma ray log shows a relative increase in sandstone, silty limestone, and shale beds and a relative decrease in grainy and crystalline limestone layers (Fig. 5.11).

Fracture Characterization

Field measurements were of fracture orientation, spacing, length, and density and included descriptions of cross-cutting relationships and surface features for limestone beds displaying HFD. Fracture mapping was conducted for several fractured layers

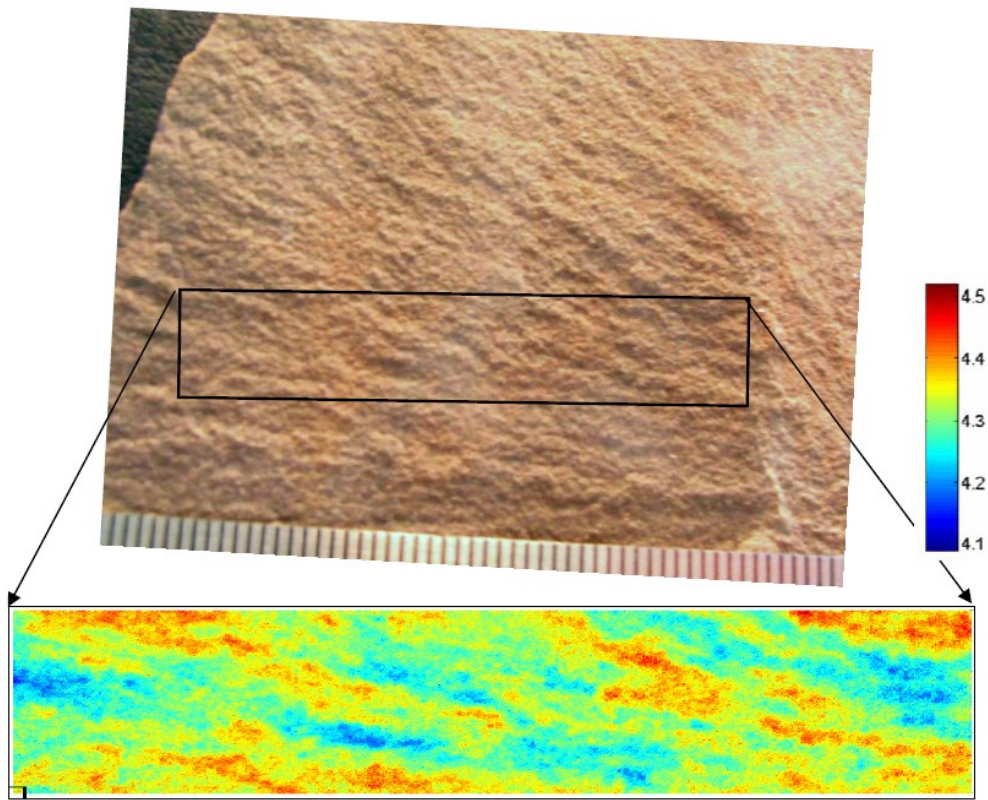


Figure 5.10. Multi-scale view on a fracture surface with plumose marks from the Cedar Mountain field location. Top photo is the surface; graded scale in millimeters. Bottom is a topographic image of a rectangular portion of the surface generated by scanning with a laser profilometer. Scale bar on the right is topographic elevation in millimeters; vertical scan resolution $\sim 40\mu\text{m}$.

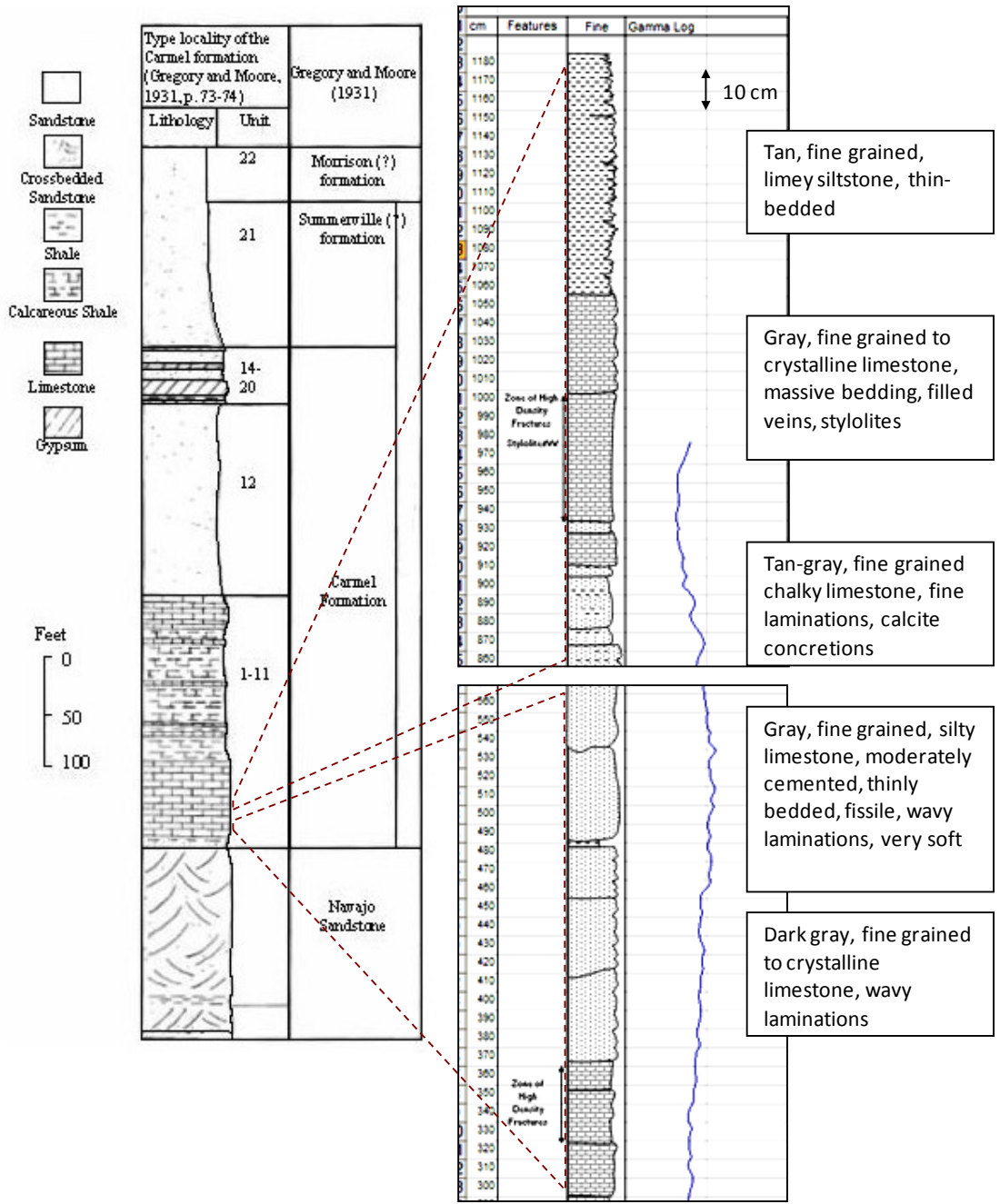


Figure 5.11. Left- Generalized stratigraphic section for the Carmel Formation (Cashion, 1967); right-section of the lower Carmel Formation of the present study with the natural gamma log.

using linear scanlines, a 4 m² surface using grid mapping (10:1 scale), and using digital photography at a 5:1 and 1:1 scale. We also documented fractographic features (Fig. 5.9) for HFD layers (Figs. 5.5a), and collected samples for laboratory analysis.

There are three dominant fracture sets at 350° (Set 1), 105° (Set 2), and 75° (Set 3) (Fig. 5.12), with corresponding densities of $D=0.4-0.5$ (set 1); $D=9.5-29.0$ (set 2); and $D=0.7$ (Set 3). Set 2 fractures displays clear, long clusters. The clustering can be detected numerically by calculating the correlation coefficient of spacing, C_v (standard deviation of spacing divided by mean spacing) (Di Naccio et al., 2005). A $C_v < 1$ describes a set with regular spacing, whereas $C_v > 1$ indicates clustered geometry; we found, $C_v=0.7$ (set 1); $C_v=2.0$ (set 2); and $C_v=0.6$ (Set 3).

Damage Characterization

On several surfaces multi-directional, shallow-seismic surveys were conducted to measure seismic velocity anisotropy due to fracture orientation. Radial arrays of 24 to 48 geophones were set up using a 16 pound sledge hammer as the source. The arrays were aligned perpendicular to and transecting the fracture sets. J. Chang at OU is currently processing the seismic data.

We also characterized the damage zone of a small normal fault (Fig. 5.12) by measuring fracture intensity and orientation as a function of distance from it and the seismic anisotropy. At the site, two fracture sets were identified. The first set contains 108 fractures, is parallel to the orientation of the fault, and has a mean orientation of 89°/345°. The second set has 54 fractures and a mean orientation of 86°/032°. The 1D log indicates that the fault parallel set intensifies approaching the fault.

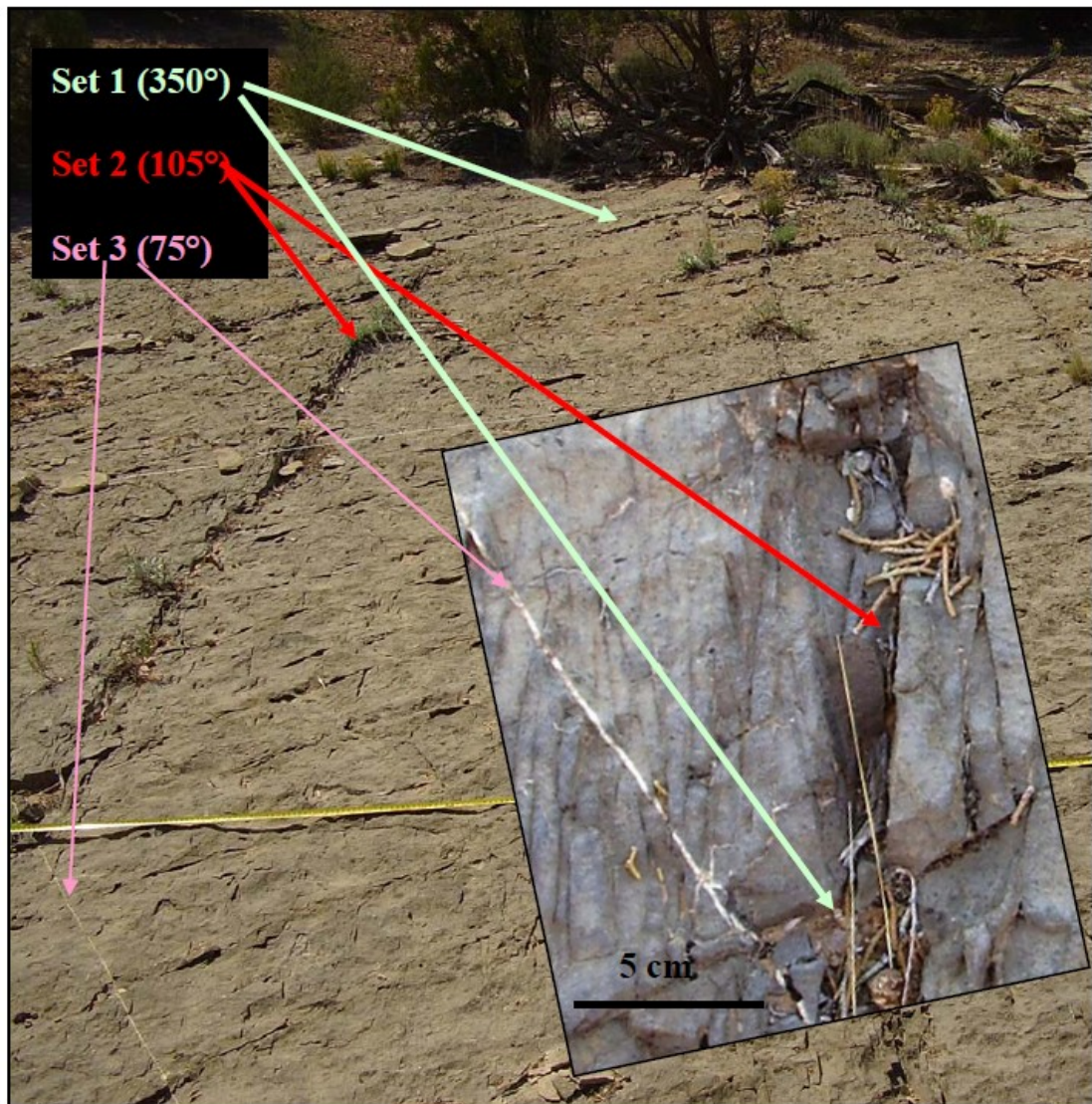


Figure 5.12. View of bedding surface of a 6cm thick layer in the Cedar Mountain area. Three dominant fracture sets oriented 350°, 105°, and 75°. The inset picture is a close up of the fracture sets with scale bar shown. The first set (bottom of inset) is continuous for several meters. The second set consists of dense, branching fractures grouped in clusters. The third set is discontinuous (segmented) and is often calcite filled.

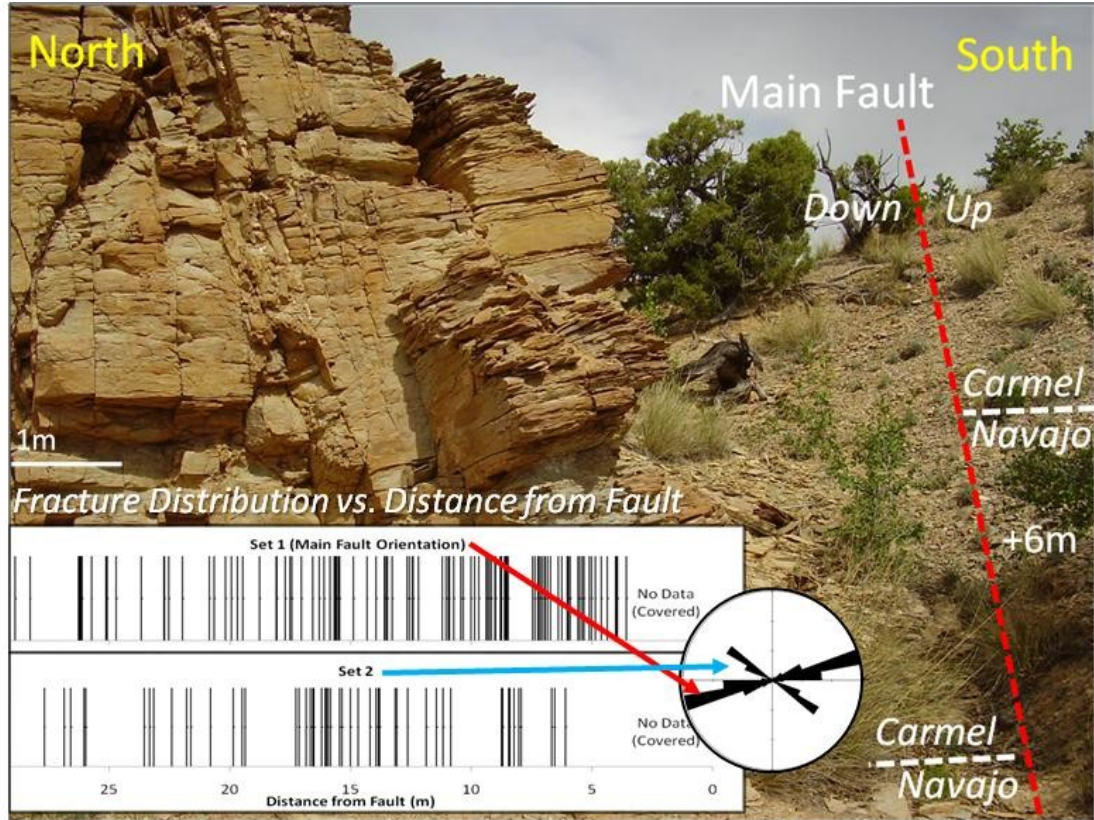


Figure 5.13. A fault zone near Cedar Mountain, Utah. Interpreted fault location shown by dashed red line. Inset 1-D fracture spacing logs and rose diagram shows fracture distribution relative to the main fault.

FIELD STUDIES OF THE JACKFORK GROUP, OKLAHOMA AND ARKANSAS

We studied fractured zones in steeply dipping and subhorizontal sandstone layers of the Jackfork Group at two rock quarries in Oklahoma and Arkansas (Fig. 5.14). These quarries and associated exposures in OK and AR have been used as field analogs of fractured reservoirs in many studies conducted in the University of Oklahoma (e.g., Slatt et al, 1997; Slatt et al, 2000; Omatsola, 2002; Busetti, 2003)

The Jackfork Group exposures in the Ouachita Mountains in southeastern Oklahoma and Arkansas represent the remnants of an extensive fold and thrust belt that contained the Ouachita trough (Suneson 1988), a long-lived depositional basin that originated during the late Proterozoic to Cambrian rifting event (Keller and Cebull, 1973). Tectonic shortening of this basin began as early as the Late Mississippian (Suneson, 1988), with diminishing orogenic pulses lasting into the Early Permian (McBee, 1995). Overall, the Ouachita orogeny resulted in 190 km (120 miles) of low angle thin-skinned thrusting. Narrowing of the Ouachita trough during the Morrowan (early Pennsylvanian) resulted in deposition of 2000 meters of Johns Valley and Jackfork flysch in the Ouachita trough. These sediments were thrust-faulted over the craton margin (Viele and Thomas, 1989), producing a series of broad folds separated by faults, some of which contain steeply dipping limbs, such as at those exposed at the Sawyer quarry.

Sawyer Quarry, OK

The subhorizontal, massive 5-20 m thick layers of well-cemented sandstone display well-exposed 3D fracture networks with rhombic geometry (Fig. 5.15). The dominant

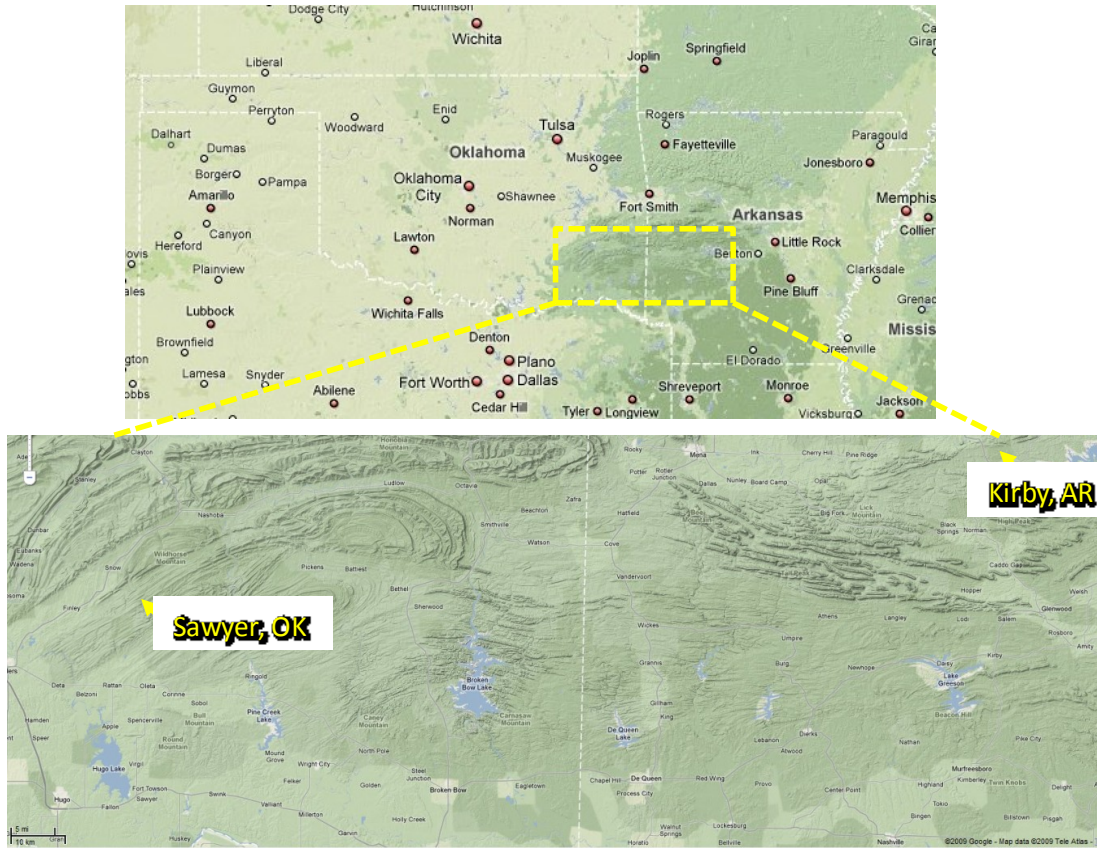


Figure 5.14. Location of the Jackfork sandstone quarries in Sawyer, OK and Kirby, AR (Google Maps).

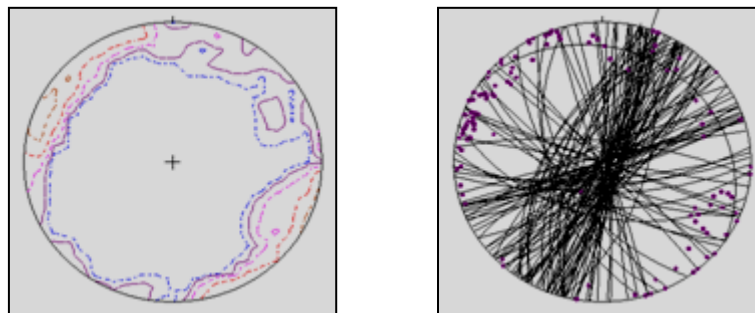
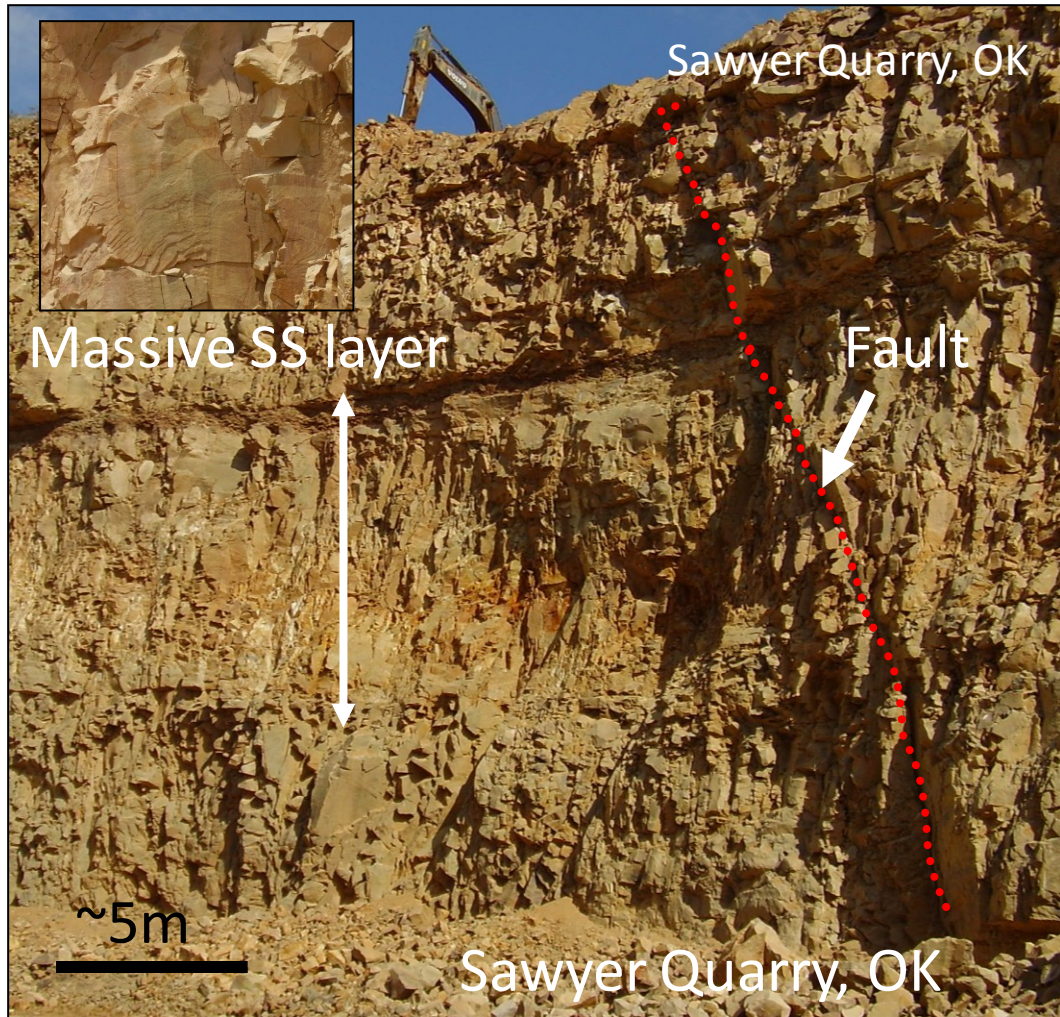


Figure 5.15. Subhorizontal, massive 5-20 m thick layers of well-cemented sandstones of the Jackfork Group at the Sawyer Quarry, OK. This layers display well-exposed 3D fracture networks with rhombic geometry; inset displays fracture surface with plumose markings. The stereonets display the orientations of joints measured in the shown exposure and its proximity.

fracture set is subvertical and oriented north-northeast. A wider distribution of fractures range from north-northeast to east-northeast. The site exhibits close fracture spacing within thick beds, suggesting that layering effects could be minimized. The mean spacing is 40.6 centimeters, $D_{avg} = 12$. The subhorizontal layers also display multiple tree-like fractures. These fracture sets dip steeply, crosscut one another, and expose plumose and arrest-line features. Many of these fractures terminate within the massive layer and often split to form 3D networks of rhombic geometry.

Baumgartner (Kirby) Quarry, AR

An investigation of fracture spacing and distributions in different lithological facies in sequence was conducted jointly with OU student B. Solarte. Nearly 200 feet of a vertical succession of strata are exposed on 3-4 benches at the quarry (Fig. 5.16). The steeply dipping layers are intensely fractured. Using digital photographs, fracture spacing and distributions were collected by digitizing fracture data from 68 layers, sorted by three interpreted facies. The fracture data are compared with the generalized stratigraphy and gamma logs.

Facies Interpretation

Stratigraphic sections were first measured by OU students Buseti, Santacruz, Solarte, and Duran. Outcrop gamma ray logs were acquired with a hand-held scintillometer tool. A cross section is shown in Figure 5.16 for the outcrop and Figure 5.17 for the facies interpretations. Seven different types of rocks were defined and sampled for all the benches in the Outcrop: F1: Orange amalgamated sheet sandstone with planar contacts, F2: Channel Fill sandstone, F3: Layered sheet sandstone, F4: Shale, F5: Slump Deposit, F6: Interlaminated sandstones and shales and F7: Dark gray

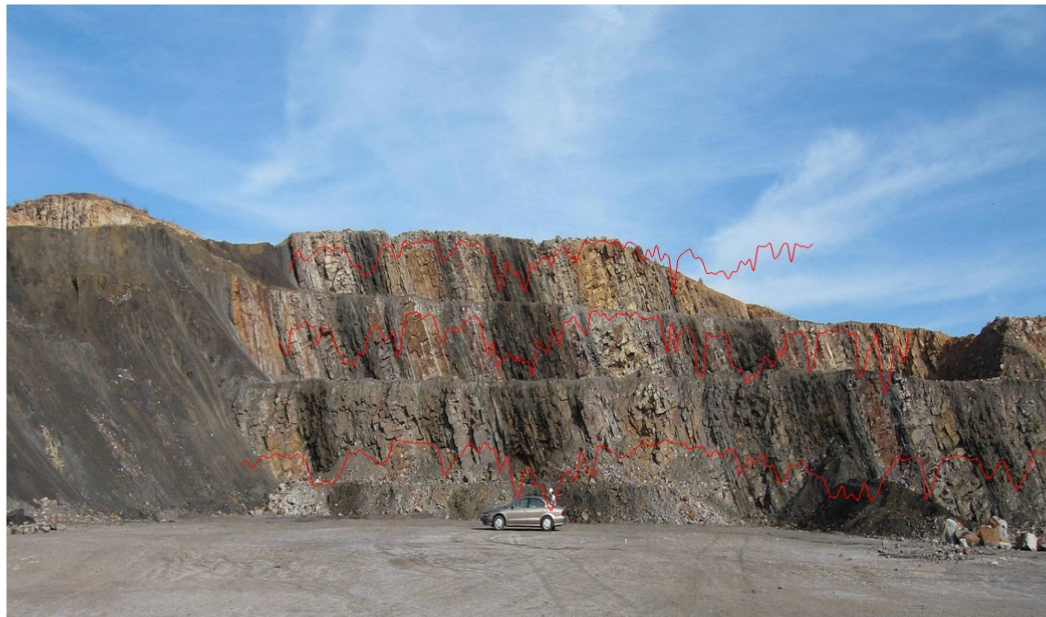


Figure 5.16. Three faces of the ‘upper sand’ in the Baumgardner (Kirby) Quarry. Superimposed on the faces are outcrop gamma-ray logs obtained by Santacruz and Solarte.

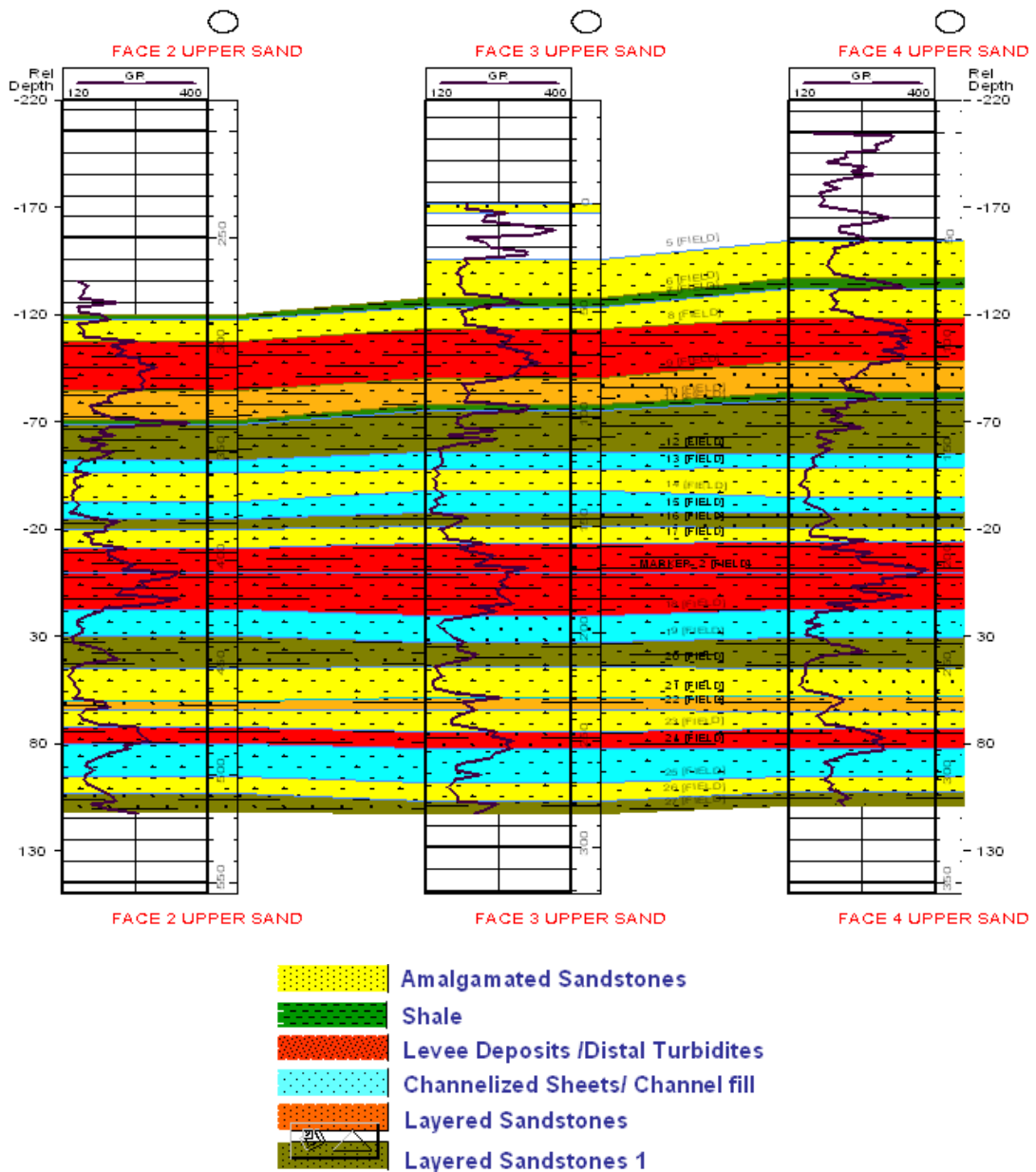


Figure 5.17. Gamma ray logs and cross section showing facies and their distribution in the upper sand of the Baumgardner (Kirby) Quarry (modified from W. Duran, 2007).

layered sheet sandstone. Only F1, F2, and F3 are used for this analysis because they have a large enough number of beds to sample statistically and can be also discernable on the digital photographs.

Gamma-ray Log Measurements

Outcrop gamma-ray log measurements were taken every two feet with a hand-held scintillometer and are compiled in Table 5.1. Data shows a grouping of at least two different rock types arranged by means, 1, 2, 5 and 7 as one group, and 3,4 and 6 as a second group. From XRD analysis, composition was determined to be predominantly quartz for the studied facies F1, F2, and F3. It was observed that the XRD peaks of the samples fit those of pure quartz powder with high precision (B. Solarte, 2007, personal communication). However, some small peaks suggest the presence of a small amount of clay minerals in each facies.

Mechanical Stratigraphy

F1: Facies type 1 amalgamated sandstone layers are the thickest (up to 2m) and most massive of the three measured sandstones deposits in general, but also vary the most in thickness and mechanical texture. Pink, reddish, and orange beds are cleaner, well cemented, and are more brittle than the gray, darker sandstone layers that are muddier and apparently weaker. In most cases, the beds with highest fracture density show evidence of reddish mineralization on the surface and in cracks. Facies type 1 beds occur in larger packages of similar sandstone and are mostly bound by sandstone with few shaley or muddy interbeds.

	Gamma ray (API)						
	Facies						
	1	2	3	4	5	6	7
Mean	189.04	197.39	220.07	249.16	186.51		194
Mode	161	160	230	210	#N/A		226
Standard deviation	39.12	39.29	43.76	61.61	22.39		28.66
Most minimum	129	138	136.33	146	162.67		132.33
Maximun	368.67	343	365	384.33	237.67		255.33

Table 5.1. Outcrop gamma-ray log measurements for each of the 7 facies.

F2: Facies type 2 channel fill sandstone layers occur within larger sequences of amalgamated sandstone layers and are on the order of 20-30 cm thick, but can be as thick as 80 cm. Most facies type 2 layers are well cemented and brittle, and show mechanical traits similar to facies type 1 with the exception that a general lack of planarity results in obliquely oriented fracture, erosion, and surface slumping patterns.

F3: Facies type 3 layered sheet sands are generally thinner (<10-30 cm) than the other facies and are interbedded with shale and thin sandstone layers. Gray, mud bearing beds are common within shale sequences and are transitional with cleaner, more brittle sheet sands.

Description of Fractures

The < 1 m thick layers of clean, well cemented sandstone exhibit both regularly spaced, layer-bound fractures of typical density and layer-normal HFD clusters. These clusters often extend through multiple layers and commonly show Fe and Mn-oxide mineralization indicating fracture connectivity and the fluid flow (Fig. 5.18). Fractures in F1 and F2 show signs of pervasive fluid penetration along the fracture network (B. Solarte, 2007, personal communication). Long fractures appear to contribute most dominantly to the flow pattern in the fluid network, though the presence of smaller, linking fractures, may also contribute to connectivity. Shale layers frequently bound the fractured sandstone layers and serve as barriers to fluid flow normal to bedding. There are two primary fracture sets, both are aligned perpendicular to bedding.

Digitization of Fracture Data

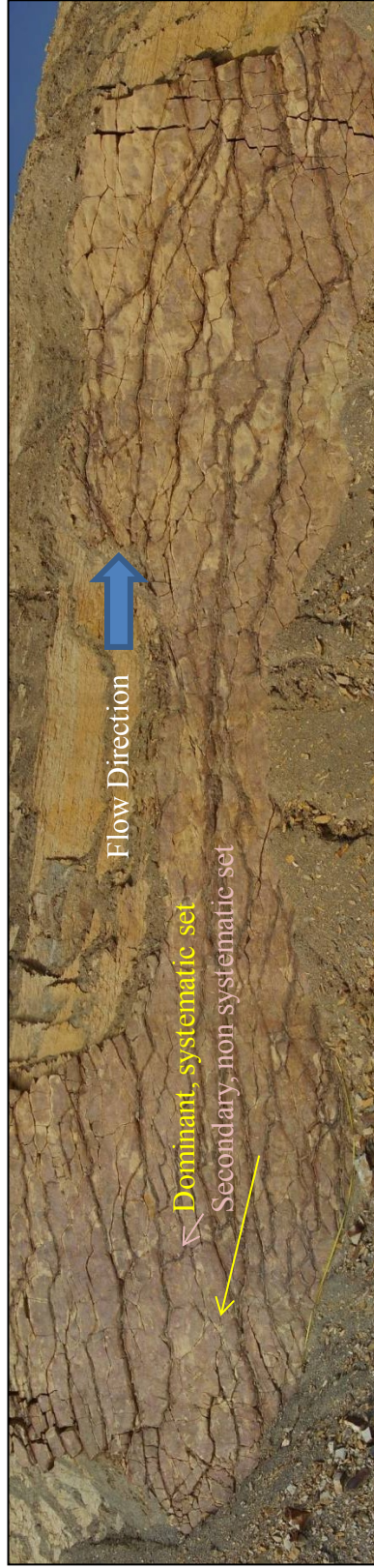


Fig 18. In this layer of Jackfork Formation sandstone exposed at the Kirby Quarry, Arkansas, fluid migration pathways are clearly evidenced by dark Fe and Mn mineralization. There is a dominant systematic fracture set characterized by wider, longer fractures, and a secondary, non-systematic set that connects the larger fractures. Note that fluid pathways follow the trend of the dominant set but flow through both sets.

For the lower section of each bench, we correlated stratigraphic columns and gamma ray logs with compiled digital photograph mosaics. Individual layers and packages of layers were designated by facies type F1, F2, or F3. From these highlighted mosaics we selected 30 layers from F1, 13 from F2, and 25 from F3, totaling 2,232 fractures recorded for analysis. Layer-parallel, fracture-normal scanlines were overlain on high resolution digital photographs and spacing increments recorded for each fracture (e.g., LaPointe and Hudson, 1985). Fractures were digitized by hand from the photographs using the Grafula software and analyzed in Microsoft Excel.

Statistical Method

Following Bonnet et al. (2001), we calculated lognormal, power-law, and exponential distributions for the three facies types. We use their recommendation that a minimum of 200 fractures be sampled to adequately define scaling exponents. It is recognized that a true lower bound to the data is controlled by the resolution of the digital camera and digitization software, and a true upper bound is controlled by the size of the region observed (Odling, 1997). This upper bound may be complicated by the presence of faults and rubble zones that are difficult to distinguish in the photographs. Nonetheless, because the length measurement of fracture spacing can be measured relatively accurately we cannot identify significant sources of influence for under-sampling or over-sampling spacing, and thus we neglect the practice of applying lower and upper cut-offs.

Results and Discussion

Facies 1 (Fig. 5.19) fits the lognormal distribution fairly well with the best fit for spacing greater than 20cm. For spacing less than 20 the fit is noisy, but generally follows the curve. The exponential distribution shows a good fit ($R^2 = 0.8473$) compared to the power law distribution ($R^2 = 0.5597$, exponent $a = 1.4121$).

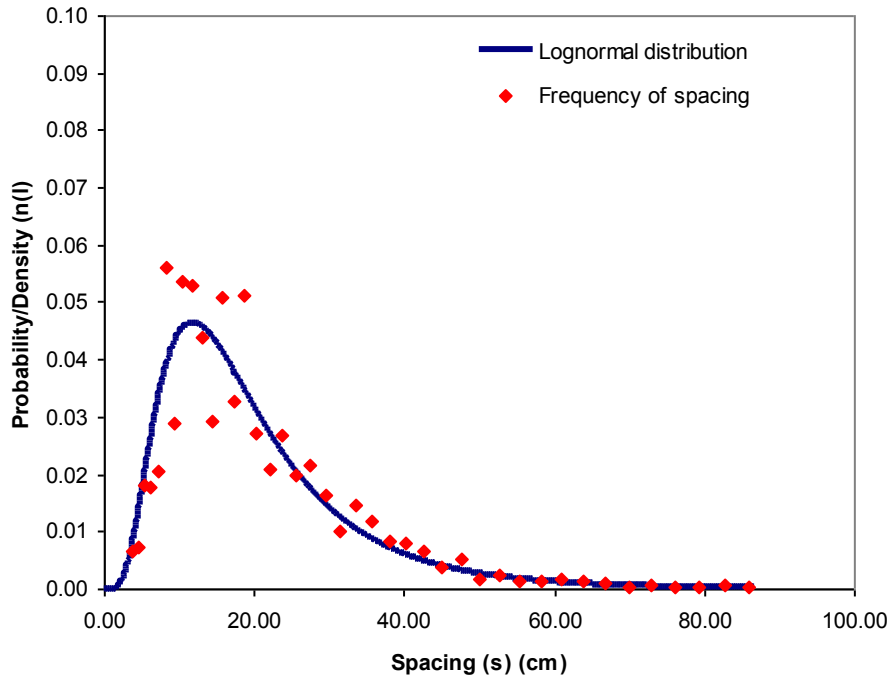
Facies 2 (Fig. 5.20) generally follows a lognormal distribution with good fit for spacing less than 10cm and greater than 30cm. For $10 < S < 30$ the lognormal fit is noisy, but follows generally follows the curve. The exponential distribution has a moderate fit ($R^2 = 0.6344$) compared to the power law distribution ($R^2 = 0.3442$, exponent $a = 0.8905$).

Facies 3 (Fig. 5.21) fits the lognormal distribution well over all spacing values, and generally fits the curve better than both F1 and F2. The exponential distribution has a reasonably good fit ($R^2 = 0.7612$) compared to the power law distribution ($R^2 = 0.5299$, exponent $a = .14087$).

Mean spacing versus layer thickness for the three facies are compared (Fig. 5.22), where thickness/spacing is given by density D . F1 beds have D ranging from 1.1 to 7.6, and have been measured as high as 12.9 in a separate study. Average D is 3.1 with a standard deviation of 1.8. F2 beds have D ranging from 1.0 to 2.5 with a standard deviation of 0.6. F3 beds have D ranging from 0.7 to 2.3 with a standard deviation of 0.5.

The lognormal distribution for all three facies suggests that fracture development follows a random process where fracture growth is mostly independent for all fractures. This relationship is clearest for facies 3. The moderate to good exponential fit may suggest that fracture processes, while spatially independent,

Lognormal Distribution



Exponential/Power Law Distributions w/o cutoffs

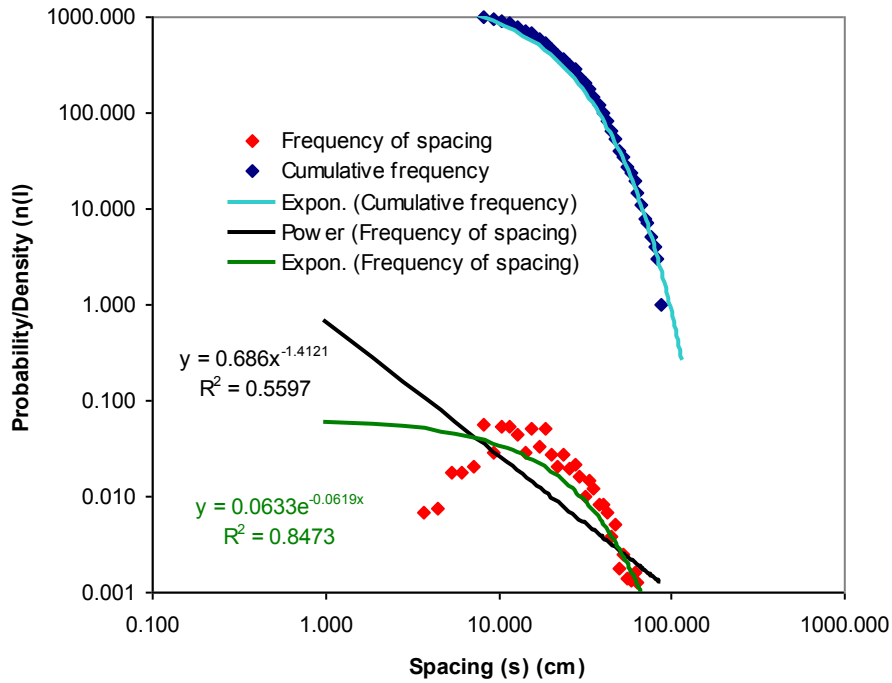
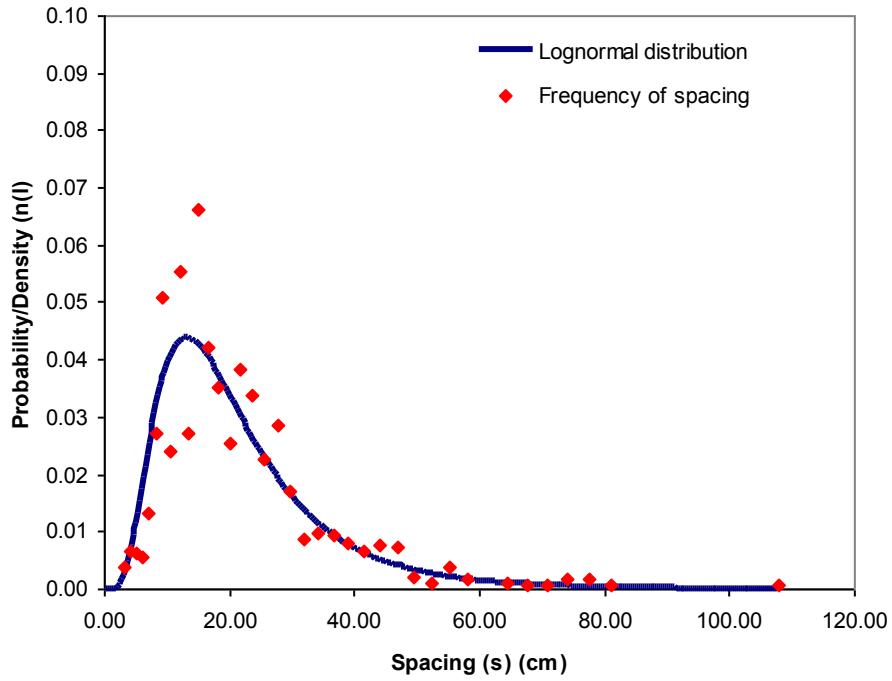


Figure 5.19. Plots showing spacing distributions for facies 1.

Lognormal Distribution



Exponential/Power Law Distributions w/o cutoffs

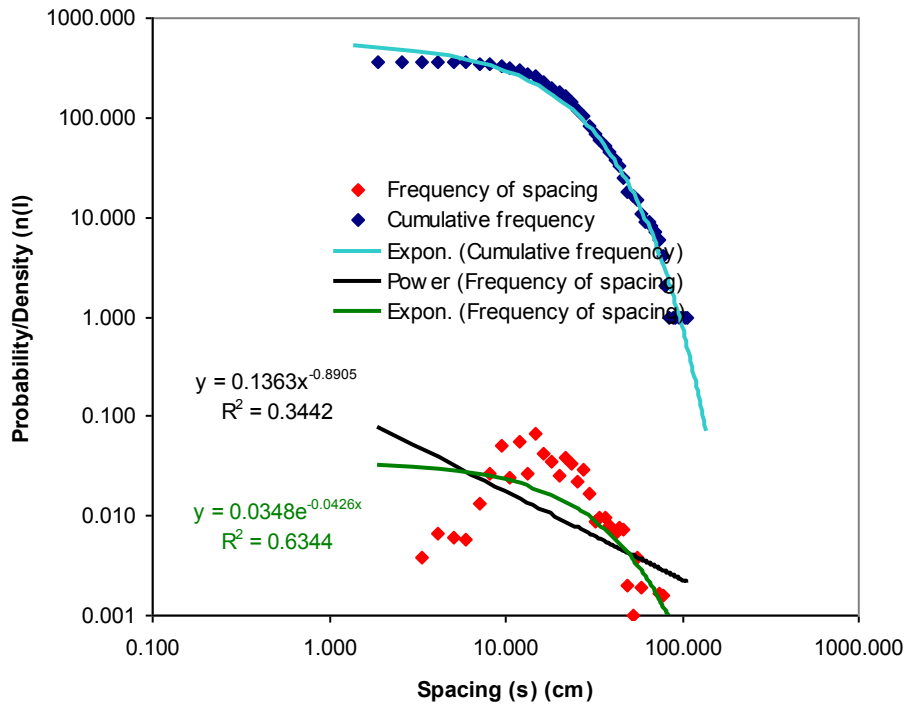
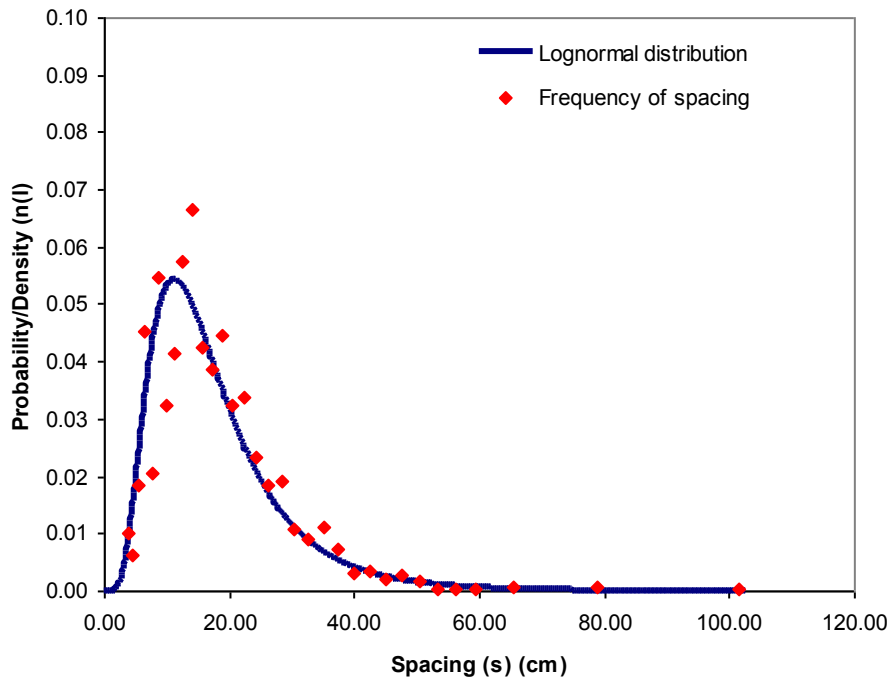


Figure 5.20. Plots showing spacing distributions for facies 2.

Lognormal Distribution



Exponential/Power Law Distributions w/o cutoffs

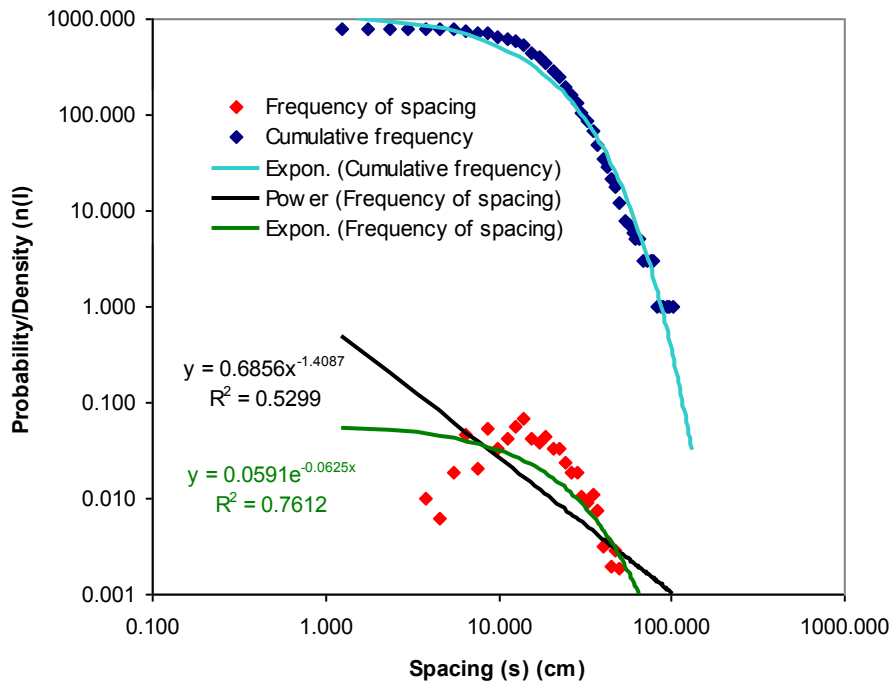


Figure 5.21. Plots showing spacing distributions for facies 3.

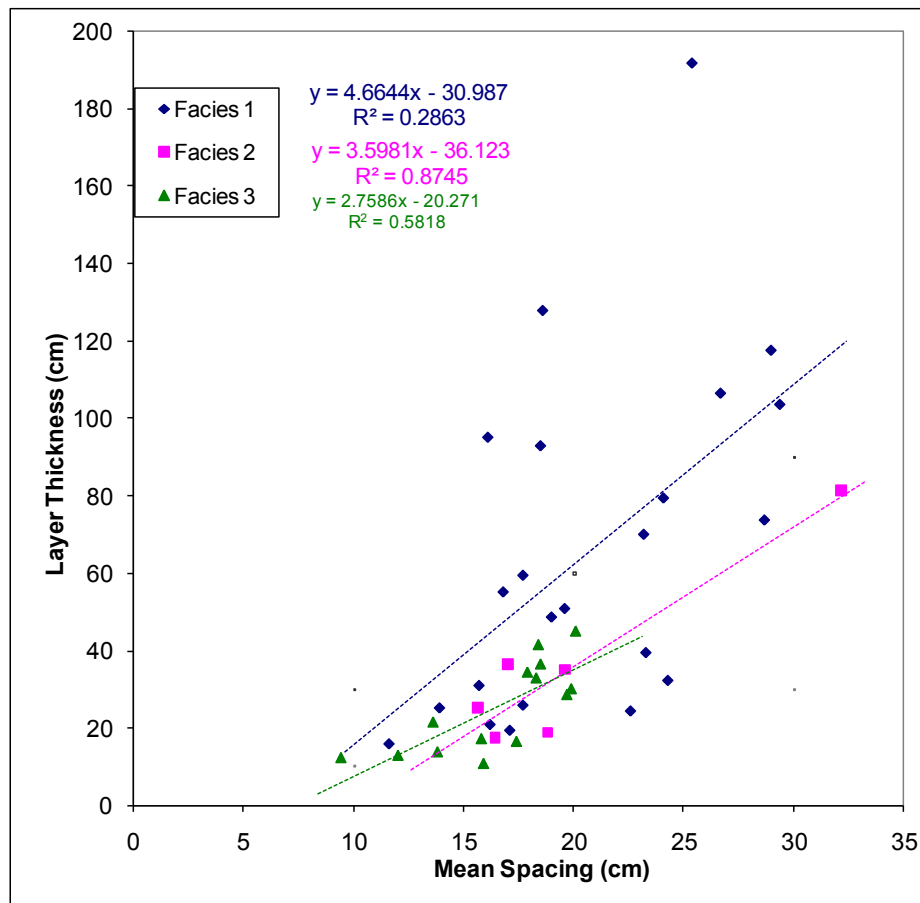


Figure 5.22. Mean spacing versus layer thickness for facies 1, 2, and 3.

follow a similar early-stage growth process. This interpretation is reasonable given that fracture development at the outcrop scale is largely due to accommodation of similar strains. The correlation between exponential fit and facies type could be identifying some influence from boundary conditions and stress amplifications resulting from contrasting rock properties, as R^2 for $F1 > F3 > F2$. There is evidence from fracture terminations at layer contacts, as well as from fractures that cross multiple layers that fracture development is sometimes restricted by the bounding layers, and sometimes not. This suggests that there is a difference in layer stresses present in the formations above and below the fractured zones that may be resolved by comparing material and boundary properties.

In general, the data shows a poor power law fit, suggesting that fracture development shows scale dependence. Power law exponents for F1 and F2 are similar, and suggest a higher level of fracture maturity than F2. This may also be reflected in the lowest power law and exponential fits being in F2. The difference in power law exponent for F1 and F3 compared with F2 is possibly related to boundary conditions and contrasting rock properties. The local mechanical conditions within F2 beds may actually inhibit fracture development to some extent.

F1 beds show the highest fracture density, but also have the most variable densities ($R^2 = 0.29$) as well as show the largest deviance in bed thickness. This suggests that F1 fracture development is poorly correlative with thickness constraints. F2 fractures are relatively well correlated to thickness ($R^2 = 0.87$) reflecting that fracture development is highly dependent on bed thickness. F3 fractures lay

somewhere in between ($R^2 = 0.5818$), such that there is a moderate interdependence between bed thickness and fracture spacing.

Relatively lower gamma ray measurements (below 200) suggest that F1 and F2 could be present, characterized by cleaner sands and stiffer rock. F1 is distinguished from F2 in that the fracture spacing tends to be represented by a good fit to the exponential frequency distribution. F1 and F2 may correspond to a network of conductive fractures which could be a storage volume of hydrocarbons. For gamma ray measurements over 200, F3 is suggested. A stronger fit to the lognormal distribution is apparent, but can also be distinguished by a well defined qualitative contrast in the geomechanical properties between the adjacent layers.

Overall, observable differences between F1, F2, and F3 are apparent from statistical analysis. Refinement of the data presented here should provide a useful tool to predict fracture characteristics from facies interpretations in other Jackfork Group analogs and in the subsurface.

SUMMARY

The occurrence of high fracture density in the layers of the Carmel Formation carbonates and Jackfork sandstones were investigated to understand the apparent contradiction between the theoretical models for fracture spacing and the field observations. Several techniques for understanding HFD were explored. While the study is still in progress, some general conclusions can be made.

(1) Fracture density increased approaching a small fault zone, but only for the fracture set in the fault-parallel orientation.

(2) A weak correlation exists between fracture spacing and layer thickness and is even weaker in very thick layers. Clustering was observed in thin and thick layers. Branching was more evident in thick layers in the Jackfork layers at the Sawyer Quarry.

(3) The correlation between fracture spacing and layer thickness breaks down in units where fracture infill is most random, i.e., exhibiting a more lognormal distribution. In the Jackfork sandstone layers, this was displayed in the more heterogeneous layered sheet sand facies.

(4) Fracture density increased in more brittle layers. However, density differences between sets in the same layers were observed. This indicates that the process of fracture infill has a strong genetic component.

(5) Furthermore, clustering was observed only in certain fractures sets in the same layer. This suggests that clustering is also related to genetic processes and should not be inferred directly from the modern day rock properties.

REFERENCES

- Bai, T. and Pollard, D.D., 2000, Fracture spacing in layered rocks: a new explanation based on stress transition. *Journal of Structural Geology*, p. 43-57.
- Bai, T., Pollard, D.D., and Gao, H., 2000, Explanation for fracture spacing in layered materials. *Nature*, v. 403, p. 753-756.
- Bonnet, E., Bour, O., Odling, N.E., Davy, P., Main, I., Cowie, P., and Berkowitz, B., 2001, Scaling of fracture systems in geological media. *Review of Geophysics*, v. 32, no. 3, p. 347-383.
- Bump, A., 2000, Laramide deformation of the northern Colorado Plateau; complex patterns from simple controls. In: *Geological Society of America, 2000 annual meeting, Anonymous, Abstracts and programs – Geological Society of America*, v. 32, no. 7, p. 43.
- Busetti, S., 2003, Fracture characterization and analysis of the Pennsylvanian Jackfork Group, Ouachita Mountains, southeastern Oklahoma. Master's thesis, University of Oklahoma, Norman, Oklahoma, 99 p.
- Cashion, W.B., 1967, Carmel Formation of the Zion Park region, southwestern Utah; a review, *USGS Bulletin*, 1244-J.
- Di Naccio, D., Boncio, D., Cirilli, S., Casaglia, F., Morettini, E., Lavecchia, G., and Brozzetti, F., 2005, Role of mechanical stratigraphy on fracture development in carbonate reservoirs: from outcropping shallow water carbonates in the Umbria-Marche Apennines, Italy. *Journal of Volcanology and Geothermal Research*, v. 148, p. 98-115.
- Eberli, G., Baechle, G.T., Anselmetti, F.S., and Incze, M.L., 2003, Factors controlling elastic properties in carbonate sediments and rocks. *The Leading Edge*, July 2003, p. 653-660.
- Ehrenberg, S.N., Eberli, G., Keramati, M., and Moallemi, S.A., 2006, Porosity-permeability relationships in interlayered limestone-dolostone reservoirs. *American Association of Petroleum Geologists Bulletin*, v. 90, no. 1, p. 91-114.
- Engelder, T., Gross, M.R., and Pinkerton, P., 1997, An analysis of joint development in thick sandstone beds of Elk basin anticline, Montana-Wyoming. In Hoak, T.E., Klawitter, A.L., and Blomquist, K., (eds.). *Fractured reservoirs: characterization and modeling*. Rocky Mountain Association of Geologists, p. 4-21.

- Fischer, M. and Christensen, R., 2004, Insights into the growth of basement uplifts deduced from a study of fracture systems in the San Rafael monocline, east central Utah. *Tectonics*, v. 23, TC1018.
- Fredrich, J.T., Evans, B., and Wong, T., 1989, Micromechanics of the brittle to plastic transition in Carrara Marble. *Journal of Geophysical Research*, no. 94, no. B4, p. 4129-4145.
- Germanovich, L.N. and Dyskin, A.V., 2000, Fracture mechanisms and instability of openings in compression (in Neville Cooke special issue). *International Journal of Rock Mechanics and Mining Sciences*, v. 37, no. 1-2, p. 263-284.
- Gross, M.R., 1993, The origin and spacing of cross joints; examples from the Monterey Formation, Santa Barbara coastline, California. *Journal of Structural Geology*, v. 15, p. 737-751.
- Gross, M.R., Fischer, M., Engelder, T., and Greenfield, R.J., 1995, Factors controlling joint spacing in interbedded sedimentary rocks; integrating numerical models with field observations from the Monterey Formation, USA. In: Ameen, M.S. (ed.). *Fractography: fracture topography as a tool in fracture mechanics and stress analysis*. Geological Society Special Publication, v. 92, p. 215-233.
- Hanks, C., Lorenz, J., Teufel, L., and Krumhardt, A.P., 1997, Lithologic and structural controls on natural fracture distribution and behavior within the Lisburne Group, northeastern Brooks Range and North Slope subsurface, Alaska. *American Association of Petroleum Geologists Bulletin*, v. 81, no. 10, p. 1700-1720.
- Hobbs, D.W., 1967, The formation of tension joints in sedimentary rocks; an explanation. *Geological magazine*, v. 104, p. 550-556.
- Ji, S., Zhu, Z., and Wang, Z., 1998, Relationship between joint spacing and bed thickness in sedimentary rocks: effects of interbed slip. *Geological Magazine*, v. 135, p. 637-655.
- Katz, O., Reches, Z., and Roegiers, J.C., 2000, Evaluation of mechanical rock properties using a Schmidt Hammer. *International Journal of Rock Mechanics and Mining Sciences*, v. 37, no. 4, p. 723-728.

- Keller, G.R. and Cebull, S.E., 1973, Plate tectonics and the Ouachita system in Texas, Oklahoma, and Arkansas. *The Geological Society of America Bulletin*, v. 83, p. 1659-1666.
- Kelly, A., and Tyson, W.R., 1965, Tensile properties of fiber-reinforced metals: Copper/Tungsten and Copper/Molybdenum. *Journal of the Mechanics and Physics of Solids*, v. 13, p. 329-350.
- Krantz, R.W., 1988, Multiple fault sets and three-dimensional strain: theory and application. *Journal of Structural Geology*, v. 10, no. 3, p. 225-237.
- Ladeira, F.L. and Price, N.J., 1981, Relationship between fracture spacing and bed thickness. *Journal of Structural Geology*, v. 3, p. 179-183.
- La Pointe, P.R., and Hudson, J.A., 1985, Characterization and interpretation of rock mass joint patterns. *Geological Society of America Special Paper* 199.
- Laubach, S.E., 2003, Practical approaches to identifying sealed and open fractures. *American Association of Petroleum Geologists Bulletin*, v. 87, no. 4, p. 561-579.
- Maerten, L., Pollard, D.D., and Maerton, F., 2001, Digital mapping of three-dimensional structures of the Chimney Rock fault system, central Utah. *Journal of Structural Geology*, v. 23, p. 585-592.
- McBee, W., 1995, Tectonic and stratigraphic synthesis of events in the region of the intersection of the Arbuckle and Ouachita structural systems, Oklahoma. *Oklahoma Geological Survey Circular* 97, p. 45-81.
- Montgomery, S.L., 1996, Jackfork Group, southeastern Oklahoma: New gas play in the Ouachita overthrust. *American Association of Petroleum Geologists Bulletin*, v. 80, p. 1695-1709.
- Narr, W., and Suppe, J., 1991, Joint spacing in sedimentary rocks. *Journal of Structural Geology*, v. 13, p. 1037-1048.
- Nelson, R.A., 1985, Geologic analysis of naturally fractured reservoirs (in *Contributions in petroleum geology and engineering*, 1). Gulf Publishing Co., Houston, TX, 320 p.
- Odling, N.E., 1997, Scaling and connectivity of joint systems in sandstones from western Norway. *Journal of Structural Geology*, v. 19, no. 10, p. 1257-1271.

- Olson, J.E., 2004, Predicting fracture swarms – the influence of subcritical crack growth and the crack-tip process zone on joint spacing in rock. From: Cosgrove, J.W. & Engelder, T. (eds.). The initiation, propagation, and arrest of joints and other fractures. Geological Society, London, Special Publications, v. 231, p. 73-87.
- Olsen, J.E., 1993, Joint pattern development; effects of subcritical crack growth and mechanical crack interaction. *Journal of Geophysical Research*, v. 98, no. B7, p. 12251-12265.
- Omatsola, T., 2002, Origin and distribution of friable and cemented sandstones in outcrops of the Pennsylvanian Jackfork Group, Southeast Oklahoma. University of Oklahoma Masters Thesis, Norman, Oklahoma.
- O'Sullivan, R.B., 2000, Correlation of Middle Jurassic Group and related rocks from Bluff to Monticello in southeastern Utah. USGS Miscellaneous Field Studies Map MF-2351.
- Ozkaya, S. I., Kolkman, W., and Amthor, J., 2003, Mechanical layer-dependent fracture characteristics from fracture density vs. TVD cross plots. Examples from horizontal wells in carbonate reservoirs, north Oman. From: 2003 American Association of Petroleum Geologists International Conference & Exhibition Technical Program, extended abstract.
- Pollard, D.D. and Segall, P., 1987, Theoretical displacements and stresses near fractures in rock: with applications to faults, joints, veins, dikes and solution surfaces. In *Fracture Mechanics of Rock* (ed. B.K. Atkinson). Academic Press, Inc., Orlando, p. 277-349.
- Putot, C., Chastanet, J., Cacas, M.C., and Daniel, J.M., 2001, Fracturation naturelle d'un massif rocheux: Diaclases et couloirs de fracturation. *Oil & Gas Science and Technology – Rev. IFP*, v. 56, no. 5, p. 431-449.
- Reches, Z., 1998, Tensile fracturing of stiff rock layers under triaxial compressive stress states. 3rd NARMS, Mexico, June 1998, *International Journal of Rock Mechanics and Mining Science*, v. 35, no. 4-5, Paper No. 70.
- Renshaw, C.E., 1997, Mechanical controls on the spatial density of opening-mode fracture networks. *Geology*, no. 25, p. 923-926.
- Renshaw, C.E. and Pollard, D.D., 1995, An experimentally verified criterion for propagation across unbounded interfaces in brittle linear elastic materials.

International Journal of Rock Mechanics and Mining Sciences and Geomechanics Abstracts, v. 32, no. 3, p. 237-259.

Rijken, P. and Cooke, M.L., 2001, Role of shale thickness on vertical connectivity of fractures in the Austin Chalk, Texas: application of crack-bridge theory. *Tectonophysics*, v. 337(1/2), p. 117-133.

Rogers, C.M. and Engelder T., 2004, The feedback between joint-zone development and downward erosion of regularly spaced canyons in the Navajo Sandstone, Zion National Park, Utah. In: *The initiation propagation, and arrest of joints and other fractures*, Geological Society Special Publications, v. 231, p. 49-71.

Sagy, A. and Reches, Z., 2006, Joint intensity in sedimentary rocks: The unsaturated, saturated, supersaturated, and clustered classes. Submitted to *Israel Journal of Earth Sciences*. <http://earthquakes.ou.edu/reches/pub.html>

Sagy, A., Reches, Z., and Roman, I., 2001, Dynamic fracturing, rock fragmentation and joint density: Field and experimental observations. *Journal of Structural Geology*, v. 23, p. 1223-1239.

Shackleton, J.R., Cooke, M.L., and Sussman, A.J., 2006, Evidence for temporally changing mechanical stratigraphy and effects on joint-network architecture. *Geology*, v. 33, no. 2, p. 101-104.

Slatt, R.M., Weimer, P., Al-Siyabi, H.A., and Williams, E.T., 2000, Outcrop analogs of turbidite petroleum reservoirs for assessing volumetric, development drilling, and simulation scenarios. In: *Marine Clastics in the southern Midcontinent, 1997 symposium*, Johnson, Circular – Oklahoma Geological Survey, p. 205.

Slatt, R.M., Al-Siyabi, H., Williams, E.T., Stone, C.G., Weimer, P., Davis, R.J., and Jordan, D.W., 1997, Arkansas turbidite studies may aid Oklahoma Jackfork exploration. *Oil and Gas Journal*, v. 95, p. 67-72.

Suneson, N.H., 1988, The geology of the TI Valley Fault in the Oklahoma Ouachita Mountains. *Oklahoma Geologic Survey Guidebook 25*, p. 33-47.

Tindall, S., 2006, Jointed deformation bands may not compartmentalize reservoirs. *American Association of Petroleum Geologists Bulletin*, v. 90, no. 2, p. 177-192.

Tindall, S. and Davis, G., 2003, Joint spacing and distribution in deformation band shear zones. *Geological Magazine*, v. 140, no. 1, p. 1-9.

- Underwood, C., Cooke, M.L., Simo, J.A., and Muldoon, M.A., 2003, Stratigraphic controls on vertical fracture patterns in Silurian dolomite, northeastern Wisconsin. American Association of Petroleum Geologists Bulletin, v. 87, no. 1, p. 121-142.
- Viele, G.W. and Thomas, W.A., 1989, Tectonic synthesis of the Ouachita orogenic belt. In: Hatcher, R.D., Jr., Thomas, W.A., and Viele, G.W., eds., The geology of North America, v. F-2: The Appalachian-Ouachita orogen in the United States, Boulder, Colorado, Geological Society of America, p. 695-728.
- Wu, H. and Pollard, D.D., 1995, An experimental study of the relationship between joint spacing and layer thickness. Journal of Structural Geology, v. 17, p. 887-905.
- Yose, L., Brown, S., Davis, T.L., Eiben, T., Kompanik, G.S., and Maxwell, S.R., 2001, 3-D geologic model of a fractured carbonate reservoir, Norman Wells Field, NWT, Canada. Bulletin of Canadian Petroleum Geology, v. 49, no. 1, p. 86-116.

CHAPTER VI

CONCLUSIONS

The main conclusions and some recommendations for future work are summarized below, following the general order of the investigation.

(1) Fracture initiation and propagation are highly dependent on the tectonic state of stress, the load conditions driving fracturing, and the rheology. Because the mechanical processes evolve over time, the local stress conditions and the local mechanical properties also progress uniquely. A result is that the character of the fracturing changes depending on the evolving stress-strain pattern. This is the case for propagation of a single fracture such as a hydraulic fracture segment, as well as for infilling or saturation of fractures in a layer or layered sequence.

(2) Failure and fracture propagation occur as regions of rock progress from elastic, recoverable deformation (infinitesimal strain) to inelastic deformation (finite strain). A useful way to characterize this behavior is by quantifying the stages of deformation as values on the stress-strain curve from rock mechanics experiments. The concept of continuum damage evolution quantifies the magnitude and mode of brittle microcracking and accurately facilitates stiffness degradation. This approach is consistent with micromechanical theory and can be implemented using finite element modeling. 3D FE simulations were run to calibrate a rheologic model to data from rock mechanics experiments on Berea sandstone. Calibration and modeling of additional rock types and loading scenarios would be useful and would help constrain the limitations of the numerical material model. A related issue that was not covered

here but should be revisited in the future is damage and fracture propagation across rheologic transitions.

(3) Since fractures tend to propagate into zones of weakness, the extent of strain localization and damage accumulation ahead of the crack dictate the character of propagation. This is further complicated by the inclusion of transient/dynamical effects, which are always physically present, but because of the mathematical difficulty are not always solved for. The FE simulations showed that branching and segmentation were related to arrest and rupture behavior, which was controlled by the local state of stress. Heterogeneous stress fields shortened the arrest/build-up periods and elongated the rupture/release periods. Regions with low differential stress did the opposite and prolonged the damage build-ups, resulting in short, but complex ruptures.

(4) The FE propagation simulations and a model for natural fracture reactivation were applied to understand hydrofracture operations in an unconventional hydrocarbon reservoir. In several Barnett Shale wells, when wellbore stress data was used, a good match was found between the predictions of the models and those interpreted from pressure-time curves, pump-in tests, and microseismic events maps. The usefulness of applying the models to the qualities of other fields is apparent.

(5) Fracture distributions from exposures in Utah, Oklahoma, and Arkansas indicate that fracture density can generally be normalized by the layer thickness, though the correlation between density and thickness varies from layer to layer and for different rock types. If the fracture spacing is predicted with the assumption of an elastic medium, the saturation concept precludes the super-saturation and clustering classes. The results indicate that the occurrence of fracture corridors and other zones

of high fracture density should be examined as a function of the evolving rock properties of the host layer. It is also suggested that the properties of neighboring layers and the fracture dimensions are important. More work is needed to test this assertion.

RECOMMENDATIONS FOR FUTURE WORK

The processes of stress-induced yielding, strain-dependent damage accumulation, strength degradation, and associated stress relaxation are all fully active during various types of structural deformation. A methodology was developed in this study to incorporate these processes to evaluate fracture development in rock layers. The focus was on the scale of micro-damage to fracturing in a single layer. However, the range of geologic problems for which this approach is valid is not limited to the small scale (Fig. 6.1). Rather, the development of large scale structures must also be understood in light of complex, nonlinear processes since they are also products of finite deformation. For example, analysis and restoration of fault-fold systems requires understanding of the mechanical processes associated with their development (Heesakkers et al., 2009). An extension of the damage modeling that was presented here is included in the simulations of Heesakkers (2009) in which the Berea sandstone rheology is applied to study ramp-induced folding. In this case, implementation of a more mechanically representative rheology produced significantly different structures that would have been difficult to explain otherwise (Fig. 6.2). It is anticipated that the methodology and hydrofracture application presented in this study will open the doors to study many other geologic problems in greater detail.

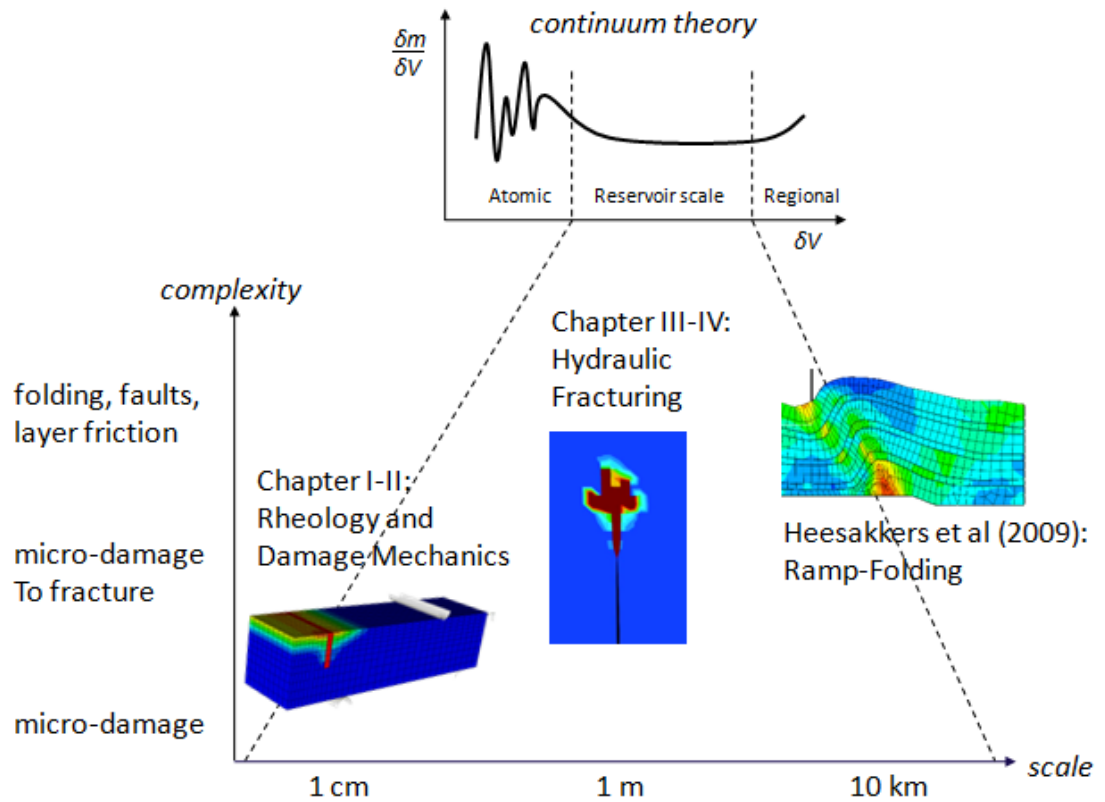


Figure 6.1. Range of scales for which the present continuum approach is valid and examples of geologic problems at each scale. The three images are from FE simulations conducted using the Berea sandstone damage rheology developed in Chapter 2.

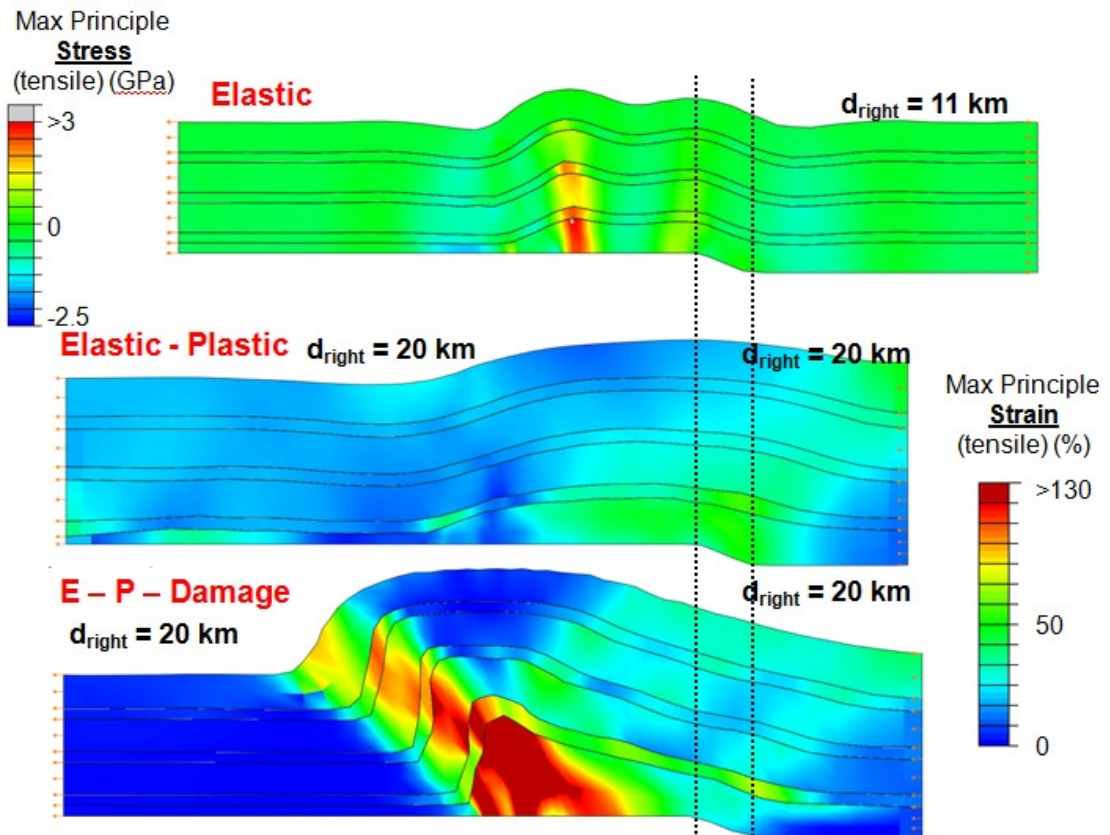


Figure 6.2. Finite element simulations of ramp-induced folds for three different levels rheologic complexity, based on the Berea sandstone model (Chapter 2) (Heesakkers, 2009; Heesakkers et al., 2009). Elastic material (top) yields harmonic, symmetric folding. Implementation of plasticity (bottom) results in strain localization and asymmetric folding. Note the elastic model also produces tensile stresses > GPa, well exceeding the stress limit for rock. Principal strains are plotted in the lower two models.

REFERENCES

Heesakkers, V., Busetti, S., and Reches, Z., 2009, Numerical simulation of reservoir structures, Part III: Folding of a layered rock sequence in flat-ramp-flat thrust system. Abstract: AAPG Annual Convention and Exhibition, Denver, Colorado, June 7-10, 2009.

Heesakkers, V., 2009, PhD dissertation, University of Oklahoma, Norman, Oklahoma, in prep.